Cryo-EM Structures Reveal How Hsp90 and Cochaperones Regulate the Glucocorticoid Receptor

by
Chari Noddings

DISSERTATION
Submitted in partial satisfaction of the requirements for degree of
DOCTOR OF PHILOSOPHY

in

Biochemistry and Molecular Biology

in the

GRADUATE DIVISION
of the
UNIVERSITY OF CALIFORNIA, SAN FRANCISCO

Approved:

DocuSigned by:
Daniel Southworth
031AA0767EFF409...
Daniel Southworth
Chair

DocuSigned by:
David A. Agard
David A. Agard

DocuSigned by:
Jason Gestwicki
Jason Gestwicki

DocuSigned by:
Geeta Narlikar
EE2E6D32EE3043B...
Geeta Narlikar

Committee Members

Acknowledgements

My time in graduate school has been an incredibly fun and rewarding experience. Of course, there were many challenges and late nights along the way, but I learned so much during my time at UCSF and I met wonderful people who have always kept my spirit high.

First, I want to thank David Agard for all his mentorship and guidance throughout the years. I truly value the scientific environment that David has fostered, in which I had the intellectual freedom to guide my projects and follow my interests. The science is rigorous and challenging, but David has always been supportive and encouraging.

Many thanks to my thesis committee for helpful suggestions, expertise, and support: Dan Southworth, Geeta Narlikar, and Jason Gestwicki.

I cannot thank Ray Wang enough for his mentorship and friendship. None of these projects would have been possible without his training and guidance, but even more so, Ray taught me how to think about science and how to be a scientist. We got to share the ups and downs of a scientific project and science feels a lot lonelier without Ray around. I will always miss our afternoon coffee chats.

To my grad student friends—Eliza Nieweglowska, Maru Jaime-Garza, Cynthia Chio, Carlos Nowotny, Sasha Dickinson, and Melissa Méndez—you all made the science fun. I can't thank you all enough for the laughter and joy in the lab and out.

The Agard lab has been such a wonderful environment because of the people, who have been so kind and generous with their time—Michelle Moritz, Tristan Owens, Evita Tsiolaki, Feng Wang, Sam Li, Deepto Mozumdar, Zhen Chen, Natalie Whitis, and

Smriti Sangwan. A special thanks to Mariano Tabios who keeps the lab going against all odds.

None of my projects would be possible without the tireless work of David Bulkley, Eric Tse, Glenn Gilbert, and Zanlin Yu, who keep the EM facility running smoothly. I especially want to thank David Bulkley for all the training, assistance with collections, and his kindness and positivity.

All of my projects built on the *in vitro* reconstituted GR chaperone cycle, which provided an amazing model system for scientific investigation. Elaine Kirschke deserves endless thanks for her pioneering work in building this system and laying the groundwork. Elaine's lab notebooks and thesis were foundational to my research.

Thank you to my mom and dad for encouraging me to pursue a PhD, but also for nurturing all my interests outside of science that make my life so enjoyable. I am lucky to have such caring parents.

To Louis—thanks for being an amazing partner. You make me laugh and bring joy to my world. Thanks for reminding me to take breaks, for bringing me food during late nights in lab, for keeping me sane during the lockdown, and for always supporting me.

Acknowledgement of Previously Published Work

Chapter 2 of this thesis was published under the following citation:

Wang, R. Y., Noddings, C. M., Kirschke, E., Myasnikov, A. G., Johnson, J. L., & Agard, D. A. (2022, Jan). Structure of Hsp90-Hsp70-Hop-GR reveals the Hsp90 client-loading mechanism. *Nature, 601*(7893), 460-464. https://doi.org/10.1038/s41586-021-04252-1

Chapter 3 of this thesis was published under the following citation:

Noddings, C. M., Wang, R. Y., Johnson, J. L., & Agard, D. A. (2022, Jan). Structure of Hsp90-p23-GR reveals the Hsp90 client-remodelling mechanism. *Nature, 601*(7893), 465-469. https://doi.org/10.1038/s41586-021-04236-1

Abstract

Cryo-EM Structures Reveal How Hsp90 and Cochaperones Regulate the Glucocorticoid Receptor

Chari Marin Noddings

Laboratory of Dr. David Agard

Maintaining protein homeostasis is fundamental for organismal survival. Integral to this process are molecular chaperones, including the highly conserved heat shock protein 90 (Hsp90). Hsp90 associates with many ‘client’ proteins throughout their lifetime, regulating the transition from partially unfolded, inactive states to native, active states. However, a mechanistic understanding of how Hsp90 remodels and regulates client proteins is lacking. One class of clinically important Hsp90 clients are the steroid hormone receptors (SHRs), including the model Hsp90 client, the glucocorticoid receptor (GR). GR is a ligand-activated transcription factor that constantly relies on Hsp90 to maintain its activity. In addition to facilitating folding of GR, Hsp90 regulates multiple steps in the GR activation pathway, including ligand binding, post-translation modifications (PTMs), nuclear translocation, and DNA binding. To perform these regulatory functions, Hsp90 requires the molecular chaperone Hsp70 as well as a collection of cochaperones (p23, Hop, FKBP51, FKBP52, PP5, and others).

Using cryo-EM, as well as biochemical and biophysical techniques, we investigated the molecular mechanisms describing how Hsp90, Hsp70, and various cochaperones modify the conformational state of GR and regulate various steps in the GR activation pathway. We present two cryo-EM structures that reveal, for the first time, the mechanism of how Hsp90 folds a client protein. We present the GR-loading

complex (GR:Hsp90:Hsp70:Hop), in which GR is stabilized in an inactive, partially unfolded conformation that cannot bind ligand, and the GR-maturation complex (GR:Hsp90:p23), in which GR is restored to a folded, ligand-bound, active state. Together, our structures reveal how Hsp70 and Hsp90 cooperate to regulate the conformational state of a client to directly control the client's ability to bind ligand for activation. We also present three additional cryo-EM structures (GR:Hsp90:FKBP51, GR:Hsp90:FKBP52, and GR:Hsp90:PP5), which demonstrate how Hsp90 acts a regulatory platform to couple the conformational state of the client protein to distinct client fates through interactions with various cochaperones.

Table of Contents

List of Figures

Chapter 1

Chapter 2

Chapter 3

Chapter 4

Chapter 5

Chapter 6

Chapter 7

List of Tables

Chapter 3

Chapter 1 Introduction

Hsp90

The maintenance of protein homeostasis (proteostasis) is necessary for cellular growth and survival (Labbadia & Morimoto, 2015; Wolff et al., 2014). Essential to this process are the molecular chaperones, which facilitate the folding of 'client' proteins (Hartl et al., 2011). Hsp90 (heat shock protein 90) is a highly abundant, evolutionary conserved molecular chaperone that facilitates the folding of hundreds of client proteins (Schopf et al., 2017; Taipale et al., 2010). Unique among molecular chaperones, Hsp90 often acts in the late stages of folding to facilitate client 'maturation' from partially unfolded, inactive states to native, active states (Fig. 1) (Kirschke et al., 2014; Verba et al., 2016). Interestingly, many clients obligately depend on Hsp90 to maintain these 'mature', functional conformations throughout their protein lifetime (Nathan & Lindquist, 1995; Nathan et al., 1997). Hsp90 clients are a highly diverse class of proteins, with seemingly no shared sequence or structural motifs, making the determinants of client-specificity unclear (a list of client proteins is maintained at https://www.picard.ch/). Hsp90 clients are enriched in signaling proteins and transcription factors, which positions Hsp90 at a clinically important regulatory hub for many essential cellular processes (Fig. 2) (Taipale et al., 2012).

In cancer cells, Hsp90 maintains the functional conformation of many oncogenic proteins, including kinases and transcription factors, making many cancer cells essentially 'addicted' to Hsp90 (Trepel et al., 2010). As such, Hsp90 has been identified as a drug target for cancer therapies with the goal of simultaneously disrupting multiple

Hsp90-dependent pathways that support cancer cell survival and growth (Blagosklonny, 2002; Neckers, 2007). Towards this 'multi-hit' therapeutic goal, numerous potent and selective Hsp90 inhibitors have been generated, but unfortunately few Hsp90 inhibitors have yet to be approved by the FDA due to limited efficacy and off-target effects (Jaeger & Whitesell, 2019; Neckers et al., 2018). Lacking is a mechanistic understanding of how Hsp90 inhibitors affect client function to regulate cellular pathways (Neckers et al., 2018). A mechanistic understanding of how Hsp90 facilitates the folding and maturation of clients, as well as how Hsp90 regulates client function beyond folding, would allow for more nuanced therapeutic strategies (Neckers et al., 2018; Sawarkar & Paro, 2013; Trepel et al., 2010).

Hsp90 is a highly dynamic protein that adopts multiple conformational states coupled to an ATPase cycle. Hsp90 contains three domains: an N-terminal domain (NTD), which binds ATP, a middle domain (MD), which binds clients, and a C-terminal domain (CTD), which is constitutively homodimerized (Schopf et al., 2017) (Fig. 3a). Between the NTD and MD is a long, approximately 50-residue flexible "charged linker", containing many basic and acidic residues. The CTD also contains a long, approximately 30-residue unstructured tail with an "MEEVD" motif at the C-terminus, which binds TPR (tetratricopeptide repeat) domains. Hsp90 functions as a constitutive dimer that undergoes large open-to-closed transitions regulated by ATP binding and ATP hydrolysis (Fig. 3b) (Krukenberg et al., 2011). In the apo state, the dimer adopts an open "v" conformation, with the Hsp90 CTDs dimerized (Krukenberg et al., 2008; Shiau et al., 2006). In the open state, the lumen of Hsp90 (the space between the Hsp90 MDs) is accessible for client binding. In contrast, the ATP or ADP-bound states adopt a

closed conformation, in which the NTDs additionally dimerize, forming a closed, slightly twisted state (Ali et al., 2006; Verba et al., 2016). In the closed state, the Hsp90 lumen forms a tight, channel-like space. The closed state can be stabilized by the addition of molybdate, an inorganic anion that mimics the γ-phosphate of ATP and traps Hsp90 in a post-hydrolysis state. Hsp90 reopening is thought to be catalyzed by ATP hydrolysis, which allows client release and resets the Hsp90 conformational cycle.

In addition, eukaryotic Hsp90 functions with a large variety of “cochaperones”, which are a group of proteins that regulate the Hsp90 conformational cycle. Cochaperones directly bind to Hsp90 and specifically interact with distinct Hsp90 conformations (Schopf et al., 2017; Taipale et al., 2010) (a list of cochaperones is maintained at https://www.picard.ch/). The Hsp90 cochaperones contain specific Hsp90-interacting domains. Two common examples are TPR domains, which bind the Hsp90 MEEVD C-terminal tail (Scheufler et al., 2000), or CS domains, which bind the closed NTD dimer interface (Ali et al., 2006). Cochaperones often bind distinct Hsp90 conformations and can regulate the Hsp90 ATPase cycle. For example, p23 inhibits Hsp90 ATP hydrolysis and specifically binds the closed Hsp90 conformation (Ali et al. 2006). Aha1 (ATPase homolog 1) accelerates Hsp90 ATP hydrolysis and also binds the closed Hsp90 conformation (Liu et al., 2020; Retzlaff et al., 2010). In contrast, Hop (Hsp70/Hsp90 organizing protein) binds a semi-closed, intermediate conformation of Hsp90 (Southworth & Agard, 2011). Some Hsp90 cochaperones function with Hsp90 in a general manner, serving a variety of different client classes, such as p23 and Hop, while other cochaperones function in a client-specific manner, such as Cdc37 (cell division cycle 37), which is kinase-specific (Taipale et al., 2010; Taipale et al., 2012). In

addition to regulating Hsp90, many Hsp90 cochaperones have their own chaperoning function and/or enzymatic function independent of Hsp90. These include, but are not limited to phosphatases, E3 ligases, and peptidyl-proline isomerases (PPIases). Thus, cochaperones can also directly regulate client function beyond Hsp90-mediated protein folding, such as client post-translational modifications (PTMs) (phosphatases, E3 ligases), client degradation (E3 ligases), client hand-off from Hsp70 (Hop), or client localization (FKBPs, Cyp40) (Fig. 4). Altogether, the cochaperones provide an additional layer of complexity that allows Hsp90 to act as a regulatory platform for client proteins. In this manner, Hsp90 can couple the conformational state of a protein to interactions with distinct cochaperones, which in turn can regulate multiple aspects of client function beyond protein folding.

The complexity of the Hsp90 conformational cycle and association with dozens of cochaperones provides Hsp90 with broad specificity to regulate the folding and maturation of a wide variety of clients. However, a mechanism describing how Hsp90 facilitates client folding is lacking. Specifically, how is Hsp90-dependent client folding coupled to the Hsp90 conformational cycle and cochaperone binding? The first picture of the Hsp90 chaperoning mechanism was revealed with a long-awaited structure of Hsp90 bound to a client protein, determined by Klim Verba in the Agard lab (Verba et al., 2016). In this cryo-EM structure, a kinase client, Cdk4 (cyclin dependent kinase 4), adopts a partially unfolded conformation, with an unstructured segment threaded through the lumen of the closed, ADP:molybdate-bound Hsp90 (Fig. 5). The two kinase lobes (N-lobe and C-lobe) are separated, binding to the either side of the Hsp90 dimer, and rendering the kinase in an inactive state. This structure demonstrated that Hsp90

acts as a clamp, that closes around the partially unfolded client, with an unfolded strand of the client encapsulated and protected by the Hsp90 lumen. Furthermore, the kinase-specific cochaperone, Cdc37, wraps around the closed Hsp90 and, surprisingly, directly binds the kinase C-lobe by mimicking part of the kinase N-lobe to stabilize this partially unfolded domain. This structure demonstrated that Hsp90 cochaperones not only stabilize distinct Hsp90 conformations, but are also directly involved in binding and stabilizing the partially unfolded conformation of the client, assisting in the client folding process. This structure provided many fundamental insights into the Hsp90 chaperoning mechanism, but many questions remain: how does Hsp90 refold a partially unfolded client to facilitate client maturation, how does Hsp90 regulate the folding of non-kinase clients, and how do other cochaperones beyond Cdc37 facilitate client maturation and/or other aspects of client function?

The Glucocorticoid Receptor

One model class of Hsp90 clients are the steroid hormone receptors (SHRs), which are a clinically important group of steroid-activated transcription factors. There are five SHRs: the glucocorticoid receptor (GR), the progesterone receptor (PR), the mineralocorticoid receptor (MR), the androgen receptor (AR), and the estrogen receptor (ER). Each SHR relies on Hsp90 for functional maturation, but to varying degrees. GR is the most highly dependent on Hsp90, requiring Hsp90 to maintain its activity throughout its lifetime. Thus, GR is a so called ‘obligate’ Hsp90 client and has been an extensively studied model Hsp90 client (Lorenz et al., 2014; Morishima et al., 2000; Nathan et al., 1997; Picard et al., 1990; Pratt & Toft, 1997; Smith & Toft, 2008). GR is a

ubiquitously expressed SHR that binds the endogenous hormone, cortisol, to regulate gene expression. Common to the other SHRs, GR has an intrinsically disordered NTD, with transcriptional activation (transactivation) activity; a zinc-finger DNA-binding domain that homodimerizes; an unstructured hinge-region; and a C-terminal ligand-binding domain that also homodimerizes (LBD) (Fig. 6) (Bledsoe et al., 2002; Luisi et al., 1991; Weikum et al., 2017). Unliganded (apo) GR is predominantly cytoplasmic, but upon binding of the endogenous ligand cortisol to the ligand binding domain (LBD), GR is rapidly translocated to the nucleus (Fig. 7). In the nucleus, the GR DNA-binding domain (DBD) cooperatively dimerizes on a GR-binding sequence (GBS) present in GR response elements (GREs) in the genome (Chandler et al., 1983; Luisi et al., 1991; Meijsing et al., 2009; Watson et al., 2013). Upon GRE binding, GR nucleates the assembly of transcription regulatory complexes, which include co-regulators, chromatin remodelers, and histone modifying enzymes (Bledsoe et al., 2002; Fryer & Archer, 1998; Weikum et al., 2017). GR is thought to act as a pioneer factor, binding to nucleosome-occupied regions and recruiting factors to alter the chromatin landscape at thousands of cell-specific genomic locations (Biddie & John, 2014; Fryer & Archer, 1998; Johnson et al., 2018; Perlmann, 1992; Zaret & Yamamoto, 1984). Ultimately, GR regulates the expression of large transcriptional programs, essential for cellular functions such as growth, inflammation, and stress response (Oakley & Cidlowski, 2013). As such, GR is a potent therapeutic target for cancer and thus it is both of basic and translational importance to gain a mechanistic understanding of how Hsp90 affects GR function (Conzen, 2008).

The GR Chaperone Cycle

Early pioneering work demonstrated that, *in vivo*, the GR LBD is complexed with Hsp90 and the molecular chaperone Hsp70, along with a variety of associated cochaperones, which 'transformed' GR into a ligand-binding competent state and were also required to maintain GR in this active state (Lorenz et al., 2014; Morishima et al., 2000; Nathan et al., 1997; Picard et al., 1990; Pratt & Toft, 1997; Smith & Toft, 2008). Why GR required Hsp90, Hsp70, and cochaperones to constantly maintain its active state beyond initial chaperone-mediated folding was puzzling. A fundamental discovery came from the work of a previous graduate student in the Agard lab, Elaine Kirschke, who pioneered the *in vitro* reconstitution of the minimal GR chaperone system, which included Hsp90, Hsp70, Hsp40, Hop, and p23 (Kirschke et al., 2014). In this groundbreaking work, Kirschke et al. purified the recombinant, apo form of the GR LBD. Surprisingly, the purified GR could bind ligand with high affinity in the absence of the chaperones. In fact, when Hsp70 and the cochaperone Hsp40 were added to the purified GR, GR ligand-binding was inhibited. Addition of Hsp90, Hop, and p23 subsequently restored GR ligand-binding (Fig. 8a). Further experiments demonstrated that the chaperone cycle increases the GR ligand-binding affinity compared with GR alone, with both the ligand on and off-rates accelerated in the chaperone cycle (Fig. 8b,c). Altogether, this work explains the Hsp90-dependence of GR ligand-binding activity and demonstrated that Hsp70 and Hsp90 operate in a functionally antagonistic manner to regulate GR activity, which was later demonstrated for other Hsp90 clients, including p53 and Ago2 (Boysen et al., 2019; Dahiya et al., 2019; Tsuboyama et al., 2018).

Additional biochemical experiments by Kirschke et al. with the *in vitro* reconstituted GR chaperone cycle revealed that GR cycles through a series of distinct chaperone complexes, which constantly inhibit and reactivate GR ligand-binding (Fig. 9). In this cycle, GR is first inhibited by Hsp70, assisted by the cochaperone Hsp40. Hsp40 accelerates the ATPase rate of Hsp70 to generate the high-affinity client-binding ADP state of Hsp70. The inhibited GR is then loaded onto Hsp90 by Hsp70 to form an inactive GR:Hsp90:Hsp70:Hop “loading complex”. Hop stabilizes Hsp90 in a semi-closed conformation to facilitate client loading and simultaneously binds the Hsp90 and Hsp70 EEVD motifs (Scheufler et al., 2000; Southworth & Agard, 2011). Then, Hsp70 and Hop are released and the cochaperone p23 is incorporated to form a GR:Hsp90:p23 “maturation complex”, which restores GR ligand-binding with enhanced affinity. Progression through this cycle is coordinated by cochaperone binding and the ATPase activity of both Hsp70 and Hsp90, which dictate the conformational rearrangements of the chaperones (Krukenberg et al., 2011; Rosenzweig et al., 2019; Schopf et al., 2017).

Altogether, the coordinated actions of Hsp70, Hsp90, and cochaperones control the ligand-binding activity of GR in order to regulate GR activation *in vivo*. Given that Hsp70 and Hsp90 are molecular chaperones, these chaperones likely remodel the conformation of GR to control the ligand-binding activity. Indeed, hydrogen deuterium exchange-mass spectrometry (HDX-MS) experiments indicated that Hsp70 partially unfolds GR to inhibit ligand-binding, thus presumably Hsp90 refolds GR to restore ligand-binding (Kirschke et al., 2014). A low resolution cryo-EM structure of the GR-maturation complex indicates that GR is likely in a folded conformation once bound to

Hsp90:p23 (Lorenz et al., 2014). How the chaperones specifically remodel the conformation of GR to control access to the buried, hydrophobic ligand-binding pocket is unclear. Furthermore, how Hsp90 would directly restore ligand-binding is unknown—specifically, does Hsp90 release GR in a folded, ligand-binding competent state or is GR ligand-binding facilitated by Hsp90 in a more direct way? Beyond regulating ligand-binding, Hsp90, aided by cochaperones, is also known to regulate other steps in GR function, including facilitating degradation, altering post-translational modifications, promoting nuclear translocation, and regulating GRE-binding (Echeverria & Picard, 2010). How Hsp90 couples the conformational state of GR to such a wide variety of functional outcomes is critical to understanding the essential role of Hsp90 in client regulation.

Thesis Project Objective

The object of this thesis project was to determine how Hsp90 remodels the conformation of GR to restore GR ligand-binding and how the cochaperones p23, FKBP51, and FKBP52 assist with the functional maturation and regulation of GR. My approach was to use the *in vitro* reconstituted GR chaperone system to trap specific GR:Hsp90 complexes in the GR chaperone cycle with a variety of bound cochaperones and utilize single-particle cryo-EM to determine high-resolution structures of these complexes. Accompanying *in vitro* and *in vivo* GR activation assays were used to validate the structural models and generate mechanistic insights.

Author Contributions

Much of this work was done in close collaboration with Dr. Ray Wang (former Agard lab post-doctoral researcher) and *in vivo* experiments were performed in collaboration with Jill Johnson (University of Idaho). Maru Jaime-Garza, Claire Kokontis, Estelle Ronayne, and Evelyn Hernandez worked on additional cochaperone projects. Elaine Kirschke provided helpful discussions.

Figures

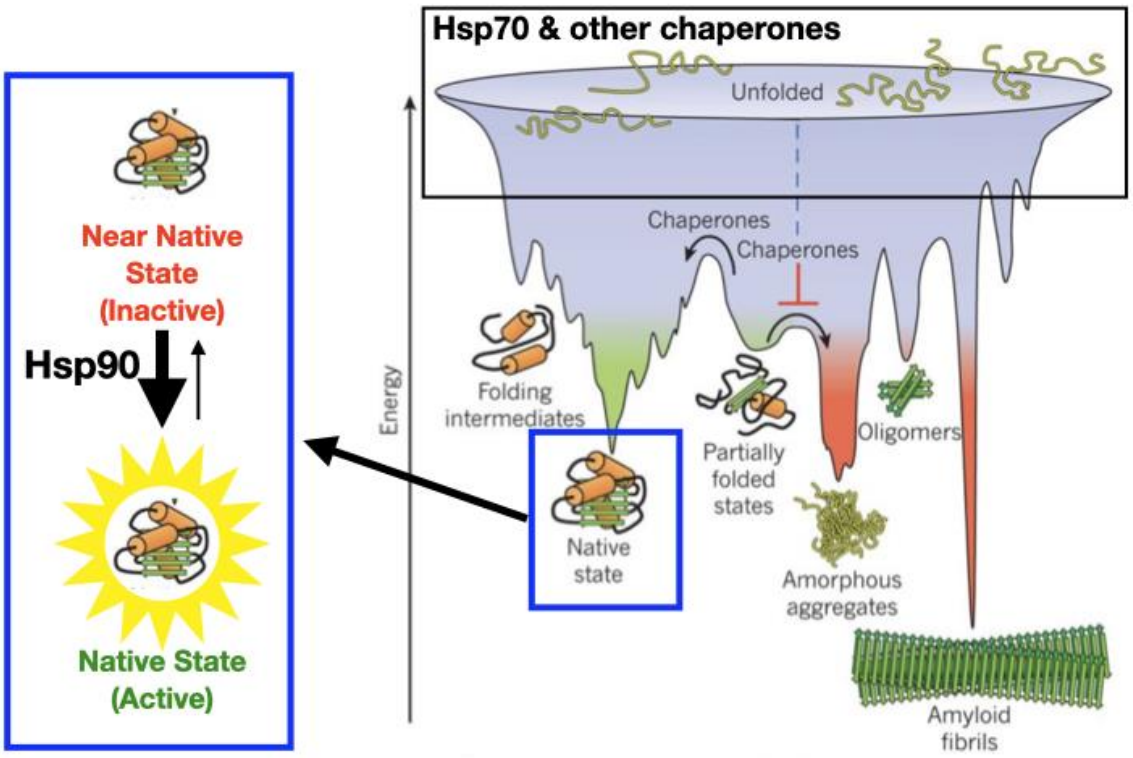

Fig. 1.1: The energy landscape of folding and role of molecular chaperones
A protein folding energy landscape adapted from Hartl et al. 2011. Unfolded proteins adopt high energy extended conformations. As protein folding occurs, the protein moves towards lower energy native states. However, folding intermediates or off-pathway aggregates can become trapped in energetic wells. The role of molecular chaperones is to help proteins overcome these energetic barriers to folding and prevent off-pathway aggregation. Most molecular chaperones, such as Hsp70, work in the early stages of folding (black box), while Hsp90 uniquely works in the late stages of folding (blue box). Hsp90 facilitates folding of near-native, inactive client conformations, to native, active conformations.

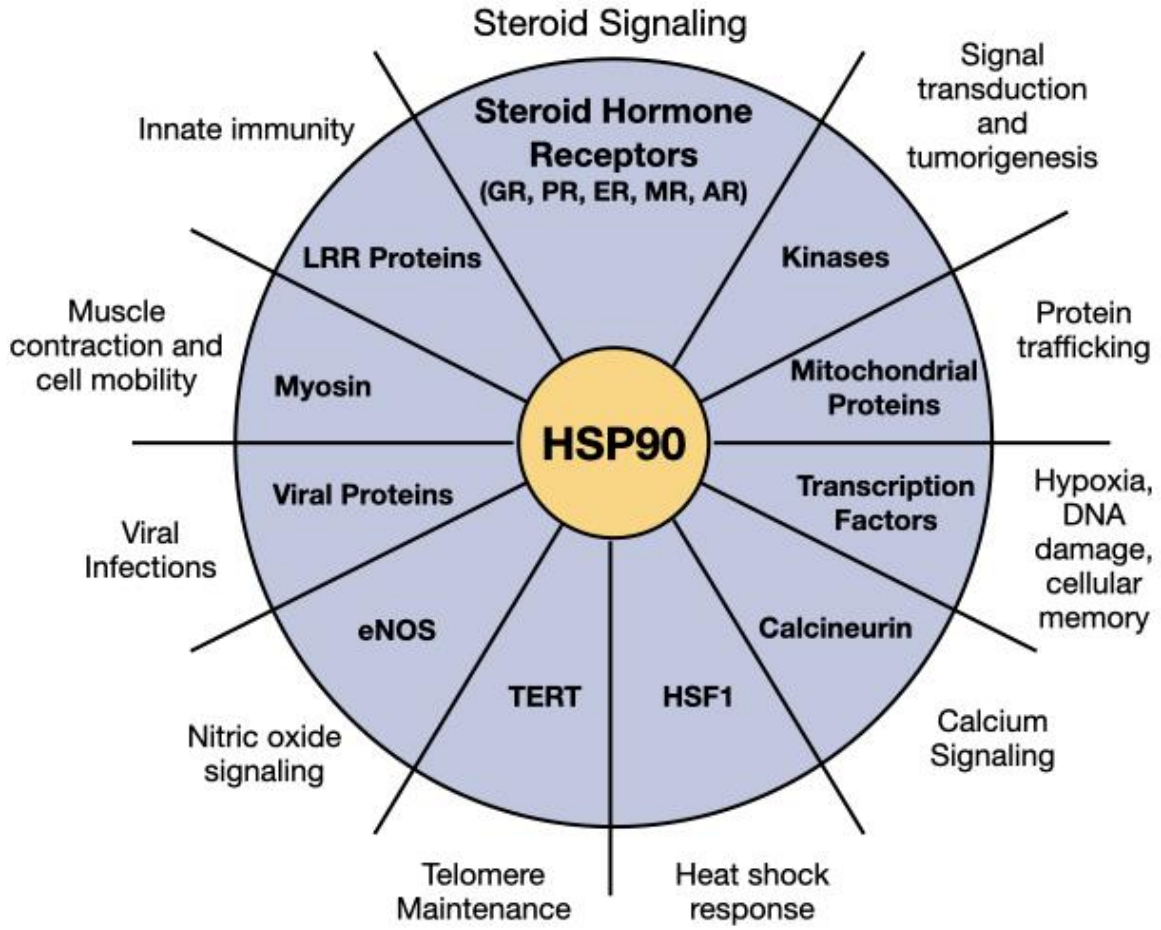

Fig. 1.2: Hsp90 clients are enriched in critical signaling molecules
A schematic adapted from Taipale et al. 2010 depicting Hsp90 at the hub of regulation for a number of critical cellular functions. Hsp90 is able to regulate this diversity of essential functions through interactions with a variety of client classes, which are enriched in signaling molecules.

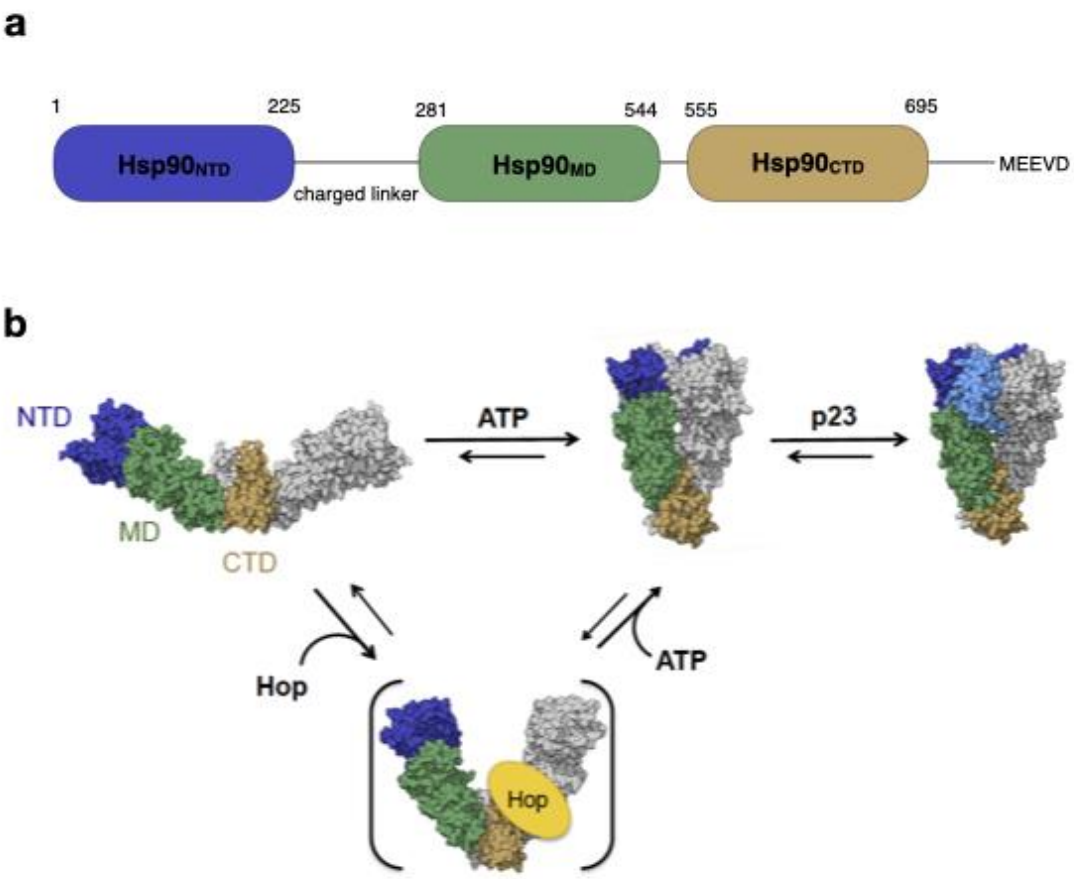

Fig. 1.3: The human, cytosolic Hsp90α domains and conformational cycle
a, The domains and motifs of human, cytosolic Hsp90α. **b**, A diagram of the Hsp90 conformational cycle (Kirschke, 2015). Hsp90 transitions from an apo, open "v" conformation on the left, to an ATP-bound closed, twisted conformation. The cochaperone Hop stabilizes an intermediate, apo, semi-open Hsp90 conformation. The cochaperone p23 stabilizes the closed, twisted conformation (right).

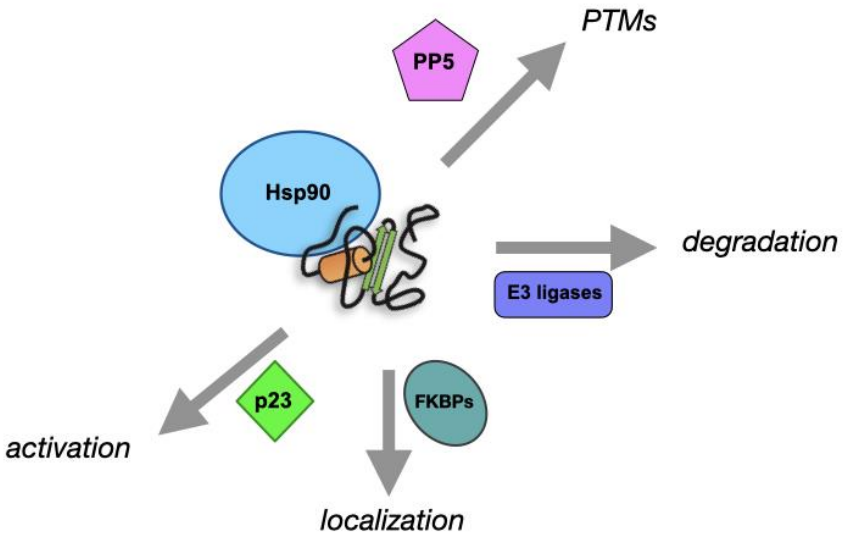

Fig. 1.4: Hsp90 associates with cochaperones to regulate client function
A diagram demonstrating that Hsp90 can act as a platform to regulate client functions beyond folding. Regulation of search a diversity of client functions is achieved by associated with a variety of different cochaperones, such as the ones depicted: p23, FKBPs, E3 ligases, and PP5.

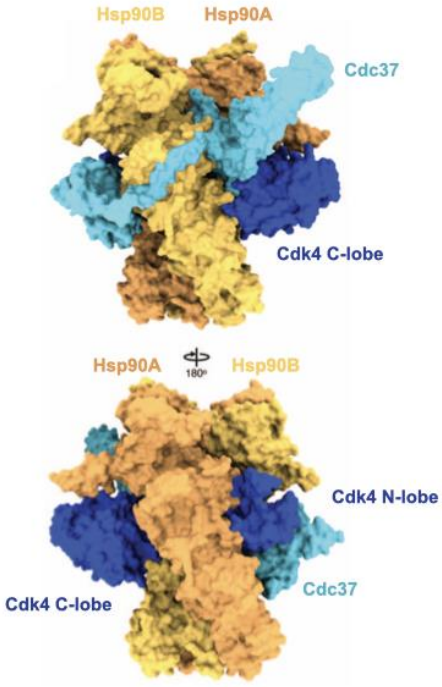

Fig. 1.5: The cryo-EM structure of Cdk4:Hsp90:Cdc37
The cryo-EM structure of the Cdk4:Hsp90:Cdc37 complex (PDB ID 5FWL) (Verba et al., 2016). This structure demonstrated for the first time that Hsp90 clients are threaded through the lumen of the closed Hsp90. In this structure, the kinase client, Cdk4, is partially unfolded, with the N-lobe and C-lobe separated on either of Hsp90. Cdc37 makes stabilizing contacts with the Cdk4 C-lobe, mimicking the kinase N-lobe.

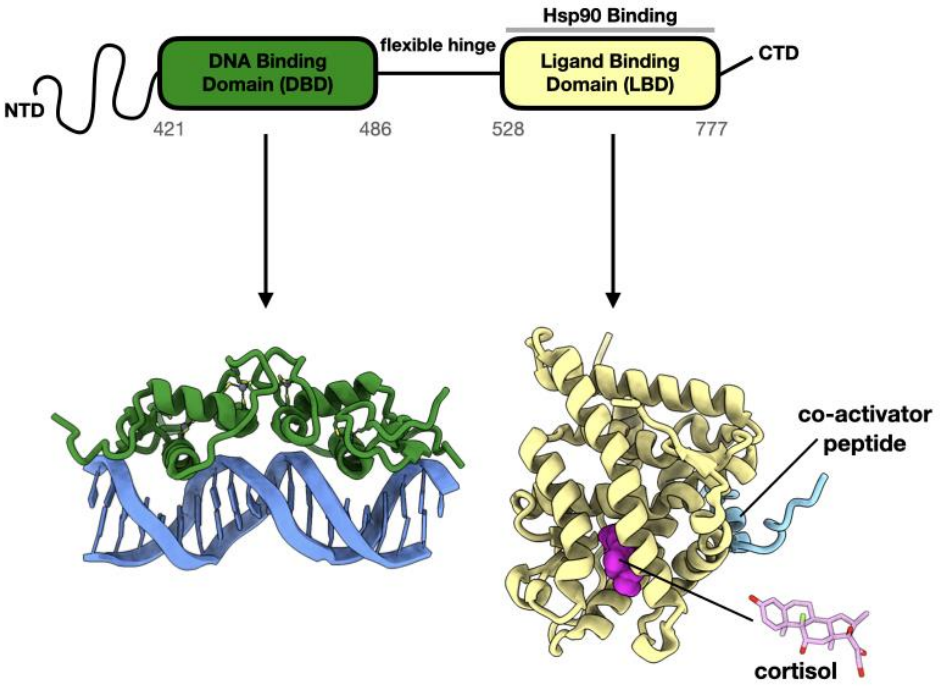

Fig. 1.6: Domain architecture of human GR
GR is a multiple domain protein consisting of an N-terminal disordered domain (NTD), DNA-binding domain, flexible hinge region, and ligand-binding domain (LBD), which is engaged by Hsp90. Structures of the individual domains are shown: the DBD on DNA (PDB ID 1GLU) (Luisi et al., 1991) and the LBD (PDB ID 1M2Z) (Bledsoe et al., 2002) bound to ligand and a co-activator peptide.

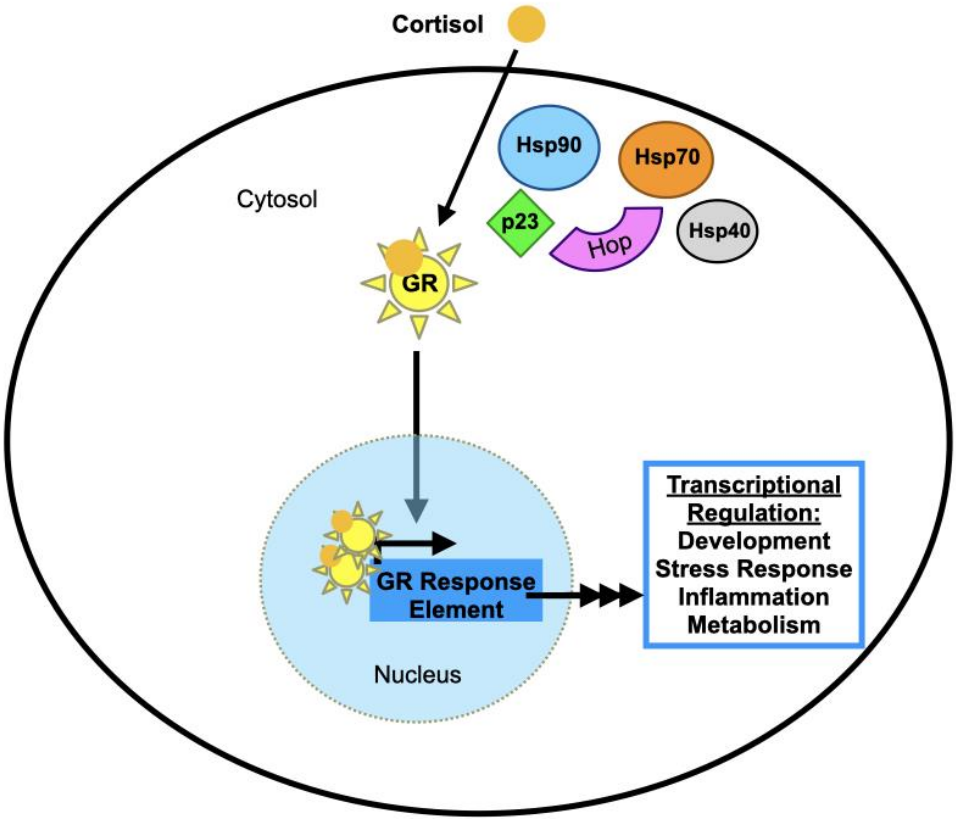

Fig. 1.7: The GR activation pathway in the cell
GR is maintained in the cytosol in a ligand-binding competent state by a group of chaperones and cochaperones: Hsp90, Hsp70, Hsp40, Hop, and p23 (Pratt & Toft, 1997). Once GR binds ligand, the receptor is rapidly translocated to the nucleus and dimerizes on GR response elements in the genome to regulate transcriptional programs (Weikum et al., 2017).

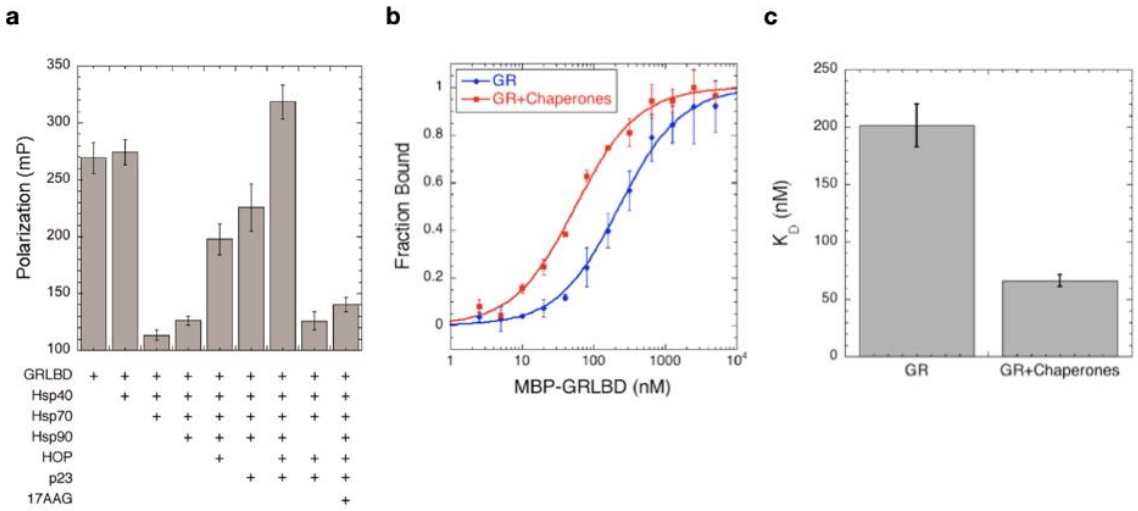

Fig. 1.8: GR ligand-binding activity is inhibited by Hsp70 and restored by Hsp90
These figures are adapted from Kirschke et al. 2014. **a**, GR ligand-binding is measured by fluorescence polarization of fluorescein-dexamethasone (Fdex). The purified, apo GR LBD is able to bind Fdex with high affinity. Addition of Hsp70 and Hsp40 inhibits GR ligand-binding. GR ligand-binding activity is restored by the addition of Hsp90, Hop, and p23. Restoration is dependent on Hsp90 ATP binding and hydrolysis, as the inhibitor 17AAG inhibits reactivation of GR ligand-binding. **b**, The GR affinity for ligand is enhanced by the addition of chaperones (Hsp70, Hsp90, Hsp40, Hop, and p23). **c**, The GR affinity for ligand is enhanced by about 2-3 fold by chaperones.

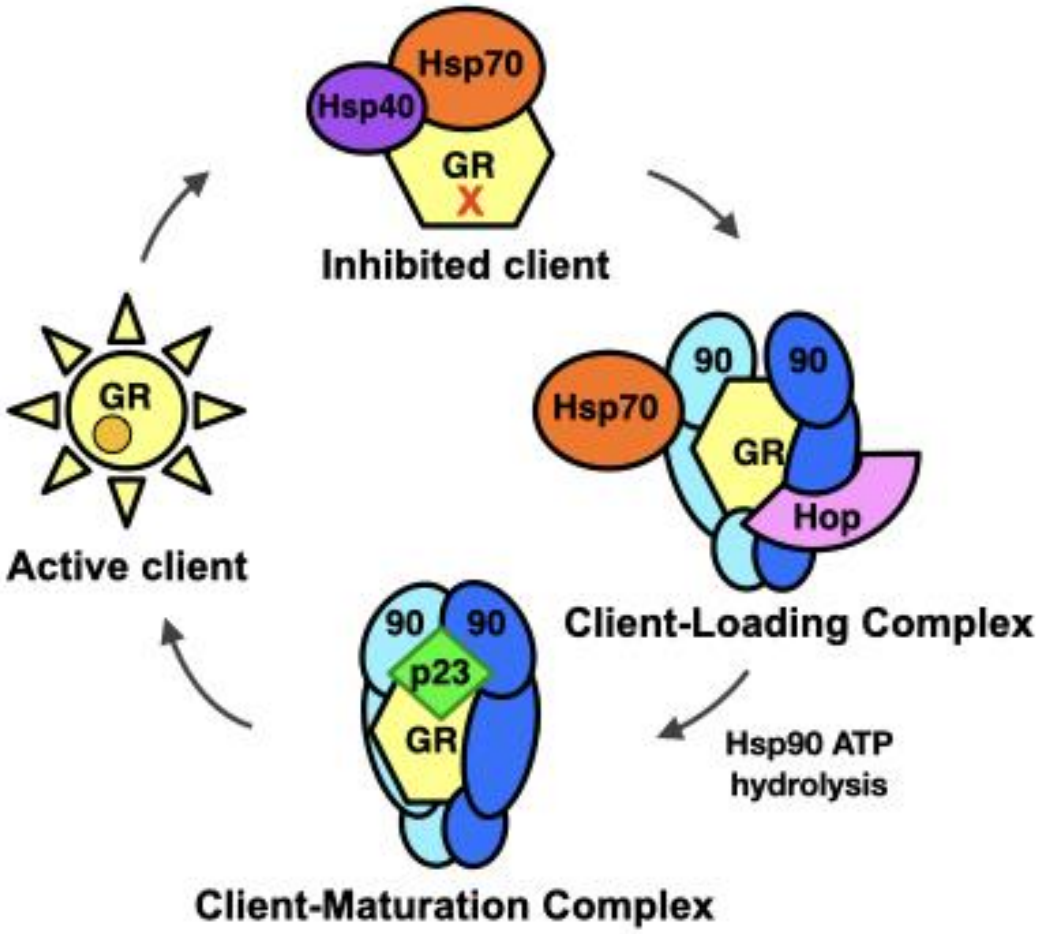

Fig. 1.9: The GR-chaperone cycle
As discussed in Kirschke et al. 2014, GR cycles through a series of distinct chaperone complexes as GR ligand-binding is inhibited and reactivated by the chaperones. First, the ligand-bound active GR is bound by Hsp70, aided by the cochaperone Hsp40 (top), which accelerates the ATPase activity of Hsp70 to facilitate high-affinity client binding. Hsp70 inhibits GR ligand-binding likely by partially unfolding the GR LBD. Next, GR is loaded onto the semi-closed Hsp90, which is stabilized by the cochaperone Hop (right). GR remains in a ligand-binding inhibited state in this “GR-loading complex”. Then, Hsp70 and Hop are released, Hsp90 binds and hydrolyzes ATP to close, and the cochaperone p23 binds to stabilize Hsp90 closure. In this “GR-maturation complex” GR is presumably remodeled to a conformation that is capable of binding ligand and the active GR is released.

References

Ali, M. M. U., Roe, S. M., Vaughan, C. K., Meyer, P., Panaretou, B., Piper, P. W., Prodromou, C., & Pearl, L. H. (2006). Crystal structure of an Hsp90–nucleotide–p23/Sba1 closed chaperone complex. *Nature, 440*(7087), 1013-1017. https://doi.org/10.1038/nature04716

Biddie, S. C., & John, S. (2014, Jan). Minireview: Conversing with chromatin: the language of nuclear receptors. *Mol Endocrinol, 28*(1), 3-15. https://doi.org/10.1210/me.2013-1247

Blagosklonny, M. V. (2002, Apr). Hsp-90-associated oncoproteins: multiple targets of geldanamycin and its analogs. *Leukemia, 16*(4), 455-462. https://doi.org/10.1038/sj.leu.2402415

Bledsoe, R. K., Montana, V. G., Stanley, T. B., Delves, C. J., Apolito, C. J., McKee, D. D., Consler, T. G., Parks, D. J., Stewart, E. L., Willson, T. M., Lambert, M. H., Moore, J. T., Pearce, K. H., & Xu, H. E. (2002). Crystal Structure of the Glucocorticoid Receptor Ligand Binding Domain Reveals a Novel Mode of Receptor Dimerization and Coactivator Recognition. *110*(1), 93-105. https://doi.org/10.1016/s0092-8674(02)00817-6

Boysen, M., Kityk, R., & Mayer, M. P. (2019). Hsp70- and Hsp90-Mediated Regulation of the Conformation of p53 DNA Binding Domain and p53 Cancer Variants. *Molecular Cell, 74*(4), 831-843.e834. https://doi.org/10.1016/j.molcel.2019.03.032

Chandler, V. L., Maler, B. A., & Yamamoto, K. R. (1983, Jun). DNA sequences bound specifically by glucocorticoid receptor in vitro render a heterologous promoter hormone responsive in vivo. *Cell, 33*(2), 489-499. https://doi.org/10.1016/0092-8674(83)90430-0

Conzen, S. D. (2008, Oct). Minireview: nuclear receptors and breast cancer. *Mol Endocrinol, 22*(10), 2215-2228. https://doi.org/10.1210/me.2007-0421

Dahiya, V., Agam, G., Lawatscheck, J., Rutz, D. A., Lamb, D. C., & Buchner, J. (2019). Coordinated Conformational Processing of the Tumor Suppressor Protein p53 by the Hsp70 and Hsp90 Chaperone Machineries. *Molecular Cell*. https://doi.org/10.1016/j.molcel.2019.03.026

Echeverria, P. C., & Picard, D. (2010, Jun). Molecular chaperones, essential partners of steroid hormone receptors for activity and mobility. *Biochim Biophys Acta, 1803*(6), 641-649. https://doi.org/10.1016/j.bbamcr.2009.11.012

Fryer, C. J., & Archer, T. K. (1998, May 7). Chromatin remodelling by the glucocorticoid receptor requires the BRG1 complex. *Nature, 393*(6680), 88-91. https://doi.org/10.1038/30032

Hartl, F. U., Bracher, A., & Hayer-Hartl, M. (2011). Molecular chaperones in protein folding and proteostasis. *Nature, 475*(7356), 324-332. https://doi.org/10.1038/nature10317

Jaeger, A. M., & Whitesell, L. (2019). HSP90: Enabler of Cancer Adaptation. *Annual Review of Cancer Biology, Vol 3, 3*, 275-297. https://doi.org/10.1146/annurev-cancerbio-030518-055533

Johnson, T. A., Chereji, R. V., Stavreva, D. A., Morris, S. A., Hager, G. L., & Clark, D. J. (2018, Jan 9). Conventional and pioneer modes of glucocorticoid receptor interaction with enhancer chromatin in vivo. *Nucleic Acids Research, 46*(1), 203-214. https://doi.org/10.1093/nar/gkx1044

Kirschke, E., Goswami, D., Southworth, D., Griffin, P., & Agard, D. (2014). Glucocorticoid Receptor Function Regulated by Coordinated Action of the Hsp90 and Hsp70 Chaperone Cycles. *Cell, 157*(7), 1685-1697. https://doi.org/10.1016/j.cell.2014.04.038

Kirschke, E. C. (2015). *Regulation of Glucocorticoid Receptor Function by the Coordinated Actions of the Hsp90 and Hsp70 Chaperone* UCSF]. Retrieved from https://escholarship.org/uc/item/3w4449wx

Krukenberg, K. A., Förster, F., Rice, L. M., Sali, A., & Agard, D. A. (2008). Multiple Conformations of E. coli Hsp90 in Solution: Insights into the Conformational Dynamics of Hsp90. *16*(5), 755-765. https://doi.org/10.1016/j.str.2008.01.021

Krukenberg, K. A., Street, T. O., Lavery, L. A., & Agard, D. A. (2011). Conformational dynamics of the molecular chaperone Hsp90. *Quarterly reviews of biophysics, 44*(2), 229-255. https://doi.org/10.1017/S0033583510000314

Labbadia, J., & Morimoto, R. I. (2015). The biology of proteostasis in aging and disease. *Annu Rev Biochem, 84*, 435-464. https://doi.org/10.1146/annurev-biochem-060614-033955

Liu, Y., Sun, M., Myasnikov, A. G., Elnatan, D., Delaeter, N., Nguyenquang, M., & Agard, D. A. (2020). Cryo-EM structures reveal a multistep mechanism of Hsp90 activation by co-chaperone Aha1. *bioRxiv*.

Lorenz, O. R., Freiburger, L., Rutz, D. A., Krause, M., Zierer, B. K., Alvira, S., Cuéllar, J., José, Madl, T., Sattler, M., & Buchner, J. (2014). Modulation of the Hsp90

Chaperone Cycle by a Stringent Client Protein. *53*(6), 941-953. https://doi.org/10.1016/j.molcel.2014.02.003

Luisi, B. F., Xu, W. X., Otwinowski, Z., Freedman, L. P., Yamamoto, K. R., & Sigler, P. B. (1991). Crystallographic analysis of the interaction of the glucocorticoid receptor with DNA. *352*(6335), 497-505. https://doi.org/10.1038/352497a0

Meijsing, S. H., Pufall, M. A., So, A. Y., Bates, D. L., Chen, L., & Yamamoto, K. R. (2009). DNA Binding Site Sequence Directs Glucocorticoid Receptor Structure and Activity. *324*(5925), 407-410. https://doi.org/10.1126/science.1164265

Morishima, Y., Murphy, P. J., Li, D. P., Sanchez, E. R., & Pratt, W. B. (2000, Jun 16). Stepwise assembly of a glucocorticoid receptor.hsp90 heterocomplex resolves two sequential ATP-dependent events involving first hsp70 and then hsp90 in opening of the steroid binding pocket. *J Biol Chem, 275*(24), 18054-18060. https://doi.org/10.1074/jbc.M000434200

Nathan, D. F., & Lindquist, S. (1995, Jul). Mutational analysis of Hsp90 function: interactions with a steroid receptor and a protein kinase. *Mol Cell Biol, 15*(7), 3917-3925. https://doi.org/10.1128/mcb.15.7.3917

Nathan, D. F., Vos, M. H., & Lindquist, S. (1997, Nov 25). In vivo functions of the Saccharomyces cerevisiae Hsp90 chaperone. *Proc Natl Acad Sci U S A, 94*(24), 12949-12956. https://doi.org/10.1073/pnas.94.24.12949

Neckers, L. (2007, Apr). Heat shock protein 90: the cancer chaperone. *J Biosci, 32*(3), 517-530. https://doi.org/10.1007/s12038-007-0051-y

Neckers, L., Blagg, B., Haystead, T., Trepel, J., Whitesell, L., & Picard, D. (2018, Jul). Methods to validate Hsp90 inhibitor specificity, to identify off-target effects, and to rethink approaches for further clinical development. *Cell Stress & Chaperones, 23*(4), 467-482. https://doi.org/10.1007/s12192-018-0877-2

Oakley, R. H., & Cidlowski, J. A. (2013). The biology of the glucocorticoid receptor: New signaling mechanisms in health and disease. *132*(5), 1033-1044. https://doi.org/10.1016/j.jaci.2013.09.007

Perlmann, T. (1992, May 1). Glucocorticoid Receptor DNA-Binding Specificity Is Increased by the Organization of DNA in Nucleosomes. *Proceedings of the National Academy of Sciences of the United States of America, 89*(9), 3884-3888. https://doi.org/DOI 10.1073/pnas.89.9.3884

Picard, D., Khursheed, B., Garabedian, M. J., Fortin, M. G., Lindquist, S., & Yamamoto, K. R. (1990, 1990/11/01). Reduced levels of hsp90 compromise steroid receptor action in vivo. *Nature, 348*(6297), 166-168. https://doi.org/10.1038/348166a0

Pratt, W. B., & Toft, D. O. (1997). Steroid Receptor Interactions with Heat Shock Protein and Immunophilin Chaperones. *Endocrine Reviews, 18*(3), 306-360. https://doi.org/10.1210/edrv.18.3.0303

Retzlaff, M., Hagn, F., Mitschke, L., Hessling, M., Gugel, F., Kessler, H., Richter, K., & Buchner, J. (2010, Feb 12). Asymmetric activation of the hsp90 dimer by its cochaperone aha1. *Mol Cell, 37*(3), 344-354. https://doi.org/10.1016/j.molcel.2010.01.006

Rosenzweig, R., Nillegoda, N. B., Mayer, M. P., & Bukau, B. (2019, Nov). The Hsp70 chaperone network. *Nat Rev Mol Cell Biol, 20*(11), 665-680. https://doi.org/10.1038/s41580-019-0133-3

Sawarkar, R., & Paro, R. (2013, Apr). Hsp90@chromatin.nucleus: an emerging hub of a networker. *Trends in Cell Biology, 23*(4), 193-201. https://doi.org/10.1016/j.tcb.2012.11.007

Scheufler, C., Brinker, A., Bourenkov, G., Pegoraro, S., Moroder, L., Bartunik, H., Hartl, F. U., & Moarefi, I. (2000, Apr 14). Structure of TPR domain-peptide complexes:

critical elements in the assembly of the Hsp70-Hsp90 multichaperone machine. *Cell, 101*(2), 199-210. https://doi.org/10.1016/S0092-8674(00)80830-2

Schopf, F. H., Biebl, M. M., & Buchner, J. (2017). The HSP90 chaperone machinery. *Nature Reviews Molecular Cell Biology, 18*(6), 345-360. https://doi.org/10.1038/nrm.2017.20

Shiau, A. K., Harris, S. F., Southworth, D. R., & Agard, D. A. (2006). Structural Analysis of E. coli hsp90 Reveals Dramatic Nucleotide-Dependent Conformational Rearrangements. *Cell, 127*(2), 329-340. https://doi.org/10.1016/j.cell.2006.09.027

Smith, D. F., & Toft, D. O. (2008, Oct). Minireview: the intersection of steroid receptors with molecular chaperones: observations and questions. *Mol Endocrinol, 22*(10), 2229-2240. https://doi.org/10.1210/me.2008-0089

Southworth, D. R., & Agard, D. A. (2011, Jun 24). Client-loading conformation of the Hsp90 molecular chaperone revealed in the cryo-EM structure of the human Hsp90:Hop complex. *Mol Cell, 42*(6), 771-781. https://doi.org/10.1016/j.molcel.2011.04.023

Taipale, M., Jarosz, D. F., & Lindquist, S. (2010). HSP90 at the hub of protein homeostasis: emerging mechanistic insights. *11*(7), 515-528. https://doi.org/10.1038/nrm2918

Taipale, M., Krykbaeva, I., Koeva, M., Kayatekin, C., Westover, K. D., Karras, G. I., & Lindquist, S. (2012, Aug 31). Quantitative analysis of HSP90-client interactions reveals principles of substrate recognition. *Cell, 150*(5), 987-1001. https://doi.org/10.1016/j.cell.2012.06.047

Trepel, J., Mollapour, M., Giaccone, G., & Neckers, L. (2010, Aug). Targeting the dynamic HSP90 complex in cancer. *Nat Rev Cancer, 10*(8), 537-549. https://doi.org/10.1038/nrc2887

Tsuboyama, K., Tadakuma, H., & Tomari, Y. (2018). Conformational Activation of Argonaute by Distinct yet Coordinated Actions of the Hsp70 and Hsp90 Chaperone Systems. *Molecular Cell, 70*(4), 722-729.e724. https://doi.org/10.1016/j.molcel.2018.04.010

Verba, K. A., Wang, R. Y. R., Arakawa, A., Liu, Y., Shirouzu, M., Yokoyama, S., & Agard, D. A. (2016). Atomic structure of Hsp90-Cdc37-Cdk4 reveals that Hsp90 traps and stabilizes an unfolded kinase. *Science, 352*(6293), 1542-1547. https://doi.org/10.1126/science.aaf5023

Watson, L. C., Kuchenbecker, K. M., Schiller, B. J., Gross, J. D., Pufall, M. A., & Yamamoto, K. R. (2013, Jul). The glucocorticoid receptor dimer interface allosterically transmits sequence-specific DNA signals. *Nat Struct Mol Biol, 20*(7), 876-883. https://doi.org/10.1038/nsmb.2595

Weikum, E. R., Knuesel, M. T., Ortlund, E. A., & Yamamoto, K. R. (2017). Glucocorticoid receptor control of transcription: precision and plasticity via allostery. https://doi.org/10.1038/nrm.2016.152

Wolff, S., Weissman, J. S., & Dillin, A. (2014, Mar 27). Differential scales of protein quality control. *Cell, 157*(1), 52-64. https://doi.org/10.1016/j.cell.2014.03.007

Zaret, K. S., & Yamamoto, K. R. (1984). Reversible and Persistent Changes in Chromatin Structure Accompany Activation of a Glucocorticoid-Dependent Enhancer Element. *Cell, 38*(1), 29-38. https://doi.org/Doi 10.1016/0092-8674(84)90523-3

Chapter 2 Structure of Hsp90-Hsp70-Hop-GR reveals the Hsp90 client-loading mechanism

Preface

The work presented in this chapter was led by Dr. Ray Wang, former post-doctoral researcher in the Agard lab, and this chapter contains excerpts from Wang et al. 2022. The goal of this project was to determine a cryo-EM structure of the GR-loading complex (GR:Hsp90:Hsp70:Hop) to elucidate how Hsp70 and Hsp90 cooperate to modulate the conformation of GR to inactivate ligand-binding activity. This project builds from decades of work investigating the role of Hsp70, Hsp90, and cochaperones in regulating the activity of GR and other SHRs (Pratt & Toft, 1997). In particular, we sought to describe in atomic detail the client hand-off mechanism between Hsp70 and Hsp90 in the GR-loading complex, which was first biochemically described in detail by Elaine Kirschke (Kirschke et al., 2014).

In this foundational work, Dr. Wang determined the structure of the GR-loading complex, establishing novel principles of the Hsp70 and Hsp90 chaperoning mechanism: how Hsp70 and Hsp90 directly associate to coordinate client hand-off, how Hsp70 and Hsp90 locally unfold GR to inhibit ligand-binding, and how Hsp70, Hsp90, and Hop directly stabilize the partially unfolded GR. My role in the GR-loading complex project was to help with manuscript preparation, analyze data, and assist with purification of GR with pBpa unnatural amino acids for cross-linking experiments to validate the structural models. Jill Johnson provided *in vivo* biochemical validation of

binding sites identified in the GR-loading complex, providing biological context to these *in vitro* experiments.

During work on this project, Dr. Wang and I also worked on a joint project to determine the structure of the related GR-maturation complex (Chapter 3) (Noddings et al., 2022). The GR-loading complex and GR-maturation complex manuscripts were co-published and together these structures establish the first complete Hsp90 chaperone cycle for any client and elucidate the Hsp90 chaperoning mechanism in atomic and mechanistic detail.

Abstract

Maintaining a healthy proteome is fundamental for organism survival (Kim et al., 2013). Integral to this are Hsp90 and Hsp70 molecular chaperones that together facilitate the folding, remodeling and maturation of Hsp90's many "client" proteins (Genest et al., 2019). The glucocorticoid receptor (GR) is a model client strictly dependent upon Hsp90/Hsp70 for activity (Lorenz et al., 2014; Nathan et al., 1997; Picard et al., 1990; Pratt et al., 2006; Smith & Toft, 2008). Chaperoning GR involves a cycle of inactivation by Hsp70, formation of an inactive GR:Hsp90:Hsp70:Hop "loading" complex, conversion to an active GR:Hsp90:p23 "maturation" complex, and subsequent GR release (Kirschke et al., 2014). Unfortunately, a molecular understanding of this intricate chaperone cycle is lacking for any client. Here, we report the cryo-EM structure of the GR loading complex, in which Hsp70 loads GR onto Hsp90, revealing the molecular basis of direct Hsp90/Hsp70 coordination. The structure reveals two Hsp70s––one delivering GR and the other scaffolding the Hop cochaperone. Unexpectedly, Hop

interacts with all components of the complex including GR, poising Hsp90 for subsequent ATP hydrolysis. GR is partially unfolded and recognized via an extended binding pocket composed of Hsp90, Hsp70 and Hop, revealing the mechanism of GR loading and inactivation. Together with the GR maturation complex (Noddings et al., 2022), we present the first complete molecular mechanism of chaperone-dependent client remodeling, establishing general principles of client recognition, inhibition, transfer and activation.

Introduction

The highly abundant and conserved Hsp90 and Hsp70 molecular chaperones are essential for proteome maintenance. Hsp70 recognizes virtually all unfolded/misfolded proteins, and generally functions early in protein folding (Rosenzweig et al., 2019). By contrast, Hsp90 typically functions later, targeting a select set of "client" proteins (Taipale et al., 2010). Despite the differences, Hsp90 and Hsp70 share clients that are highly enriched for signaling and regulatory proteins (Genest et al., 2019), making both chaperones important pharmaceutical targets for cancer (Whitesell & Lindquist, 2005) and neurodegenerative diseases (Lackie et al., 2017). Both chaperones are dynamic molecular machines with complex ATP-dependent conformational cycles that drive client binding/release. Hsp70 uses its N-terminal nucleotide-binding domain ($Hsp70_{NBD}$) to allosterically regulate its C-terminal substrate-binding domain ($Hsp70_{SBD}$), comprising a β-sandwich core ($Hsp70_{SBD\text{-}\beta}$) and an α-helical lid ($Hsp70_{SBD\text{-}\alpha}$) (Mayer & Gierasch, 2019) (Extended Data Fig. 1a). In the weak client binding ATP-bound "open" state ($Hsp70^{ATP}$), both the $Hsp70_{SBD\text{-}\alpha}$ and $Hsp70_{SBD\text{-}\beta}$ dock

onto the $Hsp70_{NBD}$. Upon ATP hydrolysis ($Hsp70^{ADP}$), the $Hsp70_{NBD}$ and $Hsp70_{SBD}$ subdomains separate, resulting in a high-affinity client-binding state. Hsp90 constitutively dimerizes through its C-terminal domain ($Hsp90_{CTD}$) (Extended Data Fig. 1a) and cycles through open and closed conformations acting as a molecular clamp (Krukenberg et al., 2011; Schopf et al., 2017). In the nucleotide-free state ($Hsp90^{Apo}$), Hsp90 populates a variety of open conformations, whereas ATP binding ($Hsp90^{ATP}$) drives clamp closure via secondary dimerization of the N-terminal domains ($Hsp90_{NTD}$). Clamp closure activates Hsp90 for ATP hydrolysis and is rate-limiting requiring $Hsp90_{NTD}$ rotation, N-terminal helix rotation and ATP-binding pocket lid closure. Unlike Hsp70, Hsp90 can engage clients independent of nucleotide state via the middle domain ($Hsp90_{MD}$) and the amphipathic helix-hairpins ($Hsp90_{amphi\text{-}\alpha}$) on the $Hsp90_{CTD}$. The glucocorticoid receptor (GR) is a steroid hormone-activated transcription factor that constitutively depends on Hsp90 to function (Nathan et al., 1997; Picard et al., 1990). Building on the pioneering work of Pratt, Smith, and Toft (Pratt et al., 2006; Smith & Toft, 2008), we previously reconstituted GR's Hsp90 dependence using an *in vitro* system (Kirschke et al., 2014), establishing a 4-step cycle (Fig. 1a) starting with active GR ligand-binding domain (hereafter GR for simplicity). Next, Hsp70 inactivates GR ligand binding, then cochaperone Hop (Hsp90/Hsp70 organizing protein) helps load Hsp70:GR onto Hsp90 forming the inactive "loading" complex (GR:Hsp90:Hsp70:Hop). Upon Hsp90 ATP hydrolysis and closure, Hsp70 and Hop are released, followed by the incorporation of p23, forming the GR:Hsp90:p23 "maturation" complex. In the maturation complex, GR is reactivated, indicating GR is conformationally remodeled during the transition. A similar pattern of Hsp70/Hsp90 functional antagonism has

subsequently been shown for other clients (Boysen et al., 2019; Dahiya et al., 2019; Moran Luengo et al., 2018), supporting a general mechanism.

Unfortunately, the molecular basis for almost all of this complex chaperone interplay remains unknown, with high-resolution structural studies hampered by the instability of clients and the highly dynamic nature of client:chaperone associations. Here, we report a high-resolution cryo-EM structure of the client-loading complex, providing much needed molecular insights into how Hsp90/Hsp70 coordinate their ATP cycles, how they are organized by Hop, and the molecular mechanisms underlying GR's functional regulation by Hsp90/Hsp70.

Results

Structure determination and architecture of the client-loading complex

The client-loading complex was prepared by reconstitution using excess ADP to enhance client binding by Hsp70 and an ATP-binding deficient Hsp90 ($Hsp90^{D93N}$) to stall the cycle at this intermediate step, followed by glutaraldehyde stabilization (Extended Data Fig. 1b,c). A ~3.6Å resolution cryo-EM reconstruction was obtained from ~4 million particles (Extended Data Fig. 1d-f,2, Materials and Methods). The resulting structure reveals an architecture drastically different than expected, with the Hsp90 dimer (Hsp90A/B) surrounded by Hop, GR and unexpectedly two Hsp70s (Hsp70"C" for client-loading and Hsp70"S" for scaffolding) (Fig. 1b,c). Hsp90 adopts a previously unseen "semi-closed" conformation, in which the $Hsp90_{NTD}$s have rotated into an $Hsp90^{ATP}$-like orientation, but have not yet reached the fully-closed ATP state (Extended Data Fig. 3b,c). The observed $Hsp90_{NTD}$ orientations are stabilized by the

Hsp70$_{NBD}$s that bind symmetrically to the Hsp90$_{NTD}$:Hsp90$_{MD}$ interface of each Hsp90 protomer. Hop intimately interacts with each Hsp90 protomer, the two Hsp70s, and remarkably, a portion of GR. Although the two Hsp70$_{SBD}$s are not visible in the high-resolution map, the Hsp70C$_{SBD-\beta}$ subdomain becomes visible in low-pass filtered maps (Fig. 1b). Also seen in the filtered maps, GR is positioned on one side of the Hsp90 dimer (Fig. 1c). Additionally, another map (~7Å) reveals a loading complex that has lost Hsp70C, but retains Hsp70S, Hop and GR (Extended Data Fig. 3d,e). The observation of the two-Hsp70 and one-Hsp70 loading complexes populated in our sample is consistent with a previous study (Morgner et al., 2015).

The nucleotide-regulated interplay between Hsp90 and Hsp70

Two major interfaces (Fig. 1d) are formed in both of the nearly identical Hsp70$_{NBD}$/Hsp90 protomer interactions (RMSD of 0.96Å, Supplementary Fig. 1a-c). In Interface I, the outer edge of the Hsp90$_{MD}$ β-sheet inserts into the cleft formed by the Hsp70$_{NBD-IA}$ and Hsp70$_{NBD-IIA}$ subdomains (Fig. 1d, Extended Data Fig. 4a). Notably, in Hsp70^{ATP} this cleft binds the Hsp70 interdomain linker and also contributes to binding Hsp40's J-domain (Mayer & Gierasch, 2019) (Extended Data Fig. 4b). Hence, the cleft is only available in Hsp70^{ADP}. Interface I is tightly packed (479Å^2 of buried surface area, BSA), and is stabilized by numerous polar interactions (Fig. 1d,e). This explains why mutations at Interface I on either Hsp90 (Bohen & Yamamoto, 1993; Kravats et al., 2018; Nathan & Lindquist, 1995) (G333, K414, K418, K419) or Hsp70 (Doyle et al., 2019) (R171, N174, D213) led to defective Hsp90:Hsp70 interaction, growth defects, and impaired client maturation of GR, v-Src, and Luciferase (Fig. 1d,e Extended Data

Fig. 4c-h; see Extended Data Table 3 for residue numbering references to the yeast chaperone proteins).

The two ATPase domains of Hsp90 and Hsp70 directly interact with each other at Interface II (Fig. 1d,f, 280Å^2 BSA), where the interactions are composed of both hydrophobic (Hsp90^{Y61,L64}:Hsp70^{V163,I164}) and polar interactions (Hsp90^{R60,Y61}: Hsp70^{D160}). Importantly, Interface II defines the Hsp90^{ATP}-like position/orientation of the Hsp90$_{NTD}$ with respect to the Hsp90$_{MD}$, explaining the observation that Hsp70 accelerates Hsp90 ATPase activity (Genest et al., 2015). Consistent with the significance of Interface II, mutation of the three Hsp90 interface residues (Hsp90^{R60,Y61,L64}) showed marked yeast growth defects at 37°C (Flynn et al., 2020). Similar to Interface I mutations Hsp90$^{G333S,K418E\ (G309S,K394E\ in\ yeast\ Hsc82)}$, an Hsp90^{R60} mutation (yHsc82^{R46G}) displayed reduced Hsp70 interaction, inviability at 37°C, and reduced v-Src activity (Extended Data Fig. 4e-h). Lastly, sequence alignments of Hsp90/Hsp70 homologs/paralogs showed that Interface I & II residues are generally conserved, suggesting a universal Hsp70-Hsp90 binding strategy across species (Genest et al., 2011; Kravats et al., 2018) and organelles (Sun et al., 2019; Sung et al., 2016) (Supplementary Fig. 2a,b).

As expected from Hsp90^{D93N}, both Hsp90$_{NTD}$ ATP-binding pockets are empty with their lids open. The Hsp90A$_{NTD}$ and Hsp90B$_{NTD}$ closely resemble the structure of an apo Hsp90$_{NTD}$ fragment (RMSD of 0.43 and 0.35Å to 3T0H, respectively, Extended Data Fig. 5a). The ATP pocket lid and the first α-helix form a novel dimerization interface (512Å^2 BSA, Extended Data Fig. 3a).The two Hsp70$_{NBD}$s clearly have ADP

bound and are similar to the ADP-bound $Hsp70_{NBD}$ crystal structure (Cα-RMSD of 0.50Å (Hsp70C) and 0.53Å (Hsp70S) to 3AY9) (Fig. 1d, Supplementary Fig. 3a,b). Coordination between the Hsp90/Hsp70 ATPase cycles is required for forming the loading complex. The $Hsp90^{ATP}$ conformation is incompatible as closure of the $Hsp90^{ATP}$ ATP pocket lid and the central helix of $Hsp90_{NTD}$ would clash with the $Hsp70_{NBD}$ (Extended Data Fig. 5b,c). Thus, Hsp90 ATP binding and lid closure would be expected to accelerate loss of the bound Hsp70s. Furthermore, the $Hsp70^{ATP}$ conformation is incompatible with the loading complex, as the entire $Hsp70_{SBD}$ would clash with $Hsp90_{NTD}$/$Hsp90_{MD}$ (Extended Data Fig. 5d,e). For Hsp70 to reenter its ATP cycle, it must first leave Hsp90, thus nucleotide exchange on Hsp70 likely times its dissociation. Notably, in the complex $Hsp70_{NBD-IIA}$s deviate from the crystal structure (Supplementary Fig. 3a,b) and $Hsp90_{MD}$ interacts with $Hsp70^{R171,N174,T177}$ in the ATP catalytic motif (Fig 2d, Supplementary Fig. 3c), suggesting how Hsp90 enhances the nucleotide exchange on Hsp70 during the GR-chaperoning cycle (Kirschke et al., 2020). The canonical nucleotide exchange factor (NEF) binding sites (Bracher & Verghese, 2015) on $Hsp70_{NBD-IIB}$ remain available, explaining how the NEF Bag-1 can accelerate GR maturation (Kirschke et al., 2020) (Supplementary Fig. 4a,b) and also how the NEF Hsp110 can be involved in GR maturation (Mandal et al., 2010) (Supplementary Fig. 4c,d).

Hop interacts extensively with all components in the loading complex

The cochaperone Hop is well conserved in eukaryotes and facilitates GR maturation *in vivo* (Sahasrabudhe et al., 2017) and *in vitro* (Kirschke et al., 2014). Hop

is thought to bring Hsp90 and Hsp70 together using its three TPR domains that bind the EEVD C-termini on both Hsp90 and Hsp70 (Scheufler et al., 2000) (Extended Data Fig. 1a). Despite using the full-length Hop construct, only three C-terminal domains (Hop_{TPR2A}, Hop_{TPR2B}, and Hop_{DP2}) are observed (Fig. 1b,c). Importantly, these three domains are necessary and sufficient for full GR activation (Schmid et al., 2012). Hop wraps around much of the loading complex, with extensive interactions made by Hop_{TPR2A} and Hop_{DP2}, demonstrating a far more integral role than anticipated (Fig. 2a,c). The structure of $Hop_{TPR2A\text{-}TRP2B}$ closely matches the yeast crystal structure(Schmid et al., 2012) (Cα-RMSD of 1.47Å to 3UQ3, Supplementary Fig. 5a,c,d), including the conserved electrostatic network ($Hop^{Y354,R389,E385,K388}$) that defines the unique inter-domain angle (Supplementary Fig. 5h-j). Focused maps revealed that the Hop_{TPR2A} and Hop_{TPR2B} are bound to the EEVD termini of Hsp90 and Hsp70, respectively (Extended Data Fig. 6d-f, Supplementary Fig. 6b-f,k,l). Although the density for the remaining Hsp70 and Hsp90 tails are missing, our structural modeling suggested the connectivity (Supplementary Fig. 7). Unexpectedly, Hop_{TPR2A} and $Hsp70S_{NBD\text{-}IIA}$ form a novel and extensive interface (578$Å^2$ BSA) composed largely of polar interactions (Fig. 2a,b and Extended Data Fig. 6a-d). Notably, $Hsp70S_{NBD\text{-}IIA}$ interacts with Hop and Hsp90 simultaneously, thereby rigidly positioning Hop with respect to Hsp90. Mutations of $Hop^{Y296A\text{-}A328H\ (Y332\text{-}T364\ in\ yeast,\ Sti1)}$ at the $Hsp70S_{NBD\text{-}IIA}$:Hop_{TPR2A} interface (Extended Data Fig. 6a-c,g) resulted in yeast growth defects (Extended Data Fig. 6i) and failed to promote v-Src maturation (Extended Data Fig. 6j). These data indicate a crucial scaffolding role for Hsp70S in the loading complex. Although Hop_{TPR2B} was in close proximity (~6 Å) to $Hsp90_{MD}$ no major contacts were observed (Fig. 2c). However, the

15Å-resolution Hsp90:Hop cryo-EM structure (Southworth & Agard, 2011) (Supplementary Fig. 8a) and previous studies(Lee et al., 2012; Schmid et al., 2012) show that Hop_{TPR2B} can make direct contacts with $Hsp90_{MD}$. This suggests that Hop may first prepare Hsp90 for Hsp70 and client interaction, and subsequently rearrange upon $Hsp70S_{NBD}$ binding (Supplementary Fig. 8b,c).

Hop_{DP2} makes extensive interactions with both Hsp90 protomers at $Hsp90A_{CTD}$ and $Hsp90B_{MD}$, thereby defining and maintaining the semi-closed Hsp90 conformation within the loading complex (Fig. 3a). Interestingly, conserved client-binding residues on Hsp90A/B are repurposed for Hop_{DP2} binding (Fig. 3d). Supporting our observations, Hsp90 mutations which would destabilize the Hop_{DP2}:Hsp90A interface ($yHsp82^{W585T,M593T}$ corresponding to $hHsp90\alpha^{W606,M614}$) cause yeast growth defects (Reidy et al., 2018). Our Hop_{DP2} structure agrees well with the yeast NMR structure (Schmid et al., 2012) (Cα-RMSD of 1.13Å to 2LLW; Extended Data Fig. 19b), adopting a hand-like α-helical structure, with many of its core hydrophobic sidechains exposed in the “palm” of the “hand” (Fig. 3d). Importantly, this hydrophobic palm is continuous with the client binding surface provided by the lumen between the Hsp90 protomers, augmenting the $Hsp90A_{amphi-\alpha}$ with a stronger, more extensive hydrophobic binding capability (Extended Data Fig. 7a).

GR is unfolded, threaded through the Hsp90 lumen and bound by Hsp90, Hop and Hsp70

In the high-resolution map, a strand of density can be seen passing through the Hsp90 lumen (Extended Data Fig. 7b,c). In the 10Å low-pass filtered map, this density

connects to the globular part of GR on one side of Hsp90 (Fig. 1c, Supplementary Fig. 7e,f). On the other side, a GR helix is surprisingly cradled in the Hop_{DP2} hydrophobic palm and the rest of GR becomes a strand embedded in the $Hsp70C_{SBD-\beta}$ substrate binding pocket (Fig. 4a-d, Extended Data Fig. 8d,9d, Supplementary Fig. 9a,b,10d-f). Thus, GR is partially unfolded and threaded through the Hsp90 lumen, reminiscent of how the CDK4 kinase was unfolded (Verba et al., 2016) by the fully closed $Hsp90^{ATP}$. To test this unexpected client:cochaperone interaction, we substituted Hop^{Q512} in Hop_{DP2} which is close to, but not directly interacting with, the GR helix with the photo-reactive unnatural amino acid p-benzoyl-phenylalanine (Extended Data Fig. 8d). In support of our structure, GR and Hop become photo-crosslinked (Extended Data Fig. 8a,b). Additionally, mutations of a Hop_{DP2} residue ($Hop^{L508\ (L553\ in\ yeast,\ Sti1)}$) in the hydrophobic palm that directly interacts with GR (Fig. 3d, Extended Data Fig. 8e) decrease yeast viability (Extended Data Fig. 8g), and completely abrogated GR (Schmid et al., 2012) and v-Src function (Extended Data Fig. 8h) in vivo. These data indicate that client binding to Hop_{DP2} is crucial for both general cellular functions and protein maturation across different client systems.

Which GR segment is captured in the loading complex lumen? The GR maturation complex structure unambiguously demonstrates that GR's pre-Helix 1 region ($GR^{517–533}$, $GR_{pre\text{-}Helix\ 1}$) is gripped in the closed Hsp90 lumen (Noddings et al., 2022). Reexamination of previous Hsp70-GR HDX-MS data (Kirschke et al., 2014) reveals that only $GR_{pre\text{-}Helix\ 1}$ becomes protected upon Hsp70 binding (Extended Data Fig. 9a,b) and $GR_{pre\text{-}Helix\ 1}$ also contains high-scoring predicted Hsp70 binding sites ($GR^{518–524}$, Extended Data Fig. 9a), strongly supporting a model in which $GR_{pre\text{-}Helix\ 1}$ is captured by

Hsp70 in the loading complex (Extended Data Fig. 9b-d). This was tested by incorporating the photo-reactive crosslinker at two positions in the $GR_{pre\text{-}Helix\ 1}$ strand: residues either before (GR^{517}) or after (GR^{527}) the predicted Hsp70 binding site (Extended Data Fig. 10a). As expected, at both positions, crosslinks between GR and Hsp70 were formed in the loading complex (Extended Data Fig. 10b,c). In addition, both positions were able to crosslink with Hop (Extended Data Fig. 10b,c), indicating it is Hsp70C that the $GR_{pre\text{-}Helix\ 1}$ strand crosslinked with, rather than Hsp70S. Consistent with our model, a previous optical-tweezer study (Suren et al., 2018) demonstrated that $GR_{Helix\ 1}$ is readily detached, correlating with ligand binding loss. Together, this indicates that perturbations to $GR_{Helix\ 1}$ by Hsp70 or the loading complex leads to loss of GR ligand binding.

Despite extensive 3D classifications, the main body of GR remained at low resolution. Nonetheless, the $Hsp90_{MD}$s from each protomer and the $Hsp90B_{amphi\text{-}\alpha}$ clearly contact GR (Extended Data Fig. 7b-d,f,g). Hsp90 residues previously found (Bohen, 1995; Bohen & Yamamoto, 1993; Genest et al., 2013; Hawle et al., 2006; Nathan & Lindquist, 1995) to impact GR maturation are highlighted in Fig. 4e. The exposed $Hsp90A^{W320,F349}$ directly contacts GR in both the loading complex (Fig. 4e, Supplementary Fig. 7g), and the maturation complex (Noddings et al., 2022). Notably, $Hsp90^{W320\ (W300\ in\ yHsp82)}$ is an important binding residue exploited by both clients and cochaperones. Not only does it interact with GR and Hop_{DP2} (Fig. 3d), but also with another cochaperone Aha1 (Liu et al., 2020). Supporting its broad functional importance, numerous studies have reported deleterious effects of $Hsp90A^{W320}$

mutations on GR activation (Hawle et al., 2006; Rutz et al., 2018) and yeast growth (Flynn et al., 2020).

Discussion

Our client-loading complex structure provides the first view of how Hsp70, Hsp90 and Hop work together to chaperone a client. Several features were unexpected: 1) two Hsp70s bind the Hsp90 dimer, one delivers client and the second scaffolds Hop. 2) Hop interacts extensively with all components, including GR, going well beyond the anticipated TPR-EEVD interactions. 3) Together Hop:Hsp90 and Hsp70:Hsp90 interactions define the Hsp90 conformation poising it for both client binding, and ultimately for ATP hydrolysis and client activation. 4) Hsp90 repurposes one side of its client-binding sites to bind Hop_{DP2}, which in turn augments the Hsp90 lumenal client-binding site, facilitating client-loading from Hsp70 (Fig. 4a).

The loading complex provides an extraordinarily extended client-binding pocket, with a large and very adaptable surface for client recognition (Fig. 3b and Extended Data Fig. 7b-d): (1) Hsp70 binds a hydrophobic strand, (2) Hop_{DP2} binds a hydrophobic/amphipathic helix, (3) the remaining part of the $Hsp90A_{amphi\text{-}\alpha}$ provides polar interactions, (4) the $Hsp90B_{amphi\text{-}\alpha}$ provides a hydrophobic surface, and (5) the Hsp90A/B lumen provides a combination of hydrophobic and polar interactions. Not only is the loading complex lumen spacious enough to bind a strand (as shown here) or intact helix (Supplementary Fig. 7c), but the flexible positioning of the $Hsp70C_{SBD}$ and the dynamic, adaptable conformation of the $Hsp90_{amphi\text{-}\alpha}$ allow even broader flexibility for client recognition (Fig. 4b,5a).

Our structural insights reveal the molecular mechanism of GR inhibition in the chaperone cycle (Fig. 1a), allowing us to propose the following pathway for loading complex formation (Fig. 4b): Hsp70C captures the flexible $GR_{pre\text{-}Helix\ 1}$, causing the following dynamic helix-strand motif to detach, thereby destabilizing the GR ligand-binding pocket (Extended Data Fig. 9b,c). Hsp70C then delivers the partially unfolded GR to Hop:Hsp70S:Hsp90. In the resultant loading complex, GR is further unfolded via engagement of $GR_{Helix\ 1}$'s LXXLL motif with Hop_{DP2} and the $GR_{post\text{-}Helix\ 1}$ strand with the Hsp90 lumen (Fig. 3b,d and Extended Data Fig. 8e), suppressing any possible ligand binding. The rest of GR remains globular and is only loosely associated with the distal surface of Hsp90.

How does the loading complex progress to the maturation complex—a process requiring Hsp90 ATP hydrolysis and release of Hop and both Hsp70s? The one-Hsp70 loading complex (Extended Data Fig. 3d,e) suggests that the process is asymmetric and sequential, with the loss of Hsp70C occurring first, while asymmetric Hsp90 ATP hydrolysis drives the release of the more tightly engaged Hsp70S-Hop. Schematically shown in Fig. 4b, we propose that a combination of Hsp90's ATP binding and NEF activities promotes Hsp70C to hand off GR and exit the complex. This leaves GR engaged with Hop_{DP2} and the Hsp90 lumen, minimizing reformation of an Hsp70:GR complex or premature release. Lastly, as discussed in detail in Noddings et al. 2022, the conversion of the semi-closed Hsp90 in the loading complex to the fully closed $Hsp90^{ATP}$ in the maturation complex may serve as a driving force for client remodeling and hence activation (Extended Data Fig. 3b,c).

GR uses a generalized chaperone (Hsp70) and cochaperone (Hop) for loading onto Hsp90 clients, making the principles learned here broadly applicable to other clients. Indeed, in this report, we show that the two most studied model clients, GR and v-Src, seemingly share a similar client-loading mechanism for their maturation (Extended Data Fig. 6j,8h). Although Hop is absent in bacteria and organellar compartments, Hsp70s are ubiquitously present and the client-binding provided by Hop_{DP2} is likely substituted by the $Hsp90_{amphi\text{-}\alpha}$. While most, if not all, proteins engage with Hsp70 at least during initial folding, only a subset are Hsp90 clients. Ultimately, client properties must dictate this selectivity. Rather than an overall client property such as stability, our loading complex structure suggests a more nuanced balance of three effects: 1) the probability of partial unfolding fluctuations in the client, 2) the ability of Hsp70 to capture a transiently exposed site, and 3) the likelihood that further unfolding events would uncover adjacent client regions that can be captured by Hop_{DP2}/Hsp90. Experiments to test these general principles can now be designed to predict and identify potential Hsp90/Hsp70 clients.

Data availability

The electron microscopy maps and atomic model have been deposited into the Electron Microscopy Data Bank (EMDB) and the Protein Data Bank (PDB). The accession codes for the GR-loading complex are EMD-23050 and 7KW7. Focused maps used for model refinements were also deposited with accession codes denoted in Extended Data Table 2 (EMD-23051, EMD-23053, EMD-23054, EMD-23055, EMD-23056).

Author Contributions

R.Y.-R.W. performed the research and drafted the manuscript. D.A.A. supervised the research. C.M.N performed pBpa-GR construct design and purification, and helped analyze data. J.L.J. carried out all *in vivo* yeast experiments. E.K. trained R.Y.-R.W. for the biochemistry of the GR reconstitution system. A.G.M. trained R.Y.-R.W. for cryo-EM operation and data acquisition. R.Y.-R.W., C.M.N., and D.A.A. wrote the manuscript with input from all authors.

Acknowledgements

We thank members of the Agard Lab for helpful discussions. We thank Dr. Tristan W. Owens for advising the photoreactive crosslinking experiment. We thank Michael Braunfeld, David Bulkley, Glenn Gilbert, Eric Tse, and Zanlin Yu from the W.M. Keck Foundation Advanced Microscopy Laboratory at the University of California San Francisco (UCSF) for maintaining the EM facility and help with data collection. We thank Matt Harrington and Joshua Baker-LePain for computational support with the UCSF

Wynton cluster. R.Y.-R.W. was a Howard Hughes Medical Institute Fellow of the Life Sciences Research Foundation. C.M.N. is a National Cancer Institute Ruth L. Kirschstein Predoctoral Individual NRSA Fellow. The work was supported by funding from Howard Hughes Medical Institute (D.A.A.) and NIH grants R35GM118099 (D.A.A.), S10OD020054 (D.A.A.), S10OD021741 (D.A.A.), P20GM104420 (J.L.J.), and R01GM127675 (J.L.J.).

Figures

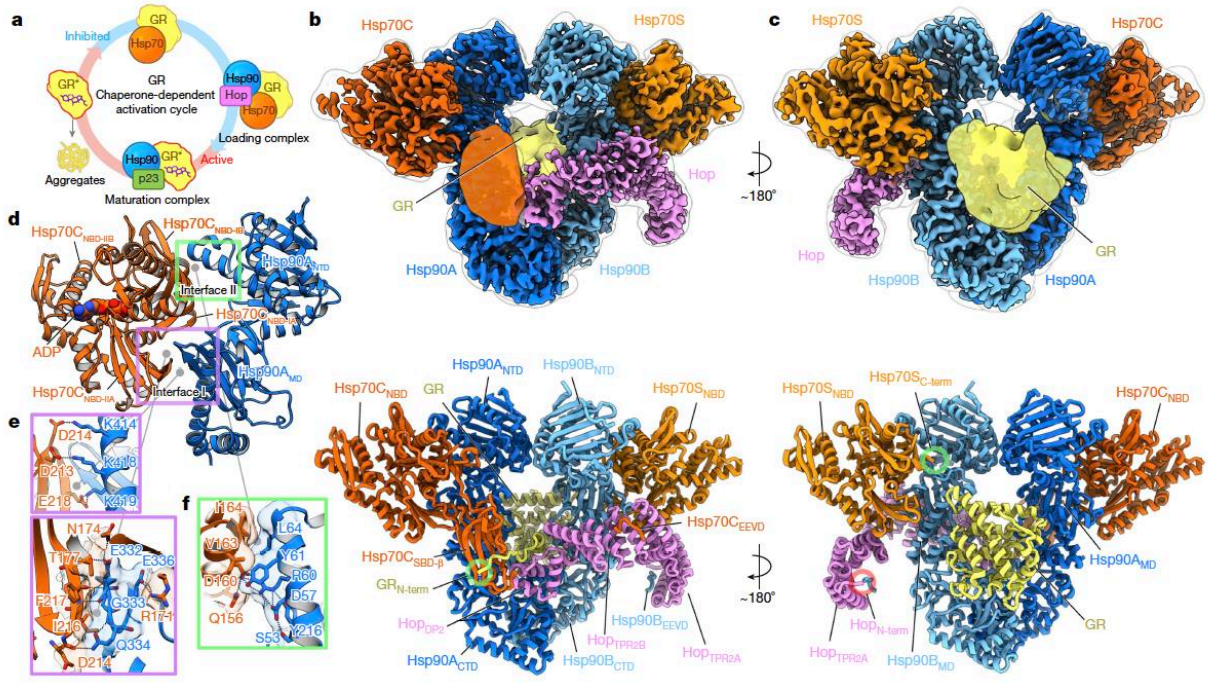

Fig. 2.1: Overview of the GR-loading complex and molecular basis of Hsp90:Hsp70 interactions

a, GR ligand-binding activity is regulated by molecular chaperones in a constant cycle of inactivation and activation. **b,c**, Front (b) and back (c) views of a composite cryo-EM map and the atomic model of the GR-loading complex. Densities of Hsp70CSBD and the globular C-terminal GR are taken from the 10Å low-pass-filtered map of the high-resolution reconstruction of the full complex. The subunit color code is used throughout. **d-f**, Hsp90:Hsp70 interactions without the aid of Hop (Hsp90A:Hsp70C) are composed with Interface I (purple rectangle (e)) and Interface II (green rectangle (f)). In the close-up views of the two interfaces (e,f), transparent surface and stick representations are shown for residues involved in the interactions, and dashed lines depict the network of polar interactions involved.

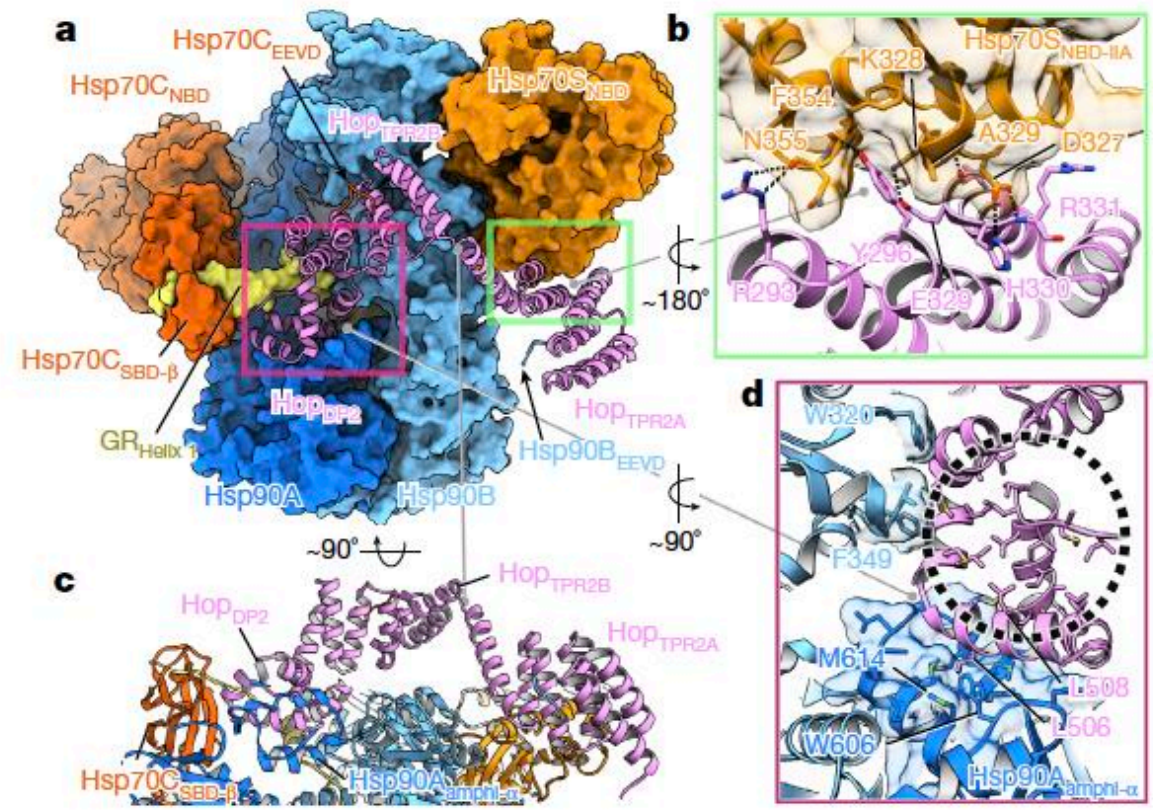

Fig. 2.2: Hop interacts intimately with all components in the loading complex
a, Hop, shown in ribbon representation while the other components are shown in surface representation, uses HopTPR2A to interact with Hsp70S (green rectangle) and HopDP2 to interacts with both Hsp90 protomers, Hsp70CSBD and a portion of GR (red rectangle), beyond the Hsp90/Hsp70 EEVD binding. **b**, Close-up view of the novel Hop:Hsp70 interface. HopY296 inserts into a cavity on Hsp70SNBD-IIA (transparent surface representation). Dashed lines depict polar interactions. **c**, A 90-degree rotation from the bottom view in (a) with ribbon model. **d**, HopDP2 uses surface-exposed hydrophobic residues, shown in sticks, to interact with Hsp90Aamphi-α (shown with transparent surface and with hydrophobic residues in sticks) and Hsp90BW320,F349. HopDP2 is loosely packed with many hydrophobic residues exposed in the “palm” (black circle) of the “hand”. Note the GR-binding to HopDP2 is not shown here.

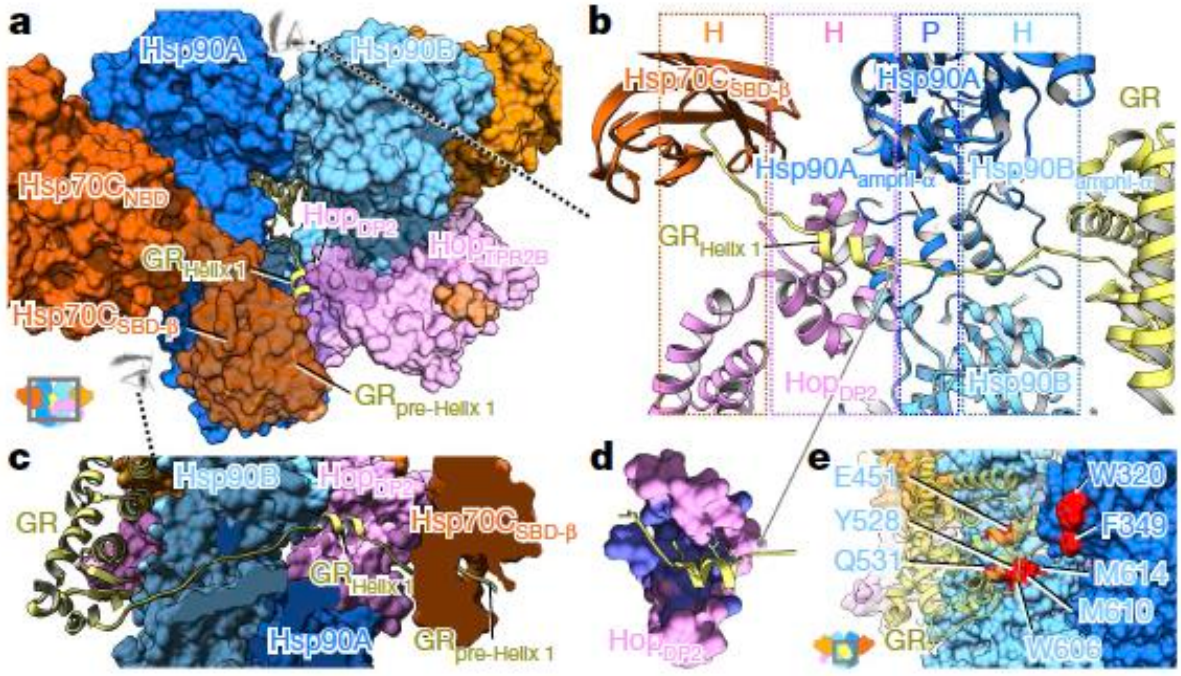

Fig. 2.3: GR is unfolded and threaded through Hsp90 lumen, binding HopDP2 and Hsp70CSBD-β

a, Close-up front view of the loading complex (shown in surface representation). GR, shown in the ribbon model, is partially unfolded, with the N-terminal residues simultaneously gripped by Hsp70CSBD-β and HopDP2, and is threaded through the semi-closed lumen of Hsp90. The remaining GR is at the other side of the loading complex; the ribbon model shown for the major body of GR is a modeling result from docking the GR crystal structure to the low-pass-filtered GR density. **b**, Top-to-bottom view of GR recognition via an extended client-binding pocket collectively formed by Hsp70CSBD-β, HopDP2, and Hsp90A/Bamphi-αs in ribbon representation. The N-terminal residues of GR (residues 517–533), which form a strand-helix-strand motif (yellow), are captured in the loading complex. The molecular properties provided by the individual binding pockets are color coded and labelled on the top panel (H and P denote hydrophobic and polar interactions, respectively). **c**, Side view (see-through) of the GR N-terminal motif captured by the loading complex. **d**, HopDP2, shown in surface representation, binds the LXXLL motif of GRHelix1, in which the hydrophobic residues of HopDP2 are colored with purple and those of GR are shown in sticks. **e**, Residues on Hsp90 (surface representation) previously reported to be important for GR (transparent yellow ribbon) activation are highlighted in red.

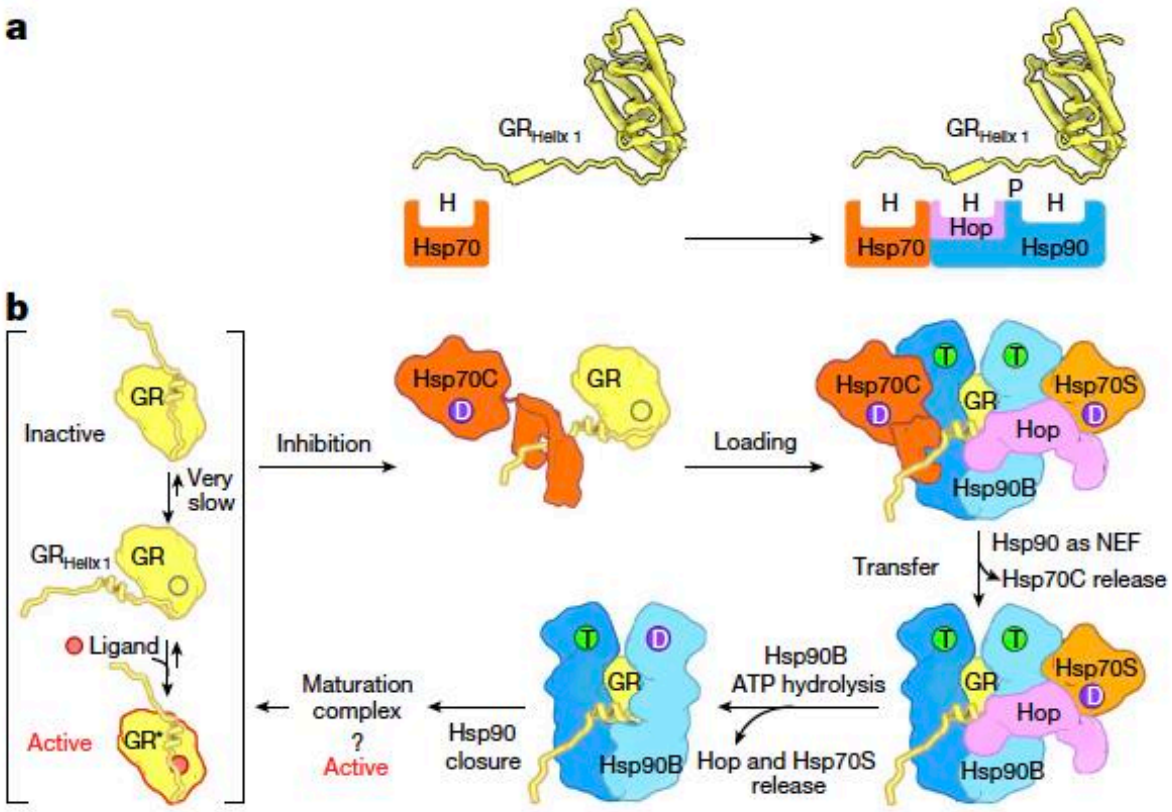

Fig. 2.4: Schematic model of how Hsp70 loads GR onto Hsp90
a, The molecular principle of GR recognition at the client-loading step. **b**, Molecular mechanism of GR transfer from Hsp70 to Hsp90 and the use of ATP hydrolysis on Hsp90. GR in physiological conditions is in an equilibrium of active and inactive states, in which the Helix 1 motif acts as a lid to stabilize ligand binding when attached. Hsp70C (dark orange) in its ADP state (D) binds GRpre-Helix 1 strand, facilitating the following motif to detach and hence inhibit GR (top-middle). Facilitated by HopDP2 recognizing the LXXLL motif on GR Helix 1, Hsp70C loads GR to Hsp90 (blue), forming the client-loading complex (top-right). Although the structure was determined in an Hsp90Apo state, we reason that in physiological conditions the high abundance of ATP would soon occupy Hsp90's ATP binding pockets (T). Hsp90's ATP binding and NEF activity facilitate Hsp70C release (bottom-right). The energy from the ATP hydrolysis (D) on Hsp90B (light blue) is used to release Hsp70S (light orange) and Hop (bottom-middle), followed by full closure of Hsp90 toward the GR-maturation complex.

Extended Data Figures and Tables

See Wang et al. 2022

Supplementary Figures

See Wang et al. 2022

Methods

See Wang et al. 2022

References

Bohen, S. P. (1995, Dec 8). Hsp90 mutants disrupt glucocorticoid receptor ligand binding and destabilize aporeceptor complexes. *J Biol Chem, 270*(49), 29433-29438. https://doi.org/10.1074/jbc.270.49.29433

Bohen, S. P., & Yamamoto, K. R. (1993, Dec 1). Isolation of Hsp90 mutants by screening for decreased steroid receptor function. *Proc Natl Acad Sci U S A, 90*(23), 11424-11428. https://doi.org/10.1073/pnas.90.23.11424

Boysen, M., Kityk, R., & Mayer, M. P. (2019, May 16). Hsp70- and Hsp90-Mediated Regulation of the Conformation of p53 DNA Binding Domain and p53 Cancer Variants. *Mol Cell, 74*(4), 831-843 e834. https://doi.org/10.1016/j.molcel.2019.03.032

Bracher, A., & Verghese, J. (2015). The nucleotide exchange factors of Hsp70 molecular chaperones. *Front Mol Biosci, 2*, 10. https://doi.org/10.3389/fmolb.2015.00010

Dahiya, V., Agam, G., Lawatscheck, J., Rutz, D. A., Lamb, D. C., & Buchner, J. (2019, May 16). Coordinated Conformational Processing of the Tumor Suppressor Protein p53 by the Hsp70 and Hsp90 Chaperone Machineries. *Mol Cell, 74*(4), 816-830 e817. https://doi.org/10.1016/j.molcel.2019.03.026

Doyle, S. M., Hoskins, J. R., Kravats, A. N., Heffner, A. L., Garikapati, S., & Wickner, S. (2019, Jul 12). Intermolecular Interactions between Hsp90 and Hsp70. *J Mol Biol, 431*(15), 2729-2746. https://doi.org/10.1016/j.jmb.2019.05.026

Flynn, J. M., Rossouw, A., Cote-Hammarlof, P., Fragata, I., Mavor, D., Hollins, C., 3rd, Bank, C., & Bolon, D. N. (2020, Mar 4). Comprehensive fitness maps of Hsp90 show widespread environmental dependence. *Elife, 9*. https://doi.org/10.7554/eLife.53810

Genest, O., Hoskins, J. R., Camberg, J. L., Doyle, S. M., & Wickner, S. (2011, May 17). Heat shock protein 90 from Escherichia coli collaborates with the DnaK chaperone system in client protein remodeling. *Proc Natl Acad Sci U S A, 108*(20), 8206-8211. https://doi.org/10.1073/pnas.1104703108

Genest, O., Hoskins, J. R., Kravats, A. N., Doyle, S. M., & Wickner, S. (2015, Dec 4). Hsp70 and Hsp90 of E. coli Directly Interact for Collaboration in Protein Remodeling. *J Mol Biol, 427*(24), 3877-3889. https://doi.org/10.1016/j.jmb.2015.10.010

Genest, O., Reidy, M., Street, T. O., Hoskins, J. R., Camberg, J. L., Agard, D. A., Masison, D. C., & Wickner, S. (2013, Feb 7). Uncovering a region of heat shock protein 90 important for client binding in E. coli and chaperone function in yeast. *Mol Cell, 49*(3), 464-473. https://doi.org/10.1016/j.molcel.2012.11.017

Genest, O., Wickner, S., & Doyle, S. M. (2019, Feb 8). Hsp90 and Hsp70 chaperones: Collaborators in protein remodeling. *J Biol Chem, 294*(6), 2109-2120. https://doi.org/10.1074/jbc.REV118.002806

Hawle, P., Siepmann, M., Harst, A., Siderius, M., Reusch, H. P., & Obermann, W. M. (2006, Nov). The middle domain of Hsp90 acts as a discriminator between different types of client proteins. *Mol Cell Biol, 26*(22), 8385-8395. https://doi.org/10.1128/MCB.02188-05

Kim, Y. E., Hipp, M. S., Bracher, A., Hayer-Hartl, M., & Hartl, F. U. (2013). Molecular chaperone functions in protein folding and proteostasis. *Annu Rev Biochem, 82*, 323-355. https://doi.org/10.1146/annurev-biochem-060208-092442

Kirschke, E., Goswami, D., Southworth, D., Griffin, P., & Agard, D. (2014). Glucocorticoid Receptor Function Regulated by Coordinated Action of the Hsp90 and Hsp70 Chaperone Cycles. *Cell, 157*(7), 1685-1697. https://doi.org/10.1016/j.cell.2014.04.038

Kirschke, E., Roe-Zurz, Z., Noddings, C., & Agard, D. (2020). The interplay between Bag-1, Hsp70, and Hsp90 reveals that inhibiting Hsp70 rebinding is essential for Glucocorticoid Receptor activity. *bioRxiv*. https://doi.org/10.1101/2020.05.03.075523

Kravats, A. N., Hoskins, J. R., Reidy, M., Johnson, J. L., Doyle, S. M., Genest, O., Masison, D. C., & Wickner, S. (2018, Mar 6). Functional and physical interaction between yeast Hsp90 and Hsp70. *Proc Natl Acad Sci U S A, 115*(10), E2210-E2219. https://doi.org/10.1073/pnas.1719969115

Krukenberg, K. A., Street, T. O., Lavery, L. A., & Agard, D. A. (2011, May). Conformational dynamics of the molecular chaperone Hsp90. *Q Rev Biophys, 44*(2), 229-255. https://doi.org/10.1017/S0033583510000314

Lackie, R. E., Maciejewski, A., Ostapchenko, V. G., Marques-Lopes, J., Choy, W. Y., Duennwald, M. L., Prado, V. F., & Prado, M. A. M. (2017). The Hsp70/Hsp90 Chaperone Machinery in Neurodegenerative Diseases. *Front Neurosci, 11*, 254. https://doi.org/10.3389/fnins.2017.00254

Lee, C. T., Graf, C., Mayer, F. J., Richter, S. M., & Mayer, M. P. (2012, Mar 21). Dynamics of the regulation of Hsp90 by the co-chaperone Sti1. *EMBO J, 31*(6), 1518-1528. https://doi.org/10.1038/emboj.2012.37

Liu, Y., Sun, M., Myasnikov, A. G., Elnatan, D., Delaeter, N., Nguyenquang, M., & Agard, D. A. (2020). Cryo-EM structures reveal a multistep mechanism of Hsp90 activation by co-chaperone Aha1. *bioRxiv*.

Lorenz, O. R., Freiburger, L., Rutz, D. A., Krause, M., Zierer, B. K., Alvira, S., Cuellar, J., Valpuesta, J. M., Madl, T., Sattler, M., & Buchner, J. (2014, Mar 20). Modulation of the Hsp90 chaperone cycle by a stringent client protein. *Mol Cell, 53*(6), 941-953. https://doi.org/10.1016/j.molcel.2014.02.003

Mandal, A. K., Gibney, P. A., Nillegoda, N. B., Theodoraki, M. A., Caplan, A. J., & Morano, K. A. (2010, May 1). Hsp110 chaperones control client fate determination in the hsp70-Hsp90 chaperone system. *Mol Biol Cell, 21*(9), 1439-1448. https://doi.org/10.1091/mbc.E09-09-0779

Mayer, M. P., & Gierasch, L. M. (2019, Feb 8). Recent advances in the structural and mechanistic aspects of Hsp70 molecular chaperones. *J Biol Chem, 294*(6), 2085-2097. https://doi.org/10.1074/jbc.REV118.002810

Moran Luengo, T., Kityk, R., Mayer, M. P., & Rudiger, S. G. D. (2018, May 3). Hsp90 Breaks the Deadlock of the Hsp70 Chaperone System. *Mol Cell, 70*(3), 545-552 e549. https://doi.org/10.1016/j.molcel.2018.03.028

Morgner, N., Schmidt, C., Beilsten-Edmands, V., Ebong, I. O., Patel, N. A., Clerico, E. M., Kirschke, E., Daturpalli, S., Jackson, S. E., Agard, D., & Robinson, C. V. (2015, May 5). Hsp70 forms antiparallel dimers stabilized by post-translational modifications to position clients for transfer to Hsp90. *Cell Rep, 11*(5), 759-769. https://doi.org/10.1016/j.celrep.2015.03.063

Nathan, D. F., & Lindquist, S. (1995, Jul). Mutational analysis of Hsp90 function: interactions with a steroid receptor and a protein kinase. *Mol Cell Biol, 15*(7), 3917-3925. https://doi.org/10.1128/mcb.15.7.3917

Nathan, D. F., Vos, M. H., & Lindquist, S. (1997, Nov 25). In vivo functions of the Saccharomyces cerevisiae Hsp90 chaperone. *Proc Natl Acad Sci U S A, 94*(24), 12949-12956. https://doi.org/10.1073/pnas.94.24.12949

Noddings, C. M., Wang, R. Y., Johnson, J. L., & Agard, D. A. (2022, Jan). Structure of Hsp90-p23-GR reveals the Hsp90 client-remodelling mechanism. *Nature, 601*(7893), 465-469. https://doi.org/10.1038/s41586-021-04236-1

Picard, D., Khursheed, B., Garabedian, M. J., Fortin, M. G., Lindquist, S., & Yamamoto, K. R. (1990, Nov 8). Reduced levels of hsp90 compromise steroid receptor action in vivo. *Nature, 348*(6297), 166-168. https://doi.org/10.1038/348166a0

Pratt, W. B., Morishima, Y., Murphy, M., & Harrell, M. (2006). Chaperoning of glucocorticoid receptors. *Handb Exp Pharmacol*(172), 111-138. https://doi.org/10.1007/3-540-29717-0_5

Pratt, W. B., & Toft, D. O. (1997). Steroid Receptor Interactions with Heat Shock Protein and Immunophilin Chaperones. *Endocrine Reviews, 18*(3), 306-360. https://doi.org/10.1210/edrv.18.3.0303

Reidy, M., Kumar, S., Anderson, D. E., & Masison, D. C. (2018, Aug). Dual Roles for Yeast Sti1/Hop in Regulating the Hsp90 Chaperone Cycle. *Genetics, 209*(4), 1139-1154. https://doi.org/10.1534/genetics.118.301178

Rosenzweig, R., Nillegoda, N. B., Mayer, M. P., & Bukau, B. (2019, Nov). The Hsp70 chaperone network. *Nat Rev Mol Cell Biol, 20*(11), 665-680. https://doi.org/10.1038/s41580-019-0133-3

Rutz, D. A., Luo, Q., Freiburger, L., Madl, T., Kaila, V. R. I., Sattler, M., & Buchner, J. (2018, Apr 16). A switch point in the molecular chaperone Hsp90 responding to client interaction. *Nat Commun, 9*(1), 1472. https://doi.org/10.1038/s41467-018-03946-x

Sahasrabudhe, P., Rohrberg, J., Biebl, M. M., Rutz, D. A., & Buchner, J. (2017, Sep 21). The Plasticity of the Hsp90 Co-chaperone System. *Mol Cell, 67*(6), 947-961 e945. https://doi.org/10.1016/j.molcel.2017.08.004

Scheufler, C., Brinker, A., Bourenkov, G., Pegoraro, S., Moroder, L., Bartunik, H., Hartl, F. U., & Moarefi, I. (2000, Apr 14). Structure of TPR domain-peptide complexes:

critical elements in the assembly of the Hsp70-Hsp90 multichaperone machine. *Cell, 101*(2), 199-210. https://doi.org/10.1016/S0092-8674(00)80830-2

Schmid, A. B., Lagleder, S., Grawert, M. A., Rohl, A., Hagn, F., Wandinger, S. K., Cox, M. B., Demmer, O., Richter, K., Groll, M., Kessler, H., & Buchner, J. (2012, Mar 21). The architecture of functional modules in the Hsp90 co-chaperone Sti1/Hop. *EMBO J, 31*(6), 1506-1517. https://doi.org/10.1038/emboj.2011.472

Schopf, F. H., Biebl, M. M., & Buchner, J. (2017, Jun). The HSP90 chaperone machinery. *Nat Rev Mol Cell Biol, 18*(6), 345-360. https://doi.org/10.1038/nrm.2017.20

Smith, D. F., & Toft, D. O. (2008, Oct). Minireview: the intersection of steroid receptors with molecular chaperones: observations and questions. *Mol Endocrinol, 22*(10), 2229-2240. https://doi.org/10.1210/me.2008-0089

Southworth, D. R., & Agard, D. A. (2011, Jun 24). Client-loading conformation of the Hsp90 molecular chaperone revealed in the cryo-EM structure of the human Hsp90:Hop complex. *Mol Cell, 42*(6), 771-781. https://doi.org/10.1016/j.molcel.2011.04.023

Sun, M., Kotler, J. L. M., Liu, S., & Street, T. O. (2019, Apr 19). The endoplasmic reticulum (ER) chaperones BiP and Grp94 selectively associate when BiP is in

the ADP conformation. *J Biol Chem, 294*(16), 6387-6396. https://doi.org/10.1074/jbc.RA118.007050

Sung, N., Lee, J., Kim, J. H., Chang, C., Tsai, F. T., & Lee, S. (2016, Aug). 2.4 A resolution crystal structure of human TRAP1NM, the Hsp90 paralog in the mitochondrial matrix. *Acta Crystallogr D Struct Biol, 72*(Pt 8), 904-911. https://doi.org/10.1107/S2059798316009906

Suren, T., Rutz, D., Mossmer, P., Merkel, U., Buchner, J., & Rief, M. (2018, Nov 13). Single-molecule force spectroscopy reveals folding steps associated with hormone binding and activation of the glucocorticoid receptor. *Proc Natl Acad Sci U S A, 115*(46), 11688-11693. https://doi.org/10.1073/pnas.1807618115

Taipale, M., Jarosz, D. F., & Lindquist, S. (2010, Jul). HSP90 at the hub of protein homeostasis: emerging mechanistic insights. *Nat Rev Mol Cell Biol, 11*(7), 515-528. https://doi.org/10.1038/nrm2918

Verba, K. A., Wang, R. Y., Arakawa, A., Liu, Y., Shirouzu, M., Yokoyama, S., & Agard, D. A. (2016, Jun 24). Atomic structure of Hsp90-Cdc37-Cdk4 reveals that Hsp90 traps and stabilizes an unfolded kinase. *Science, 352*(6293), 1542-1547. https://doi.org/10.1126/science.aaf5023

Whitesell, L., & Lindquist, S. L. (2005, Oct). HSP90 and the chaperoning of cancer. *Nat Rev Cancer, 5*(10), 761-772. https://doi.org/10.1038/nrc1716

Chapter 3 Structure of Hsp90-p23-GR reveals the Hsp90 client-remodeling mechanism

Preface

The work presented in this chapter resulted from a joint project with Dr. Ray Wang, a former post-doctoral researcher in the Agard lab. The goal of this project was to determine a cryo-EM structure of the GR-maturation complex (GR:Hsp90:p23) to elucidate how Hsp90 remodels the conformation of GR to restore GR ligand-binding after Hsp70 inhibition. As with the GR-loading complex project (Chaper 2), this project builds from decades of work investigating the role of Hsp70, Hsp90, and cochaperones in regulating the activity of GR and other SHRs (Pratt & Toft, 1997). In particular, we sought to describe in atomic detail the chaperoning mechanism of Hsp90, by describing how Hsp90 refolds GR after Hsp70 partially unfolds GR to inhibit ligand-binding, which was first biochemically described in detail by Elaine Kirschke (Kirschke et al., 2014).

In this work, we determined the structure of the GR-maturation complex, revealing Hsp90 refolds GR to a completely native conformation. Unexpectedly, the native GR is further stabilized by a C-terminal helix on the structurally uncharacterized tail of p23, demonstrating p23 directly contributes to GR folding maturation. Surprisingly, the structure revealed that GR is also bound to ligand, indicating GR ligand-binding occurs in the transition from the GR-loading complex to the GR-maturation complex, and therefore, ligand-binding is directly coordinated by the chaperoning actions of Hsp70 and Hsp90.

The GR-loading complex (Chaper 2) (Wang et al., 2022) and GR-maturation complex manuscripts were co-published and together these structures established the first complete Hsp90 chaperone cycle for any client. These findings elucidated the Hsp90 chaperoning mechanism in atomic and mechanistic detail. In this mechanism, Hsp90 refolds GR by allowing segments of the partially unfolded client to slide through the lumen of Hsp90 and refold onto the body of GR in a protected manner. The folded, ligand-bound GR is extensively stabilized by Hsp90 and p23. Hsp90 also protects GR from Hsp70 re-binding and re-inhibition by occluding the Hsp70 binding site. Thus, GR is refolded and activated by Hsp90, aided by the cochaperone p23.

During this project, Dr. Ray Wang trained me in all aspects of biochemistry and cryo-EM, including how to prepare and work with the *in vitro* reconstituted GR-chaperone cycle. Jill Johnson (University of Idaho) performed *in vivo* experiments on the role of the p23 tail-helix in GR activation.

Abstract

Hsp90 is a conserved and essential molecular chaperone responsible for the folding and activation of hundreds of ‘client’ proteins (Schopf et al., 2017; Taipale et al., 2010; Taipale et al., 2012). The glucocorticoid receptor (GR) is a model client that constantly depends on Hsp90 for activity (Lorenz et al., 2014; Morishima et al., 2000; Nathan & Lindquist, 1995; Picard et al., 1990; Pratt & Toft, 1997; Smith & Toft, 2008). Previously, we revealed GR ligand binding is inhibited by Hsp70 and restored by Hsp90, aided by the cochaperone p23 (Kirschke et al., 2014). However, a molecular understanding of the chaperone-mediated remodeling that occurs between the inactive

Hsp70:Hsp90 ‘client-loading complex’ and an activated Hsp90:p23 ‘client-maturation complex’ is lacking for GR, or any client. Here, we present a 2.56Å cryo-EM structure of the GR-maturation complex (GR:Hsp90:p23), revealing that the GR ligand-binding domain is, surprisingly, restored to a folded, ligand-bound conformation, while simultaneously threaded through the Hsp90 lumen. Also, unexpectedly, p23 directly stabilizes native GR using a previously unappreciated C-terminal helix, resulting in enhanced ligand-binding. This is the highest resolution Hsp90 structure to date and the first atomic resolution structure of a client bound to Hsp90 in a native conformation, sharply contrasting with the unfolded kinase:Hsp90 structure (Verba et al., 2016). Thus, aided by direct cochaperone:client interactions, Hsp90 can directly dictate client-specific folding outcomes. Together with the GR-loading complex structure (Wang et al., 2022), we present the molecular mechanism of chaperone-mediated GR remodeling, establishing the first complete chaperone cycle for any client.

Introduction

Hsp90 is required for the functional maturation of ~10% of the eukaryotic proteome, including signaling proteins such as GR, a steroid hormone receptor (SHR) (Taipale et al., 2010; Taipale et al., 2012; Zhao et al., 2005). We previously uncovered the biochemical basis for GR’s Hsp90 dependence using *in vitro* reconstitution starting with an active GR ligand-binding domain (hereafter GR, for simplicity) (Kirschke et al., 2014). We demonstrated that GR ligand binding is regulated by a cycle of GR:chaperone complexes in which GR is first inhibited by Hsp70, then loaded onto Hsp90:Hop (Hsp70/Hsp90 organizing protein) forming an inactive

GR:Hsp90:Hsp70:Hop loading complex (Wang et al., 2022). Upon ATP hydrolysis on Hsp90, Hsp70 and Hop are released, and p23 is incorporated to form an active GR:Hsp90:p23 maturation complex, restoring GR ligand binding with enhanced affinity. Progression through this cycle is coordinated by the ATPase activities of Hsp70 and Hsp90, enabling large conformational rearrangements (Rosenzweig et al., 2019; Schopf et al., 2017). Particularly, Hsp90 functions as a constitutive dimer that undergoes an open-to-closed transition upon ATP binding and this conformational cycle is further regulated by cochaperones (Krukenberg et al., 2011). The cochaperone p23 specifically binds and stabilizes the closed Hsp90 conformation (Ali et al., 2006) and is required for full reactivation of GR ligand binding *in vitro* (Kirschke et al., 2014) and proper GR function *in vivo* (Sahasrabudhe et al., 2017).

While the Hsp90/Hsp70 chaperone systems are fundamental in maintaining protein homeostasis and regulating numerous crucial cellular functions (Taipale et al., 2010), the absence of client:chaperone structures has precluded a mechanistic understanding of the remodeling process for GR, or any client. The kinase:Hsp90 structure (Verba et al., 2016) first revealed how Hsp90 can stabilize an inactive client, but provided no insights to explain how Hsp90 can reactivate a client, such as GR. Here, we report the high-resolution cryo-EM structure of the GR-maturation complex, providing a long-awaited molecular mechanism for chaperone-mediated client remodeling and activation.

Results

Structure determination

The GR-maturation complex was prepared through *in vitro* reconstitution of the GR chaperone cycle, where the MBP (maltose-binding protein)-GR ligand-binding domain (LBD) was incubated with Hsp70, Hsp40, Hop, Hsp90, and p23, allowing GR to progress through the chaperone cycle to reach the maturation complex (Materials and Methods, Extended Data Fig. 1a-e). A 2.56Å cryo-EM reconstruction of the maturation complex was obtained (Fig. 1a; Extended Data Fig. 2a,b; Supplementary Table 1) using RELION (Scheres, 2012) and atomic models were built in Rosetta (Wang et al., 2016) starting from previously published atomic structures. The structure reveals a fully closed, nucleotide-bound Hsp90 dimer (Hsp90A and B) (Extended Data Fig. 2c) complexed with a single GR and a single p23, which occupy the same side of Hsp90 (Fig. 1a,b).

Hsp90 stabilizes GR in an active state

GR and Hsp90 have three major interfaces (Fig. 1c-e): (1) Hsp90 lumen:$GR_{pre\text{-}Helix\ 1}$; (2) $Hsp90_{MD/CTD}$:$GR_{Helix\ 1}$, and (3) $Hsp90_{MD/CTD}$:$GR_{Helices\ 3,\ 4,\ and\ 9}$. In the first interface, the N-terminal $GR_{pre\text{-}Helix\ 1}$ ($GR^{523\text{-}531}$) is threaded through the closed Hsp90 lumen (~735$Å^2$ buried surface area (BSA))(Fig. 1c). The Hsp90 lumen provides a mostly hydrophobic 'tunnel' that captures $GR_{pre\text{-}Helix\ 1}$ (Fig. 1c; Extended Data Fig. 3a). Specifically, two residues ($GR^{L525,L528}$) occupy hydrophobic binding pockets within the Hsp90 lumen. The interaction is further stabilized by multiple hydrogen bonds from Hsp90 to the backbone and side chains of $GR_{pre\text{-}Helix\ 1}$ (Extended Data Fig. 3b). Interface

2 is mainly comprised of the short $GR_{Helix\ 1}$ ($GR^{532\text{-}539}$) packing up against the amphipathic helical hairpin ($Hsp90_{amphi\text{-}\alpha}$) in the C-terminal domain of Hsp90B ($Hsp90B_{CTD}$) and $GR_{Helices\ 8\ and\ 9}$ interacting with $Hsp90B_{MD/CTD}$ (~488Å^2 BSA)(Fig. 1d, Extended Data Fig. 3c). In interface 3, the $Hsp90B_{amphi\text{-}\alpha}$ packs against $GR_{Helix\ 3}$ and the conserved, solvent exposed hydrophobic residues $Hsp90^{W320,F349}$, located in the middle domain of Hsp90A ($Hsp90A_{MD}$), make contact with $GR_{Helices\ 4\ and\ 9}$ (~467Å^2 BSA)(Fig. 1e, Extended Data Fig. 3d). Notably, $Hsp90^{W320,F349}$ also make contact with GR in the loading complex (Wang et al., 2022) and $Hsp90^{W320}$ is critical for client activation *in vivo* (Hawle et al., 2006; Meyer et al., 2003; Rutz et al., 2018).

Surprisingly, in the maturation complex, despite being bound to Hsp90, GR adopts an active, folded conformation (Cα RMSD of 1.24Å to crystal structure Protein Data Bank (PDB) ID 1M2Z (Bledsoe et al., 2002)). Specifically, $GR_{Helix\ 12}$, a dynamic motif responsive to ligand binding, is in the agonist-bound position, as in the crystal structure (PDB ID 1M2Z) (Extended Data Fig. 4a). Unlike the crystal structure, $GR_{Helix\ 12}$ is not stabilized by a co-activator peptide, although co-activator peptide binding would be sterically allowed (Extended Data Fig. 4b). Unexpectedly, the density also revealed that GR is ligand-bound (Extended Data Fig. 4c). The only ligand source was the initial GR purification with agonists, after which GR was extensively dialyzed, removing the majority of ligand (Kirschke et al., 2014). During preparation of the maturation complex, GR likely rebound residual ligand and despite multiple washes, the ligand remained bound, suggesting a high affinity and slow ligand off-rate from the maturation complex. Based on the ligand density and positions of GR^{Y735}, the bound ligand is likely dexamethasone (Extended Data Fig. 4c). The native, ligand-bound GR LBD is known to

dimerize for function (Bledsoe et al., 2002); however, in the GR-maturation complex, while the putative dimerization interface is solvent accessible, the binding of a second GR would clash with the $Hsp90B_{CTD}$ (Extended Data Fig. 4d).

p23 interacts directly with GR

The Hsp90:p23 interface is comparable to the crystal structure of the yeast Hsp90:p23 complex (PDB ID 2CG9) (Ali et al., 2006), where p23 makes extensive contacts with the N-terminal domains of Hsp90 ($Hsp90_{NTD}$s) to stabilize the Hsp90 closed state (~1274$Å^2$ BSA)(Extended Data Fig. 5a-d). Only one p23 is bound to the Hsp90 dimer, consistent with a previous report (Lorenz et al., 2014), although a 2-fold excess of p23 was added during complex preparation and two p23 molecules are in the yeast Hsp90:p23 structure (Ali et al., 2006). The slight asymmetry observed here between the $Hsp90_{NTD}$ dimer interfaces (Extended Data Fig. 5e) combined with the avidity afforded by simultaneous interactions with Hsp90 and GR likely provides a molecular explanation.

Unexpectedly, p23 also makes direct and extensive contacts with GR (~702$Å^2$ BSA) through the early part ($p23^{112-133}$) of its ~58 residue C-terminal tail ($p23^{103-160}$), while the following 27 tail residues ($p23^{134-160}$) were not visible. As observed in the yeast Hsp90:p23 crystal structure (PDB ID 2CG9), the beginning of the p23 tail ($p23^{F103,N104,W106}$) interacts with the $Hsp90B_{NTD}$ (Extended Data Fig. 5c). The following loop ($p23^{108-118}$) forms polar interactions with both GR and Hsp90 (Fig. 2a,c). Although the tail was previously thought to be unstructured (Weikl et al., 1999), we found a 13-residue helix ($p23^{119-131}$, $p23_{tail\text{-}helix}$) bound to GR (Fig. 2a,c; Extended Data Fig. 6a,b).

This newly identified $p23_{tail\text{-}helix}$ was also predicted by multiple state-of-the-art secondary structure prediction algorithms and AlphaFold v2.0 (Jumper et al., 2021) (Extended Data Fig. 6d). Furthermore, a peptide corresponding to this region ($p23^{118\text{-}131}$) was previously found to have helical propensity (Seraphim et al., 2015) and an interaction between $p23^{117\text{-}127}$ and GR has been suggested (Biebl et al., 2021). In the GR maturation complex, the hydrophobic surface of the $p23_{tail\text{-}helix}$ packs against an exposed hydrophobic patch on the GR surface made by $GR_{Helices\ 9\ and\ 10}$ (Extended Data Fig. 6a,b). The $p23_{tail\text{-}helix}$ also contacts the C-terminal strand of GR (GR^{H775}), potentially allosterically stabilizing the dynamic $GR_{Helix\ 12}$ ($GR^{750\text{-}767}$) in the agonist-bound position (Fig. 2c, Extended Data Fig. 6e).

Notably, in both p23 and GR, residues involved in this novel p23:GR interface are conserved across vertebrates (Fig. 2b, Extended Data Fig. 6f). The GR hydrophobic patch at the p23:GR interface is also conserved across SHRs, which are thought to undergo similar regulation by Hsp90/Hsp70 (Extended Data Fig. 6c) (Pratt & Toft, 1997). Attesting to its importance beyond SHRs, the $p23_{tail\text{-}helix}$ motif is conserved in yeast, which lack SHRs (Extended Data Fig. 6f). Due to the high level of conservation of the $p23_{tail\text{-}helix}$ and the hydrophobic patch on SHRs, we reasoned other proteins may utilize a $p23_{tail\text{-}helix}$-like motif to bind SHRs. Using ScanProsite (de Castro et al., 2006) to search the human proteome for a $p23_{tail\text{-}helix}$-like motif ("FXXMMN"), remarkably, Nuclear Coactivator 3 (NCoA3/SRC-3), a canonical co-activator protein for SHRs, was among the top 10 hits. The identified NCoA3 motif (FNSMMNQM) aligns with the $p23_{tail\text{-}helix}$ sequence (FSEMMNNM) and contains the key conserved hydrophobic residues that interact with GR (Fig. 2a,c; Extended Data Fig. 6f). This suggests NCoA3 may use this

newly identified motif to bind GR at the novel interface, in addition to the canonical NCoA3 LXXLL motif:SHR$_{Helix\ 12}$ interface (McKenna & O'Malley, 2002).

The p23$_{tail\text{-}helix}$ potentiates GR

To quantitatively assess the importance of the p23:GR interface for the enhanced ligand binding in the *in vitro* chaperone cycle, we compared full length p23 to two p23 tail mutants: p23$^{1\text{-}133}$ (p23$_{\Delta tail}$) and p23$^{1\text{-}112}$ (p23$_{\Delta helix\Delta tail}$) (Extended Data Fig. 7a). In both mutants, critical Hsp90:p23 contacts were unperturbed. While p23$_{\Delta tail}$ had no significant effect on the chaperone-mediated enhancement of ligand binding, p23$_{\Delta helix\Delta tail}$ abolished the enhancement, reducing binding almost to GR alone levels (Fig. 2d, Extended Data Fig. 7b). Thus, the observed chaperone-mediated ligand-binding enhancement is dependent upon the p23$_{tail\text{-}helix}$. Importantly, p23$_{\Delta helix\Delta tail}$ did not reduce the GR ligand-binding activity to the same extent as omitting p23, indicating the p23 core plays a distinct and critical role in stabilizing the closed Hsp90 conformation in the maturation complex. We also found p23 had no significant effect on GR ligand binding *in vitro,* independent of the chaperone cycle (Extended Data Fig. 7c), although p23 has general Hsp90-independent chaperoning properties (Freeman et al., 1996; Weaver et al., 2000; Weikl et al., 1999).

To assess the importance of the p23$_{tail\text{-}helix}$ *in vivo*, we tested the ability of human p23 and the p23 tail mutants to rescue yeast growth defects due to the absence of Sba1 (yeast p23) in a strain expressing a sensitizing yeast Hsp90 mutant (Hsc82$^{I588A\text{-}M589A}$) (Extended Data Fig. 7d). At 37°C, in the absence of *SBA1* (*sba1*), exogenous expression of full-length human p23 and p23$_{\Delta tail}$ rescued the *sba1* growth defect and, in

fact, exhibited enhanced viability compared to exogenous expression of Sba1. The enhanced viability is dependent on the $p23_{tail\text{-}helix}$, as $p23_{\Delta helix\Delta tail}$ abolished this enhancement, indicating the $p23_{tail\text{-}helix}$ is functionally important *in vivo*.

We also tested whether the $p23_{tail\text{-}helix}$ is important for GR activity *in vivo,* given that p23 can substitute for Sba1 in yeast GR transactivation assays (Bohen, 1998; Freeman et al., 2000). We measured GR activity with exogenous expression of p23, p23 tail mutants, or Sba1 (Extended Data Fig. 7e). All p23/Sba1 constructs showed equivalent expression levels (Extended Data Fig. 7f) and expression of p23 significantly enhanced GR activity relative to Sba1, consistent with a previous report (Freeman et al., 2000). However, both $p23_{\Delta tail}$ and $p23_{\Delta helix\Delta tail}$ significantly reduced GR activity equivalently compared to p23. The effect of deleting the unstructured part of the p23 tail ($p23^{134\text{-}160}$) on GR activity *in vivo* may be related to p23-dependent regulation of GR functions downstream of ligand binding (Freeman & Yamamoto, 2002), which may dominate any effect of the $p23_{tail\text{-}helix}$ on GR activation *in vivo*.

Hsp90 lumen density in the absence of GR

From the same GR:Hsp90:p23 dataset, we also obtained reconstructions of Hsp90:p23 (2.66Å resolution) (Extended Data Fig. 8a,b) and MBP:Hsp90:p23 (3.63Å resolution) (Extended Data Fig. 9a,b), which both contain Hsp90 lumen density (Extended Data Fig. 8c,d; 9d,e). In the MBP:Hsp90:p23 complex, one p23 with low occupancy is bound to Hsp90 on the opposite side of MBP. Notably, MBP is partially unfolded, as density for the two C-terminal helices is missing. The MBP C-terminal region likely threads through Hsp90, accounting for the lumen density. The MBP is also

in an apo state, consistent with the unfolding of the last two helices, which form part of its binding pocket (Extended Data Fig. 9c).

Discussion

We present the first atomic resolution structure of a client bound to Hsp90 in a native folded conformation, as well as the highest resolution structure of full-length Hsp90 to date. In the maturation complex, GR simultaneously threads through the closed Hsp90 lumen and adopts a native, ligand-bound conformation that is extensively stabilized by both Hsp90 and the $p23_{tail\text{-}helix}$. The active, native GR in our complex starkly contrasts with the only other structure of a closed Hsp90:client complex, which stabilizes an unfolded kinase client (Verba et al., 2016). Both clients are threaded through the closed Hsp90 lumen, suggesting a universal binding mode for Hsp90 clients (Liu et al., 2020; Verba et al., 2016) (Extended Data Fig. 10a,b). Although the overall Hsp90:client interactions are similar, the outcomes for folding and function of these two clients are opposing, demonstrating evolutionarily determined, client-specific conformational remodeling by Hsp90 (Extended Data Fig. 10c).

While previously thought to be a general cochaperone whose primary function is to stabilize closed Hsp90, our structure reveals that p23 also makes extensive contacts with GR through a previously unappreciated helix in the p23 tail. This $p23_{tail\text{-}helix}$ is necessary for the enhanced GR ligand-binding activity *in vitro*; thus, p23 not only serves as a cochaperone to stabilize the closure of Hsp90, but also directly contributes to client maturation. In support of this essential p23:GR interaction, the $p23_{tail\text{-}helix}$ and GR hydrophobic groove are well conserved, and a helix in the yeast p23 tail supports GR

transactivation *in vivo* (Biebl et al., 2021). Furthermore, the hydrophobic groove is conserved across SHRs, suggesting that the $p23_{tail\text{-}helix}$ contributes to Hsp90-dependent chaperoning of all SHRs. Indeed, where examined, SHR activity has been dependent on p23 (Sahasrabudhe et al., 2017) and the progesterone receptor (PR) requires the p23 tail for chaperone-mediated ligand-binding activity (Weaver et al., 2000). Intriguingly, NCoA3 contains a $p23_{tail\text{-}helix}$-like motif, suggesting other GR coregulators may utilize this novel helix motif to bind the hydrophobic groove on GR and compete with p23, potentially facilitating GR release. These findings support an emerging paradigm in which Hsp90 cochaperones make specific, direct contact with Hsp90 clients to aid in client recognition and function (Verba et al., 2016; Wang et al., 2022).

Together with the structure of the GR-loading complex (Wang et al., 2022), we provide for the first time, a complete picture of the chaperone cycle for any client (Fig. 3b-d). These two structures reveal how GR is remodeled from a partially unfolded conformation in the loading complex to an active, folded conformation in the maturation complex. In the loading complex, $GR_{pre\text{-}Helix\ 1}$ is captured by Hsp70, $GR_{Helix\ 1}$ is stabilized by Hop, and $GR_{post\text{-}Helix\ 1}$ is threaded through the semi-closed Hsp90 lumen. First, Hsp70 and Hop release from the loading complex, driven by Hsp90 ATP binding/hydrolysis (Kirschke et al., 2014; Wang et al., 2022). Then, $GR_{pre\text{-}Helix\ 1}$ can slide into the Hsp90 lumen, allowing $GR_{Helix\ 1}$ to refold onto the GR core, thereby generating a ligand binding capable, native GR, stabilized by the $p23_{tail\text{-}helix}$ (Fig. 3b,c). During this transition, Hsp90 twists to the p23-stabilized closed conformation, likely facilitating client sliding and rearranging the client-binding site to fully enclose $GR_{pre\text{-}Helix\ 1}$ (Fig. 3a,b). Given that $GR_{Helix\ 1}$ is proposed to function as a lid over the ligand-binding pocket (Suren et al.,

2018), ligand likely binds during the loading complex to maturation complex transition, just as $GR_{Helix\ 1}$ slides through the Hsp90 lumen to seal the ligand-binding pocket (Fig. 3c). The ligand-bound GR becomes protected from Hsp70 rebinding and re-inhibition once it is in the maturation complex, allowing protected nuclear translocation (Czar et al., 1997; Freeman & Yamamoto, 2002; Galigniana et al., 2001).

The proposed sliding mechanism may be a general theme for Hsp90's client remodeling. Our two other reconstructions, Hsp90:p23 and MBP:Hsp90:p23, have density in the Hsp90 lumen, suggesting Hsp90 has bound regions in our construct other than GR. Given that $GR_{Helix\ 1}$ slides through the Hsp90 lumen, it is possible that Hsp90 can act processively to remodel other client domains beyond the one initially engaged, potentially explaining the other reconstructions. The mechanism of $GR_{Helix\ 1}$ sliding explains how Hsp90 can provide protected refolding of client domains as they exit the lumen to become directly stabilized by cochaperones. How eukaryotes overcome the folding challenges of large, multi-domain proteins remains unclear (Netzer & Hartl, 1997). While here we show how GR sliding through Hsp90 regulates GR function, more generally, sliding could also ensure folding fidelity in multi-domain proteins by allowing domains to fold independently on either side of the lumen or allowing misfolded/cross-folded domains to be annealed.

Data availability

The cryo-EM maps generated in this study have been deposited in the Electron Microscopy Data Bank (EMDB) under the accession codes EMD-23004 (GR:Hsp90:p23), EMD-23006 (Hsp90:p23), and EMD-23005 (MBP:Hsp90:p23). The atomic coordinates have been deposited in the PDB under the accession code 7KRJ (GR:Hsp90:p23). Publicly available PDB entries used in this study are: 5FWK, 1M2Z, 4P6X, 1EJF, 2CG9, 1OMP, and 1ANF. The human p23 structure prediction is available from AlphaFold v2.0 with the accession code P83868 (https://alphafold.ebi.ac.uk/entry/P83868). Protein sequence data for sequence alignments are available from Uniprot (see Methods for accession codes). Source data related to Fig. 2d and Extended Data Fig. 7b,c,e are provided with this paper.

Author Contributions

C.M.N. and R.Y.-R.W. designed and executed biochemical experiments, cryo-EM sample preparation, data collection, data processing, and model building. J.L.J. executed yeast *in vivo* assays and interpreted the results. C.M.N., R.Y.-R.W., and D.A.A. conceived the project, interpreted the results, and wrote the manuscript.

Acknowledgements

We thank members of the Agard Lab and Elaine Kirschke for helpful discussions. We thank David Bulkley, Glenn Gilbert, Zanlin Yu, and Eric Tse from the W.M. Keck Foundation Advanced Microscopy Laboratory at the University of California, San Francisco (UCSF) for EM facility maintenance and help with data collection. We also

thank Matt Harrington and Joshua Baker-LePain for computational support with the UCSF Wynton cluster. C.M.N. is a National Cancer Institute Ruth L. Kirschstein Predoctoral Individual NRSA Fellow. R.Y.-R.W was a Howard Hughes Medical Institute Fellow of the Life Sciences Research Foundation. The work was supported by funding from Howard Hughes Medical Institute (D.A.A.) and NIH grants R35GM118099 (D.A.A.), S10OD020054 (D.A.A.), S10OD021741 (D.A.A.), P20GM104420 (J.L.J.), and R01GM127675 (J.L.J.).

Figures

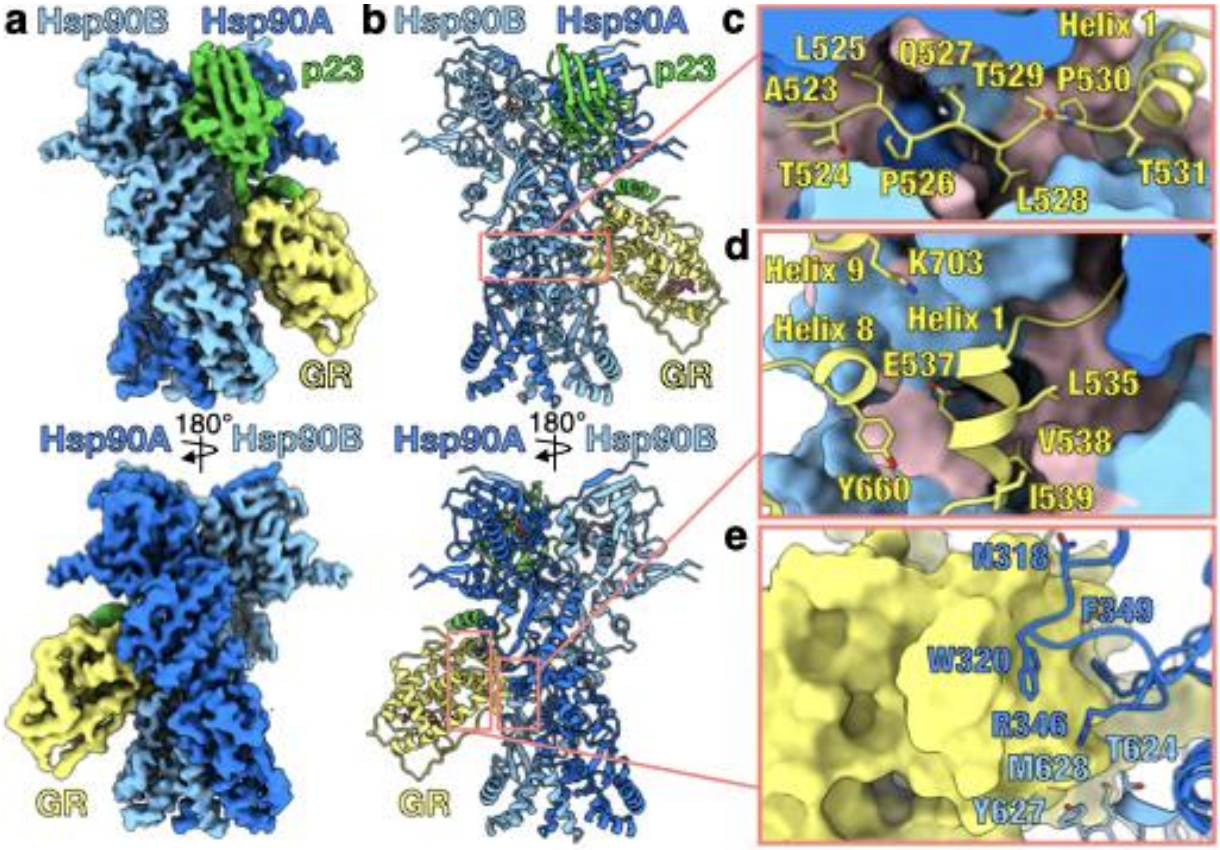

Fig. 3.1: Architecture of the GR-maturation complex
a, Composite cryo-EM map of the GR-maturation complex. Hsp90A (dark blue), Hsp90B (light blue), GR (yellow), p23 (green). Color scheme is maintained throughout. **b**, Atomic model in cartoon representation. **c**, Interface 1 of the Hsp90:GR interaction depicting $GR_{pre\text{-}Helix\ 1}$ ($GR^{523\text{-}531}$) threading through the Hsp90 lumen. Hsp90A/B are in surface representation with hydrophobic residues colored in pink. **d**, Interface 2 of the Hsp90:GR interaction depicting $GR_{Helix\ 1}$ ($GR^{532\text{-}539}$) packing against the entrance to the Hsp90 lumen. Hsp90A/B are in surface representation with hydrophobic residues colored in pink. **e**, Interface 3 of the Hsp90:GR interaction depicting residues on the $Hsp90A_{MD}$ loops ($Hsp90A^{N318,W320,R346,F349}$) and $Hsp90B_{amphi\text{-}\alpha}$ ($Hsp90B^{T624,Y627,M628}$) packing against GR (surface representation).

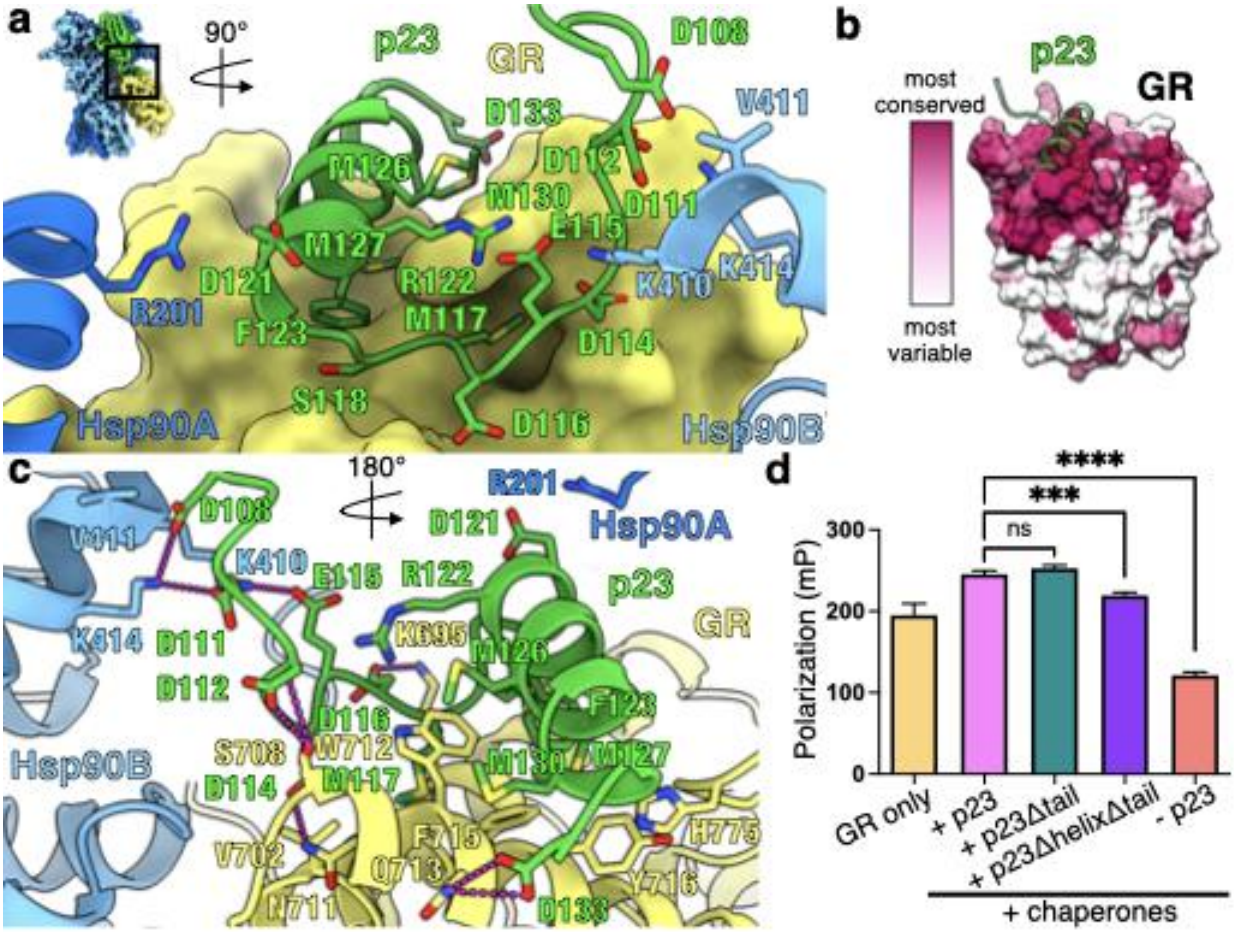

Fig. 3.2: p23$_{tail\text{-}helix}$ interactions and effect on GR ligand binding
a, Interface between the p23$_{tail\text{-}helix}$ (green), GR (yellow, surface representation), Hsp90A (dark blue), and Hsp90B (light blue). The p23$_{tail\text{-}helix}$ (p23$^{119\text{-}131}$) binds GR, while the preceding p23 loop (p23$^{108\text{-}118}$) interacts with GR and Hsp90. **b**, GR protein sequence conservation mapped onto the GR surface colored from most variable (white) to most conserved residues (maroon). The p23$_{tail\text{-}helix}$ (green) is overlaid to indicate the p23:GR interface. **c**, Interface between the p23$_{tail\text{-}helix}$, GR, and Hsp90 showing interacting side chains and hydrogen bonds (dashed pink lines). **d**, Equilibrium binding of 20nM fluorescent dexamethasone to 250nM GR with chaperones and p23 tail mutants measured by fluorescence polarization (mean±SD). n=3 biologically independent samples per condition (n=6 biologically independent samples for the GR only condition). See Extended Data Fig. 8b for data points. Significance was evaluated using a one-way ANOVA ($F_{(3,8)}$ = 636.2; p < 0.0001) with *post-hoc* Dunnett's test (n.s. P ≥ 0.05; * P ≤ 0.05; ** P ≤ 0.01; *** P ≤ 0.001; **** P ≤ 0.0001). P-values: p(p23 vs. p23Δtail) = 0.1512, p(p23 vs. p23ΔhelixΔtail) = 0.0002, p(p23 vs. no p23) = <0.0001.

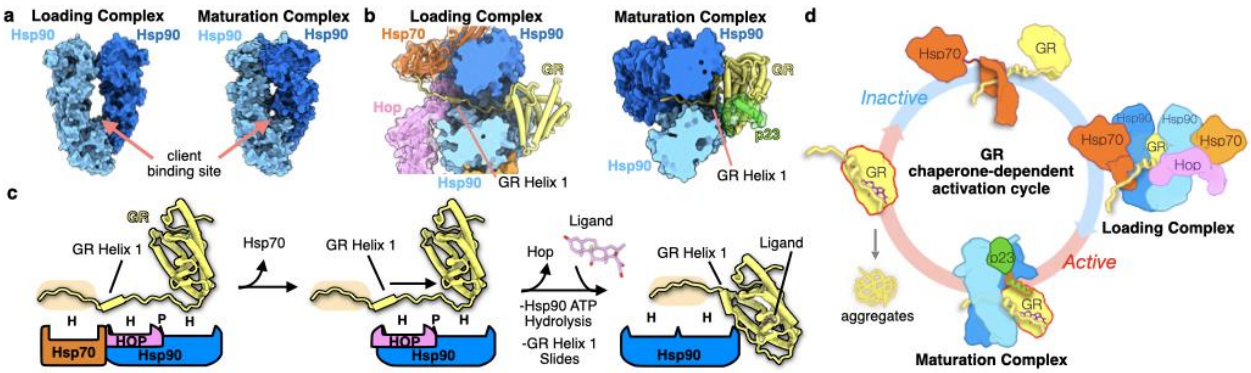

Fig. 3.3: Mechanism of GR activation by Hsp90
a, Surface representation of the Hsp90 dimer in the GR-loading complex[12] versus the GR-maturation complex, showing the Hsp90 conformational change. Hsp90A (dark blue), Hsp90B (light blue). **b**, Top view of the loading complex (left) with $GR_{Helix\ 1}$ extended through the Hsp90 lumen. Top view of the maturation complex (right) with $GR_{Helix\ 1}$ docked onto GR. Hsp70 (orange, transparent surface), Hop (pink, transparent surface), Hsp90A (dark blue, surface representation), Hsp90B (light blue, surface representation), GR (yellow), p23 (green, transparent surface). **c**, Schematic showing the conformational change of $GR_{Helix\ 1}$ from the loading complex to the maturation complex. Boxes represent chaperone and cochaperone binding sites along the $GR_{Helix\ 1}$ region (H=hydrophobic interface, P=polar interface). The $GR_{pre\text{-}Helix\ 1}$ strand is highlighted (tan). Color scheme maintained from (b). **d**, Schematic of the GR chaperone-dependent activation cycle. Ligand-bound, active GR (left) is aggregation prone under physiological conditions. GR ligand binding is inhibited by Hsp70. Inactive GR is loaded onto Hsp90, with Hop, to form the loading complex, where $GR_{Helix\ 1}$ is extended through the Hsp90 lumen. Hsp70/Hop release and p23 binds to form the maturation complex, where $GR_{Helix\ 1}$ is redocked back onto the body of GR and ligand binding is restored.

Extended Data Figures and Tables

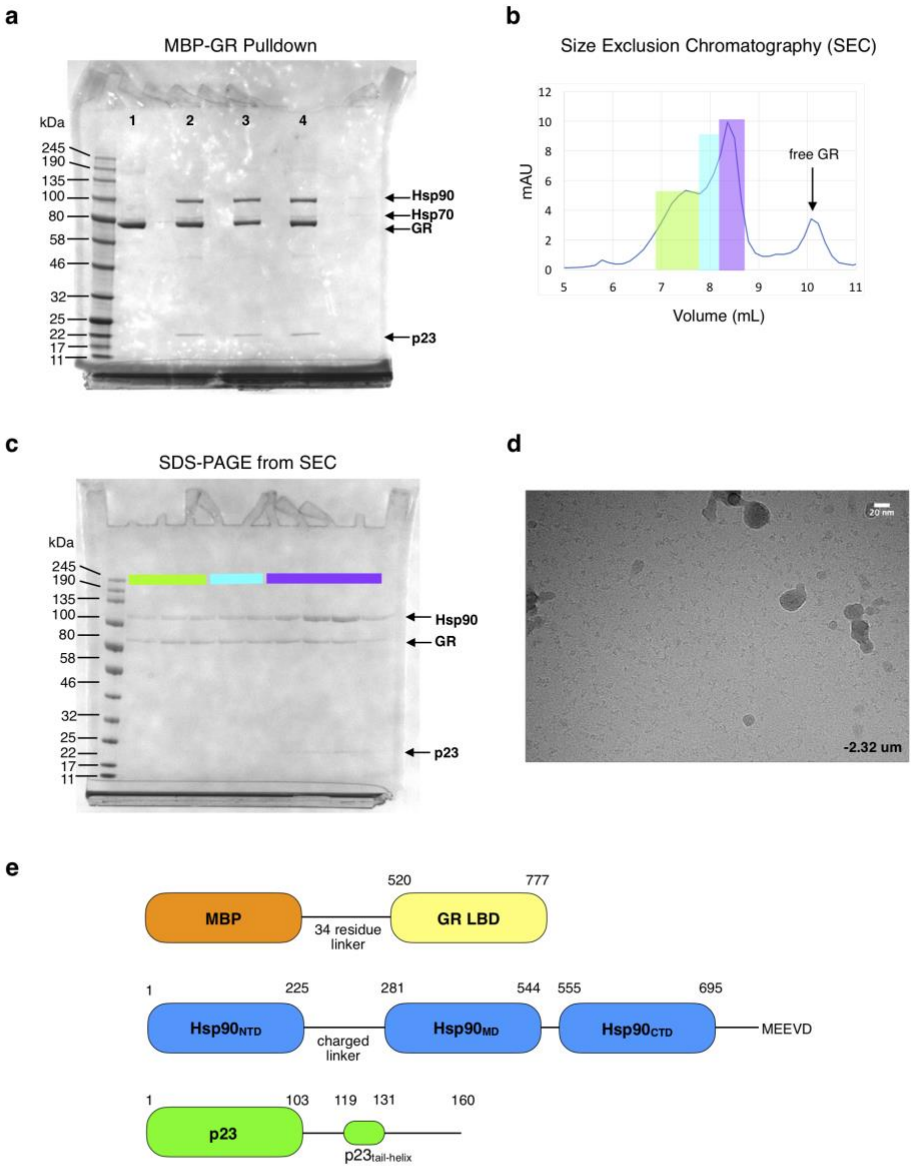

Extended Data Fig. 3.1: Sample Preparation
a, Coomassie-stained raw, uncropped SDS-PAGE (4-12% acrylamide gel) with elution from the MBP-GR pulldown from the *in vitro* reconstituted GR chaperone cycle. Assay conditions are as follows- Lane 1: 5 μM MBP-GR only; Lane 2-5: 5 μM MBP-GR, 2 μM Hsp40, 5 μM Hsp70, 5 μM Hop, 15 μM Hsp90, 15 μM Bag-1, 30 μM p23, 5 mM ATP. Lane 2: no Molybdate addition, Lane 3: addition of 20mM Molybdate, Lane 4: addition of 20 mM Molybdate after 1 hour pre-incubation (see Methods) **b**, Shodex KW-804 size exclusion chromatography profile of the GR-maturation complex purified by MBP-GR pulldown from the reconstituted GR chaperone cycle. mAU=milli-absorbance units. **c**, Coomassie-stained raw, uncropped SDS-PAGE (4-12% acrylamide gel) of the fractions from size exclusion chromatography. Colors indicate which gel lanes correspond to specific regions of the size exclusion chromatography profile. Sample fractions from the region highlighted in purple were collected and used for cryo-EM data collection. This experiment was repeated 4 independent times with similar results. **d**, Representative electron micrograph for the cryo-EM dataset (-2.32 μm defocus). A total of 5608 micrographs were obtained. Scale bar is 20nm. e, Domain organization of the proteins in the GR-maturation complex.

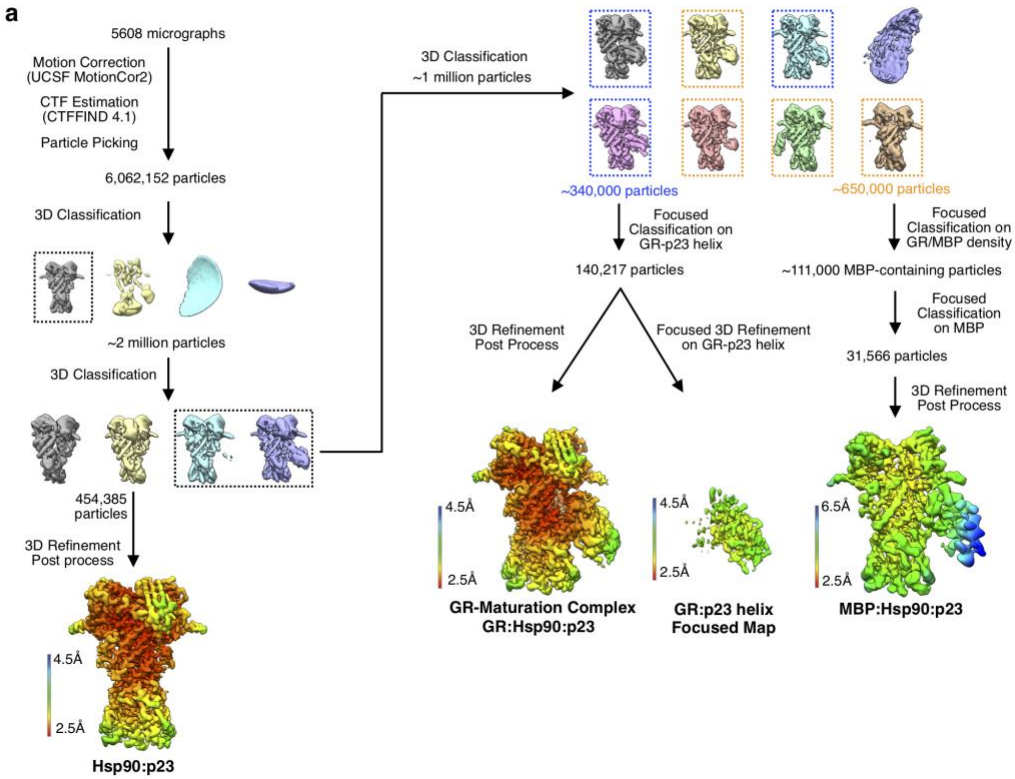
a
5608 micrographs
Motion Correction (UCSF MotionCor2)
CTF Estimation (CTFFIND 4.1)
Particle Picking
6,062,152 particles
3D Classification
~2 million particles
3D Classification
454,385 particles
3D Refinement Post process
4.5Å
2.5Å
Hsp90:p23
3D Classification ~1 million particles
~340,000 particles
~650,000 particles
Focused Classification on GR-p23 helix
140,217 particles
3D Refinement Post Process
Focused 3D Refinement on GR-p23 helix
4.5Å
2.5Å
GR-Maturation Complex GR:Hsp90:p23
4.5Å
2.5Å
GR:p23 helix Focused Map
Focused Classification on GR/MBP density
~111,000 MBP-containing particles
Focused Classification on MBP
31,566 particles
3D Refinement Post Process
6.5Å
2.5Å
MBP:Hsp90:p23

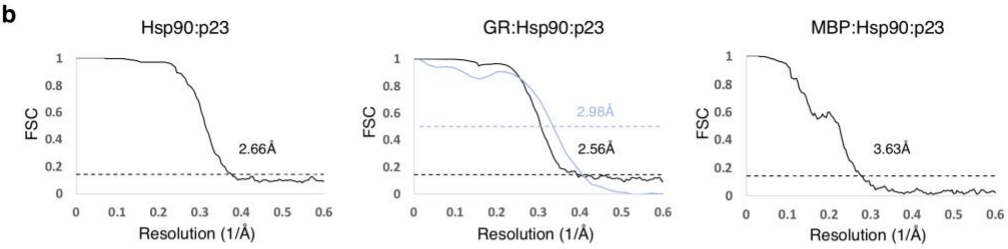
b
Hsp90:p23
FSC
2.66Å
Resolution (1/Å)
GR:Hsp90:p23
FSC
2.98Å
2.56Å
Resolution (1/Å)
MBP:Hsp90:p23
FSC
3.63Å
Resolution (1/Å)

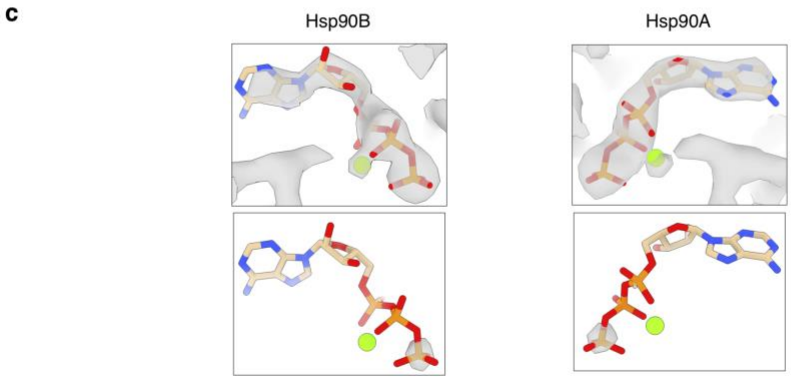
c
Hsp90B
Hsp90A

Extended Data Fig. 3.2: Cryo-EM Data Analysis
a, Cryo-EM data processing procedure with 3D reconstructions colored by local resolution. **b**, Gold-standard Fourier shell correlation (FSC) curves of the 3D reconstructions. The black dashed lines intercept the y-axis at an FSC value of 0.143. For the GR:Hsp90:p23 reconstruction, the map-model FSC is plotted in blue, with the blue dashed line intercepting the y-axis at an FSC value of 0.5. **c**, GR maturation complex map density with atomic model showing ATP-magnesium density in both Hsp90 protomers (Hsp90A/B). Bottom images show increased contour level on the map density to indicate that the ATP γ-phosphate position has much stronger density relative to the α and β-phosphates, likely corresponding to molybdate, which may act as a γ-phosphate analog (see Methods).

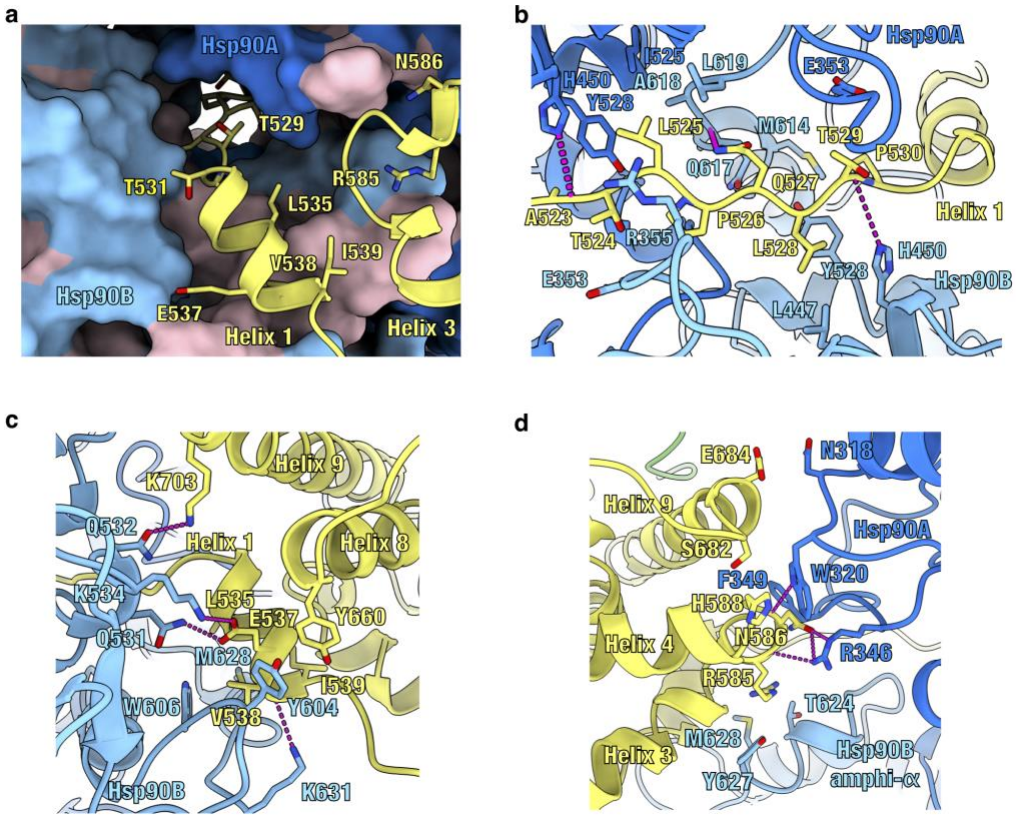

Extended Data Fig. 3.3: Hsp90:GR Interfaces

Atomic model of the maturation complex with Hsp90A (dark blue), Hsp90B (light blue), GR (yellow). **a**, View of the $GR_{pre\text{-}helix\ 1}$ strand threaded through the Hsp90 lumen and GR helices 1 and 3 packing against the entrance to the Hsp90 lumen. Side chains on GR in contact with Hsp90 are shown. Hsp90A/B are in surface representation. Hydrophobic residues on Hsp90 are colored in pink. **b**, Interface 1 of the Hsp90:GR interaction depicting the $GR_{pre\text{-}Helix\ 1}$ region ($GR^{523\text{-}531}$) threading through the Hsp90 lumen. Side chains in contact between GR and Hsp90 are shown, along with hydrogen bonds (dashed pink lines). **c**, Interface 2 of the Hsp90:GR interaction depicting $GR_{Helix\ 1}$ ($GR^{532\text{-}539}$) packing against Hsp90B. Side chains in contact between GR and Hsp90 are shown, along with hydrogen bonds (dashed pink lines). **d**, Interface 3 of the Hsp90:GR interaction depicting residues on the $Hsp90A_{MD}$ loops ($Hsp90A^{N318,W320,F349,R346}$) and $Hsp90B_{amphi\text{-}\alpha}$ ($Hsp90B^{T624,Y627,M628}$) packing against GR. Side chains in contact between GR and Hsp90 are shown, along with hydrogen bonds (dashed pink lines).

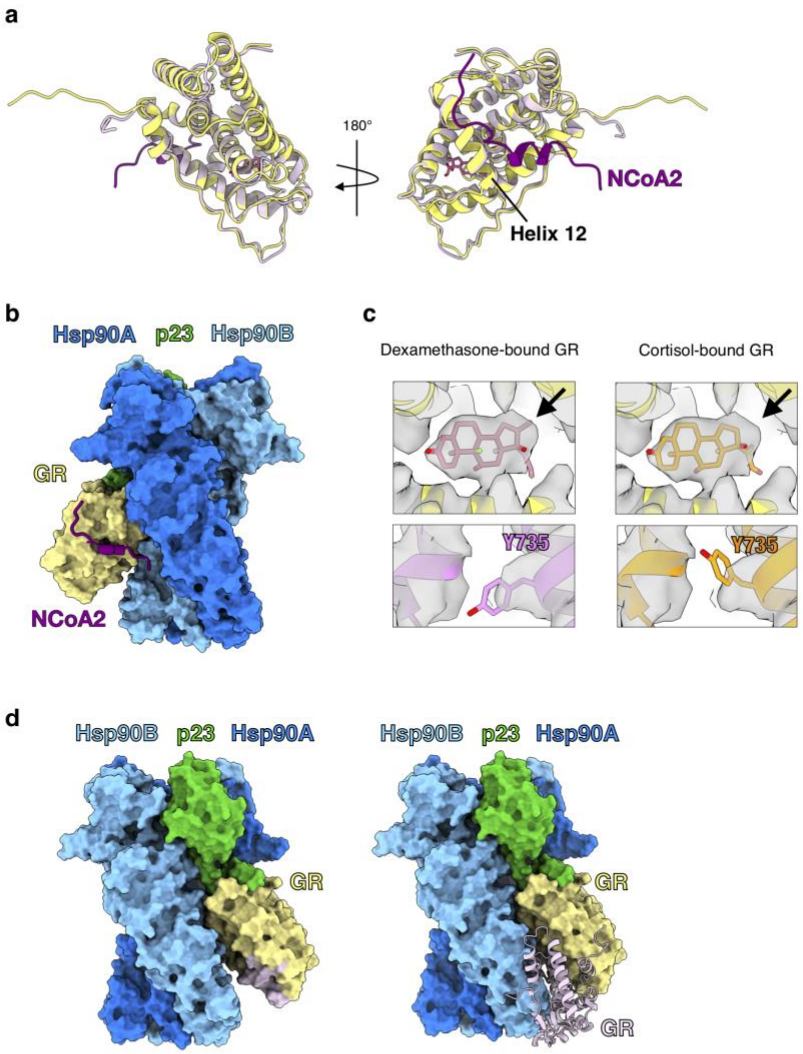
a
180°
NCoA2
Helix 12
b
Hsp90A p23 Hsp90B
GR
NCoA2
c
Dexamethasone-bound GR
Cortisol-bound GR
Y735
Y735
d
Hsp90B p23 Hsp90A
GR
Hsp90B p23 Hsp90A
GR
GR

Extended Data Fig. 3.4: GR is in a Native, Ligand-Bound State in the Maturation Complex

a, Atomic model of GR from the maturation complex (yellow) compared with GR from the crystal structure (PDB ID 1M2Z) (light pink) with co-activator peptide NCoA2 (purple) and ligand (pink). $GR_{Helix\ 12}$ is indicated. **b**, GR-maturation complex atomic model in surface representation with the co-activator peptide NCoA2 (purple) docked based on the GR:NCoA2 crystal structure (PDB ID M2Z). The NCoA2 peptide binding interface is available and the bound NCoA2 peptide does not clash with Hsp90. Hsp90A (dark blue), Hsp90B (light blue), GR (yellow), p23 (green). **c**, GR maturation complex map density (sharpened with B factor -40) with either the dexamethasone-bound crystal structure docked (left panel, PDB ID 1M2Z) or the cortisol-bound crystal structure docked (right panel, PDB ID 4P6X) into the GR map density. In the top images, the ligand density is shown with the agonist dexamethasone (left) or the agonist cortisol (right) from the docked crystal structures. Arrow indicates the extra carbon atom in dexamethasone compared to cortisol. In the bottom images, density for GR^{Y735} is shown with either the dexamethasone-bound crystal structure docked (left) or the cortisol-bound crystal structure docked (right). **d**, GR-maturation complex atomic model in surface representation depicting the GR LBD dimerization interface. Hsp90A (dark blue), Hsp90B (light blue), GR (yellow), p23 (green). Left, the GR LBD dimerization interface is highlighted (light pink). Right, while the dimerization interface is solvent accessible in the GR-maturation complex, the binding of a second GR LBD (light pink) clashes with the Hsp90B CTD. The dimerization interface is based on the GR LBD dimer crystal structure (PDB ID 1M2Z).

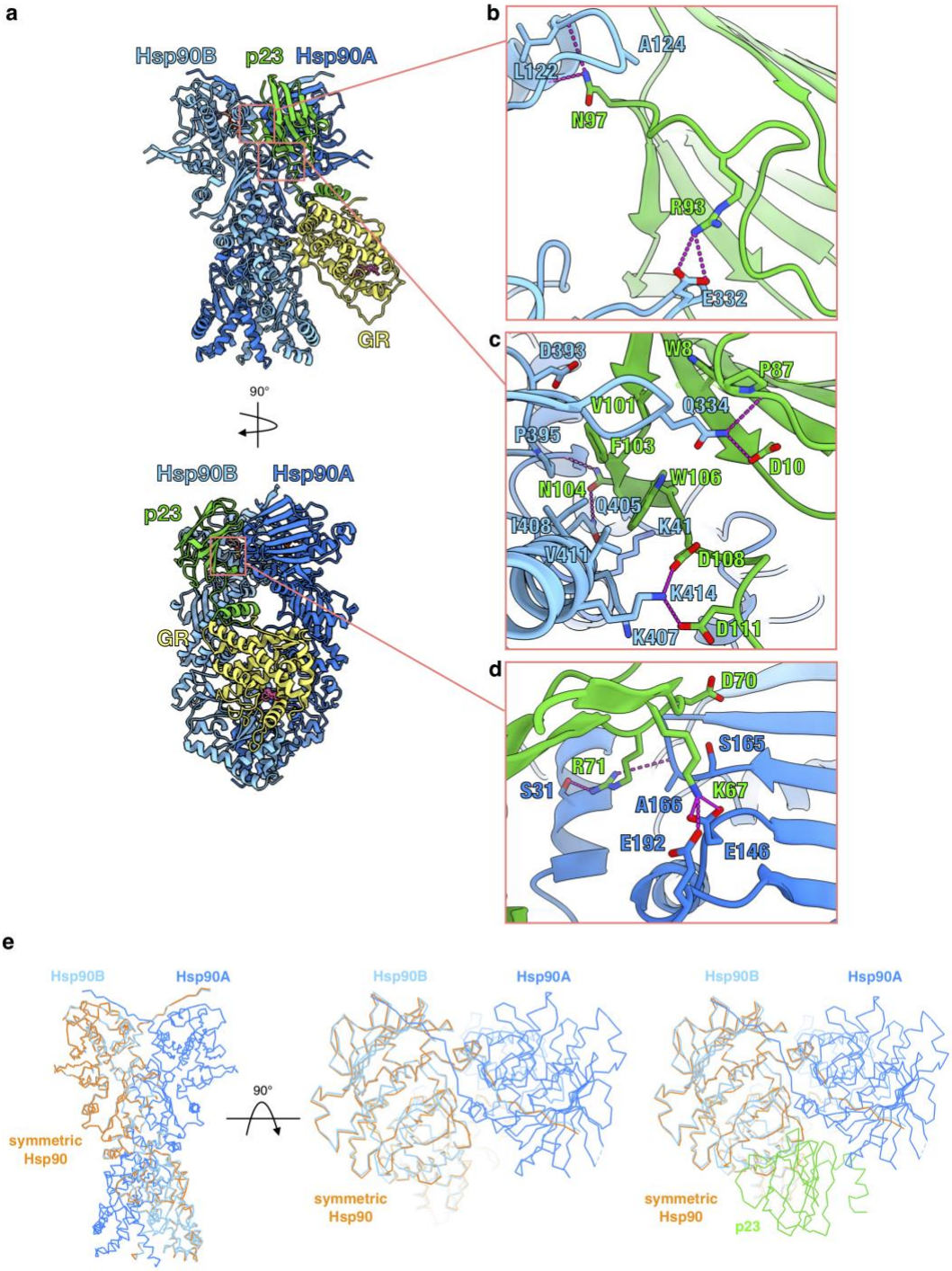
a
Hsp90B
p23
Hsp90A
GR
90°
Hsp90B
Hsp90A
p23
GR
b
A124
L122
N97
R93
E332
c
D393
W8
P87
V101
Q334
P395
F103
D10
W106
N104
Q405
I408
K41
V411
D108
K414
K407
D111
d
D70
S165
R71
S31
K67
A166
E192
E146
e
Hsp90B
Hsp90A
symmetric
Hsp90
90°
Hsp90B
Hsp90A
symmetric
Hsp90
Hsp90B
Hsp90A
symmetric
Hsp90
p23

Extended Data Fig. 3.5: Hsp90:p23 Interfaces
a, Atomic model of the maturation complex with Hsp90A (dark blue), Hsp90B (light blue), GR (yellow), p23 (green). **b**, Interface 1 of the Hsp90:p23 interaction depicting Hsp90B interacting with one side of the p23 core. Side chains in contact between p23 and Hsp90B are shown, along with hydrogen bonds (dashed pink lines). **c**, Interface 2 of the Hsp90:p23 interaction depicting Hsp90B interacting with the base of the p23 core. Side chains in contact between p23 and Hsp90B are shown, along with hydrogen bonds (dashed pink lines). **d**, Interface 3 of the Hsp90:p23 interaction depicting Hsp90A interacting with the side of the p23 core. Side chains in contact between p23 and Hsp90 are shown, along with hydrogen bonds (dashed pink lines). **e**, Atomic model of a symmetric Hsp90 dimer (orange) compared with Hsp90 from the maturation complex atomic model, indicating a slight asymmetry in the Hsp90 dimer interface in the maturation complex. Hsp90A (dark blue), Hsp90B (light blue), p23 (green).

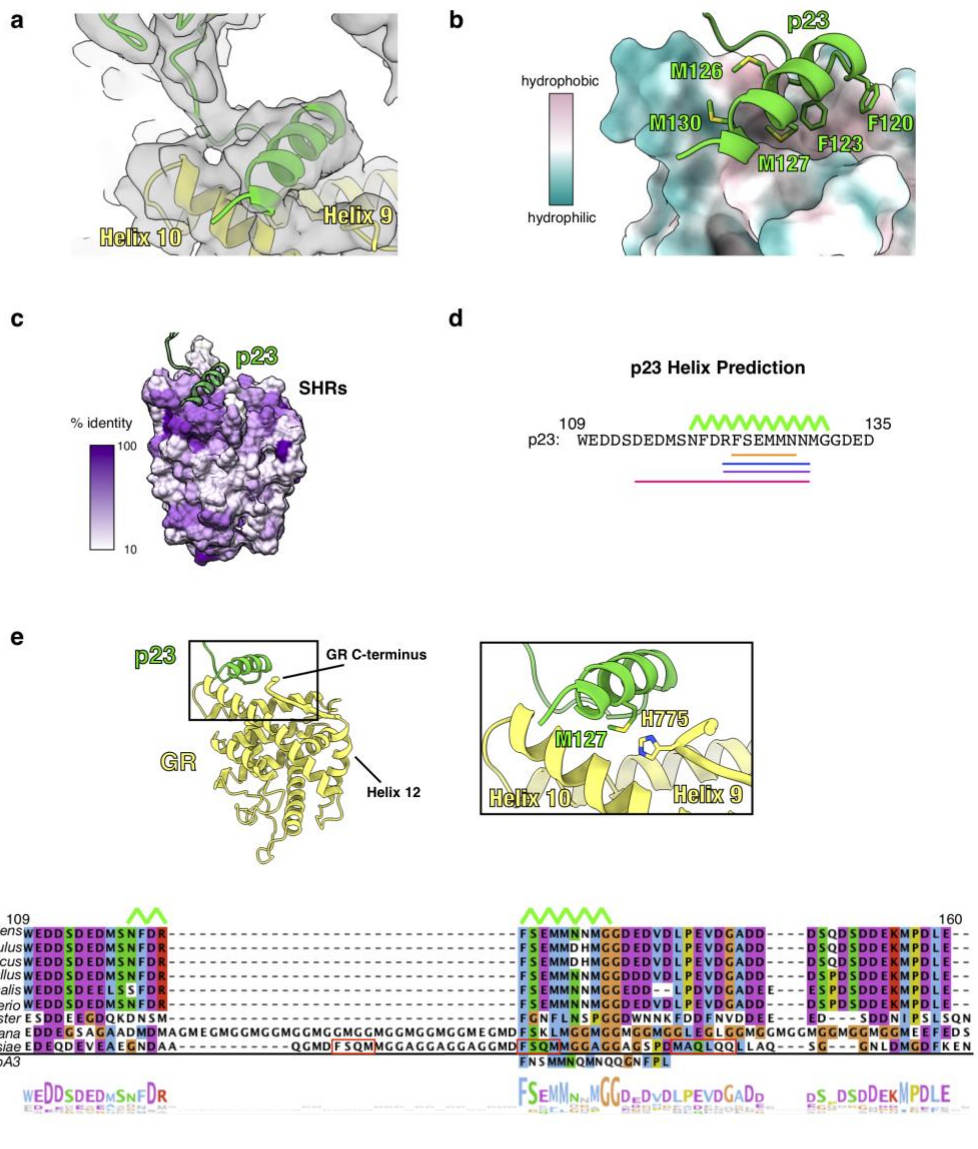
a
Helix 10
Helix 9
b
p23
M126
M130
F120
F123
M127
hydrophobic
hydrophilic
c
p23
SHRs
% identity
100
10
d
p23 Helix Prediction
109
135
p23: WEDDSDEDMSNFDRFSEMMNNMGGDED
e
p23
GR C-terminus
GR
Helix 12
M127
H775
Helix 10
Helix 9
f
109
160
H. sapiens
M. musculus
R. norvegicus
G. gallus
X. tropicalis
D. rerio
D. melanogaster
A. thaliana
S. cerevisiae
NCoA3

Extended Data Fig. 3.6: The $p23_{tail\text{-}helix}$:GR Interface
a, Focused map of GR:$p23_{tail\text{-}helix}$ showing density for the p23 tail with the atomic model built in. GR (yellow), p23 (green). **b**, Interface between the $p23_{tail\text{-}helix}$ (green) and GR (colored by hydrophobicity, surface representation) showing that the $p23_{tail\text{-}helix}$ binds to a hydrophobic patch on GR. p23 side chains interacting with GR are shown. **c**, Sequence identity across human steroid hormone receptors (GR, mineralocorticoid receptor, androgen receptor, progesterone receptor, estrogen receptor α and β) plotted onto the GR structure. The $p23_{tail\text{-}helix}$ (light green) was overlaid to indicate the p23:GR interface. **d**, Secondary structure predictions for human p23 from three different servers. Porter 4.0 (orange), RaptorX (blue), Psipred (purple), AlphaFold v2.0 (pink). The $p23_{tail\text{-}helix}$ from the maturation complex atomic model is shown with the top green line. **e**, Atomic model of GR (yellow) and p23 (green) from the maturation complex highlighting the interaction between the $p23_{tail\text{-}helix}$ and the GR C-terminus, which connects to $GR_{Helix\ 12}$. **f**, Sequence alignment of eukaryotic p23 showing conservation of the $p23_{tail\text{-}helix}$ sequence. The $p23_{tail\text{-}helix}$ from the maturation complex atomic model is shown with the top green line. The bottom aligned sequence is the $p23_{tail\text{-}helix}$-like motif identified in NCoA3 using the ScanProsite server. Red boxes on the *S. cerevisiae* p23 sequence indicate predicted helices from the PsiPred server. The alignment is colored according to the ClustalW convention.

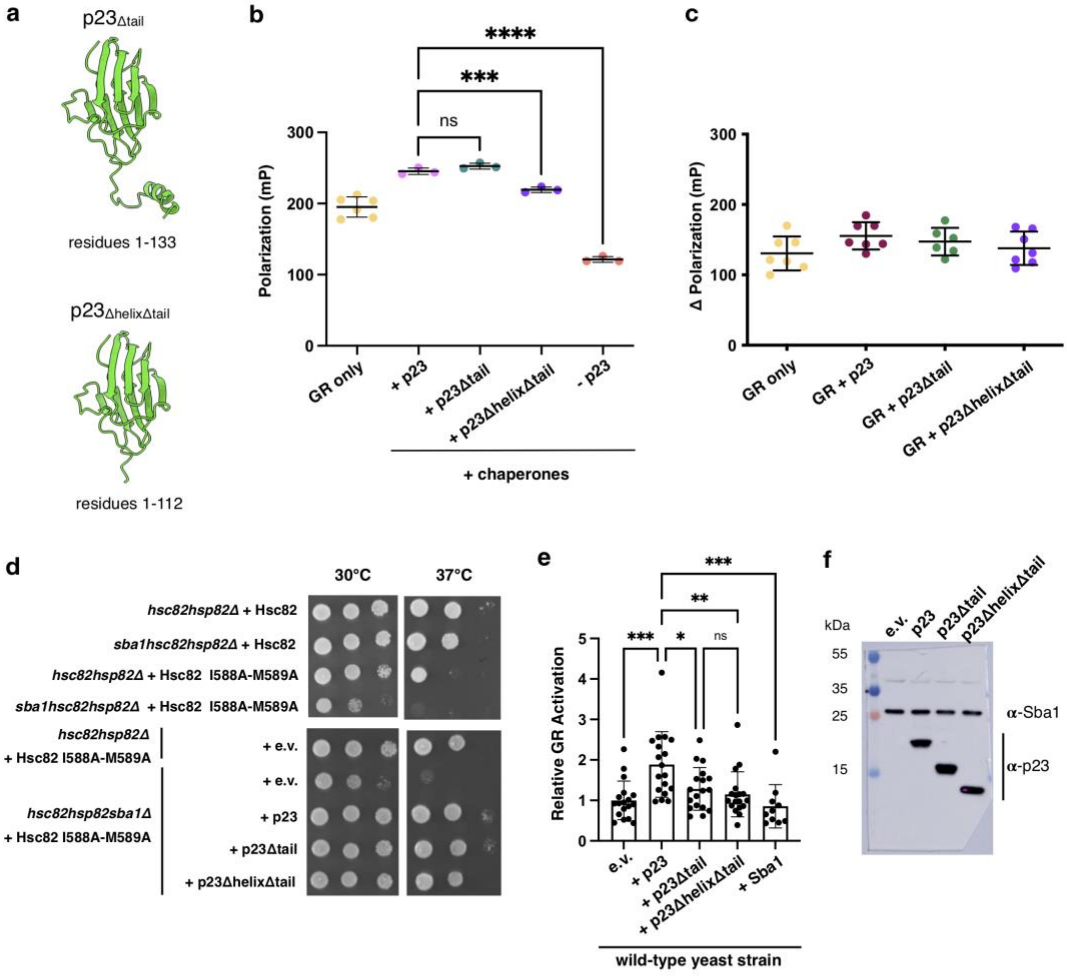
a
p23Δtail
residues 1-133
p23ΔhelixΔtail
residues 1-112
b
****
***
ns
Polarization (mP)
300
200
100
0
GR only
+ p23
+ p23Δtail
+ p23ΔhelixΔtail
- p23
+ chaperones
c
Δ Polarization (mP)
300
200
100
0
GR only
GR + p23
GR + p23Δtail
GR + p23ΔhelixΔtail
d
30°C
37°C
hsc82hsp82Δ + Hsc82
sba1hsc82hsp82Δ + Hsc82
hsc82hsp82Δ + Hsc82 I588A-M589A
sba1hsc82hsp82Δ + Hsc82 I588A-M589A
hsc82hsp82Δ
+ Hsc82 I588A-M589A
+ e.v.
+ e.v.
hsc82hsp82sba1Δ
+ Hsc82 I588A-M589A
+ p23
+ p23Δtail
+ p23ΔhelixΔtail
e
***
**
***
*
ns
Relative GR Activation
5
4
3
2
1
0
e.v.
+ p23
+ p23Δtail
+ p23ΔhelixΔtail
+ Sba1
wild-type yeast strain
f
kDa
e.v.
p23
p23Δtail
p23ΔhelixΔtail
55
35
25
15
α-Sba1
α-p23

Extended Data Fig. 3.7: Effect of p23 Tail Mutants on GR Activity and Cell Survival **a**, Depiction of the two p23 tail mutants used in the GR activity assays. **b**, Individual data points corresponding to Fig. 2d. Equilibrium binding of 20 nM fluorescent dexamethasone to 250 nM GR with chaperones and p23 tail mutants measured by fluorescence polarization (mean±SD). n=3 biologically independent samples per condition (n=6 biologically independent samples for the GR only condition). Significance was evaluated using a one-way ANOVA ($F_{(3,8)}$ = 636.2; p < 0.0001) with *post-hoc* Dunnett's multiple comparisons test (n.s. P ≥ 0.05; * P ≤ 0.05; ** P ≤ 0.01; *** P ≤ 0.001; **** P ≤ 0.0001). P-values: p(p23 vs. p23Δtail) = 0.1512, p(p23 vs. p23ΔhelixΔtail) = 0.0002, p(p23 vs. no p23) = <0.0001. **c**, Equilibrium binding of 20 nM fluorescent dexamethasone to 250 nM GR with addition of 15 μM p23 or p23 tail mutants measured by fluorescence polarization (mean±SD). n=7 biologically independent samples per condition (n=6 biologically independent samples for the GR + p23Δtail condition). Fluorescence polarization values are baseline subtracted in accordance with the measured fluorescent dexamethasone baseline polarization value. There were no statistically significant differences between group means as determined by a one-way ANOVA ($F_{(3,23)}$ = 1.708; p=0.1933). **d**, Yeast survival assay with human p23 or p23 tail mutants. Top panels: *hsc82hsp82Δ* yeast expressing Hsc82 I588A-M589A exhibit a growth defect at 37°C in the presence of *SBA1* and enhanced defects in cells lacking *SBA1* (*sba1*). Bottom panels: Growth is restored by addition of human p23, although p23ΔhelixΔtail exhibits reproducibly reduced growth relative to p23 or p23Δtail. **e**, GR activation assay in wild-type yeast strain JJ762 expressing p23, p23 mutants, or Sba1 in addition to wild-type amounts of Sba1 from the native promoter. The fold increase in GR activities compared to the empty vector (e.v.) control are shown (mean±SD). n=18 biologically independent samples per condition (10 independent samples for the +Sba1 condition). Significance was evaluated using a one-way ANOVA ($F_{(4,77)}$ = 7.077; p < 0.0001) with *post-hoc* Šídák's multiple comparisons test (n.s. P ≥ 0.05; * P ≤ 0.05; ** P ≤ 0.01; *** P ≤ 0.001). P-values: p(e.v. vs. p23) = 0.0001, p(p23 vs p23Δtail) = 0.0164, p(p23 vs. p23ΔhelixΔtail) = 0.0021, p(p23 vs. Sba1) = 0.0002, p(p23Δtail vs. p23ΔhelixΔtail) = 0.9721. **f**, Expression of human p23 or p23 tail mutants in wild-type yeast strain JJ762 assayed by immunoblot with polyclonal antisera raised against Sba1 or human p23.

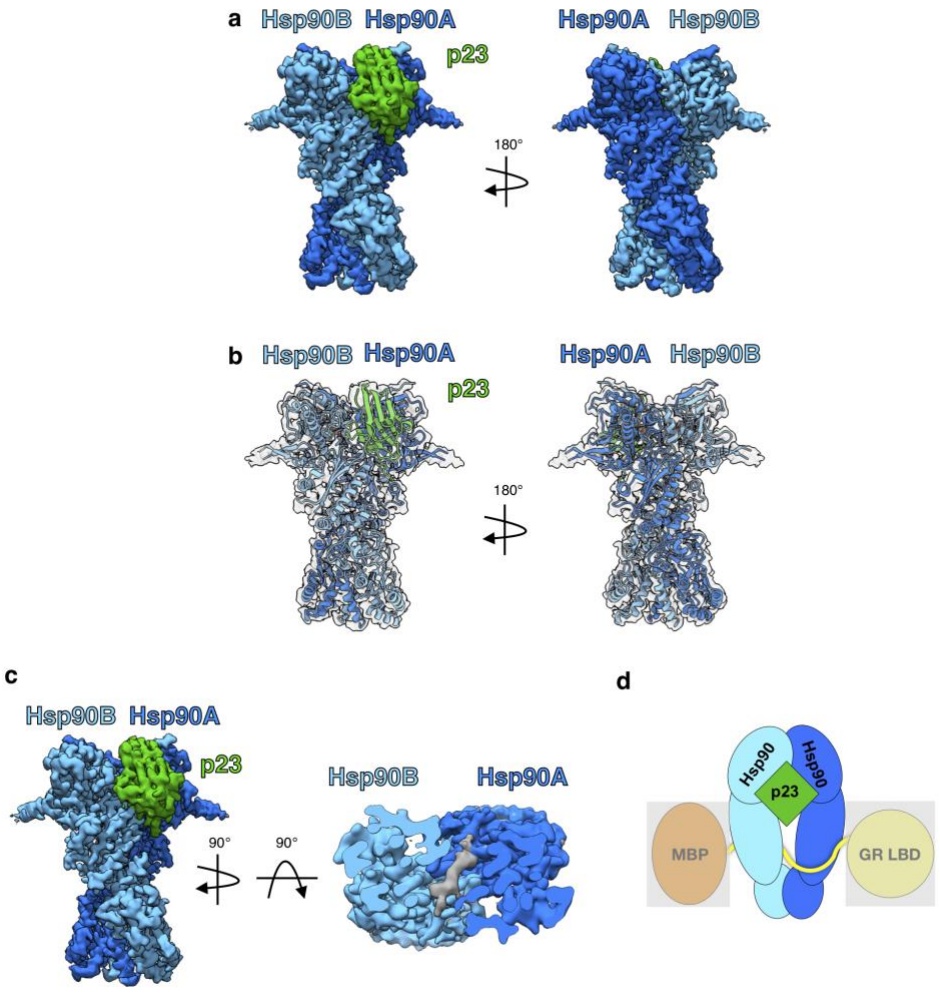

Extended Data Fig. 3.8: Hsp90:p23 Complex
a, Cryo-EM density map of the Hsp90:p23 complex. Hsp90A (dark blue), Hsp90B (light blue), p23 (green). This color scheme is maintained in all figures that show the structure. **b**, Atomic model of Hsp90 and p23 from the GR-maturation complex docked into the Hsp90:p23 map density. **c**, Top view of the Hsp90:p23 complex density map with clipping plane to show unidentified density (gray) through the Hsp90 lumen. d, Cartoon representation of the Hsp90:p23 complex illustrating that MBP and GR LBD are not present in the map density (represented by a gray box).

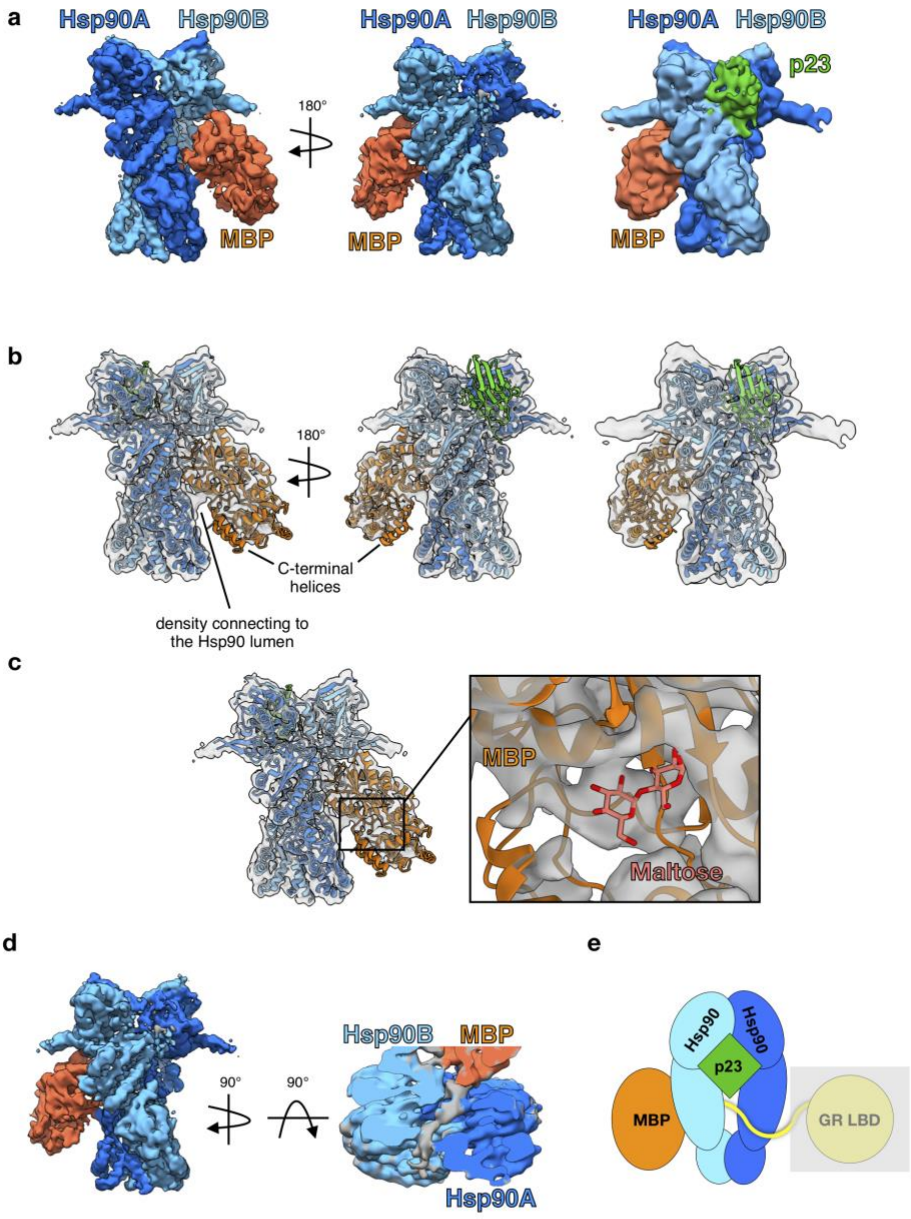
a
Hsp90A Hsp90B
MBP
180°
Hsp90A Hsp90B
MBP
Hsp90A Hsp90B
p23
MBP
b
180°
C-terminal
helices
density connecting to
the Hsp90 lumen
c
MBP
Maltose
d
90°
90°
Hsp90B MBP
Hsp90A
e
Hsp90
Hsp90
p23
MBP
GR LBD

Extended Data Fig. 3.9: MBP:Hsp90:p23 Complex
a, Cryo-EM density map of the MBP:Hsp90:p23 complex. Far right image shows the density map lowpass-filtered to 8Å. Hsp90A (dark blue), Hsp90B (light blue), p23 (green), MBP (orange). This color scheme is maintained throughout. **b**, Apo MBP crystal structure (PDB ID 1OMP) and atomic model of Hsp90 and p23 from the GR-maturation complex docked into the MBP:Hsp90:p23 map density. Note the missing density for the two MBP C-terminal helices. Far right image shows the density map lowpass-filtered to 8Å. **c**, Maltose-bound MBP crystal structure (PDB ID 1ANF) docked into the MBP:Hsp90:p23 map density. MBP (orange), maltose (pink). **d**, Top view of the MBP:Hsp90:p23 complex density map with clipping plane to show unidentified density (gray) through the Hsp90 lumen. **e**, Cartoon representation of the MBP:Hsp90:p23 complex illustrating the GR LBD is not present in the map density (represented by a gray box).

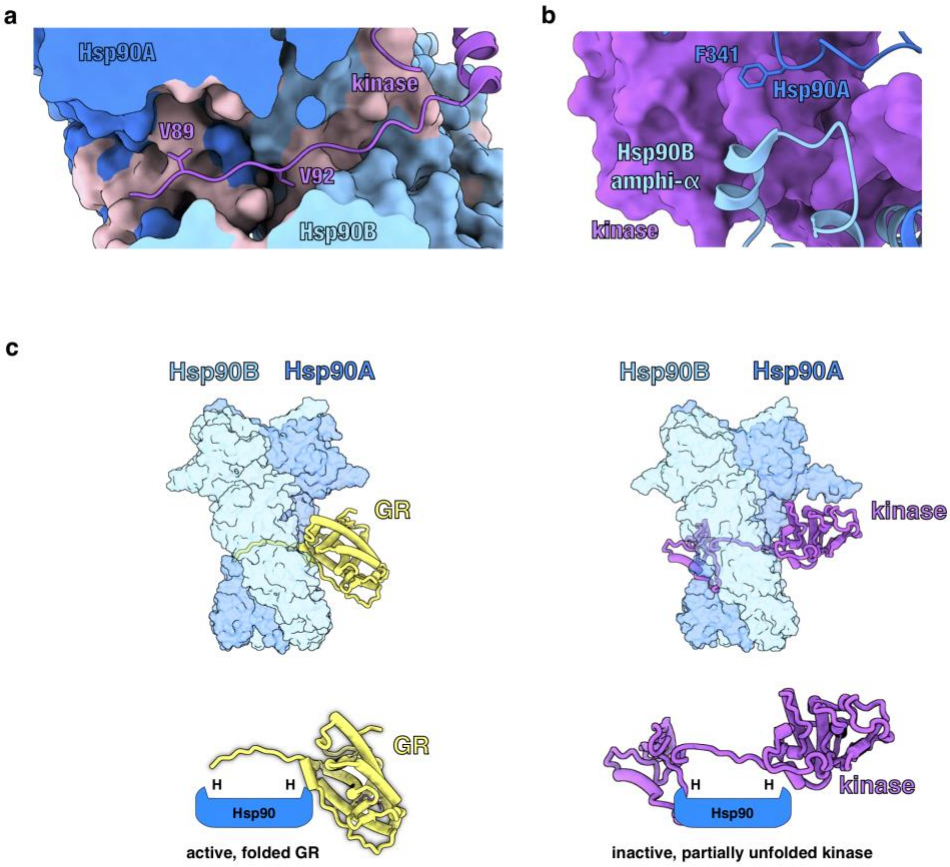
a
Hsp90A
kinase
V89
V92
Hsp90B
b
F341
Hsp90A
Hsp90B
amphi-α
kinase
c
Hsp90B
Hsp90A
GR
Hsp90B
Hsp90A
kinase
GR
H
H
Hsp90
active, folded GR
H
H
Hsp90
kinase
inactive, partially unfolded kinase

Extended Data Fig. 3.10: Comparison of the GR-Maturation Complex with the Hsp90:Kinase Complex

a, Structure of Hsp90 bound to an unfolded kinase client (PDB ID 5FWK) with a strand of the kinase client threaded through the Hsp90 lumen. The two hydrophobic residues on the kinase ($Cdk4^{V89,V92}$) that occupy the Hsp90 hydrophobic pockets are displayed. In the GR-maturation complex, two hydrophobic residues on GR ($GR^{L525,L528}$) occupy the Hsp90 hydrophobic pockets, demonstrating a conserved client binding mode. Hsp90A (dark blue, surface representation), Hsp90B (light blue, surface representation), Cdk4 kinase (purple). Hydrophobic residues on Hsp90 are colored in pink. **b**, Structure of Hsp90 bound to an unfolded kinase client (PDB ID 5FWK) depicting $Hsp90A^{F341}$ (Hsp90 isoform β) and $Hsp90B_{amphi\text{-}\alpha}$ packing against the kinase. In the GR-maturation complex, the corresponding residue $Hsp90A^{F349}$ (Hsp90 isoform α) and the $Hsp90B_{amphi\text{-}\alpha}$ also pack against GR, demonstrating a conserved Hsp90:client binding interface. Hsp90A (dark blue), Hsp90B (light blue), Cdk4 kinase (purple, surface representation). **c**, Top, atomic models of the GR-maturation complex and Hsp90:kinase complex showing that both clients thread through the closed Hsp90 lumen. Hsp90A (dark blue, surface representation), Hsp90B (light blue, surface representation), GR (yellow), Cdk4 kinase (purple). Bottom, schematics demonstrating that both clients thread through the mostly hydrophobic Hsp90 lumen, but have different folding outcomes (H=hydrophobic interface).

Supplementary Table 3.1: Cryo-EM data collection, refinement and validation statistics

	GR:Hsp90:p23 (EMDB-23004) (PDB 7KRJ)	Hsp90:p23 (EMDB-23006)	MBP:Hsp90:p23 (EMDB-23005)
Data collection and processing			
Magnification	105,000	105,000	105,000
Voltage (kV)	300	300	300
Electron exposure (e–/Å^2)	60	60	60
Defocus range (μm)	0.8-2.0	0.8-2.0	0.8-2.0
Pixel size (Å)	0.835	0.835	0.835
Symmetry imposed	C1	C1	C1
Initial particle images (no.)	6,062,152	6,062,152	6,062,152
Final particle images (no.)	140,217	454,385	31,566
Map resolution (Å)	2.56	2.66	3.63
FSC threshold	0.143	0.143	0.143
Map resolution range (Å)	2.4-3.6	2.5-3.5	3.4-6.9
Refinement			
Initial model used (PDB code)	5FWK, 1M2Z, 1EJF		
Model resolution (Å)	2.98		
FSC threshold	0.5		
Map sharpening *B* factor (Å^2)	-32		
Model composition			
Non-hydrogen atoms	13460		
Protein residue atoms	13368		
Ligand atoms	92		
Mean *B* factors [min-max] (Å^2)			
Protein	76.2 [38.3-238.7]		
Ligand	57.6 [26.5-119.7]		
R.m.s. deviations			
Bond lengths (Å)	0.0261		
Bond angles (°)	1.81		
Validation			
MolProbity score	0.67		
Clashscore	0.48		
Poor rotamers (%)	0.07		
Ramachandran plot			
Favored (%)	97.98		
Allowed (%)	1.90		
Disallowed (%)	0.12		

Methods

Data analysis and figure preparation

Figures were created using UCSF Chimera v.1.14 (Pettersen et al., 2004) and UCSF ChimeraX v0.94 (Goddard et al., 2018). GR ligand binding data was analyzed using Prism v.9.1.1 (GraphPad).

Protein expression and purification

Human Hsp90α, Hsp70 (Hsp70A1A), Hop, p23, p23$_{\Delta tail}$ (1-133), p23$_{\Delta helix\Delta tail}$ (1-112), and yeast Ydj1 (Hsp40) were expressed in the pET151 bacterial expression plasmid with a cleavable N-terminal, 6x-His tag. Human Bag-1 isoform 4 (116-345) was expressed in a pET28a vector with a cleavable N-terminal, 6x-His tag. Proteins were expressed and purified by the following procedure. Proteins were expressed in *E. coli* BL21 star (DE3) strain. Cells were grown in either LB or TB at 37°C until OD_{600} reached 0.6-0.8 and then induced with 0.5 mM IPTG overnight at 16°C. Cells were harvested and lysed in 50 mM Potassium Phosphate pH 8, 500 mM KCl, 10 mM imidazole pH 8, 10% glycerol, 6 mM βME, and Roche cOmplete, mini protease inhibitor cocktail using an EmulsiFlex-C3 (Avestin). Lysate was centrifuged and the soluble fraction was affinity purified by gravity column with Ni-NTA affinity resin (QIAGEN). The protein was eluted with 30 mM Tris pH 8, 50 mM KCl, 250 mM imidazole pH 8, and 6 mM βME. For Hsp90, Hsp70, and Ydj1, an extra wash step with 0.1% Tween20 and 2 mM ATP/$MgCl_2$ was added to the Ni-NTA resin before eluting. The 6x-His tag was removed with TEV protease during the following overnight dialysis in 30 mM Tris pH 8, 50 mM KCl, and 6

mM βME. Cleaved protein was then loaded onto an ion exchange column, MonoQ 10/100 GL (GE Healthcare), with 30 mM Tris pH 8, 50 mM KCl, and 6 mM βME and eluted with a linear gradient of 50-500 mM KCl. Protein was further purified by size exclusion in 30 mM HEPES pH 7.5, 50 mM KCl, 10% glycerol, 1-2 mM DTT using a HiLoad 16/60 Superdex 200 (GE Healthcare) or Hi Load 16/60 Superdex 75 (GE Healthcare). For Hsp70, each peak from ion exchange was collected separately and purified by size exclusion in 30 mM HEPES pH 7.5, 100 mM KCl, 10% glycerol, 4 mM DTT, where only the monomeric peak was then collected. Protein was concentrated, flash frozen, and stored at -80$^{\circ C}$.

GR LBD expression and purification

For GR, the ligand binding domain (LBD) (F602S) (520-777) was codon optimized and expressed in the pMAL-c3X derivative with an N-terminal cleavable 6x-His-MBP tag. GR LBD was expressed and purified as previously described (Kirschke et al., 2014).

GR-maturation complex sample preparation

The GR chaperone cycle was reconstituted *in vitro* with purified components as previously described (Kirschke et al., 2014). Buffer conditions were 30 mM HEPES pH 8, 50 mM KCl, 0.05% Tween20, and 2 mM TCEP. Proteins and reagents were added at the following concentration: 5 μM MBP-GR LBD, 2 μM Hsp40, 5 μM Hsp70, 5 μM Hop, 15 μM Hsp90, 15 μM p23, 5 mM ATP/$MgCl_2$. This reaction was incubated at room temperature for 60 minutes, then 15 μM p23, 15 μM Bag-1, and 20 mM sodium

molybdate (used to stabilize the closed conformation of Hsp90 (Csermely et al., 1993; Johnson & Toft, 1995; Verba et al., 2016), likely by acting as a γ-phosphate analog to stabilize the post-ATP hydrolysis transition state of Hsp90 (Extended Data Fig. 2c)) were added, and the reaction was incubated at room temperature for another 30 minutes. Following incubation, amylose resin (New England Biolabs) was added to the reactions in a 1:1 ratio and incubated at 4°C with nutation. Resin was then washed 4 times with wash buffer (30 mM HEPES pH 8, 50 mM KCl, 5 mM ATP/$MgCl_2$, 0.05% Tween20, 2 mM TCEP, 20 mM sodium molybdate) and eluted with 50 mM maltose in elution buffer (30 mM HEPES pH 8, 50 mM KCl, 2 mM TCEP, 20 mM sodium molybdate). The elution was analyzed by SDS-PAGE (4-12% acrylamide gel) (Extended Data Fig. 1a). The elution was concentrated and purified by size exclusion using a Shodex KW-804 on an Ettan LC (GE Healthcare) and fractions were analyzed by SDS-PAGE (4-12% acrylamide gel) (Extended Data Fig. 1b,c). Fractions containing the full complex were concentrated to ~2 μM. 2.5 μL of sample was applied to glow-discharged QUANTIFOIL R1.2/1.3, 400-mesh, copper holey carbon grid (Quantifoil Micro Tools GmbH) and plunge-frozen in liquid ethane using a Vitrobot Mark IV (FEI) with a blotting time of 15 seconds, blotting force 3, at 10°C, and with 100% humidity.

Cryo-EM data acquisition

The images were collected on a FEI Titan Krios electron microscope (Thermo Fisher Scientific) operating at 300kV using a K3 direct electron camera (Gatan) and equipped with a Bioquantum energy filter (Gatan) set to a slit width of 20 eV (example micrograph Extended Data Fig. 1d). Images were recorded at a nominal magnification

of 105,000×, corresponding to a physical pixel size of 0.835Å. A nominal defocus range of 0.8 μm –2.0 μm underfocus was used. A total exposure of 5.9 seconds was used with 0.05 second subframes (117 total frames). The total accumulated electron dose was 60 electrons/Å^2 and 0.5128 electrons/Å^2/frame. Data was acquired using SerialEM software v.3.8-beta (Schorb et al., 2019).

A small dataset on the GR-maturation complex was collected before the larger dataset described above. The smaller dataset was collected from the same GR-maturation complex sample preparation concentrated to 1.2 μM with grids prepared in a similar manner. Images were collected on a FEI Titan Krios electron microscope (Thermo Fisher Scientific) operating at 300kV using a K3 direct electron camera (Gatan). Images were recorded at a nominal magnification of 105,000×, corresponding to a physical pixel size of 0.835Å. A nominal defocus range of 0.8 μm –2.0 μm underfocus was used. A total exposure of 3.0 seconds was used with 0.0255 second subframes (118 total frames). Data was acquired using SerialEM software.

Cryo-EM data processing

The smaller dataset consisted of ~1500 dose-fractionated image stacks, which were motion corrected using UCSF MotionCor2 (Zheng et al., 2017) and analyzed with RELION v.3.0.8 (Scheres, 2012). Motion corrected images without dose weighting were used for contrast transfer function (CTF) estimation using CTFFIND v.4.1 (Rohou & Grigorieff, 2015) and template-based particle picking was done with Gautomatch v.0.53 (http://www.mrc-lmb.cam.ac.uk/kzhang/) with the Hsp90:p23 crystal structure (PDB ID: 2CG9) as a reference to select a total of 718,080 particles. Multiple rounds of 3D

classification were performed with 2CG9 as a low-pass-filtered (40 Å) initial model until a medium-resolution (~8 Å) GR:Hsp90:p23 reconstruction was obtained from 13,570 particles. This reconstruction was used as a reference for the larger dataset.

The larger dataset consisted of 5,608 dose-fractionated image stacks, which were motion corrected using UCSF MotionCor2 and analyzed with RELION v.3.0.8. Motion corrected images with dose weighting were used for contrast transfer function (CTF) estimation using CTFFIND v.4.1 and reference-free particle picking was done with RELION v.3.0.8 Laplacian-of-Gaussian auto-picking to select a total of 6,062,152 particles. The processing scheme is depicted in Extended Data Fig. 2a. An initial round of three-dimensional (3D) classification was performed without symmetry using a reference model from the previously collected smaller dataset (see above). The class with clearly recognizable Hsp90 density was used for a second round of 3D classification. In this second round, a class with only Hsp90:p23 density was obtained (454,385 particles). This class was refined after per-particle CTF refinement and beam-tilt correction in RELION to a nominal resolution of 2.66 Å. Particles from two other classes, which contained GR density, were combined (~1 million particles) for a third round of 3D classification. After the third round of 3D classification, particles from classes with the best GR density were then combined (~340,000 particles) and refined. To improve the resolution of GR and the $p23_{tail\text{-}helix}$, the particles were further classified using focused classification with a mask including GR and the $p23_{tail\text{-}helix}$. The best focused classes were combined (140,217 particles) and refined to a nominal resolution of 2.56 Å. Using the 2.56 Å reconstruction, per-particle CTF and beam-tilt were refined using RELION. Although the FSC showed slightly improvement over the pre-refined

reconstruction at medium resolution range (5–10 Å), the nominal resolution at 0.143 FSC remained unchanged. Nevertheless, we used the CTF/beam-tilt refined particles for the following focused refinement on GR:$p23_{tail\text{-}helix}$ and for the resulting reconstructions used for model building. To further improve the resolution of GR and the $p23_{tail\text{-}helix}$ for model building, these regions were refined using focused refinement with a mask including GR and the $p23_{tail\text{-}helix}$.

From the third round of 3D classification, particles from 3D classes with MBP density were combined (~650,000 particles) and refined. To improve the resolution of MBP, the particles were further classified using focused classification with a mask on MBP. The best focused 3D classes were combined (31,556 particles) and refined to a nominal resolution of 3.63 Å after per-particle CTF refinement and beam-tilt correction in RELION.

No ligand-free GR complexes were identified during image analysis, despite many rounds of focused classification using masks of different sizes on GR at various stages of data processing. Only classes with clear ligand density in the GR ligand binding pocket were obtained, suggesting ligand-free GR is either too dynamic or quickly released from the complex.

All final reconstructions were post-processed in RELION in which the nominal resolution was determined by the gold standard Fourier shell correlation (FSC) using the 0.143 criterion (Extended Data Fig. 2b). Maps were sharpened and filtered automatically as determined by RELION according to an estimated overall map B-factor and filtered to their estimated resolution. RELION was used to estimate the local resolution of each map (Extended Data Fig. 2a). For GR:Hsp90:p23, a composite map

was generated by combining the overall refinement map with the GR:p23 tail focused refinement map using vop maximum in Chimera. Note that the composite map was only used for presentation in Fig. 1a, but not used in atomic model building or refinement.

Model building and refinement

For the GR-maturation complex atomic model, the dexamethasone-bound human GR crystal structure (PDB ID: 1M2Z) and the human p23 crystal structure (PDB ID: 1EJF) were used as a starting model for model building. A homolog model of human Hsp90α was derived from human Hsp90β from the Hsp90:Cdk4:Cdc37 cryo-EM structure (PDB ID: 5FWK) with the sequence alignment (86% sequence identity) obtained from HHpred server (Zimmermann et al., 2018) and this was also used as a starting model for model building (Supplementary Table 1). Models were refined using Rosetta v.3.11 throughout. Following the split map approach (Wang et al., 2016) to prevent and monitor overfitting, the Rosetta iterative backbone rebuilding procedure was used to refine models against one of the half maps obtained from RELION, with the other half map only used for validations. The structurally uncharacterized $p23_{tail\text{-}helix}$ was first *de novo* built into the focused map of GR:$p23_{tail\text{-}helix}$ using RosettaCM (Song et al., 2013) and then was further refined using the same Rosetta iterative backbone rebuilding procedure. With a proper density weight obtained using the half maps, the final model of the GR:Hsp90:p23 complex was refined against the full reconstruction allowing only sidechain and small-scale backbone refinement. The final refinement statistics are provided (Supplementary Table 1). For the Hsp90:p23 and MBP:Hsp90:p23 cryo-EM maps (Extended Data Fig. 8a,b and Extended Data Fig.

9a,b), the Hsp90:p23 atomic model from the GR-maturation complex was rigid-body docked into the maps using Chimera. For MBP:Hsp90:p23, the apo MBP crystal structure (Sharff et al., 1992) (PDB ID: 1OMP) was rigid-body docked into the map using Chimera. For Extended Data Fig. 9c, the maltose-bound MBP crystal structure (Quiocho et al., 1997) (PDB ID: 1ANF) was rigid-body docked into the map for comparison.

Fluorescence polarization assays

Fluorescence polarization of fluorescent dexamethasone (F-dex) (Thermo Fisher) was measured on a SpectraMax M5 plate reader (Molecular Devices) with excitation/emission wavelengths of 485/538 nm, temperature control set at 25°C. Buffer conditions were 50 mM HEPES pH 8, 100 mM KCl, 2 mM DTT. For equilibrium ligand binding in Fig. 2d and Extended Data Fig. 7b, proteins were pre-equilibrated together at room temperature for 60 minutes prior to F-dex addition. Proteins and reagents were added at the following concentration: 20 nM F-dex, 250 nM GR, 2 μM Hsp40, 15 μM Hsp70, 15 μM Hsp90, 15 μM Hop, 15 μM p23 or p23 tail mutants, and 5 mM ATP/$MgCl_2$. Note that the dissociation constant (K_D) between GR and F-dex is ~150 nM (Kirschke et al., 2014). Ligand binding was initiated with 20 nM F-dex and association was measured until reaching equilibrium. For the GR control sample, 3 experiments were done with a 1-hour room temperature preincubation of GR in the reaction buffer and 3 experiments were done without a preincubation of GR to account for small effects on equilibrium ligand binding from the preincubation. The plotted equilibrium values in Fig. 2d and Extended Data Fig. 7b represent the mean of 3 biologically independent

samples (except the GR control reaction, which represents the mean of 6 biologically independent samples), with error bars representing the standard deviation. Statistical significance was evaluated by an ordinary one-way ANOVA with *post-hoc* Dunnett's multiple comparisons test using Prism v.9.1.1 (GraphPad). For equilibrium ligand binding in Extended Data Fig. 7c, proteins were pre-equilibrated together at room temperature for 60 minutes prior to F-dex addition. Proteins and reagents were added at the following concentration: 20 nM F-dex, 250 nM GR and 15 μM p23 or p23 tail mutants. Ligand binding was initiated with 20 nM F-dex and association was measured until reaching equilibrium. The plotted data points for each reaction represent 7 biologically independent samples (6 biologically independent samples for the GR + p23Δtail reaction) and polarization values were baseline subtracted in accordance with the measured F-dex only baseline polarization value. Statistical significance was evaluated by an ordinary one-way ANOVA using Prism v.9.1.1 (GraphPad). GR ligand binding behavior was affected by buffer conditions; therefore, reactions were always normalized such that each reaction had equivalent amounts of buffer reagents.

Sequence alignments and p23$_{tail\text{-}helix}$ motif search

For the p23 sequence alignments in Extended Data Fig. 6f, sequences were obtained from Uniprot (UniProt, 2021), aligned in Clustal Omega (Madeira et al., 2019) (https://www.ebi.ac.uk/Tools/msa/clustalo/), and visualized in JalView 2.11.1.0 (Waterhouse et al., 2009). Sequences in the alignment are: *H. sapiens* p23, *M. musculus* p23, *R. norvegicus* p23, *G. gallus* p23, *X. tropicalis* p23, *D. melanogaster* p23, *A. thaliana* p23, and *S. cerevisiae* p23 (Uniprot accession codes: Q15185,

Q9R0Q7, P83868, Q90955, Q5U4Z0, Q7SZQ8, A0A0B4K6D2, Q8L7U4, P28707, respectively). Secondary structure prediction for the *S. cerevisiae* p23 protein sequence was performed using Psipred v.4.0 (Jones, 1999) (http://bioinf.cs.ucl.ac.uk/psipred/). For Fig. 2b, the ConSurf server (Ashkenazy et al., 2016; Landau et al., 2005) (https://consurf.tau.ac.il/) was used to select and align 87 GR protein sequences as follows: the human GR crystal structure (He et al., 2014) (PDB ID: 4P6X) was used to select sequences from UNIREF90 with maximal percent ID at 95% and minimal percent ID at 65%. Conservation scores were calculated and provided by the server. The conservation scores calculated by the ConSurf server were mapped onto GR from the maturation complex atomic model using Chimera.

For Extended Data Fig. 6c, the sequences were obtained from Uniprot (UniProt, 2021), aligned in Clustal Omega (Madeira et al., 2019) (https://www.ebi.ac.uk/Tools/msa/clustalo/), and mapped onto GR from the maturation complex using Chimera. Sequences in the alignment are the human steroid hormone receptors: glucocorticoid receptor, mineralocorticoid receptor, androgen receptor, progesterone receptor, estrogen receptor α and β (Uniprot accession codes: P04150, P08235, P10275, P06401, E3WH19, Q92731, respectively). Conservation was calculated using AL2CO (Pei & Grishin, 2001) parameters (unweighted frequency estimation and entropy-based conservation measurement). Relating to Extended Data Fig. 6f, the $p23_{tail\text{-}helix}$ motif search was performed using the ScanProsite server (de Castro et al., 2006) (https://prosite.expasy.org/scanprosite/). The motif “FXXMMN” was used to search the UniProtKB sequence database with taxonomy restricted to *Homo Sapiens*. There were 10 total hits on the motif, which included p23 and NCoA3/SRC-3.

Relating to Extended Data Fig. 6d, the human p23 helix predictions were performed using state-of-the-art secondary structure prediction algorithms: Porter 4.0 (Mirabello & Pollastri, 2013) (http://distillf.ucd.ie/porterpaleale/), RaptorX (Kallberg et al., 2012) (http://raptorx.uchicago.edu/StructurePrediction/predict/), and Psipred v.4.0 (Jones, 1999) (http://bioinf.cs.ucl.ac.uk/psipred/). The human p23 structure prediction is available from AlphaFold v2.0 (Jumper et al., 2021) with the accession code P83868

Yeast survival assays

Relating to Extended Data Fig. 7d, yeast survival assays were performed using *S. cerevisiae* strain *hsc82hsp82Δ* (JJ816) or *sba1hsc82hsp82Δ* (JJ94) expressing either wild-type Hsc82 or a mutant in pRS313GPDHis-Hsc82 (*hsc82-I588A, M589A*)(Johnson et al., 2007). The *sba1hsc82hsp82Δ* strain expressing *hsc82-I588A, M589A* was transformed with either empty vector (pR416GPD), human p23, or p23 tail mutants constitutively expressed from the p416GPD plasmid. Cells were grown overnight at 30°, then serially diluted 10-fold and grown on selective media at the indicated temperature for 2 days.

Expression of human p23 tail mutants

Human p23 and Sba1 protein expression levels in wild-type strain (JJ762 (PJ51-3a), a derivate of W303) (Johnson & Craig, 2000) were assessed by SDS-PAGE (12.5% acrylamide gel) followed by immunoblot analysis with polyclonal antisera raised against human p23 (Novus NBP1-85485)(1:200 dilution) or Sba1 (Johnson et al., 2007) (1:500 dilution) (Extended Data Fig. 7f).

In vivo GR activity assays

Relating to Extended Data Fig. 7e, GR transactivation was measured in the wild-type *S. cerevisiae* strain (JJ762) expressing GR on a single copy plasmid (p414GPD-GR) and a single copy LacZ reporter plasmid (pRS317-GRE-lacZ) that were constructed using multicopy versions of each plasmid(Johnson & Craig, 2000). Human p23, p23 tail mutants, or Sba1 were constitutively expressed from the p416-GPD plasmid. Cells were grown at 30°C with shaking overnight in selective media, diluted 10-fold and grown to OD_{600} 0.4-0.5. Cultures were split in two and one set was induced with ligand (10 μM DOC, deoxycorticosterone) (Sigma) for 1 hour. After 1 hour, cultures were put on ice to stop growth. The β-galactosidase (β-gal) activity of paired samples in the presence and absence of hormone was measured as described using the yeast β-galactosidase assay kit from Thermo Scientific (Catalog number #75768).

GR activity was determined by the fold difference in β-gal activity between the hormone treated duplicate relative to the untreated duplicate. Relative GR activation was calculated by normalizing the GR activity of each experimental sample to the average GR activity of strain JJ762 expressing p416GPD (empty vector [e.v.]). GR activity was measured with 18 biologically independent samples (10 biologically independent samples for the + Sba1 condition). Statistical significance was evaluated by an ordinary one-way ANOVA with *post-hoc* Šídák's multiple comparisons test using Prism v.9.1.1 (GraphPad).

Quantification and statistical analysis

All data were tested for statistical significance with Prism v.9.1.1 (GraphPad). Statistical significance was determined by ordinary one-way ANOVA (with *post-hoc* Dunnett's or Šídák's multiple comparisons test). All experiments were performed at least three times. Statistical details (including sample sizes (*n*), F-statistics, p-values, and degrees of freedom) are included in the figure legends for each experiment. Relating to Fig. 2d and Extended Data Fig. 7b, the one-way ANOVA with *post-hoc* Dunnett's test p-values are as follows: p(p23 vs. $p23_{\Delta tail}$) = 0.1512, p(p23 vs. $p23_{\Delta helix\text{-}tail}$) = 0.0002, p(p23 vs. no p23) = <0.0001. Relating to Extended Data Fig. 7e, the one-way ANOVA with *post-hoc* Šídák's test p-values are as follows: p(e.v. vs. p23) = 0.0001, p(p23 vs $p23_{\Delta tail}$) = 0.0164, p(p23 vs. $p23_{\Delta helix\text{-}tail}$) = 0.0021, p(p23 vs. Sba1) = 0.0002, p($p23_{\Delta tail}$ vs. $p23_{\Delta helix\text{-}tail}$) = 0.9721. For all statistical tests performed, variances across groups were not significantly different (as evaluated using the Brown-Forsythe test) and therefore no corrections were used (Fig. 2d and Extended Data Fig. 7b [Brown-Forsythe test p = 0.9966]; Extended Data Fig. 7c [Brown-Forsythe test p = 0.9224]; Extended Data Fig. 7e [Brown-Forsythe test p = 0.1696]).

References

Ali, M. M. U., Roe, S. M., Vaughan, C. K., Meyer, P., Panaretou, B., Piper, P. W., Prodromou, C., & Pearl, L. H. (2006). Crystal structure of an Hsp90–nucleotide–p23/Sba1 closed chaperone complex. *Nature, 440*(7087), 1013-1017. https://doi.org/10.1038/nature04716

Ashkenazy, H., Abadi, S., Martz, E., Chay, O., Mayrose, I., Pupko, T., & Ben-Tal, N. (2016, Jul 8). ConSurf 2016: an improved methodology to estimate and visualize evolutionary conservation in macromolecules. *Nucleic Acids Res, 44*(W1), W344-350. https://doi.org/10.1093/nar/gkw408

Biebl, M. M., Lopez, A., Rehn, A., Freiburger, L., Lawatscheck, J., Blank, B., Sattler, M., & Buchner, J. (2021, Feb 5). Structural elements in the flexible tail of the co-chaperone p23 coordinate client binding and progression of the Hsp90 chaperone cycle. *Nat Commun, 12*(1), 828. https://doi.org/10.1038/s41467-021-21063-0

Bledsoe, R. K., Montana, V. G., Stanley, T. B., Delves, C. J., Apolito, C. J., McKee, D. D., Consler, T. G., Parks, D. J., Stewart, E. L., Willson, T. M., Lambert, M. H., Moore, J. T., Pearce, K. H., & Xu, H. E. (2002). Crystal Structure of the Glucocorticoid Receptor Ligand Binding Domain Reveals a Novel Mode of Receptor Dimerization and Coactivator Recognition. *110*(1), 93-105. https://doi.org/10.1016/s0092-8674(02)00817-6

Bohen, S. P. (1998, Jun). Genetic and biochemical analysis of p23 and ansamycin antibiotics in the function of Hsp90-dependent signaling proteins. *Mol Cell Biol, 18*(6), 3330-3339. https://doi.org/10.1128/MCB.18.6.3330

Csermely, P., Kajtar, J., Hollosi, M., Jalsovszky, G., Holly, S., Kahn, C. R., Gergely, P., Soti, C., Mihaly, K., & Somogyi, J. (1993, Jan 25). Atp Induces a Conformational Change of the 90-Kda Heat-Shock Protein (Hsp90). *Journal of Biological Chemistry, 268*(3), 1901-1907. <Go to ISI>://WOS:A1993KH62000062

Czar, M. J., Galigniana, M. D., Silverstein, A. M., & Pratt, W. B. (1997, Jun 24). Geldanamycin, a heat shock protein 90-binding benzoquinone ansamycin, inhibits steroid-dependent translocation of the glucocorticoid receptor from the cytoplasm to the nucleus. *Biochemistry, 36*(25), 7776-7785. https://doi.org/10.1021/bi970648x

de Castro, E., Sigrist, C. J., Gattiker, A., Bulliard, V., Langendijk-Genevaux, P. S., Gasteiger, E., Bairoch, A., & Hulo, N. (2006, Jul 1). ScanProsite: detection of PROSITE signature matches and ProRule-associated functional and structural residues in proteins. *Nucleic Acids Res, 34*(Web Server issue), W362-365. https://doi.org/10.1093/nar/gkl124

Freeman, B. C., Felts, S. J., Toft, D. O., & Yamamoto, K. R. (2000). The p23 molecular chaperones act at a late step in intracellular receptor action to differentially affect ligand efficacies. *Genes & development, 14*(4), 422-434. https://www.ncbi.nlm.nih.gov/pubmed/10691735

https://www.ncbi.nlm.nih.gov/pmc/PMC316379/

Freeman, B. C., Toft, D. O., & Morimoto, R. I. (1996, Dec 6). Molecular chaperone machines: chaperone activities of the cyclophilin Cyp-40 and the steroid aporeceptor-associated protein p23. *Science, 274*(5293), 1718-1720. https://doi.org/10.1126/science.274.5293.1718

Freeman, B. C., & Yamamoto, K. R. (2002). Disassembly of Transcriptional Regulatory Complexes by Molecular Chaperones. *Science, 296*(5576), 2232. https://doi.org/10.1126/science.1073051

Galigniana, M. D., Radanyi, C., Renoir, J. M., Housley, P. R., & Pratt, W. B. (2001, May 4). Evidence that the peptidylprolyl isomerase domain of the hsp90-binding immunophilin FKBP52 is involved in both dynein interaction and glucocorticoid receptor movement to the nucleus. *J Biol Chem, 276*(18), 14884-14889. https://doi.org/10.1074/jbc.M010809200

Goddard, T. D., Huang, C. C., Meng, E. C., Pettersen, E. F., Couch, G. S., Morris, J. H., & Ferrin, T. E. (2018, Jan). UCSF ChimeraX: Meeting modern challenges in

visualization and analysis. *Protein Sci, 27*(1), 14-25. https://doi.org/10.1002/pro.3235

Hawle, P., Siepmann, M., Harst, A., Siderius, M., Reusch, H. P., & Obermann, W. M. J. (2006). The middle domain of Hsp90 acts as a discriminator between different types of client proteins. *Molecular and Cellular Biology, 26*(22), 8385-8395. https://doi.org/10.1128/MCB.02188-05

He, Y., Yi, W., Suino-Powell, K., Zhou, X. E., Tolbert, W. D., Tang, X., Yang, J., Yang, H., Shi, J., Hou, L., Jiang, H., Melcher, K., & Xu, H. E. (2014, Jun). Structures and mechanism for the design of highly potent glucocorticoids. *Cell Res, 24*(6), 713-726. https://doi.org/10.1038/cr.2014.52

Johnson, J. L., & Craig, E. A. (2000, May). A role for the Hsp40 Ydj1 in repression of basal steroid receptor activity in yeast. *Mol Cell Biol, 20*(9), 3027-3036. https://doi.org/10.1128/MCB.20.9.3027-3036.2000

Johnson, J. L., Halas, A., & Flom, G. (2007, Jan). Nucleotide-dependent interaction of Saccharomyces cerevisiae Hsp90 with the cochaperone proteins Sti1, Cpr6, and Sba1. *Mol Cell Biol, 27*(2), 768-776. https://doi.org/10.1128/MCB.01034-06

Johnson, J. L., & Toft, D. O. (1995, Jun). Binding of p23 and hsp90 during assembly with the progesterone receptor. *Mol Endocrinol, 9*(6), 670-678. https://doi.org/10.1210/mend.9.6.8592513

Jones, D. T. (1999, Sep 17). Protein secondary structure prediction based on position-specific scoring matrices. *Journal of Molecular Biology, 292*(2), 195-202. https://doi.org/DOI 10.1006/jmbi.1999.3091

Jumper, J., Evans, R., Pritzel, A., Green, T., Figurnov, M., Ronneberger, O., Tunyasuvunakool, K., Bates, R., Zidek, A., Potapenko, A., Bridgland, A., Meyer, C., Kohl, S. A. A., Ballard, A. J., Cowie, A., Romera-Paredes, B., Nikolov, S., Jain, R., Adler, J., Back, T., Petersen, S., Reiman, D., Clancy, E., Zielinski, M., Steinegger, M., Pacholska, M., Berghammer, T., Bodenstein, S., Silver, D., Vinyals, O., Senior, A. W., Kavukcuoglu, K., Kohli, P., & Hassabis, D. (2021, Jul 15). Highly accurate protein structure prediction with AlphaFold. *Nature*. https://doi.org/10.1038/s41586-021-03819-2

Kallberg, M., Wang, H. P., Wang, S., Peng, J., Wang, Z. Y., Lu, H., & Xu, J. B. (2012, Aug). Template-based protein structure modeling using the RaptorX web server. *Nature Protocols, 7*(8), 1511-1522. https://doi.org/10.1038/nprot.2012.085

Kirschke, E., Goswami, D., Southworth, D., Griffin, P., & Agard, D. (2014). Glucocorticoid Receptor Function Regulated by Coordinated Action of the Hsp90

and Hsp70 Chaperone Cycles. *Cell, 157*(7), 1685-1697. https://doi.org/10.1016/j.cell.2014.04.038

Krukenberg, K. A., Street, T. O., Lavery, L. A., & Agard, D. A. (2011). Conformational dynamics of the molecular chaperone Hsp90. *Quarterly reviews of biophysics, 44*(2), 229-255. https://doi.org/10.1017/S0033583510000314

Landau, M., Mayrose, I., Rosenberg, Y., Glaser, F., Martz, E., Pupko, T., & Ben-Tal, N. (2005, Jul 1). ConSurf 2005: the projection of evolutionary conservation scores of residues on protein structures. *Nucleic Acids Res, 33*(Web Server issue), W299-302. https://doi.org/10.1093/nar/gki370

Liu, Y., Elnatan, D., Sun, M., Myasnikov, A. G., & Agard, D. A. (2020). Cryo-EM reveals the dynamic interplay between mitochondrial Hsp90 and SdhB folding intermediates. *bioRxiv*, 2020.2010.2006.327627. https://doi.org/10.1101/2020.10.06.327627

Lorenz, O. R., Freiburger, L., Rutz, D. A., Krause, M., Zierer, B. K., Alvira, S., Cuéllar, J., José, Madl, T., Sattler, M., & Buchner, J. (2014). Modulation of the Hsp90 Chaperone Cycle by a Stringent Client Protein. *53*(6), 941-953. https://doi.org/10.1016/j.molcel.2014.02.003

Madeira, F., Park, Y. M., Lee, J., Buso, N., Gur, T., Madhusoodanan, N., Basutkar, P., Tivey, A. R. N., Potter, S. C., Finn, R. D., & Lopez, R. (2019, Jul 2). The EMBL-EBI search and sequence analysis tools APIs in 2019. *Nucleic Acids Res, 47*(W1), W636-W641. https://doi.org/10.1093/nar/gkz268

McKenna, N. J., & O'Malley, B. W. (2002, Feb 22). Combinatorial control of gene expression by nuclear receptors and coregulators. *Cell, 108*(4), 465-474. https://doi.org/10.1016/s0092-8674(02)00641-4

Meyer, P., Prodromou, C., Hu, B., Vaughan, C., Roe, S. M., Panaretou, B., Piper, P. W., & Pearl, L. H. (2003, 2003/03/01/). Structural and Functional Analysis of the Middle Segment of Hsp90: Implications for ATP Hydrolysis and Client Protein and Cochaperone Interactions. *Molecular Cell, 11*(3), 647-658. https://doi.org/10.1016/S1097-2765(03)00065-0

Mirabello, C., & Pollastri, G. (2013, Aug 15). Porter, PaleAle 4.0: high-accuracy prediction of protein secondary structure and relative solvent accessibility. *Bioinformatics, 29*(16), 2056-2058. https://doi.org/10.1093/bioinformatics/btt344

Morishima, Y., Murphy, P. J., Li, D. P., Sanchez, E. R., & Pratt, W. B. (2000, Jun 16). Stepwise assembly of a glucocorticoid receptor.hsp90 heterocomplex resolves two sequential ATP-dependent events involving first hsp70 and then hsp90 in

opening of the steroid binding pocket. *J Biol Chem, 275*(24), 18054-18060. https://doi.org/10.1074/jbc.M000434200

Nathan, D. F., & Lindquist, S. (1995, Jul). Mutational analysis of Hsp90 function: interactions with a steroid receptor and a protein kinase. *Mol Cell Biol, 15*(7), 3917-3925. https://doi.org/10.1128/mcb.15.7.3917

Netzer, W. J., & Hartl, F. U. (1997, Jul 24). Recombination of protein domains facilitated by co-translational folding in eukaryotes. *Nature, 388*(6640), 343-349. https://doi.org/10.1038/41024

Pei, J., & Grishin, N. V. (2001, Aug). AL2CO: calculation of positional conservation in a protein sequence alignment. *Bioinformatics, 17*(8), 700-712. https://doi.org/10.1093/bioinformatics/17.8.700

Pettersen, E. F., Goddard, T. D., Huang, C. C., Couch, G. S., Greenblatt, D. M., Meng, E. C., & Ferrin, T. E. (2004, Oct). UCSF Chimera--a visualization system for exploratory research and analysis. *J Comput Chem, 25*(13), 1605-1612. https://doi.org/10.1002/jcc.20084

Picard, D., Khursheed, B., Garabedian, M. J., Fortin, M. G., Lindquist, S., & Yamamoto, K. R. (1990, 1990/11/01). Reduced levels of hsp90 compromise steroid receptor action in vivo. *Nature, 348*(6297), 166-168. https://doi.org/10.1038/348166a0

Pratt, W. B., & Toft, D. O. (1997). Steroid Receptor Interactions with Heat Shock Protein and Immunophilin Chaperones. *Endocrine Reviews, 18*(3), 306-360. https://doi.org/10.1210/edrv.18.3.0303

Quiocho, F. A., Spurlino, J. C., & Rodseth, L. E. (1997, Aug 15). Extensive features of tight oligosaccharide binding revealed in high-resolution structures of the maltodextrin transport/chemosensory receptor. *Structure, 5*(8), 997-1015. https://doi.org/10.1016/s0969-2126(97)00253-0

Rohou, A., & Grigorieff, N. (2015, Nov). CTFFIND4: Fast and accurate defocus estimation from electron micrographs. *J Struct Biol, 192*(2), 216-221. https://doi.org/10.1016/j.jsb.2015.08.008

Rosenzweig, R., Nillegoda, N. B., Mayer, M. P., & Bukau, B. (2019, Nov). The Hsp70 chaperone network. *Nat Rev Mol Cell Biol, 20*(11), 665-680. https://doi.org/10.1038/s41580-019-0133-3

Rutz, D. A., Luo, Q., Freiburger, L., Madl, T., Kaila, V. R. I., Sattler, M., & Buchner, J. (2018, 2018/04/16). A switch point in the molecular chaperone Hsp90 responding to client interaction. *Nature Communications, 9*(1), 1472. https://doi.org/10.1038/s41467-018-03946-x

Sahasrabudhe, P., Rohrberg, J., Biebl, M. M., Rutz, D. A., & Buchner, J. (2017, Sep 21). The Plasticity of the Hsp90 Co-chaperone System. *Mol Cell, 67*(6), 947-961.e945. https://doi.org/10.1016/j.molcel.2017.08.004

Scheres, S. H. (2012, Dec). RELION: implementation of a Bayesian approach to cryo-EM structure determination. *J Struct Biol, 180*(3), 519-530. https://doi.org/10.1016/j.jsb.2012.09.006

Schopf, F. H., Biebl, M. M., & Buchner, J. (2017). The HSP90 chaperone machinery. *Nature Reviews Molecular Cell Biology, 18*(6), 345-360. https://doi.org/10.1038/nrm.2017.20

Schorb, M., Haberbosch, I., Hagen, W. J. H., Schwab, Y., & Mastronarde, D. N. (2019, Jun). Software tools for automated transmission electron microscopy. *Nat Methods, 16*(6), 471-477. https://doi.org/10.1038/s41592-019-0396-9

Seraphim, T. V., Gava, L. M., Mokry, D. Z., Cagliari, T. C., Barbosa, L. R., Ramos, C. H., & Borges, J. C. (2015, Jan 1). The C-terminal region of the human p23 chaperone modulates its structure and function. *Arch Biochem Biophys, 565*, 57-67. https://doi.org/10.1016/j.abb.2014.10.015

Sharff, A. J., Rodseth, L. E., Spurlino, J. C., & Quiocho, F. A. (1992, Nov 10). Crystallographic evidence of a large ligand-induced hinge-twist motion between

the two domains of the maltodextrin binding protein involved in active transport and chemotaxis. *Biochemistry, 31*(44), 10657-10663. https://doi.org/10.1021/bi00159a003

Smith, D. F., & Toft, D. O. (2008, Oct). Minireview: the intersection of steroid receptors with molecular chaperones: observations and questions. *Mol Endocrinol, 22*(10), 2229-2240. https://doi.org/10.1210/me.2008-0089

Song, Y., DiMaio, F., Wang, R. Y., Kim, D., Miles, C., Brunette, T., Thompson, J., & Baker, D. (2013, Oct 8). High-resolution comparative modeling with RosettaCM. *Structure, 21*(10), 1735-1742. https://doi.org/10.1016/j.str.2013.08.005

Suren, T., Rutz, D., Mößmer, P., Merkel, U., Buchner, J., & Rief, M. (2018). Single-molecule force spectroscopy reveals folding steps associated with hormone binding and activation of the glucocorticoid receptor. *Proceedings of the National Academy of Sciences, 115*(46), 11688. https://doi.org/10.1073/pnas.1807618115

Taipale, M., Jarosz, D. F., & Lindquist, S. (2010). HSP90 at the hub of protein homeostasis: emerging mechanistic insights. *11*(7), 515-528. https://doi.org/10.1038/nrm2918

Taipale, M., Krykbaeva, I., Koeva, M., Kayatekin, C., Westover, K. D., Karras, G. I., & Lindquist, S. (2012, Aug 31). Quantitative analysis of HSP90-client interactions

reveals principles of substrate recognition. *Cell, 150*(5), 987-1001. https://doi.org/10.1016/j.cell.2012.06.047

UniProt, C. (2021, Jan 8). UniProt: the universal protein knowledgebase in 2021. *Nucleic Acids Res, 49*(D1), D480-D489. https://doi.org/10.1093/nar/gkaa1100

Verba, K. A., Wang, R. Y. R., Arakawa, A., Liu, Y., Shirouzu, M., Yokoyama, S., & Agard, D. A. (2016). Atomic structure of Hsp90-Cdc37-Cdk4 reveals that Hsp90 traps and stabilizes an unfolded kinase. *Science, 352*(6293), 1542-1547. https://doi.org/10.1126/science.aaf5023

Wang, R. Y., Noddings, C. M., Kirschke, E., Myasnikov, A. G., Johnson, J. L., & Agard, D. A. (2022, Jan). Structure of Hsp90-Hsp70-Hop-GR reveals the Hsp90 client-loading mechanism. *Nature, 601*(7893), 460-464. https://doi.org/10.1038/s41586-021-04252-1

Wang, R. Y., Song, Y., Barad, B. A., Cheng, Y., Fraser, J. S., & DiMaio, F. (2016, Sep 26). Automated structure refinement of macromolecular assemblies from cryo-EM maps using Rosetta. *Elife, 5*. https://doi.org/10.7554/eLife.17219

Waterhouse, A. M., Procter, J. B., Martin, D. M., Clamp, M., & Barton, G. J. (2009, May 1). Jalview Version 2--a multiple sequence alignment editor and analysis

workbench. *Bioinformatics, 25*(9), 1189-1191. https://doi.org/10.1093/bioinformatics/btp033

Weaver, A. J., Sullivan, W. P., Felts, S. J., Owen, B. A. L., & Toft, D. O. (2000). Crystal Structure and Activity of Human p23, a Heat Shock Protein 90 Co-chaperone. *J Biol Chem, 275*(30), 23045-23052. https://doi.org/10.1074/jbc.m003410200

Weikl, T., Abelmann, K., & Buchner, J. (1999, Oct 29). An unstructured C-terminal region of the Hsp90 co-chaperone p23 is important for its chaperone function. *J Mol Biol, 293*(3), 685-691. https://doi.org/10.1006/jmbi.1999.3172

Zhao, R., Davey, M., Hsu, Y. C., Kaplanek, P., Tong, A., Parsons, A. B., Krogan, N., Cagney, G., Mai, D., Greenblatt, J., Boone, C., Emili, A., & Houry, W. A. (2005, Mar 11). Navigating the chaperone network: an integrative map of physical and genetic interactions mediated by the hsp90 chaperone. *Cell, 120*(5), 715-727. https://doi.org/10.1016/j.cell.2004.12.024

Zheng, S. Q., Palovcak, E., Armache, J. P., Verba, K. A., Cheng, Y., & Agard, D. A. (2017, Apr). MotionCor2: anisotropic correction of beam-induced motion for improved cryo-electron microscopy. *Nat Methods, 14*(4), 331-332. https://doi.org/10.1038/nmeth.4193

Zimmermann, L., Stephens, A., Nam, S. Z., Rau, D., Kubler, J., Lozajic, M., Gabler, F., Soding, J., Lupas, A. N., & Alva, V. (2018, Jul 20). A Completely Reimplemented MPI Bioinformatics Toolkit with a New HHpred Server at its Core. *J Mol Biol, 430*(15), 2237-2243. https://doi.org/10.1016/j.jmb.2017.12.007

Chapter 4 Cryo-EM reveals how Hsp90 and FKBP cochaperones regulate the Glucocorticoid Receptor

Preface

The work presented in this chapter is from a manuscript in preparation. This project was conceived as a follow-up to the GR-maturation complex manuscript (Chapter 3) to determine how additional cochaperones, FKBP51 and FKBP52, integrate with the GR chaperone cycle to regulate GR activity. My goals were to 1) determine structures of FKBP51 and FKBP52 bound to complexes in the GR chaperone cycle and 2) characterize the effect of FKBP51 and FKBP52 on GR ligand-binding activity *in vitro*. Jill Johnson (University of Idaho) performed *in vivo* experiments validating the novel binding sites revealed in these structures and demonstrated the importance of FKBP:GR interactions in regulating GR activity *in vivo*.

Abstract

Hsp90 is an essential molecular chaperone responsible for the folding and activation of hundreds of ‘client’ proteins, including the glucocorticoid receptor (GR) (Schopf et al., 2017; Taipale et al., 2010; Taipale et al., 2012). Previously, we revealed that GR ligand binding activity is inhibited by Hsp70 and restored by Hsp90, aided by cochaperones (Kirschke et al., 2014). We then presented cryo-EM structures mechanistically detailing how Hsp70 and Hsp90 remodel the conformation of GR to regulate ligand binding (Noddings et al., 2022; Wang et al., 2022). *In vivo*, GR-chaperone complexes are found associated with numerous Hsp90 cochaperones, including the immunophilins FKBP51 and FKBP52, which further regulate the activity of

GR and other steroid receptors (Pratt & Toft, 1997; Storer et al., 2011; Zgajnar et al., 2019). A molecular understanding of how FKBP51 and FKBP52 integrate with the GR-chaperone cycle and couple the GR ligand-binding state to nuclear translocation is lacking. Here, we present a 2.96 Å cryo-EM structure of the GR:Hsp90:FKBP52 complex, revealing that FKBP52 directly binds to the folded, ligand-bound GR using three distinct interfaces, which we show are critical *in vivo*. We demonstrate FKBP52 advances GR to the next stage of maturation and potentiates GR ligand binding *in vitro,* in a process dependent upon a single residue at the GR:FKBP52 interface. We also present a 3.29 Å cryo-EM structure of the GR:Hsp90:FKBP51 complex, which largely mimics the GR:Hsp90:FKBP52 structure. Surprisingly, FKBP51 and FKBP52 advance GR to the next stage of maturation and in the process allosterically compete with p23 for GR binding. Altogether, we reveal for the first time how FKBP51 and FKBP52 integrate into the GR chaperone cycle, how FKBP52 potentiates GR activity *in vitro* and *in vivo*, and how FKBP51 and FKBP52 compete to bind GR, leading to functional antagonism**.**

Introduction

Hsp90 is required for the functional maturation of 10% of the eukaryotic proteome (Zhao et al., 2005). Hsp90 ‘clients’ are enriched in signaling proteins and transcription factors, such as steroid hormone receptors (SHRs), making Hsp90 an important clinical target (Taipale et al., 2010). SHRs, which include GR, are hormone-regulated transcription factors that depend on Hsp90 for function throughout their functional lifetimes (Morishima et al., 2000; Nathan & Lindquist, 1995; Picard et al.,

1990; Pratt & Toft, 1997; Smith & Toft, 2008; Weikum et al., 2017). We previously established *in vitro* reconstitution of the 'GR-chaperone cycle', revealing that GR depends on Hsp90 for function due to constant inactivation of ligand binding by Hsp70 and subsequent reactivation by Hsp90 (Kirschke et al., 2014). In the GR-chaperone cycle, now understood in atomic detail through cryo-EM, GR ligand binding is regulated by a cycle of three distinct chaperone complexes (Noddings et al., 2022; Wang et al., 2022). In this chaperone cycle, GR is first inhibited by Hsp70 and Hsp40, then loaded onto Hsp90:Hop (Hsp70/Hsp90 organizing protein cochaperone) forming an inactive GR-loading complex (GR:Hsp70:Hsp90:Hop) (Wang et al., 2022). Upon hydrolysis of one of the two ATPs on Hsp90, two Hsp70s and Hop are released, and p23 is incorporated to form an active GR-maturation complex (GR:Hsp90:p23), restoring GR ligand-binding with enhanced affinity (Noddings et al., 2022). The cryo-EM structures of the GR-loading complex and GR-maturation complex reveal Hsp70 and Hsp90 locally unfold and refold the GR LBD in a controlled manner to directly regulate ligand binding.

In vivo, additional Hsp90 cochaperones are found associated with the GR-chaperone cycle, including the large immunophilins, FKBP51 and FKBP52 (Pratt & Toft, 1997). FKBP51 and FKBP52 are peptidyl proline isomerases (PPIases) that contain an N-terminal FK1 domain with PPIase activity, an FK2 domain lacking PPIase activity, and a C-terminal TPR domain, which canonically binds the EEVD motifs at the C-termini of Hsp90 and Hsp70 (Kumar et al., 2017; Pirkl & Buchner, 2001; Sinars et al., 2003; Wu et al., 2004). Additionally, the TPR domain contains a helical extension at the C-terminus (Helix 7e), which was previously described to bind the C-terminal Domain (CTD) closed dimer interface of Hsp90 (Cheung-Flynn et al., 2003; Lee et al., 2021). Although

FKBP51 and FKBP52 are 70% similar in sequence, these cochaperones have antagonistic functional effects on GR *in vivo* (Storer et al., 2011). FKBP51 inhibits GR ligand binding, transcriptional activity, and nuclear translocation, while FKBP52 potentiates each of these fundamental GR activities (Davies et al., 2005; Denny et al., 2000; Echeverría et al., 2009; Galigniana et al., 2001; Hinds et al., 2014; Riggs et al., 2007; Riggs et al., 2003; Tatro et al., 2009; Vandevyver et al., 2012; Wochnik et al., 2005; Wolf et al., 2009). FKBP51 and FKBP52 have also been implicated in the regulation of all other SHRs (Storer et al., 2011; Zgajnar et al., 2019). Due to the critical importance of steroid hormone signaling in the cell, altered expression of FKBP51 and FKBP52 is associated with various endocrine-related disease states, including a wide variety of cancers, infertility, stress and anxiety disorders, and immune-related diseases (Kolos et al., 2018; Storer et al., 2011; Zgajnar et al., 2019). Despite their importance, the absence of structures of FKBP cochaperones bound to Hsp90:client complexes precludes a mechanistic understanding of how these cochaperones integrate with Hsp90:client complexes to regulate client function or how to design selective small-molecule therapeutics (Bauder et al., 2021; Feng et al., 2015; Gaali et al., 2015; Guy et al., 2015; Kolos et al., 2018; Sabbagh et al., 2018). Here we present a 2.96 Å cryo-EM structure of the GR:Hsp90:FKBP52 complex, revealing for the first time how FKBP52 integrates into the GR-chaperone cycle and directly binds to the active client, potentiating GR activity *in vitro* and *in vivo*. We also present a 3.29 Å cryo-EM structure of the GR:Hsp90:FKBP51 complex, revealing how FKBP51 competes with FKBP52 for GR:Hsp90 binding and demonstrating how FKBP51 can act a potent antagonist to FKBP52.

Results

GR:Hsp90:FKBP52 Structure Determination

The GR:Hsp90:FKBP52 complex was prepared by *in vitro* reconstitution of the complete GR-chaperone cycle. GR DBD-LBD (amino acids 418-777) (hereafter, GR for simplicity) with an N-terminal maltose-binding protein (MBP) tag was incubated with Hsp70, Hsp40, Hop, Hsp90, p23, and FKBP52, allowing GR to progress through the chaperone cycle to reach the GR:Hsp90:FKBP52 complex (Extended Data Fig. 1a,b). The complex was stabilized with sodium molybdate and then purified by affinity purification on MBP-GR followed by size exclusion chromatography and light crosslinking (Extended Data Fig. 1c,d). A 2.96 Å cryo-EM reconstruction of the GR:Hsp90:FKBP52 complex was obtained using RELION and CryoSparc with atomic models built using Rosetta (Fig. 1a,b; Extended Data Fig. 1e, 2). The structure revealed a fully closed, nucleotide bound Hsp90 dimer (Hsp90A and Hsp90B) complexed with a single GR and a single FKBP52, which occupied the same side of Hsp90 (Fig. 1a,b, ED. Fig. 3a). Despite using a multi-domain GR construct, only the GR LBD was visible in the density map.

Hsp90 Stabilizes the GR LBD in a Folded, Ligand-Bound State

In the GR:Hsp90:FKBP52 complex, GR adopts a fully folded, ligand-bound conformation (Extended Data Fig. 3b) distinct from that adopted in the GR:Hsp90:p23 maturation complex (discussed below). The folded GR is stabilized by Hsp90 at three major interfaces (Fig. 1c-e, Extended Data Fig. 1c-f): (1) Hsp90 Src loop:GR

hydrophobic patch, (2) Hsp90 MD/CTD:GR Helix 1, and (3) Hsp90 lumen:GR pre-helix 1. In the first interface, the Hsp90A Src loop ($Hsp90^{345-360}$), flips out from the Hsp90 lumen, to interact with the previously described hydrophobic patch formed by GR Helices 9/10 and the GR C-terminus (Noddings et al., 2022) (approximately 767 $Å^2$ of buried surface area (BSA)) (Fig. 1c, Extended Data Fig. 1c). Along the Src loop, $Hsp90A^{F349,L351,F352,E353,}$ contact GR helices 9/10 and the conserved, solvent exposed $Hsp90A^{W320}$ interacts with GR^{F774} on the GR C terminus. Notably, $Hsp90A^{W320,F349}$ also make contact with GR in the GR-loading complex and GR-maturation complex, although at different locations (Noddings et al., 2022; Wang et al., 2022). Additionally, there are multiple hydrogen bonds formed between the Hsp90 NTD/MD to GR Helix 10 and the GR C-terminus (GR^{K777}).

Interface 2 is comprised of $Hsp90^{Y604}$ packing against GR Helix 1 ($GR^{532-539}$) and $Hsp90^{Y627}$ sticking into a hydrophobic pocket on GR formed by Helices 3, 4, and 9 (approximately 345 $Å^2$ BSA) (Fig. 1d, Extended Data Fig. d,e). This hydrophobic pocket was previously identified in the androgen receptor (AR) as a druggable hydrophobic site (Estebanez-Perpina et al., 2007). In interface 3, the unstructured GR pre-helix 1 region ($GR^{519-531}$) is threaded through the closed Hsp90 lumen (approximately 758 $Å^2$ BSA)(Fig. 1e, Extended Data Fig. 3f). Two hydrophobic residues on GR ($GR^{P522,P526}$) occupy two hydrophobic pockets within the Hsp90 lumen. The interaction is further stabilized by multiple polar and hydrophobic interactions between GR pre-helix 1 and the Hsp90A/B amphipathic helical hairpin ($Hsp90^{606-628}$).

FKBP52 Interacts with the Closed Hsp90

FKBP52 engages the closed Hsp90 at three major interfaces (Fig. 1f,g, ED Fig.4a,b): (1) FKBP52 TPR H7e:Hsp90A/B CTDs, (2) FKBP52 TPR:Hsp90B MEEVD, and (3) FKBP52 TPR:Hsp90B CTD. In Interface 1, the extended C-terminal H7e ($FKBP52^{387-424}$) from the TPR domain binds in a hydrophobic cleft formed by the Hsp90A/B CTDs at the closed dimer interface (approximately 1109 $Å^2$ BSA)(Fig. 1f, Extended Data Fig. 1a). As compared to the crystal structure, H7e breaks at positions $FKBP52^{411-414}$ to allow hydrophobic residues ($FKBP52^{L410,Y411,M414,F415,L418}$) to flip into the hydrophobic cleft formed by the Hsp90 CTDs, consistent with the FKBP51 H7e:Hsp90 interaction observed by cryo-EM (Lee et al., 2021). Mutating the corresponding conserved residues on FKBP51 H7e ($FKBP51^{M412,F413}$ corresponding to $FKBP52^{M414,F415}$) abolishes FKBP51:Hsp90 binding, indicating the importance of this binding site (Lee et al., 2021). The interface is further stabilized by multiple hydrogen bonds and salt bridges from Hsp90A/B to H7e flanking the helix break (Extended Data Fig. 4a). Furthermore, a portion of the Hsp90B MEEVD linker ($Hsp90B^{700-706}$) binds along FKBP52 H7e stabilized by polar interactions and salt bridges (Extended Data Fig. 4a).

In Interface 2, the C-terminal MEEVD peptide motif of Hsp90B binds in the FKBP52 TPR helical bundle (approximately 779 $Å^2$ BSA) (Fig. 1g, Extended Data Fig. 4b), with multiple hydrogen bonds, salt bridges, and hydrophobic interactions, analogous to other FKBP51:$Hsp90^{MEEVD}$ structures (Kumar et al., 2017; Lee et al., 2021). However, the MEEVD peptide binds in an opposite orientation relative to the FKBP52:$Hsp90^{MEEVD}$ crystal structure (Wu et al., 2004), which may have been incorrectly modeled as previously suggested (Blundell et al., 2017; Kumar et al., 2017).

Interface 3 is comprised of the FKBP52 TPR helices 5/6 binding to the Hsp90B CTD, stabilized by multiple hydrogen bonds (approximately 193 Å^2 BSA) (Extended Data Fig. 4c), also observed in the FKBP51:Hsp90 cryo-EM structure (Lee et al., 2021). While the interactions between FKBP52 TPR/H7e:Hsp90 are conserved in the FKBP51:Hsp90 structure, the positions of the FKBP52 FK1 and FK2 domains are significantly altered (Extended Data Fig. 4d), owing to the presence of the bound GR client, as discussed below.

FKBP52 Directly Interacts with GR, which is Functionally Important in vivo

Unexpectedly, FKBP52 directly and extensively interacts with GR, where the three FKBP52 domains wrap around GR, cradling the folded, ligand-bound client near the GR ligand-binding pocket (Fig. 2a). The tertiary structure within each FKBP52 domain closely matches isolated domains from FKBP52 crystal structures; however, the interdomain angles are significantly different (Extended Data Fig. 4d), likely owing to the extensive interaction with GR. There are three major interfaces between FKBP52 and GR (Fig. 2b-d): (1) FKBP52 FK1:GR, (2) FKBP52 FK2:GR, and (3) FKBP52 FK2-TPR linker:GR Helix 12.

In interface 1, FKBP52 FK1 interacts with a large surface on GR, canonically used for GR dimer formation, consisting of the GR post-helix 1 strand (helix 1-3 loop), helix 5, and β1,2 (approximately 280 Å^2 BSA) (Fig. 2b). 3D variability analysis in CryoSparc reveals that the interaction between FKBP52 FK1 and GR is highly dynamic, even as the other FKBP52 domains (FK2, TPR) remain stably associated with GR (Supplemental Movie 1). At the FK1:GR interface, GR^{Y545} on the post-Helix 1 strand

interacts with a hydrophobic surface formed by the FKBP52$^{81\text{-}88}$ loop and forms a hydrogen bond with FKBP52^{Y113}. Species-specific differences in the GR post-helix 1 strand (GR$^{544\text{-}546}$) have previously been implicated in cortisol resistance in an FKBP51/52-dependent manner (Cluning et al., 2013; Fuller et al., 2004). In addition, the FKBP52 proline-rich loop (β4-β5 loop or 80S loop) contacts GR Helix 5 and β1,2. 3D variability analysis in CryoSparc reveals that the proline-rich loop positioning is flexible, deviating from the position in the crystal structure (PDB ID: 4LAV) (Bracher et al., 2013) and adopting different interfaces with GR (Supplemental Movie 2). In the consensus 3D refinement map, the proline-rich loop adopts a position similar to the crystal structure, and FKBP52^{A116,S118,P119} interact with the tip of GR Helix 5 and β1,2. The mutation FKBP52^{P119L} has been shown to reduce GR and AR activation *in vivo*, while FKBP52^{A116V} has been shown to increase AR activation *in vivo* (Riggs et al., 2007), demonstrating the functional significance of this interaction site. FKBP52^{S118} has been identified as a phosphorylation site in FKBP52 (qPTM database (Yu et al., 2022)), but not FKBP51, possibly due to the unique adjacent FKBP52^{P119} as a signal for proline-directed protein kinases. We demonstrate that the mutation FKBP52^{S118A} significantly reduces FKBP52-dependent GR potentiation *in vivo* (Fig. 2e), suggesting phosphorylation at FKBP52^{S118} may help promote interaction between the proline-rich loop and GR.

While the FKBP52 FK1 domain is known to have PPIase enzymatic activity, GR is not bound in the PPIase active site and accordingly, no GR prolines were found to have been isomerized compared to other GR structures (PDB ID: 1M2Z (Bledsoe et al., 2002), 7KRJ (Noddings et al., 2022)). Consistent with this, mutation of GR prolines does

not disrupt FKBP52-dependent regulation of GR (Cluning et al., 2013). Additionally, mutations that disrupt PPIase activity do not affect FKBP52-dependent GR potentiation *in vivo* (Riggs et al., 2007). Conversely, PPIase inhibitors have been shown to block the FKBP52-dependent potentiation of GR *in vivo* (Riggs et al., 2003). This can know be understood, as docking of PPIase inhibitors (FK506, rapamycin) into the PPIase active site based on previous structures demonstrate that the inhibitors would sterically block the FKBP52 FK1:GR interface (Extended Data Fig. 4e), as previously hypothesized (Riggs et al., 2007; Riggs et al., 2003).

Interface 2 is comprised of the FKBP52 FK2^{Y161} sticking into a shallow hydrophobic pocket formed by GR Helix 3 and the Helix 11-12 loop (GR^{M565,T561,E748}) and a hydrogen bond between the FKBP52 backbone and GR^{E748} (approximately 125 Å^2 BSA) (Fig. 2c). Supporting this interaction, we show that the FKBP52^{Y161D} mutation significantly reduces FKBP52-dependent GR potentiation *in vivo* (Fig. 2e). In interface 3, the solvent exposed, conserved W259 on the FKBP52 FK2-TPR linker makes electrostatic and hydrophobic interactions with GR Helix 12 (approximately 235 Å^2 BSA) (Fig. 2d), which adopts the canonical agonist-bound position even in the absence of a stabilizing coactivator peptide interaction (Bledsoe et al., 2002) (Extended Data Fig. 3b). We show that the corresponding FKBP52^{W259D} mutation significantly reduces FKBP52-dependent GR potentiation *in vivo*, demonstrating the functional importance of this single residue (Fig. 2e). Interestingly, FKBP52^{W259} is also conserved in the FKBP-like cochaperone XAP2 and a recent structure reveals XAP2 engages with an Hsp90-client using this same conserved residue interaction, suggesting this residue is critical more broadly for FKBP cochaperone:client engagement. At interface 3, FKBP52^{K254,E257,Y302} make further polar

interactions between the FK2-TPR linker and GR Helix 12 (Fig. 2d). While a significant portion of the GR AF2 co-activator binding site is available in the FKBP52-bound GR, the N-terminus of a co-activator peptide would sterically clash with the FKBP52 TPR based on the GR:NCoA2 structure (Bledsoe et al., 2002) (Extended Data Fig. 5b). In agreement with our finding that single point mutations at each of the three FKBP52:GR interfaces has a significant effect on GR function *in vivo*, the residues at the FKBP52:GR interfaces are conserved across metazoans (Fig. 2f,g).

FKBP52 advances GR to the next stage of maturation

We previously described another GR-chaperone complex, the GR-maturation complex(Noddings et al., 2022), which has important similarities and differences when compared to the GR:Hsp90:FKBP52 complex. Both the GR-maturation complex (GR:Hsp90:p23) and the GR:Hsp90:FKBP52 complex are comprised of a closed Hsp90 dimer and a folded, ligand-bound GR (Fig. 3a). In the GR:Hsp90:FKBP52 complex, GR is rotated by approximately 45° relative to the GR-maturation complex (Fig. 3a). The Hsp90A Src loop, which interacts with GR in the Hsp90 lumen, flips out and stabilizes the rotated GR position by interacting with the GR hydrophobic patch (GR Helices 9/10)(Fig.3b-c). In both complexes, the pre-Helix 1 strand of GR is threaded through the Hsp90 lumen; however, in the GR:Hsp90:FKBP52 complex, GR has translocated through the Hsp90 lumen by two residues, positioning two prolines ($GR^{P522,P526}$) in the hydrophobic pockets in the Hsp90 lumen (Fig. 3d). This translocation positions the GR LBD further from Hsp90, likely allowing enough space for the observed GR rotation and potentially allowing the GR LBD to dimerize, which is on pathway to activation

(Extended Data Fig. 5c). Despite the translocation and rotation of GR, Hsp90 uses the same surfaces to bind GR (Hsp90B amphipathic helical hairpin, Hsp90A Src loop, Hsp90A^{W320}); however, the GR contact surfaces are different.

FKBP52 Competes with p23 for GR:Hsp90 Binding through Allostery

Surprisingly, FKBP52 competes with p23 to bind the GR:Hsp90 complex, although there is no direct steric conflict between FKBP52 and p23 binding (Fig. 3a). During 3D classification on the cryo-EM dataset, GR:Hsp90:p23 complexes were observed at low abundance; however, the GR:Hsp90:FKBP52 complexes showed no apparent p23 density (Extended Data Fig. 2), despite p23 being present at high concentration. Furthermore, FKBP52 was found only associated with the rotated GR position, while the GR position in the p23-containing classes were only consistent with the GR-maturation complex. Thus, FKBP52 appears to specifically bind the rotated GR position, which is not compatible with p23 binding. This is consistent with mass spectrometry studies, demonstrating FKBP52 competes off p23 to form a stable GR:Hsp90:FKBP52 complex (Ebong et al., 2016). In the rotated GR position, the Hsp90A Src loop flips out of the lumen to bind the conserved GR hydrophobic patch, which was previously engaged by the p23 tail-helix (Fig. 3a-c). Thus, p23 and Hsp90 compete for binding to the same GR hydrophobic patch and the rotation of GR dictates the accessibility of the hydrophobic patch to either Hsp90 or p23. FKBP52 stabilizes the rotated position of GR and therefore favors Hsp90 binding to GR over p23 and this in turn leads to p23 dissociation.

FKBP52 Potentiates GR Ligand Binding in vitro

To quantitatively assess the functional significance of FKBP52 on GR activation, we added FKBP52 to the *in vitro* reconstituted GR-chaperone cycle, using the extended GR construct (residues 418-777) and monitored GR ligand binding, as previously described (Kirschke et al., 2014; Noddings et al., 2022). Addition of FKBP52 resulted in the enhancement of GR ligand binding above the already enhanced GR + chaperones control reaction at equilibrium (Fig. 3e), strongly suggesting FKBP52 increases the GR ligand binding affinity, consistent with reports *in vivo* (Riggs et al., 2003). Given that FKBP52 appears to stabilize the folded, ligand-bound GR, we hypothesized that FKBP52 could functionally replace the p23 tail-helix, which we previously found stabilizes the ligand-bound GR (Noddings et al., 2022). As previously described, removal of the p23 tail-helix (p23Δhelix) resulted in a decrease in GR ligand binding activity in the GR-chaperone system; however, addition of FKBP52 to the reaction fully rescued GR ligand binding in the p23Δhelix background (Fig. 3e), suggesting FKBP52 functions in a similar manner to the p23 tail-helix in stabilizing the ligand-bound GR. Additionally, in the p23Δhelix background, FKBP52 potentiated ligand binding to a greater extent than in the wildtype p23 background. We hypothesize that removing the p23 tail-helix alleviates the competition between p23 and FKBP52, allowing p23 to remain bound to the GR:Hsp90:FKBP52 complex. Given that p23 is known to stabilize the closed Hsp90 conformation (Ali et al., 2006; Noddings et al., 2022), the enhanced ligand binding in the p23Δhelix background may be due to stabilization of closed Hsp90 by p23. Interestingly, FKBP52 also affected GR ligand binding independent of Hsp90, with addition of FKBP52 to GR resulting in enhanced ligand binding, likely due to an

Hsp90-independent chaperoning effect (Bose et al., 1996; Pirkl & Buchner, 2001) (Extended Data Fig. 5d).

FKBP52 Functionally Replaces p23 in vitro when Hsp90 Closure is Stabilized

Given that FKBP52 can functionally replace the p23 tail-helix, we wondered whether FKBP52 could also functionally replace p23 altogether. p23 is known to stabilize Hsp90 NTD closure through the globular p23 domain (Ali et al., 2006; Noddings et al., 2022) in addition to stabilizing the ligand-bound GR through the p23 tail-helix. Omitting p23 from the GR-chaperone cycle drastically reduces GR ligand binding, as previously described (Kirschke et al., 2014; Noddings et al., 2022). The addition of FKBP52 in place of p23 results in a modest increase in ligand binding, but does not fully rescue ligand binding activity (Fig. 3f). We reasoned this could be due to the inability of FKBP52 to sufficiently stabilize closure of the Hsp90 NTDs. Therefore, we added molybdate to these reactions, which stabilizes NTD closure by acting as a γ-phosphate analogue in the Hsp90 NTD ATP-binding site (Noddings et al., 2022; Verba et al., 2016). Addition of molybdate to the reaction lacking p23 resulted in a small increase in GR ligand binding, but did not fully rescue ligand binding activity. However, addition of molybdate to the reactions containing FKBP52 without p23, resulted in a full reactivation of ligand binding and even potentiated ligand binding over the control GR + chaperones reaction (Fig. 3f). Thus, FKBP52 is able to functionally replace p23 if Hsp90 NTD closure is stabilized. Taken together, these results suggest FKBP52 can stabilize the ligand-bound GR, like p23, but cannot stabilize the closed Hsp90 NTD

conformation, which requires p23.

GR:Hsp90:FKBP51 Structure Determination

In vivo the interplay between FKBP52 and the highly similar FKBP51 have profound implications on GR activity. FKBP51 is functionally antagonistic to FKBP52-dependent potentiation of GR *in vivo,* thus the relative ratios of FKBP51 and FKBP52 dictate GR activity levels (Davies et al., 2005). In order to understand mechanistically how FKBP51 antagonizes FKBP52, we prepared the GR:Hsp90:FKBP51 complex in the same manner as the GR:Hsp90:FKBP52 complex (Extended Data Fig. 1c-e). We obtained a 3.29 Å cryo-EM reconstruction of GR:Hsp90:FKBP51 using RELION and CryoSparc with atomic models built using Rosetta (Fig. 4a,b, Extended Data Fig. 6). Somewhat surprisingly, the FKBP51-containing structure appears nearly identical to the FKBP52-containing structure. The GR:Hsp90:FKBP51 structure reveals a fully closed, nucleotide bound Hsp90 dimer complexed with a single GR and a single FKBP51, which occupy the same side of Hsp90 (Fig. 4a,b, Extended Data Fig. 7a). FKBP51 binds to the closed Hsp90 CTD interface in an analogous manner to the FKBP52:Hsp90 interface, including the Helix 7e break at the Hsp90 CTD interface and the Hsp90B MEEVD peptide binding to the FKBP52 TPR domain (Fig. 4b, Extended Data Fig. 7b-d). The GR:Hsp90 interfaces are nearly identical when comparing the FKBP51 and FKBP52-containing complexes, including the Hsp90 Src loop:GR hydrophobic patch interface and the Hsp90 lumen:GR pre-Helix 1 strand interface (Fig. 4b, Extended Data Fig. 7e-g). FKBP51 also binds GR in an analogous manner to the FKBP52:GR interaction (Fig. 4c-e). FKBP51 binds a folded, ligand-bound, and rotated GR using the

same three major interfaces (1) FKBP51 FK1:GR, (2) FKBP51 FK2:GR Helix 3, and (3) FKBP51 FK2-TPR linker:GR Helix 12. The GR:FKBP52 interaction residues are largely conserved for GR:FKBP51 (Fig. 2f). As with the FKBP52-containing structure, no GR prolines appear to be isomerized and PPIase inhibitors would likely block the FKBP51 FK1:GR interface (Extended Data Fig. 7h). Furthermore, the FKBP51 FK1 domain and FK1 proline-rich loop are highly dynamic, as revealed by CryoSparc 3D variability analysis, analogous to the FKBP52-containing structure (Supplemental Movie 3). However, in the GR:Hsp90:FKBP51 consensus map and corresponding atomic model, the FK1 domain contacts GR at a different angle relative to the GR:Hsp90:FKBP52 model; thus, the FK1:GR interface is distinct between the two complexes, specifically at the functionally important, but divergent, residue 119 in the proline-rich loop ($FKBP51^{L119}$, $FKBP52^{P119}$) (Fig. 2b, 3c) (Riggs et al., 2007), which we investigated further below.

Functional Difference Between FKBP51 and FKBP52 Depends on Residue 119

To quantitatively assess the functional effect of FKBP51 on GR *in vitro*, we added FKBP51 to the GR-chaperone cycle and measured ligand binding activity. FKBP51 had no effect on the GR equilibrium value, unlike FKBP52, which potentiates GR ligand binding (Extended Data Fig. 8a). However, we found FKBP51 can functionally replace the p23 tail-helix or p23 (if molybdate is added), just as we observed with FKBP52 (Fig. 4f, Extended Data Fig. 8b). However, FKBP51 does not potentiate GR ligand binding in any of these conditions, unlike FKBP52.

The residues responsible for the functional difference between FKBP51 and FKBP52 *in vivo* has been suggested to come from the proline-rich loop on the FK1 domain, specifically the divergent residue 119 ($FKBP51^{L119}$, $FKBP52^{P119}$) (Riggs et al., 2007). To assess whether this residue is responsible for the functional difference between FKBP51 and FKBP52 *in vitro*, we swapped residue 119 in FKBP51 and FKBP52 and added these mutants (FKBP51 L119P, FKBP52 P119L) to the *in vitro* reconstituted GR-chaperone cycle. We then measured ligand binding activity in the p23∆helix background, where the largest potentiation due to FKBP52 is observed. Surprisingly, the residue 119 swapped mutants almost fully reversed the FKBP51/52 effects on GR—FKBP51 L119P potentiated GR ligand binding over the GR + chaperones control reaction, while FKBP52 P119L showed significantly less potentiation of ligand binding compared to wildtype FKBP52 (Fig. 4f). These results are consistent with the effects of the FKBP51/52 residue 119 swapped mutants *in vivo* (Riggs et al., 2007). Thus, residue 119 on the proline-rich loop provides a critical function difference between the activities of FKBP51 and FKBP52 toward GR *in vitro* and *in vivo*.

Discussion

We present the first structures of the FKBP51 and FKBP52 cochaperones bound to an Hsp90 client complex. The 2.96 Å GR:Hsp90:FKBP52 structure reveals that FKBP52 directly and extensively binds the client, stabilizing the folded, ligand-bound conformation of GR. We show for the first time, that FKBP52 enhances GR ligand binding *in vitro*, consistent with *in vivo* reports, and that each of the three GR:FKBP52

interfaces is critical for FKBP52-dependent potentiation *in vivo*. We also provide a 3.29 Å GR:Hsp90:FKBP51 structure, demonstrating FKBP51 binds to the GR:Hsp90 in a similar manner to FKBP52. The FKBP51 interaction with closed Hsp90 is distinct from a previous NMR model (Oroz et al., 2018), but consistent with a recent cryo-EM structure demonstrating FKBP51 binds closed Hsp90 (Lee et al., 2021). Thus, these structures provide a molecular explanation for the functional antagonism between these two cochaperones.

Surprisingly, we show FKBP51 and FKBP52 compete with p23 to bind the GR:Hsp90 complex through an allosteric mechanism. Previous reports showed FKBP51 and p23 could simultaneously bind the closed Hsp90 in the absence of client (Lee et al., 2021). We demonstrate that the position of the client can dictate which cochaperone is bound, with the FKBPs and p23 binding to distinct GR positions. FKBP51 and FKBP52 both stabilize a rotated position of GR relative to the GR-maturation complex. One functional consequence of this rotated position may be to promote GR dimerization, which is a required step in GR activation. The rotated GR position relieves this steric hindrance to dimerization in the GR-maturation complex and would allow the GR LBD to dimerize once FKBP51/52 release (Extended Data Fig. 5c). Indeed, a previous report has suggested FKBP51/52 promote AR dimerization *in* vivo (Maeda et al., 2022), raising the possibility that the FKBPs promote this next step in SHR maturation.

Our structures also contribute to an emerging theme in which Hsp90 cochaperones bind to distinct Hsp90 conformations, while simultaneously binding to specific client conformations (Gruszczyk et al., 2022; Jaime-Garza et al., 2022; Noddings et al., 2022; Verba et al., 2016; Wang et al., 2022). FKBP51 and FKBP52

each wrap around the folded, ligand-bound client using all three FKBP domains, while FKBP Helix 7e binds the closed Hsp90 conformation. The Helix 7e is found in many TPR-containing cochaperones (Lee et al., 2021), however, our structures, along with others, reveal Helix 7e can bind Hsp90 in distinct positions due to sequence divergence of H7e at the Hsp90 binding site (Gruszczyk et al., 2022; Jaime-Garza et al., 2022).

While FKBP51 binds similarly to FKBP52, competing with p23 and stabilizing the rotated GR, we find that FKBP51 does not significantly enhance GR ligand binding *in vitro*, like FKBP52, consistent with *in vivo* reports (Denny et al., 2000; Riggs et al., 2003). Interestingly, we find residue 119 on FKBP51/52 is critical for enhancement of ligand binding *in vitro*, also consistent with *in vivo* reports (Riggs et al., 2007). NMR studies have found the proline at residue 119 on FKBP52 decreases dynamics of the proline-rich loop (also called 80S loop or β4-β5 loop) relative to the leucine at FKBP51 (Mustafi et al., 2014). Analysis of dynamics of our structures using 3D variability analysis demonstrates that the proline-rich loop is highly dynamic in its interaction with GR. Thus, the dynamics of this loop may dictate the specificity and/or stability of this interaction, leading to distinct regulation of GR activity.

Many models have been proposed for FKBP51/52 regulation of GR. Here, we show that FKBP51/52 do not alter the GR conformation by isomerizing prolines or engaging with the GR NLS1 (nuclear localization signal 1) ($GR^{467-505}$) (Savory et al., 1999) to directly regulate GR translocation, as previously hypothesized (Pratt et al., 2004; Rein, 2020; Sivils et al., 2011; Smith & Toft, 2008). Instead, the FKBPs bind the folded, ligand-bound GR and compete with p23 through GR sliding and rotation on Hsp90. We propose additional steps in the GR-chaperone cycle that account for

FKBP51/52 incorporation and subsequent regulation of GR activity in the cell (Fig. 5). Once the folded, ligand-bound GR reaches the GR maturation complex, either FKBP51 or FKBP52 can bind, competing with p23. The p23 and FKBP51/52 complexes are likely in a dynamic equilibrium, given that each of these complexes appear to be in the same Hsp90 nucleotide state and conformation; however, our data suggest that FKBP51/52 outcompete p23, advancing GR to the next state of its maturation. FKBP52 binds and stabilizes the ligand-bound GR, resulting in enhanced ligand affinity, and connects the active GR to dynein for translocation to the nucleus, releasing GR from the chaperone cycle(Galigniana et al., 2010; Galigniana et al., 2001; Tatro et al., 2009; Wochnik et al., 2005). FKBP51 in contrast binds the folded GR, either in the ligand-bound or apo forms (Davies et al., 2002) and sequesters GR in the cytosol until GR release from Hsp90 upon ATP hydrolysis. Interestingly, the expression of FKBP51 is upregulated by GR (as well as PR and AR), leading to a short negative feedback loop (Baughman et al., 1997; Cheung & Smith, 2000; Denny et al., 2000; Jaaskelainen et al., 2011; Zannas & Binder, 2014; Zannas et al., 2016). The relative concentrations of FKBP51 and FKBP52 dictate the equilibrium between GR:Hsp90:FKBP51 and GR:Hsp90:FKBP52 complexes, resulting in alterations to GR activity levels *in vivo* (Reynolds et al., 1999). Beyond GR, FKBP51/52 are known to regulate the entire SHR class and given the sequence and structural conservation of the SHR LBDs at the FKBP51/FKBP52 contact sites, we propose FKBP51 and FKBP52 engage with the rest of the SHRs in a similar manner to GR (Extended Data Fig. 9a,b). Thus, FKBP51/52 can fine-tune the activity of these critical and clinically important signaling molecules and allow for crosstalk between the hormone signaling pathways. Altogether, we demonstrate how Hsp90 provides a

platform for the FKBP cochaperones to engage Hsp90 clients after Hsp90-dependent folding and promote the next step of client maturation, providing a critical layer of functional regulation.

Author Contributions

C.M.N. designed and executed biochemical experiments, cryo-EM sample preparation, data collection, data processing, and model building. J.L.J. executed yeast *in vivo* assays and interpreted the results. C.M.N. and D.A.A. conceived the project, interpreted the results, and wrote the manuscript.

Acknowledgements

We thank members of the Agard Lab, past and present, including Ray Wang, for suggestion of this project, and Elaine Kirschke, for helpful discussions. We thank members of the José-Maria Carazo lab for continuous flexibility analysis on the cryo-EM datasets. We thank Jason Gestwicki for noting the potential importance of different phosphorylation on the FKBPs. We thank David Bulkley, Glenn Gilbert, Zanlin Yu, and Eric Tse from the W.M. Keck Foundation Advanced Microscopy Laboratory at the University of California, San Francisco (UCSF) for EM facility maintenance and help with data collection. We also thank Matt Harrington and Joshua Baker-LePain for computational support with the UCSF Wynton cluster. C.M.N. is a National Cancer Institute Ruth L. Kirschstein Predoctoral Individual NRSA Fellow. The work was supported by funding from Howard Hughes Medical Institute (D.A.A.) and NIH grants R35GM118099 (D.A.A.), S10OD020054 (D.A.A.), S10OD021741 (D.A.A.), P20GM104420 (J.L.J.), and R01GM127675 (J.L.J.).

Figures

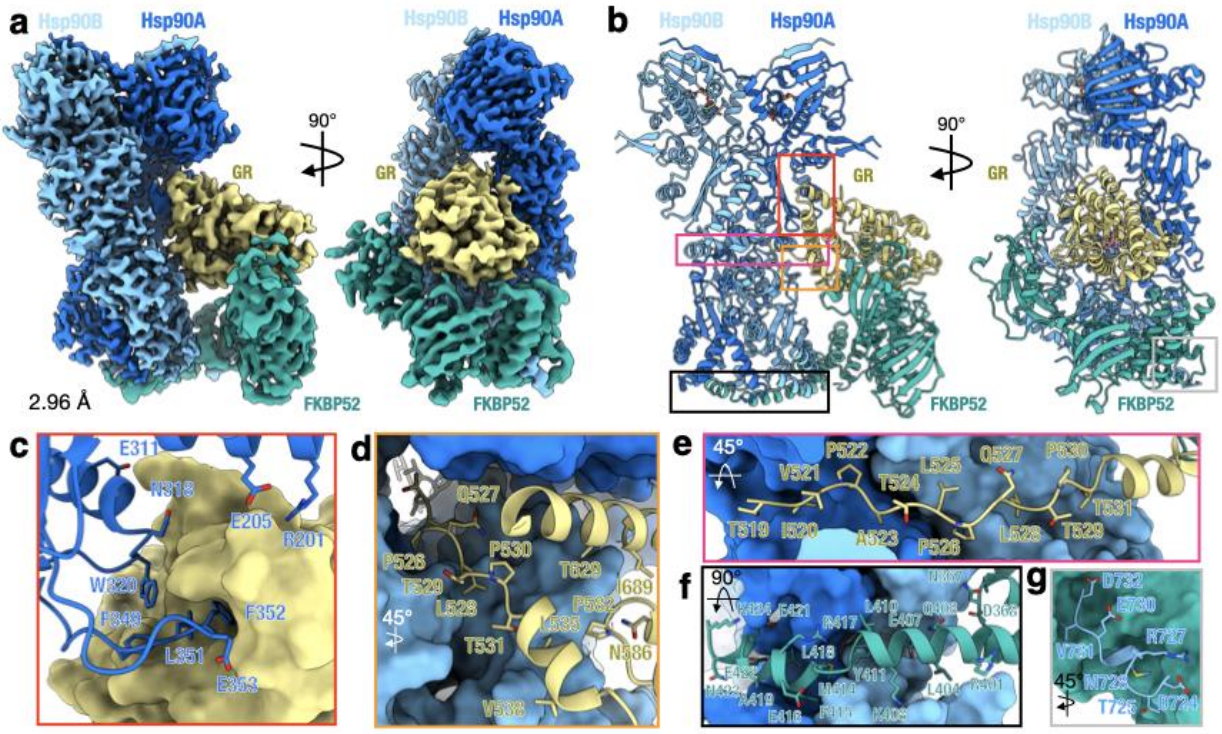

Fig. 4.1: Architecture of the GR:Hsp90:FKBP52 complex
a, Composite cryo-EM map of the GR:Hsp90:FKBP52 complex. Hsp90A (dark blue), Hsp90B (light blue), GR (yellow), FKBP52 (teal). Color scheme is maintained throughout. **b**, Atomic model in cartoon representation with boxes corresponding by color to the interfaces shown in detail in b-g. **c**, Interface 1 of the Hsp90:GR interaction, depicting the Hsp90A Src loop ($Hsp90A^{345-360}$) interacting with the GR hydrophobic patch. GR is in surface representation. **d**, Interface 2 of the Hsp90:GR interaction, depicting $GR_{Helix\ 1}$ ($GR^{532-539}$) packing against the entrance to the Hsp90 lumen. Hsp90A/B are in surface representation. **e**, Interface 3 of the Hsp90:GR interaction, depicting $GR_{pre\text{-}Helix\ 1}$ ($GR^{519-531}$) threading through the Hsp90 lumen. Hsp90A/B are in surface representation. **f**, Interface 1 of the Hsp90:FKBP52 interaction, depicting FKBP52 TPR H7e ($FKBP52^{387-424}$) interacting with the Hsp90A/B CTD dimer interface. Hsp90A/B are in surface representation. **g**, Interface 2 of the Hsp90:FKBP52 interaction, depicting the Hsp90B MEEVD motif ($Hsp90B^{700-706}$) binding in the helical bundle of the FKBP52 TPR domain. FKBP52 is in surface representation.

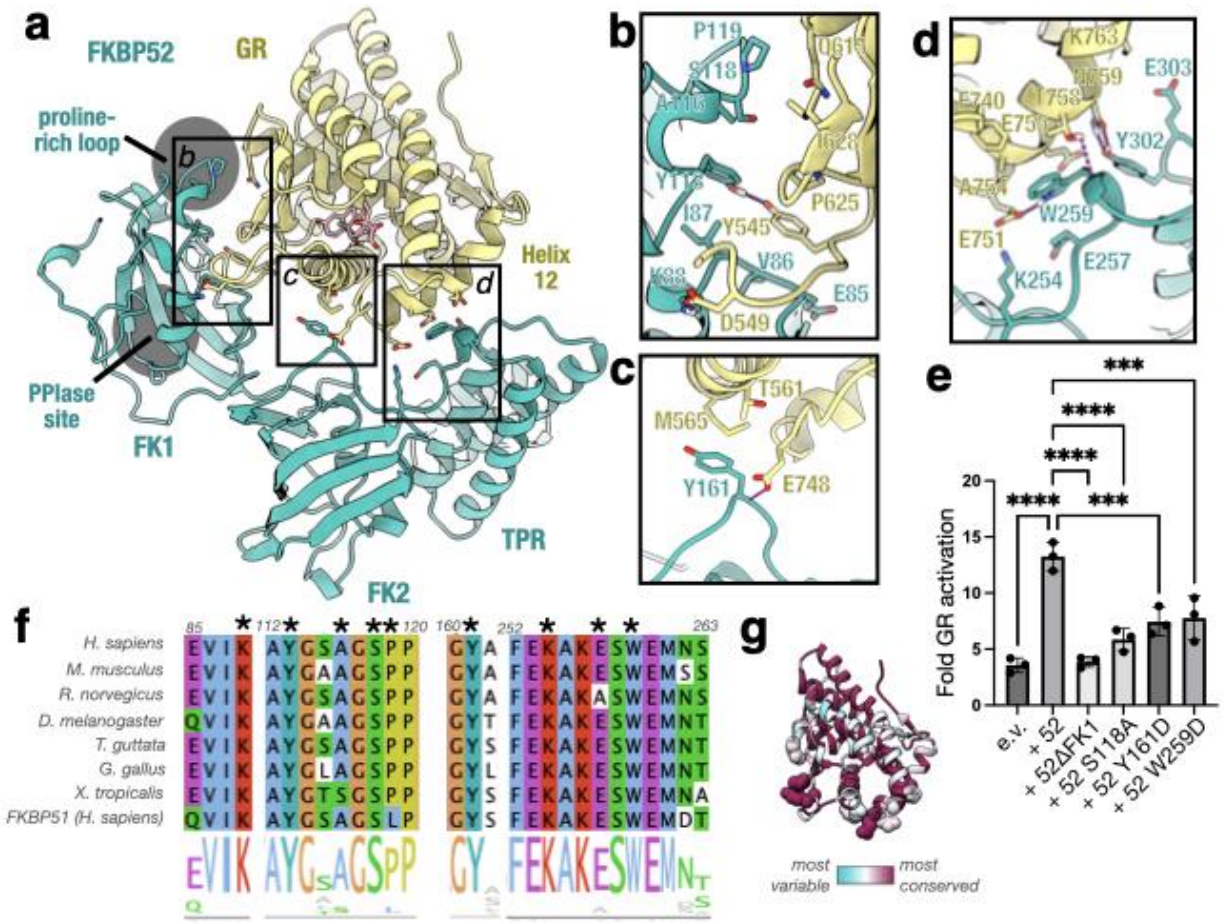
a
FKBP52
GR
proline-rich loop
b
c
d
Helix 12
PPIase site
FK1
FK2
TPR
b
P119
S118
Q615
A116
T628
Y114
P625
I87
Y545
V86
E85
D549
c
T561
M565
Y161
E748
d
K763
E759
E303
E740
I758
E751
Y302
A754
W259
E751
E257
K254
e
***
****
****
****
***
Fold GR activation
20
15
10
5
0
e.v.
+ 52
+ 52ΔFK1
+ 52 S118A
+ 52 Y161D
+ 52 W259D
f
H. sapiens
M. musculus
R. norvegicus
D. melanogaster
T. guttata
G. gallus
X. tropicalis
FKBP51 (H. sapiens)
85
112
120
160
252
263
g
most variable
most conserved

Fig. 4.2: The GR:FKBP52 interaction and functional significance
a, Atomic model depicting the three interfaces between GR (yellow) and FKBP52 (teal) in the GR:Hsp90:FKBP52 complex. The FKBP52 proline-rich loop and PPIase site catalytic site are highlighted in gray. **b**, Interface 1 between GR (yellow) and the FKBP52 FK1 domain (teal), showing interacting side chains and hydrogen bonds (dashed pink lines). **c**, Interface 2 between GR (yellow) and the FKBP52 FK2 domain (teal), showing interacting side chains and hydrogen bonds (dashed pink lines). **d**, Interface 3 between GR (yellow) and the FKBP52 FK2-TPR linker (teal), showing interacting side chains and hydrogen bonds (dashed pink lines). **e**, GR activation assay in wild-type yeast strain JJ762 expressing FKBP52 ("52") or FKBP52 mutants. The fold increase in GR activities compared to the empty vector (e.v.) control are shown (mean±SD). n=3 biologically independent samples per condition. Significance was evaluated using a one-way ANOVA ($F_{(6,14)} = 67.82$; $p < 0.0001$) with *post-hoc* Dunnett's multiple comparisons test (n.s. $P \geq 0.05$; * $P \leq 0.05$; ** $P \leq 0.01$; *** $P \leq 0.001$). See Methods for p-values. **f**, Sequence alignment of eukaryotic FKBP52 showing conservation residues involved in the GR:FKBP52 interaction (denoted by a black asterisk). The bottom aligned sequence is human FKBP51. The alignment is colored according to the ClustalW convention. **g**, GR protein sequence conservation mapped onto the GR atomic model from the GR:Hsp90:FKBP52 complex. Residue conservation is depicted from most variable (cyan) to most conserved residues (maroon).

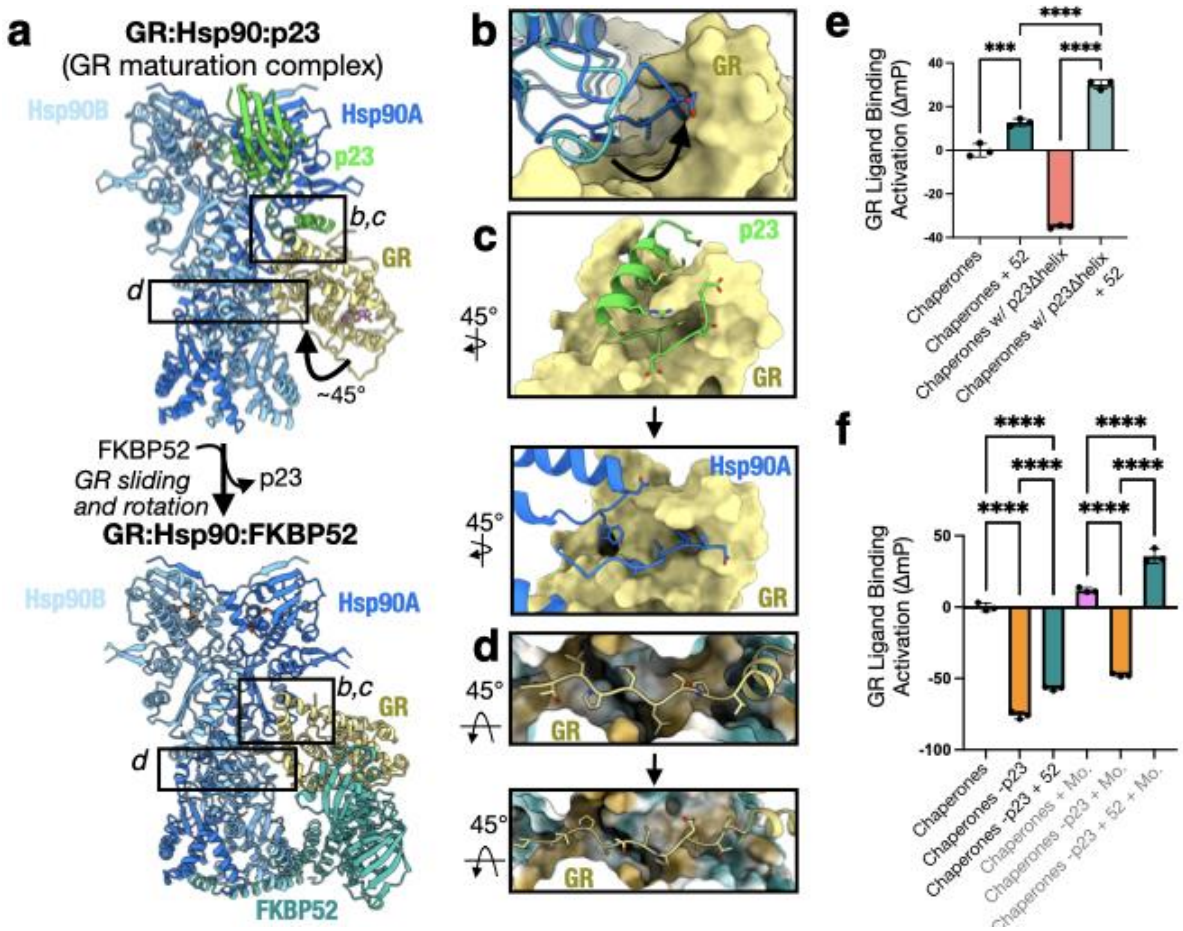
a
GR:Hsp90:p23
(GR maturation complex)
Hsp90B
Hsp90A
p23
b,c
GR
d
~45°
FKBP52
GR sliding
and rotation
p23
GR:Hsp90:FKBP52
Hsp90B
Hsp90A
b,c
GR
d
FKBP52
b
GR
c
p23
45°
GR
Hsp90A
45°
GR
d
45°
GR
45°
GR
e
GR Ligand Binding
Activation (ΔmP)
***
****
****
40
20
0
-20
-40
Chaperones
Chaperones + 52
Chaperones w/ p23Δhelix
Chaperones w/ p23Δhelix
+ 52
f
GR Ligand Binding
Activation (ΔmP)
****
****
****
****
****
****
50
0
-50
-100
Chaperones
Chaperones -p23
Chaperones -p23 + 52
Chaperones + Mo.
Chaperones -p23 + Mo.
Chaperones -p23 + 52 + Mo.

Fig. 4.3: FKBP52 competes with p23 to bind GR:Hsp90
a, Atomic model of the GR-maturation complex (above) and the GR:Hsp90:FKBP52 complex (below) in cartoon representation with boxes corresponding to the interfaces shown in detail in b-d. FKBP52 competes off p23 and re-positions GR in an approximately 45° rotated position. Hsp90A (dark blue), Hsp90B (light blue), GR (yellow), p23 (green), FKBP52 (teal). **b**, Position of the Hsp90A Src loop in the GR-maturation complex (Hsp90A, cyan) versus the GR:Hsp90:FKBP52 complex (Hsp90A, dark blue). The Hsp90A Src loop flips up in the GR:Hsp90:FKBP52 complex to interact with the hydrophobic patch on the rotated GR (yellow, surface representation). Hsp90A Src loop residues interacting with the GR hydrophobic patch are shown. **c**, Interface between the p23 tail-helix (green) and the GR hydrophobic patch (yellow, surface representation) in the GR-maturation complex (top). The p23 tail-helix is replaced by the Hsp90A Src loop (dark blue) in the GR:Hsp90:FKBP52 complex (bottom), which flip up to interact with the GR hydrophobic patch (yellow, surface representation). Interacting side chains are shown. **d**, Interaction between the $GR_{pre\text{-}Helix\ 1}$ ($GR^{523\text{-}531}$) threading through the Hsp90 lumen in the GR-maturation complex (top) versus the $GR_{pre\text{-}Helix\ 1}$ ($GR^{519\text{-}531}$) threading through the Hsp90 lumen in the GR:Hsp90:FKBP52 complex (bottom). Hsp90A/B are in surface representation colored by hydrophobicity. The $GR_{pre\text{-}Helix\ 1}$ region translocates through the Hsp90 lumen by 2 residues in the transition from the GR-maturation complex to the GR:Hsp90:FKBP52 complex. Two hydrophobic residues on $GR_{pre\text{-}Helix\ 1}$ ($GR^{L525,L528}$ or $GR^{P522,P526}$) remain bound in the Hsp90 lumen hydrophobic pockets in both complexes. **e**, Equilibrium binding of 10nM fluorescent dexamethasone to 100nM GR with chaperones, FKBP52 (“52”), and mutants. “Chaperones”= 15uM Hsp70, Hsp90, Hop, and p23 or p23Δhelix, 2uM Ydj1 and Bag-1. Significance was evaluated using a one-way ANOVA ($F_{(3,8)}$ = 541.2; $p < 0.0001$) with *post-hoc* Šídák’s test (n.s. $P \geq 0.05$; * $P \leq 0.05$; ** $P \leq 0.01$; *** $P \leq 0.001$; **** $P \leq 0.0001$). See Methods for p-values. **f**, Equilibrium binding of 10nM fluorescent dexamethasone to 100nM GR with chaperones and FKBP52 (“52”). “Chaperones”= 15uM Hsp70, Hsp90, Hop, and p23 or p23Δhelix, 2uM Ydj1 and Bag-1. Significance was evaluated using a one-way ANOVA ($F_{(5,12)}$ = 761.5; $p < 0.0001$) with *post-hoc* Šídák’s test (n.s. $P \geq 0.05$; * $P \leq 0.05$; ** $P \leq 0.01$; *** $P \leq 0.001$; **** $P \leq 0.0001$). P-values < 0.0001 for each comparison.

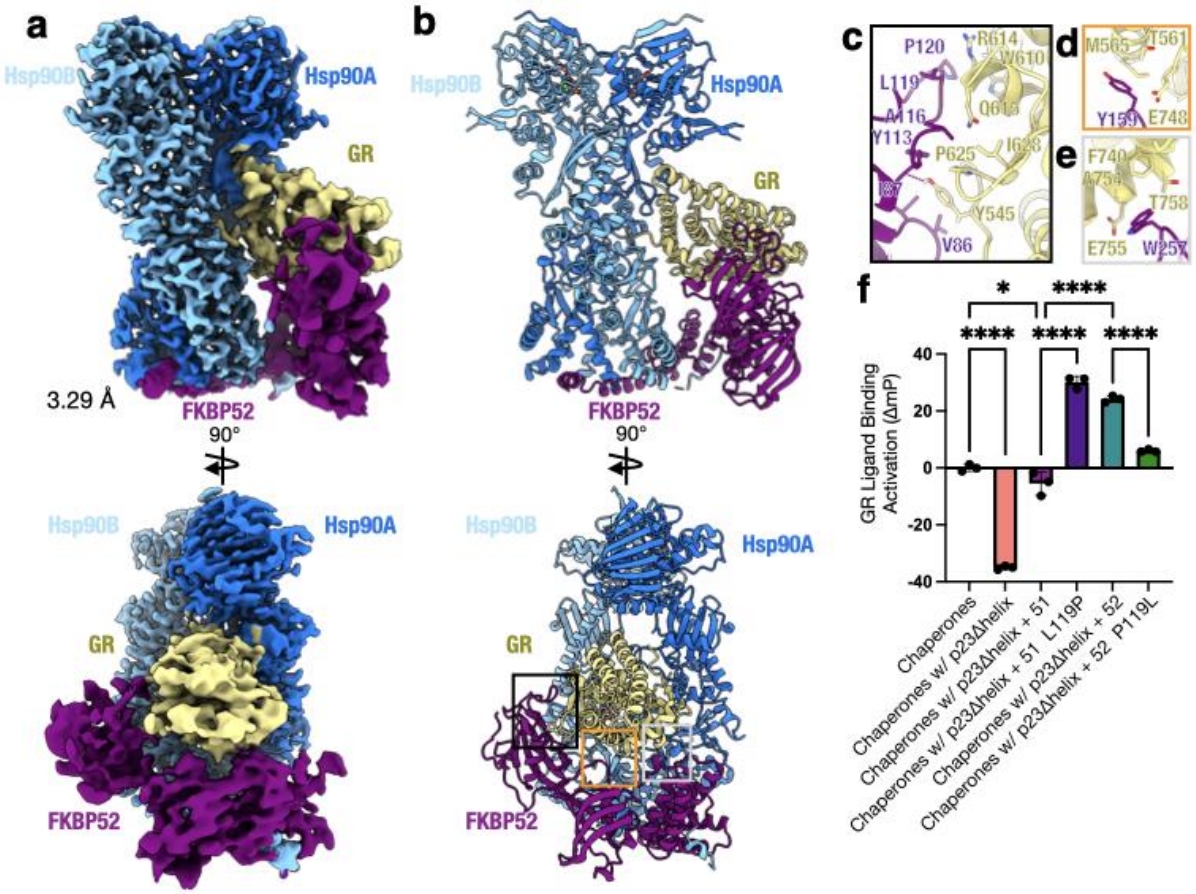

Fig. 4.4: Architecture of the GR:Hsp90:FKBP51 complex
a, Composite cryo-EM map of the GR:Hsp90:FKBP51 complex. Hsp90A (dark blue), Hsp90B (light blue), GR (yellow), FKBP51 (purple). Color scheme is maintained throughout. **b**, Atomic model in cartoon representation with boxes corresponding by color to the interfaces shown in detail in c-e. **c**, Interface 1 between GR (yellow) and the FKBP51 FK1 domain (purple), showing interacting side chains and hydrogen bonds (dashed pink lines). **d**, Interface 2 between GR (yellow) and the FKBP51 FK2 domain (purple), showing interacting side chains and hydrogen bonds (dashed pink lines). **e**, Interface 3 between GR (yellow) and the FKBP51 FK2-TPR linker (yellow), showing interacting side chains and hydrogen bonds (dashed pink lines). **f**, Equilibrium binding of 10nM fluorescent dexamethasone to 100nM GR with chaperones, FKBP51 (“51”), FKBP52 (“52”), or mutants. “Chaperones”= 15uM Hsp70, Hsp90, Hop, and p23 or p23Δhelix, 2uM Ydj1 and Bag-1. Significance was evaluated using a one-way ANOVA ($F_{(5,12)}$ = 404.1; $p < 0.0001$) with *post-hoc* Šídák’s test (n.s. $P \geq 0.05$; * $P \leq 0.05$; ** $P \leq 0.01$; *** $P \leq 0.001$; **** $P \leq 0.0001$). See Methods for p-values.

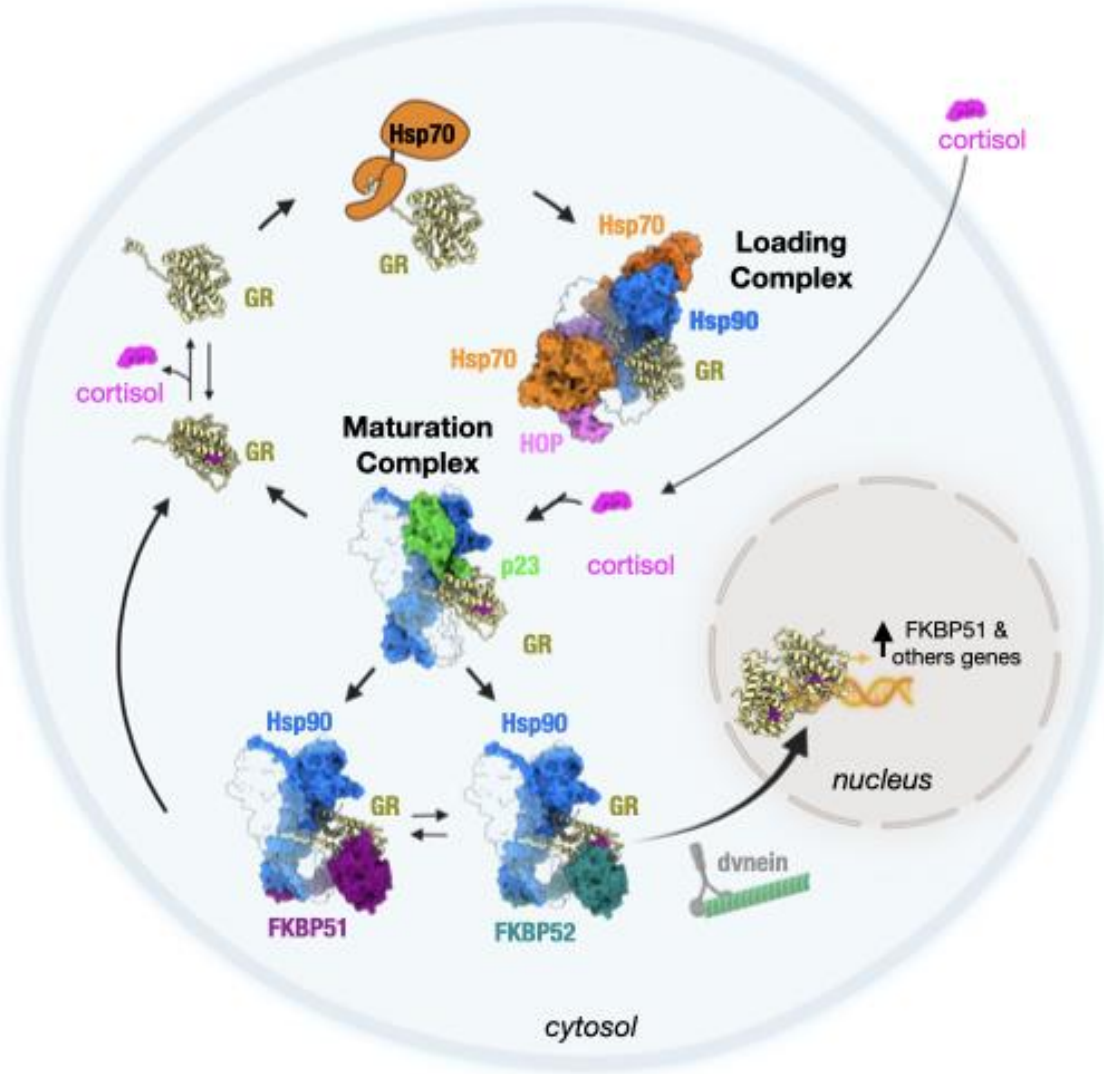
Hsp70
GR
Hsp70
Loading
Complex
Hsp90
Hsp70
GR
HOP
cortisol
GR
cortisol
Maturation
Complex
p23
cortisol
GR
FKBP51 &
others genes
nucleus
Hsp90
Hsp90
GR
GR
dynein
FKBP51
FKBP52
cytosol

Fig. 4.5: Mechanism of GR regulation by FKBP51 and FKBP52 in the GR chaperone cycle

Schematic of the GR chaperone cycle in the cell. Starting on the top left, GR (yellow, cartoon representation) is in dynamic equilibrium between cortisol-bound and unbound (apo) states. Hsp70 (orange) binds GR and locally unfolds GR to inhibit cortisol-binding, stabilizing GR in a partially unfolded, apo state. Hsp70 transfers the partially unfolded GR to Hsp90 (light and dark blue):Hop (pink) to form the GR-loading complex (Wang et al. 2022), in which GR is stabilized in a partially unfolded, apo state with the cortisol-binding pocket accessible. Cortisol (pink), which enters the cell through diffusion, binds to GR during the transition from the GR-loading complex to the GR-maturation complex when Hsp90 refolds the GR to a native conformation, sealing the cortisol-binding pocket through the refolding of the GR Helix 1 region (Noddings et al. 2022). In GR-maturation complex, the cortisol-bound, folded GR is stabilized by Hsp90 and p23 (green), and is protected from Hsp70 re-binding. Depending on the relative concentrations of the FKBPs, either FKBP51 (purple) or FKBP52 (teal) can bind the GR:Hsp90 complex, competing off p23, and stabilizing the rotated position of GR. FKBP51 sequesters GR:Hsp90 in the cytosol until ATP hydrolysis on Hsp90 allows release of GR back to the chaperone cycle. In contrast, FKBP52 promotes rapid nuclear translocation of GR:Hsp90 by acting as an adapter to the dynein/dynactin motor complex. Once in the nucleus, the cortisol-bound GR can dimerize, nucleate the assembly of transcriptional regulatory complexes, and activate the transcription of thousands of genes, including the gene for FKBP51 (*FKBP5*), leading to a negative feedback loop that regulates GR activity in the cell. The GR chaperone cycle also occurs in the absence of ligand and evidence supports preferential binding of FKBP51 over FKBP52 to apo GR:Hsp90 complexes, insuring the apo (inactivated) GR is not improperly translocated to the nucleus to regulate transcription.

Extended Data Figures and Tables

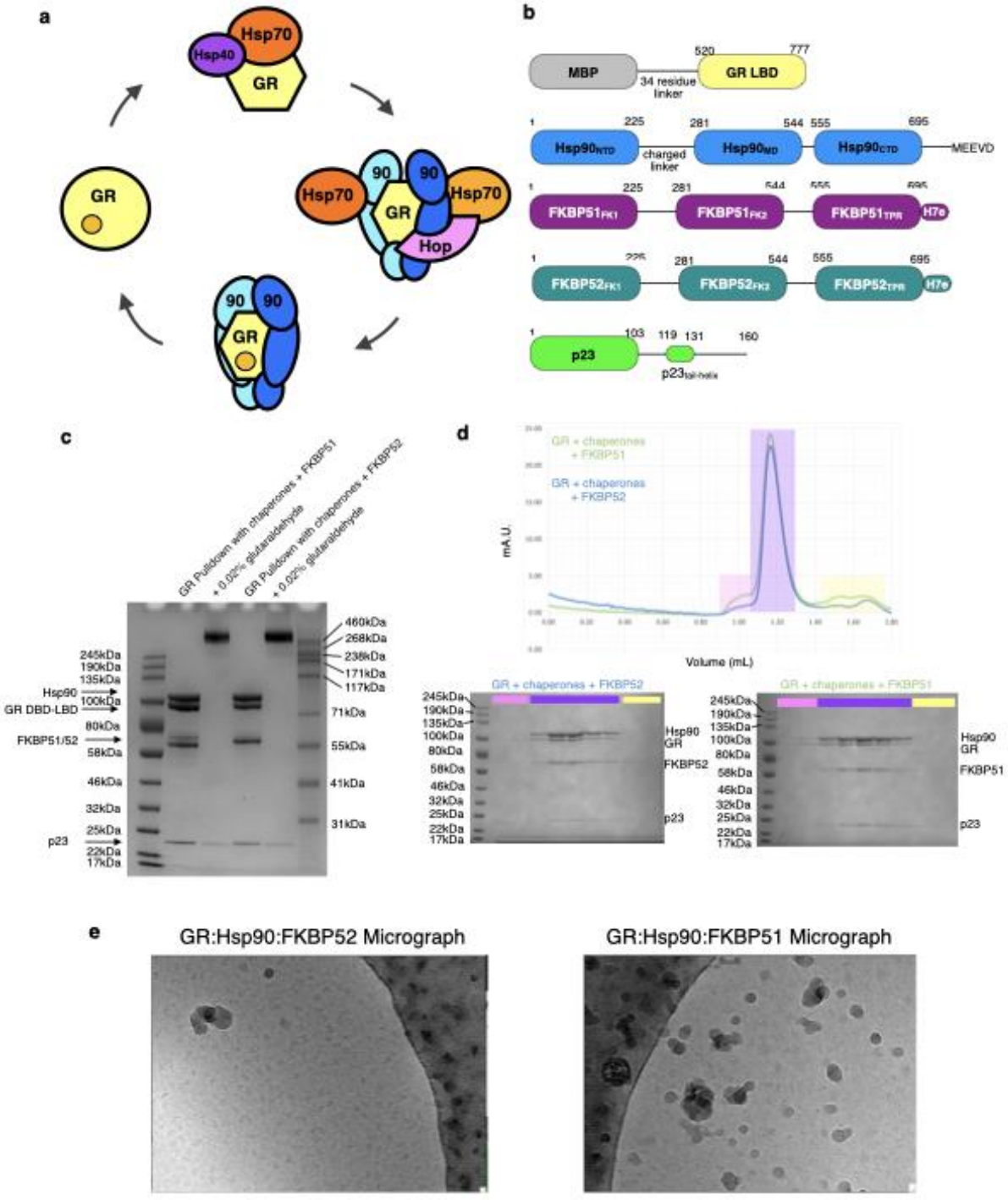

Extended Data Fig. 4.1: Sample preparation of GR:Hsp90:FKBP51 and GR:Hsp90:FKBP52 complexes for cryo-EM

a, The *in vitro* reconstituted GR-chaperone cycle. On the left, GR alone is active and able to bind ligand. Hsp70, aided by the co-chaperone Hsp40, engages GR and inhibits ligand binding. Hsp70 loads GR onto Hsp90 and Hop, which forms the "GR-loading complex". GR is stabilized in an inhibited, partially unfolded conformation by semi-closed Hsp90, Hsp70, and Hop (PDB ID 7KW7). Hsp70 and Hop are released, Hsp90 hydrolyzes ATP to fully close, and the co-chaperone p23 binds, forming the "GR-maturation complex" (PDB ID 7KRJ). GR binds ligand in the transition from the GR-loading complex to the GR-maturation complex. In the maturation complex, GR is in a fully folded, native conformation and bound to ligand. Upon Hsp90 re-opening, GR is released from the complex to return to the cycle. **b,** Domain organization of the proteins in the GR:Hsp90:FKBP complexes as well as p23. **c,** Coomassie-stained SDS-PAGE (4-12% acrylamide gel) with elution from the MBP-GR pulldown from the *in vitro* reconstituted GR chaperone cycle. Lanes 1 and 2 show the elution from the FKBP51-containing sample, while Lanes 3 and 4 show the elution from the FKBP52-containing sample. Assay conditions are as follows- Lane 1: 5 μM MBP-GR, 2 μM Hsp40, 5 μM Hsp70, 5 μM Hop, 15 μM Hsp90, 15 μM Bag-1, 30 μM FKBP51, 5 mM ATP, 20mM Sodium Molybdate; Lane 2: sample from Lane 1 after size exclusion chromatography (**d**) and chemical crosslinking with 0.02% glutaraldehyde; Lane 3: 5 μM MBP-GR, 2 μM Hsp40, 5 μM Hsp70, 5 μM Hop, 15 μM Hsp90, 15 μM Bag-1, 30 μM FKBP52, 5 mM ATP, 20mM Sodium Molybdate; Lane 4: sample from Lane 3 after size exclusion chromatography (**d**) and chemical crosslinking with 0.02% glutaraldehyde. **d,** S200 3.2/300 size exclusion chromatography (SEC) profile of the elution from the MBP-GR pulldown. The green trace represents the SEC profile of the from the reconstituted GR chaperone cycle with FKBP51, while the blue trace represents the SEC profile from the reconstituted GR chaperone cycle with FKBP52. mAU=milli-absorbance units. Coomassie-stained SDS-PAGE (4-12% acrylamide gel) of the fractions from size exclusion chromatography corresponding to the GR:Hsp90:FKBP52 sample (left) or the GR:Hsp90:FKBP51 sample (right). Colors indicate which gel lanes correspond to specific regions of the size exclusion chromatography profile. Sample fractions from the region highlighted in purple were collected and used for cryo-EM data collection. This experiment was repeated 11 independent times with similar results. **e,** Representative electron micrograph for the cryo-EM dataset of the GR:Hsp90:FBKP52 complex (left) (-1.48 μm defocus) and GR:Hsp90:FKBP51 complex (right) (-2.23 μm defocus). A total of 11,162 and 26,413 micrographs were obtained, respectively.

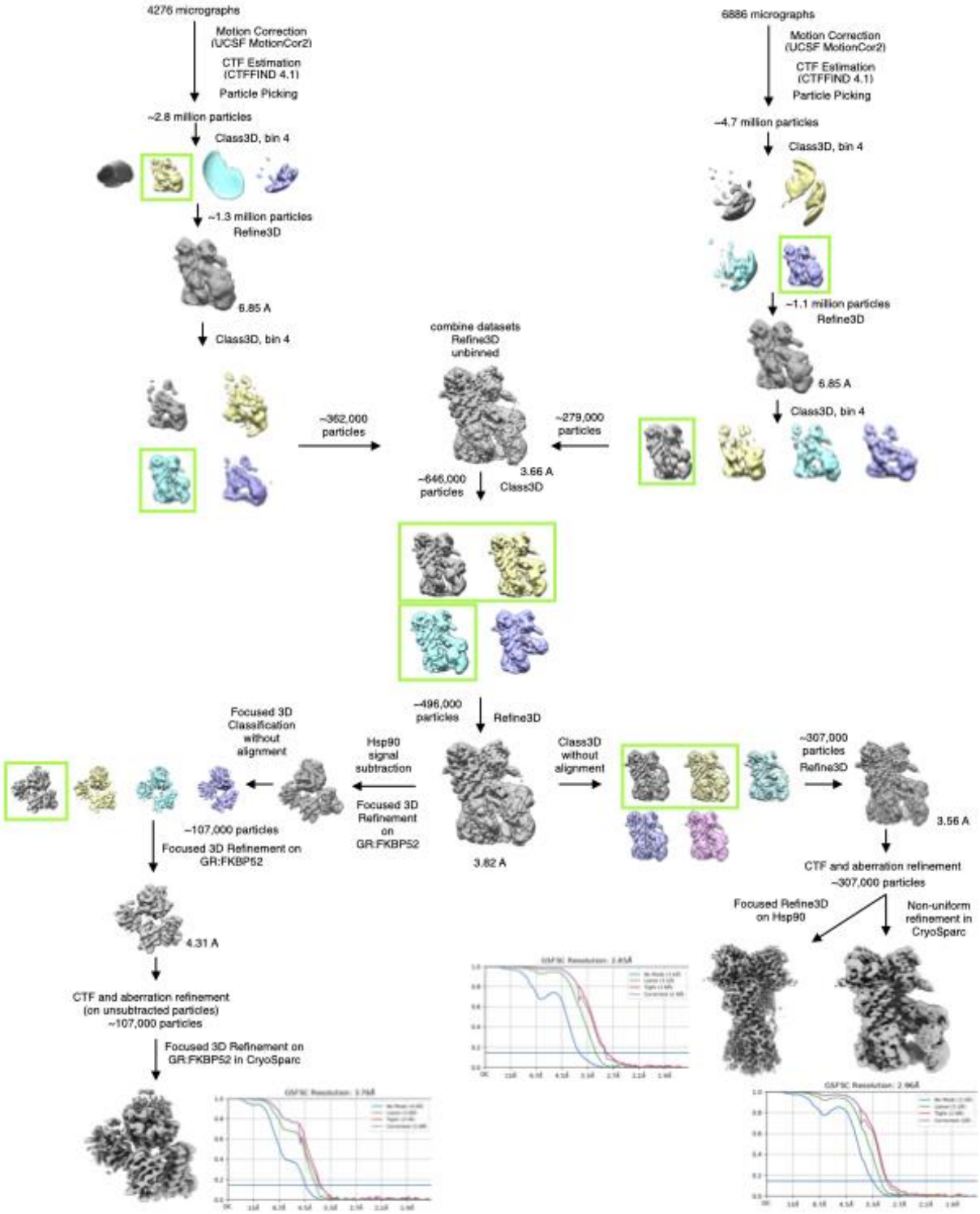
4276 micrographs
Motion Correction (UCSF MotionCor2)
CTF Estimation (CTFFIND 4.1)
Particle Picking
~2.8 million particles
Class3D, bin 4
~1.3 million particles
Refine3D
6.85 A
Class3D, bin 4
6886 micrographs
Motion Correction (UCSF MotionCor2)
CTF Estimation (CTFFIND 4.1)
Particle Picking
~4.7 million particles
Class3D, bin 4
~1.1 million particles
Refine3D
6.85 A
Class3D, bin 4
~362,000 particles
~279,000 particles
combine datasets
Refine3D
unbinned
3.66 A
~646,000 particles
Class3D
~496,000 particles
Refine3D
3.82 A
Class3D without alignment
~307,000 particles
Refine3D
3.56 A
CTF and aberration refinement
~307,000 particles
Focused Refine3D on Hsp90
Non-uniform refinement in CryoSparc
Hsp90 signal subtraction
Focused 3D Refinement on GR:FKBP52
Focused 3D Classification without alignment
~107,000 particles
Focused 3D Refinement on GR:FKBP52
4.31 A
CTF and aberration refinement (on unsubtracted particles)
~107,000 particles
Focused 3D Refinement on GR:FKBP52 in CryoSparc

Extended Data Fig. 4.2: Cryo-EM data analysis for the GR:Hsp90:FKBP52 complex
Cryo-EM data processing procedure for the GR:Hsp90:FKBP52 complex performed in RELION and CryoSparc. Gold-standard Fourier shell correlation (GSFSC) curves of the final 3D reconstructions, including the focused maps and the consensus map, are shown (bottom). The blue lines intercept the y-axis at an FSC value of 0.143.

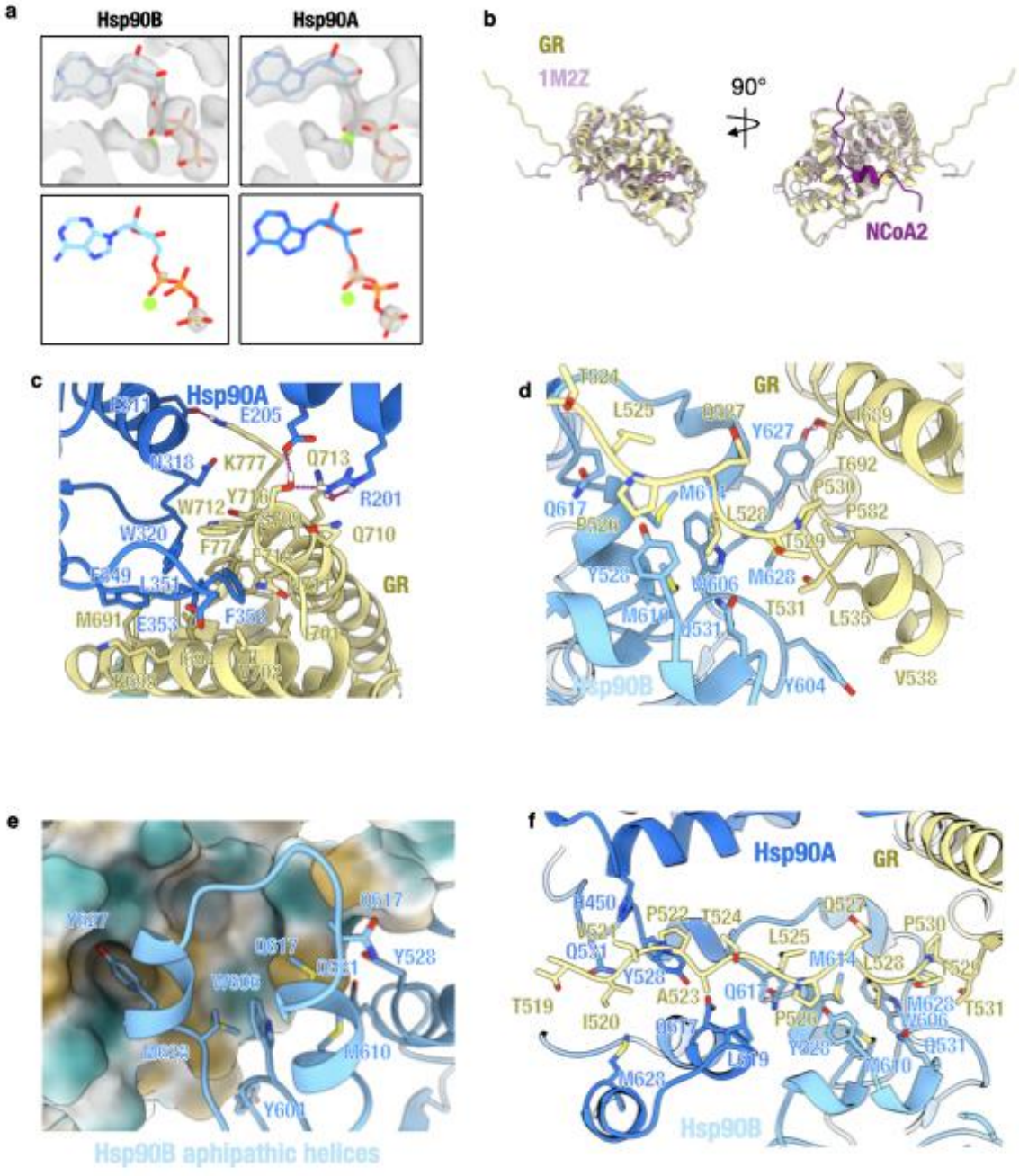
a
Hsp90B
Hsp90A
b
GR
1M2Z
90°
NCoA2
c
Hsp90A
E205
K777
Q713
R201
Q710
GR
M691
E353
d
GR
L525
Y627
T692
P530
Q617
M614
L528
P582
T529
Y528
M628
M606
T531
L535
M610
Q531
Y604
V538
e
Y627
Q617
Y528
M610
Y604
Hsp90B aphipathic helices
f
Hsp90A
GR
P522
T524
L525
P530
Q531
Y528
M614
L528
T519
A523
M628
T531
I520
P520
Y528
M606
Q531
M610
M628
Hsp90B

Extended Data Fig. 4.3: Hsp90:GR interfaces in the GR:Hsp90:FKBP52 structure **a,** Hsp90:GR:FKBP52 complex map density with atomic model showing ATP-magnesium density in both Hsp90 protomers (Hsp90A/B). Bottom images show increased contour level on the map density to indicate that the ATP γ-phosphate position has much stronger density relative to the α and β-phosphates, likely corresponding to molybdate, which may act as a γ-phosphate analog (see **Methods**). **b,** Atomic model of GR from the GR:Hsp90:FKBP52 complex (yellow) compared with GR from the crystal structure (PDB ID 1M2Z) (light pink) with co-activator peptide NCoA2 (purple) and ligand (dark pink). $GR_{Helix\ 12}$ is indicated. **c-f,** Atomic model of GR:Hsp90:FKBP52 complex with Hsp90A (dark blue), Hsp90B (light blue), GR (yellow). Side chains in contact between GR and Hsp90 are shown, along with hydrogen bonds (dashed pink lines).**c,** Interface 1 of the GR:Hsp90 interaction depicting the GR hydrophobic patch (GR Helices 9 and 10) interacting with the Hsp90A Src loop ($Hsp90^{345-360}$), $Hsp90A^{W320}$, and Hsp90A NTD/MD helices. **d,** Interface 2 of the GR:Hsp90 interaction depicting GR pre-Helix 1 strand and Helix 1 packing up against the Hsp90B amphipathic α-helices. **e,** Interface 2 of the GR:Hsp90 interaction depicting GR in surface representation colored by hydrophobicity (green = polar, brown = nonpolar) with $Hsp90B^{Y627}$ sticking into a the BF3 druggable hydrophobic pocket. **f,** Interface 3 of the GR:Hsp90 interaction depicting the GR pre-Helix 1 strand threading through the Hsp90 lumen between Hsp90A and Hsp90B.

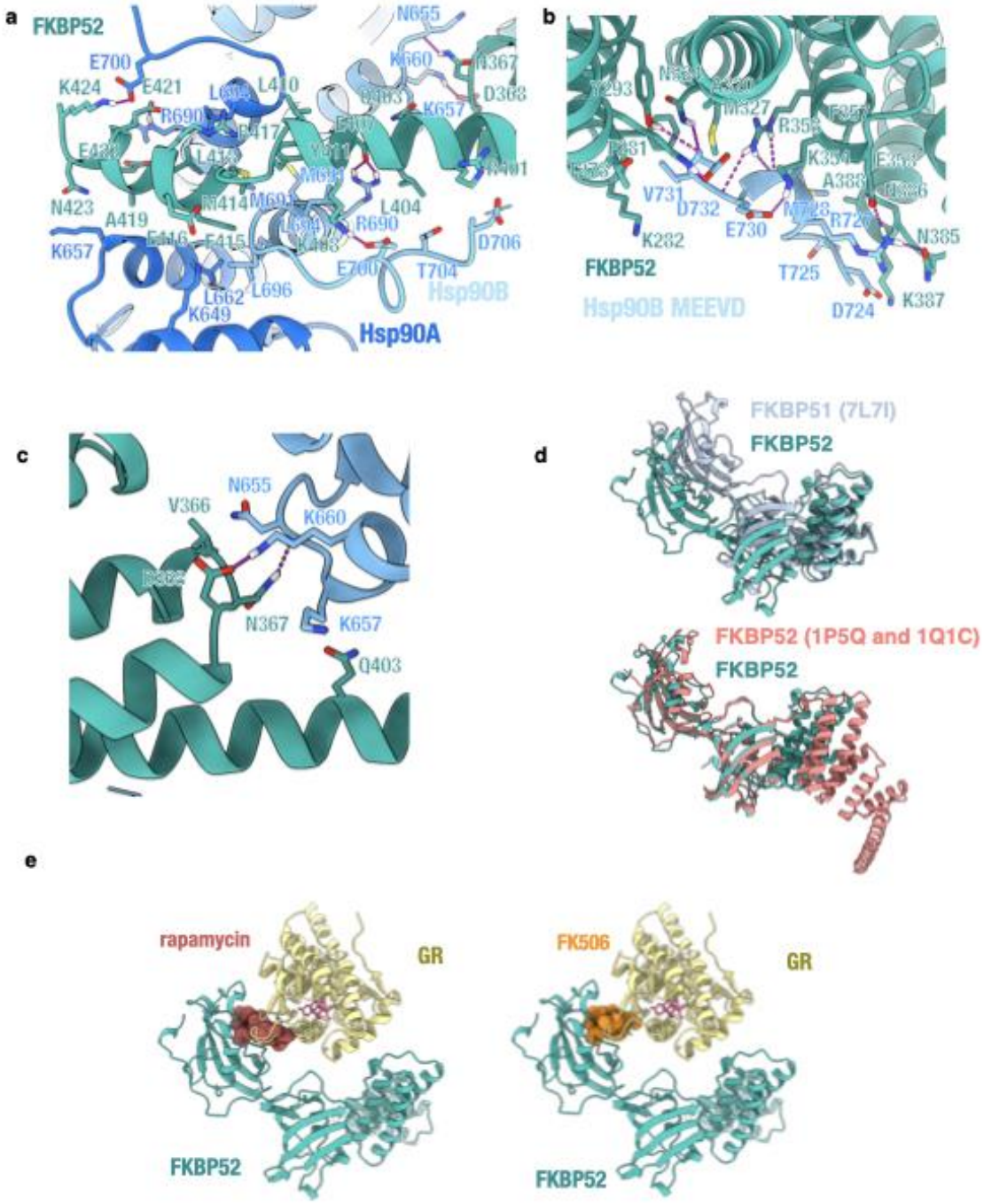
a
FKBP52
E700
K424
E421
N655
K660
N367
D368
K657
R690
N423
A419
N414
L404
K657
R690
D706
T704
L662
L696
K649
Hsp90B
Hsp90A
b
V731
D732
E730
K232
FKBP52
T725
D724
K387
N385
Hsp90B MEEVD
c
V366
N655
K660
N367
K657
Q403
d
FKBP51 (7L7I)
FKBP52
FKBP52 (1P5Q and 1Q1C)
FKBP52
e
rapamycin
GR
FKBP52
FK506
GR
FKBP52

Extended Data Fig. 4.4: GR:FKBP52 interfaces in the GR:Hsp90:FKBP52 structure Atomic model of the GR:Hsp90:FKBP52 complex with Hsp90A (dark blue), Hsp90B (light blue), GR (yellow), and FKBP52 (teal). Side chains in contact between Hsp90 and FKBP52 are shown, along with hydrogen bonds (dashed pink lines). **a,** Interface 1 of the Hsp90:FKBP52 interaction depicting the FKBP52 TPR H7e binding to the Hsp90A/B CTD dimer interface. The helix of FKBP52 H7e breaks to fit into the cleft formed by the Hsp90 CTDs. **b,** Interface 2 of the Hsp90:FKBP52 interaction depicting the Hsp90B MEEVD motif binding the FKBP52 TPR helical bundle. **c,** Interface 3 of the Hsp90:FKBP52 interaction depicting the FKBP52 TPR helices 5 and 6 binding to the Hsp90B CTD. **d,** FKBP52 (teal) from the GR:Hsp90:FKBP52 atomic model aligned with the cryo-EM structure of FKBP51 (light blue) (PDB ID 7L7I) (top) and crystal structures of FKBP52 (PDB ID 1P5Q, 1Q1C) (bottom) showing the difference in interdomain angles. 1P5Q contains the FKBP52 FK1 and FK2 domain, while 1Q1C contains the FKBP52 FK2 and TPR domains. **e,** The GR:Hsp90:FKBP52 atomic model with FKBP52 (teal), GR (yellow), and dexamethasone (pink) with proline-isomerase inhibitors, rapamycin (brown) or FK506 (orange), docked into the atomic model to indicate the steric clash with GR. Rapamycin was docked in based on the FKBP52:rapamycin crystal structure (PDB ID 4DRJ) and FK506 was docked in based on the FKBP52:FK506:FRB crystal structure (PDB ID 4LAX).

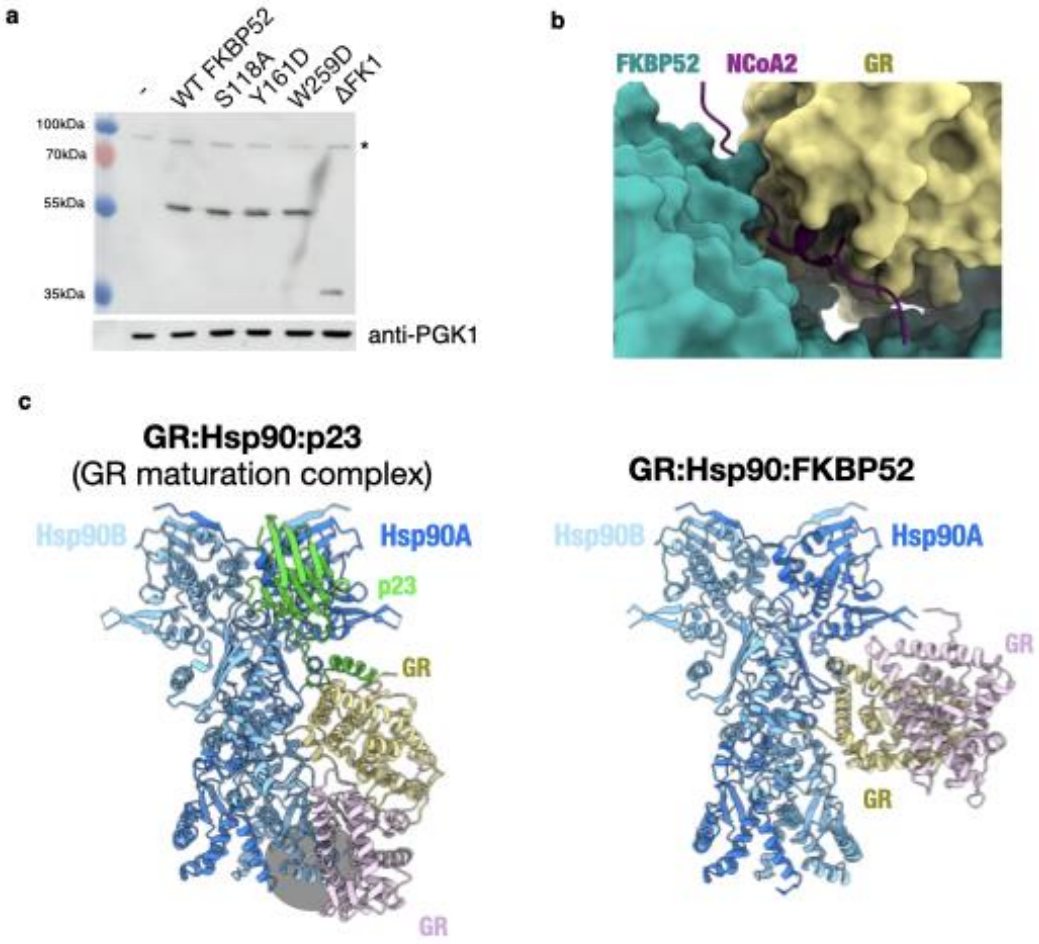
a
-
WT FKBP52
S118A
Y161D
W259D
ΔFK1
100kDa
70kDa
55kDa
35kDa
*
anti-PGK1
b
FKBP52
NCoA2
GR
c
GR:Hsp90:p23
(GR maturation complex)
Hsp90B
Hsp90A
p23
GR
GR
GR:Hsp90:FKBP52
Hsp90B
Hsp90A
GR
GR
d
GR Ligand Binding
Activation (ΔmP)
150
100
50
0
****
***
****
GR
GR + FKBP51
GR + FKBP52

Extended Data Fig. 4.5: Analysis of the GR:Hsp90:FKBP52 structure
a, Expression of human FKBP52 or FKBP52 mutants in wild-type yeast strain JJ762 assayed by immunoblot with a monoclonal antibody specific for FKBP52. An antibody against PGK1 was used as a loading control. The asterisk marks an unknown protein that cross reacts with the anti-FKBP52 antibody. **b,** Atomic model of the GR:Hsp90:FKBP52 complex shown in surface representation. FKBP52 (teal), GR (yellow). The NCoA2 (nuclear coactivator 2) co-activator peptide is docked in based on the GR:NCoA2 crystal structure (PDB ID 1M2Z). While most of the coactivator peptide binding is sterically permitted, the N-terminus of NCoA2 clashes with the FKBP52 TPR domain (red circle). **c,** Atomic models of the GR-maturation complex (GR:Hsp90:p23) (left) and the GR:Hsp90:FKBP52 complex without FKBP52 (right) depicting GR LBD dimerization. Hsp90A (dark blue), Hsp90B (light blue), GR (yellow). In both complexes, the GR LBD dimerization site is accessible, however; binding of the second GR LBD (light pink) to the GR-maturation complex clashes with the Hsp90B CTD, highlighted in gray (left). Binding of the second GR LBD (light pink) to the GR:Hsp90:FKBP52 complex is permitted once FKBP52 is released (right). Docking of the dimerized GR LBD is based on the GR LBD dimer crystal structure (PDB ID 1M2Z). **d,** Equilibrium binding of 10 nM fluorescent dexamethasone to 100 nM GR DBD-LBD with addition of 15 μM FKBP51 (“51”) or FKBP52 (“52”) measured by fluorescence polarization (mean±SD). n=3 biologically independent samples per condition. Fluorescence polarization values are baseline subtracted in accordance with the measured fluorescent dexamethasone baseline polarization value. Statistical significance was evaluated by an ordinary one-way ANOVA ($F_{(2,6)} = 1414$, $p < 0.0001$) with *post-hoc* Tukey’s multiple comparisons test. P-values: p(GR vs. GR + 51) < 0.0001, p(GR vs. GR + 52) < 0.0001, p(GR + 51 vs. GR + 52) = 0.004. (n.s. $P \geq 0.05$; * $P \leq 0.05$; ** $P \leq 0.01$; *** $P \leq 0.001$; **** $P \leq 0.0001$)**.**

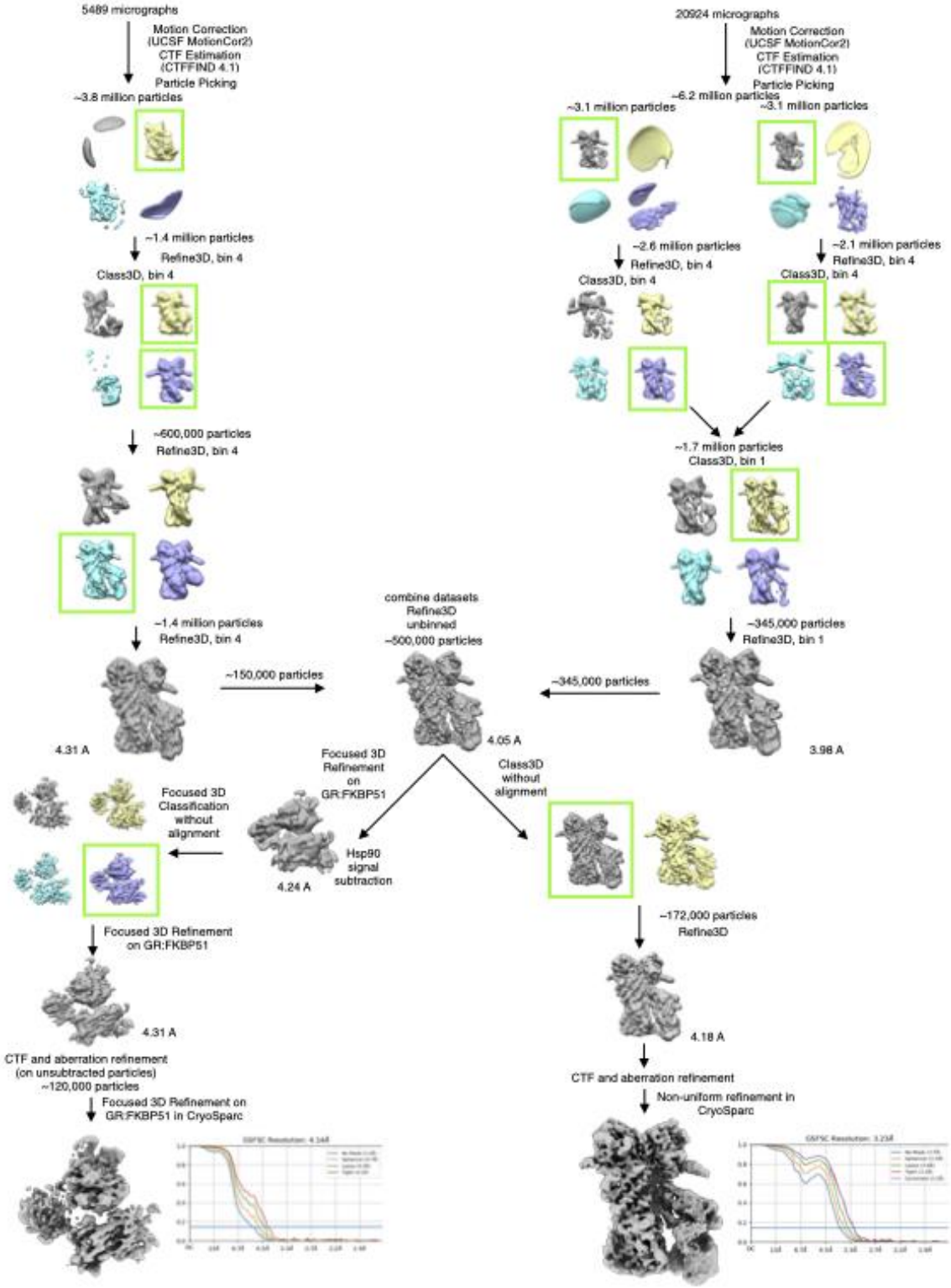
5489 micrographs
Motion Correction (UCSF MotionCor2)
CTF Estimation (CTFFIND 4.1)
Particle Picking
~3.8 million particles
~1.4 million particles
Refine3D, bin 4
Class3D, bin 4
~600,000 particles
Refine3D, bin 4
~1.4 million particles
Refine3D, bin 4
4.31 A
Focused 3D Classification without alignment
Focused 3D Refinement on GR:FKBP51
4.31 A
CTF and aberration refinement (on unsubtracted particles)
~120,000 particles
Focused 3D Refinement on GR:FKBP51 in CryoSparc
20924 micrographs
Motion Correction (UCSF MotionCor2)
CTF Estimation (CTFFIND 4.1)
Particle Picking
~6.2 million particles
~3.1 million particles
~3.1 million particles
~2.6 million particles
Refine3D, bin 4
Class3D, bin 4
~2.1 million particles
Refine3D, bin 4
Class3D, bin 4
~1.7 million particles
Class3D, bin 1
~345,000 particles
Refine3D, bin 1
3.98 A
~345,000 particles
combine datasets
Refine3D
unbinned
~500,000 particles
4.05 A
~150,000 particles
Focused 3D Refinement on GR:FKBP51
Hsp90 signal subtraction
4.24 A
Class3D without alignment
~172,000 particles
Refine3D
4.18 A
CTF and aberration refinement
Non-uniform refinement in CryoSparc

Extended Data Fig. 4.6: Cryo-EM data analysis for the GR:Hsp90:FKBP51 complex
Cryo-EM data processing procedure for the GR:Hsp90:FKBP51 complex performed in RELION and CryoSparc. Gold-standard Fourier shell correlation (GSFSC) curves of the final 3D reconstructions, including the focused maps and the consensus map, are shown (bottom). The blue lines intercept the y-axis at an FSC value of 0.143.

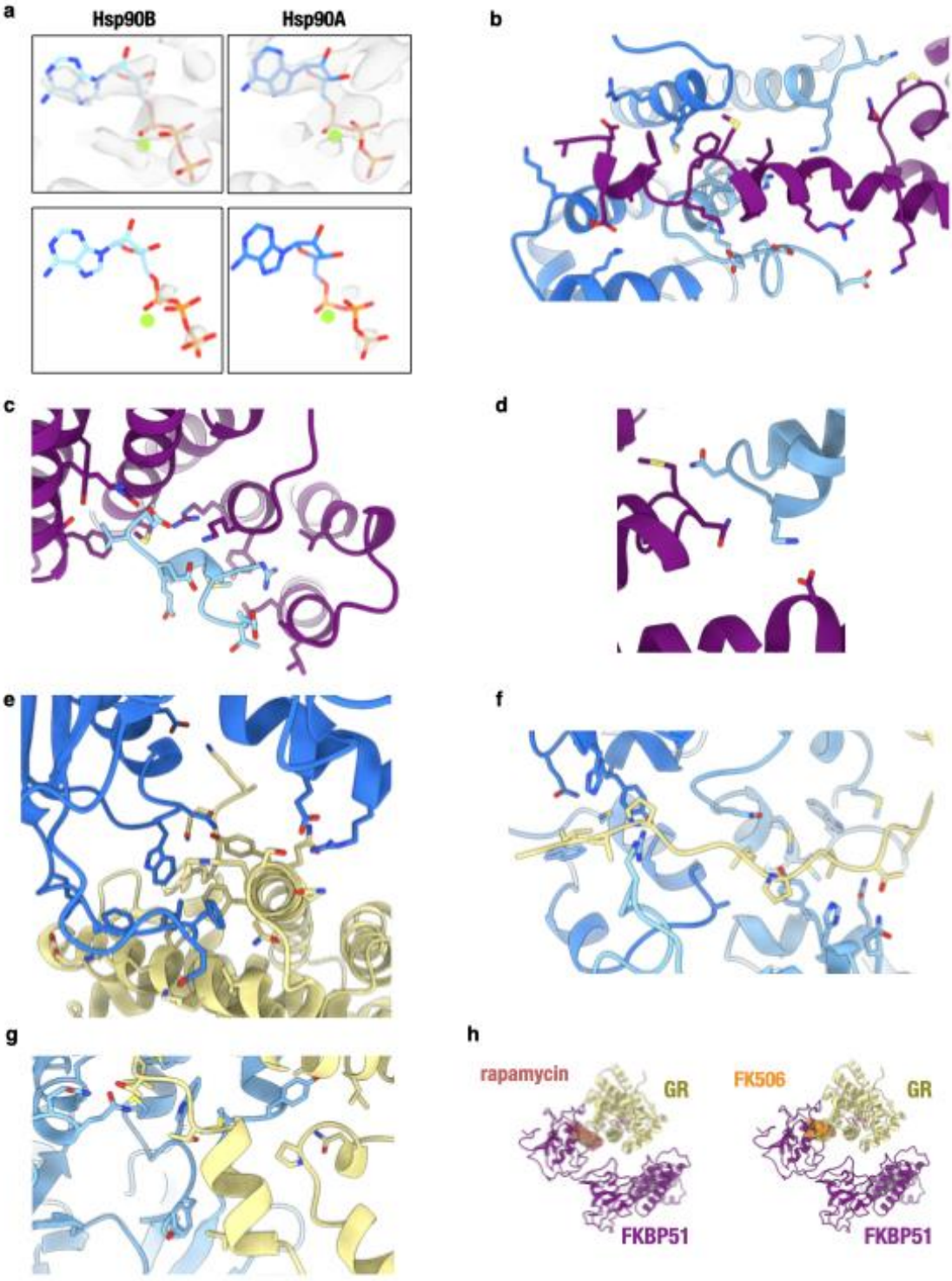
a
Hsp90B
Hsp90A
b
c
d
e
f
g
h
rapamycin
GR
FKBP51
FK506
GR
FKBP51

Extended Data Fig. 4.7: Hsp90:FKBP51 and GR:Hsp90 interfaces in the GR:Hsp90:FKBP51 structure

Atomic model of the GR:Hsp90:FKBP51 complex with Hsp90A (dark blue), Hsp90B (light blue), GR (yellow), and FKBP51 (purple). Side chains in contact between Hsp90 and FKBP51 or Hsp90 and GR are shown, along with hydrogen bonds (dashed pink lines). **a,** Hsp90:GR:FKBP51 complex map density with atomic model showing ATP-magnesium density in both Hsp90 protomers (Hsp90A/B). Bottom images show increased contour level on the map density to indicate that the ATP γ-phosphate position has much stronger density relative to the α and β-phosphates, likely corresponding to molybdate, which may act as a γ-phosphate analog (see **Methods**). **b,** Interface 1 of the Hsp90:FKBP51 interaction depicting the FKBP51 TPR H7e binding to the Hsp90A/B CTD dimer interface. The helix of FKBP51 H7e breaks to fit into the cleft formed by the Hsp90 CTDs. **c,** Interface 2 of the Hsp90:FKBP51 interaction depicting the Hsp90B MEEVD motif binding the FKBP51 TPR helical bundle **d,** Interface 3 of the Hsp90:FKBP51 interaction depicting the FKBP51 TPR helices 5 and 6 binding to the Hsp90B CTD. **e,** Interface 1 of the GR:Hsp90 interaction depicting the GR hydrophobic patch (GR Helices 9 and 10) interacting with the Hsp90A Src loop ($Hsp90^{345-360}$), $Hsp90A^{W320}$, and Hsp90A NTD/MD helices. **f,** Interface 2 of the GR:Hsp90 interaction depicting GR pre-Helix 1 strand and Helix 1 packing up against the Hsp90B amphipathic α-helices. **g,** Interface 3 of the GR:Hsp90 interaction depicting the GR pre-Helix 1 strand threading through the Hsp90 lumen between Hsp90A and Hsp90B. **h,** The GR:Hsp90:FKBP51 atomic model with FKBP51 (purple), GR (yellow), and dexamethasone (pink) with proline-isomerase inhibitors, rapamycin (brown) or FK506 (orange) docked into the atomic model to indicate the steric clash with GR. Rapamycin was docked in based on the FKBP52:rapamycin crystal structure (PDB ID 4DRJ) and FK506 was docked in based on the FKBP52:FK506:FRB crystal structure (PDB ID 4LAX). The FKBP52-specific inhibitor SAFit2 was docked into the atomic model to indicate there is no steric clash with GR at the backbone level (although some side chains do clash). SAFit2 was docked in based on the FKBP51:SAFit2 crystal structure (PDB ID 6TXX).

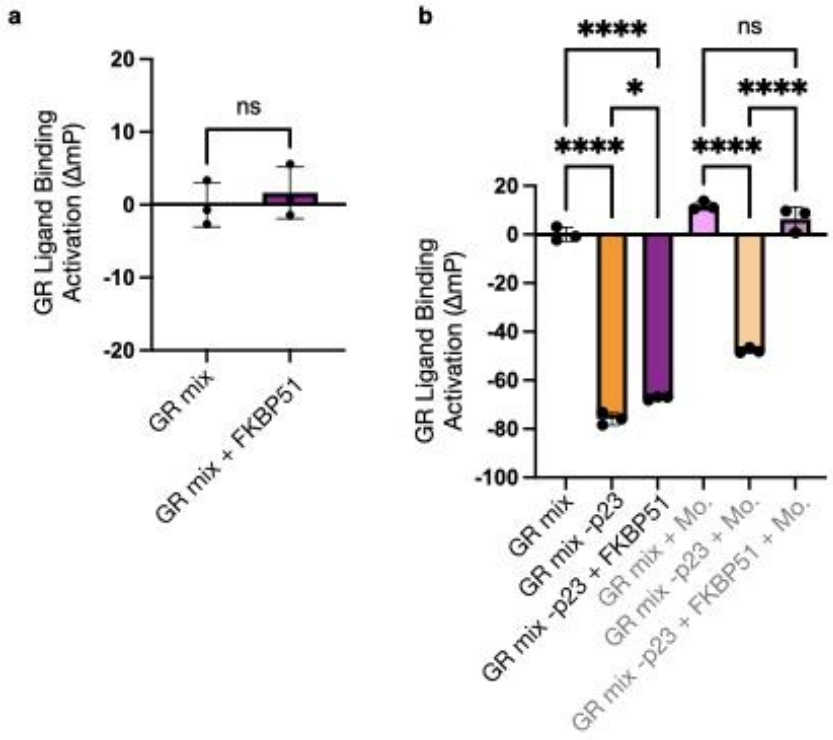

Extended Data Fig. 4.8: Effect of FKBP51 on GR ligand-binding activity
a, Equilibrium binding of 10nM fluorescent dexamethasone to 100nM GR DBD-LBD with chaperones and FKBP51. “Chaperones”= 15uM Hsp70, Hsp90, Hop, and p23, 2uM Ydj1 and Bag-1. Statistical significance was evaluated by an unpaired two-tailed t test, p-value =0.5737. (n.s. $P \geq 0.05$; * $P \leq 0.05$; ** $P \leq 0.01$; *** $P \leq 0.001$; **** $P \leq 0.0001$.**b,** Equilibrium binding of 10nM fluorescent dexamethasone to 100nM GR DBD-LBD with chaperones, FKBP51, and sodium molybdate (“Mo”). “Chaperones”= 15uM Hsp70, Hsp90, Hop, and p23, 2uM Ydj1 and Bag-1. Statistical significance was evaluated by an ordinary one-way ANOVA ($F_{(6,12)} = 647.1$, $p < 0.0001$) with *post-hoc* Šídák’s multiple comparisons test. P-values: p(Chaperones vs. Chaperones -p23) < 0.0001, p(Chaperones vs. Chaperones -p23 + 51) < 0.0001= 0.0287, p(Chaperones -p23 vs. Chaperones -p23 + 51) = 0.0123, p(Chaperones + Mo. Vs. Chaperones -p23 + Mo.) < 0.0001, p(Chaperones + Mo. Vs. Chaperones -p23 + 51 + Mo.) = 0.1640, p(Chaperones -p23 + Mo. Vs. Chaperones -p23 + 51 + Mo.) < 0.0001. (n.s. $P \geq 0.05$; * $P \leq 0.05$; ** $P \leq 0.01$; *** $P \leq 0.001$; **** $P \leq 0.0001$)**.**

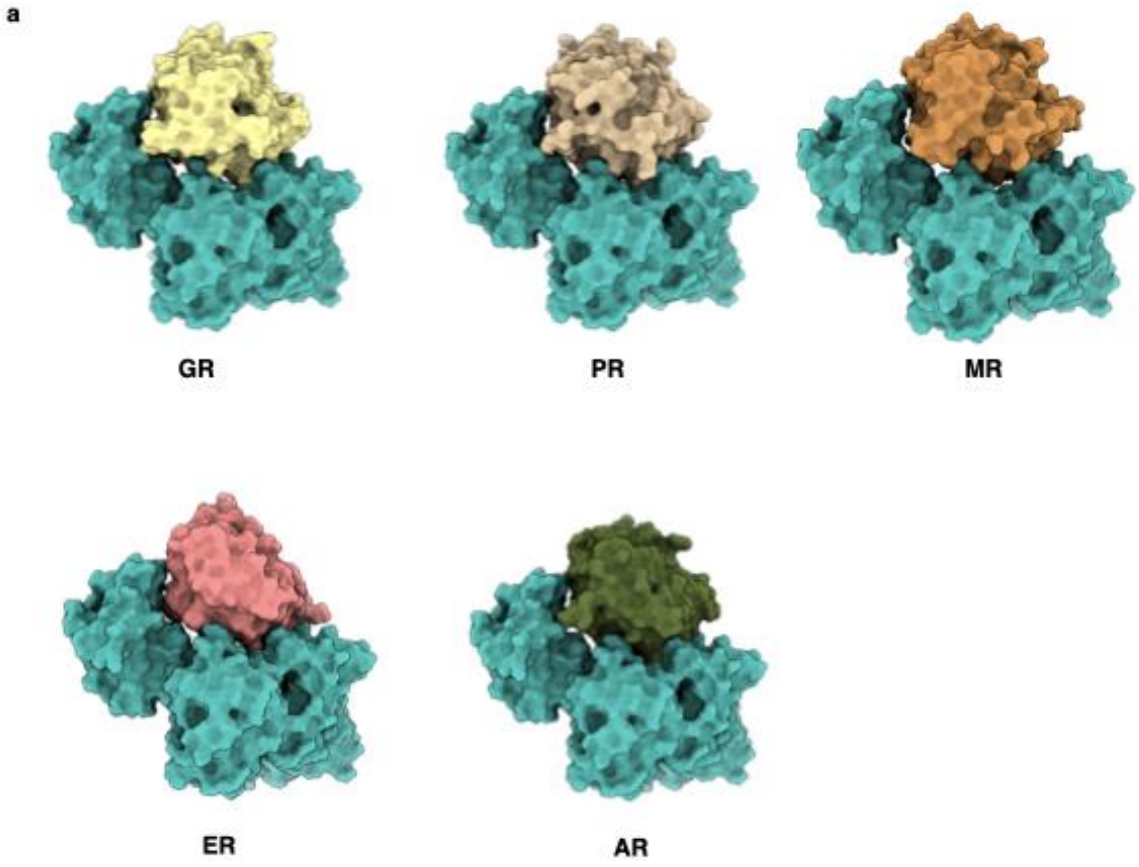
a
GR
PR
MR
ER
AR
b
most
conserved
most
variable

Extended Data Fig. 4.9: Model of all five SHRs binding to FKBP52 and sequence conservation across the SHRs at the putative SHR:FKBP52 interface
a, The FKBP52 bound to the glucocorticoid receptor (GR, yellow), progesterone receptor (PR, tan), mineralocorticoid receptor (MR, orange), estrogen receptor (ERα, pink), or androgen receptor (AR, green) based on the structure of the GR:Hsp90:FKBP52 complex. Due to the structural conservation of the LBDs across the five SHRs, all SHRs fit well with FKBP52 from the GR:Hsp90:FKBP52 atomic model, with no backbone clashes between the SHRs and FKBP52. The PDB IDs used to dock in the SHRs are as follows: PR (1A28), MR (2AA7), ERα (1ERE), AR (1T7R). **b,** Sequence conservation across human steroid hormone receptors (GR, MR, ERα, ERβ, AR) plotted onto the GR structure from the GR:Hsp90:FKBP52 atomic model. Residues are colored from most variable (blue) to most conserved (red).

Methods

Data analysis and figure preparation

Figures were created using UCSF Chimera v.1.14 (Pettersen et al., 2004) and UCSF ChimeraX v1.0.0 (Goddard et al., 2018). GR ligand binding data was analyzed using Prism v.9.4.0 (GraphPad).

Protein expression and purification

Human Hsp90α, Hsp70 (gene *Hsp70A1A*), Hop, p23, p23Δhelix (1-112),FKBP51, FKBP52, and yeast Ydj1 (Hsp40) were expressed in the pET151 bacterial expression plasmid with a cleavable N-terminal, 6x-His tag. Human Bag-1 isoform 4 (116-345) was expressed in a pET28a vector with a cleavable N-terminal, 6x-His tag. Proteins were expressed and purified by the following procedure. Proteins were expressed in *E. coli* BL21 star (DE3) strain. Cells were grown in either LB or TB at 37°C until OD_{600} reached 0.6-0.8 and then induced with 0.5 mM IPTG overnight at 16°C. Cells were harvested and lysed in 50 mM Potassium Phosphate pH 8, 500 mM KCl, 10 mM imidazole pH 8, 10% glycerol, 6 mM βME, and Roche cOmplete, mini protease inhibitor cocktail using an EmulsiFlex-C3 (Avestin). Lysate was centrifuged and the soluble fraction was affinity purified by gravity column with Ni-NTA affinity resin (QIAGEN). The protein was eluted with 30 mM Tris pH 8, 50 mM KCl, 250 mM imidazole pH 8, and 6 mM βME. For Hsp90, Hsp70, and Ydj1, an extra wash step with 0.1% Tween20 and 2 mM ATP/$MgCl_2$ was added to the Ni-NTA resin before eluting. The 6x-His tag was removed with TEV protease during the following overnight dialysis in 30 mM Tris pH 8, 50 mM KCl, and 6

mM βME. Cleaved protein was then loaded onto an ion exchange column, MonoQ 10/100 GL (GE Healthcare), with 30 mM Tris pH 8, 50 mM KCl, and 6 mM βME and eluted with a linear gradient of 50-500 mM KCl. Protein was further purified by size exclusion in 30 mM HEPES pH 7.5, 50 mM KCl, 10% glycerol, 1-2 mM DTT using a HiLoad 16/60 Superdex 200 (GE Healthcare) or Hi Load 16/60 Superdex 75 (GE Healthcare). For Hsp70, each peak from ion exchange was collected separately and purified by size exclusion in 30 mM HEPES pH 7.5, 100 mM KCl, 10% glycerol, 4 mM DTT, where only the monomeric peak was then collected. Protein was concentrated, flash frozen, and stored at -80°C.

GR DBD-LBD expression and purification

The human GR DBD-LBD construct contains the GR DNA binding domain (DBD), hinge, and ligand binding domain (LBD) (418-777) with solubilizing mutation F602S. The construct was codon optimized and expressed in the pMAL-c3X derivative with an N-terminal cleavable 6x-His-MBP tag. For datasets I, II, and III, GR DBD-LBD was expressed and purified with ligand as follows. GR DBD-LBD were expressed in *E. coli* BL21 star (DE3) strain. Cells were grown in either LB or TB at 37°C until OD_{600} reached 0.6 and then 100 μM dexamethasone and 50 μM $ZnCl_2$ were added. Cells were induced with 1 mM IPTG at OD_{600} 0.8. Cells were grown overnight (~16-18 hours) at 16°C. Cells were harvested and lysed in 50 mM Tris pH 8, 300 mM KCl, 50 μM dexamethasone, 5 mM imidazole pH 8, 10% glycerol, 2 mM DTT, and 0.2 mM PMSF. Lysate was centrifuged and the soluble fraction was affinity purified by gravity column

with Ni-NTA affinity resin (QIAGEN). During Ni-NTA affinity purification, the resin was washed with a buffer containing 30mM Tris pH 8, 500mM KCl, 50 μM dexamethasone, 10% glycerol, 2mM DTT, 2mM ATP, 5mM $MgCl_2$, and 0.1% Tween20. Then the resin was washed with a buffer containing 30mM Tris pH 8, 500mM KCl, 50 μM dexamethasone, 10% glycerol, 2mM DTT, and 5mM EDTA. The protein was eluted with 30 mM Tris pH 8, 150 mM KCl, 50 μM dexamethasone, 300 mM imidazole pH 8, 10% glycerol, and 3mM DTT. Protein was then purified by size exclusion in 30 mM HEPES pH 7.5, 150 mM KCl, 50 μM dexamethasone, 10% glycerol, and 4 mM DTT using a HiLoad 16/60 Superdex 200 (GE Healthcare). Protein was purified a second time by size exclusion using a HiLoad 16/60 Superdex 200 (GE Healthcare) with the same buffer to further remove degradation products. Protein was concentrated, flash frozen, and stored at -80°C.

For dataset IV and GR ligand binding assays, apo GR DBD-LBD was expressed and purified as follows. GR DBD-LBD were expressed in *E. coli* BL21 star (DE3) strain. Cells were grown in either LB or TB at 37°C until OD_{600} reached 0.6 and then 180 μM dexamethasone and 50 μM $ZnCl_2$ were added. Cells were induced with 1 mM IPTG at OD_{600} 0.8. Cells were grown overnight (~16-18 hours) at 16°C. Cells were harvested and lysed in 50 mM Tris pH 7.5, 300 mM KCl, 50 μM dexamethasone, 20 mM imidazole pH 8, 10% glycerol, 2 mM DTT, 0.04% CHAPS, 1 mM PMSF, and Roche cOmplete, mini protease inhibitor cocktail using an EmulsiFlex-C3 (Avestin). Lysate was centrifuged and the soluble fraction was affinity purified by gravity column with Ni-NTA affinity resin (QIAGEN). During Ni-NTA affinity purification, the resin was washed with a buffer containing 50mM Tris pH 7.5, 300mM KCl, 50 μM dexamethasone, 20 mM

imidazole pH 8, 10% glycerol, 2mM DTT, 2mM ATP, 5mM $MgCl_2$, 0.04% CHAPS, 1 mM PMSF, and Roche cOmplete, mini protease inhibitor cocktail using an EmulsiFlex-C3 (Avestin). The protein was eluted with 30 mM Tris pH 7.5, 150 mM KCl, 100 μM cortisol, 300 mM imidazole pH 8, 10% glycerol, and 3mM DTT. Protein was then dialyzed overnight in a buffer containing 30mM Tris pH 7.5, 150mM KCl, 10% glycerol, and 2mM DTT. Protein was then purified by hydrophobic interaction chromatography (HIC) on a HiScreen Butyl-S FF (4.7mL) column (Cytiva Life Sciences) to remove degradation products. First, solid KCl was slowly added to the protein solution at 4°C to a final concentration of 2mM KCl. Then the protein was injected onto the HIC column and eluted over a gradient of 2 M KCl to 0 M KCl overs 10 column volumes in a buffer containing 30mM Tris pH 7.5, 10% glycerol, and 2mM DTT. Then the protein was further purified by size exclusion in 30 mM HEPES pH 8, 150 mM KCl, 10% glycerol, and 0.5mM TCEP using a HiLoad 16/60 Superdex 200 (GE Healthcare). Protein was then dialyzed for 3 days, with fresh buffer each day, in a buffer containing 30mM HEPES pH 8, 150 mM KCl, 10% glycerol, and 2mM DTT. Protein was concentrated, flash frozen, and stored at -80°C.

GR:Hsp90:FKBP complex sample preparation

The GR chaperone cycle was reconstituted *in vitro* with purified components as previously described (Kirschke et al., 2014). Buffer conditions were 30 mM HEPES pH 8, 50 mM KCl, 0.05% Tween20, and 2 mM TCEP. Proteins and reagents were added at the following concentration: 5 μM MBP-GR LBD, 2 μM Hsp40, 5 μM Hsp70, 5 μM Hop, 15 μM Hsp90, 15 μM p23, 15 μM FKBP51 or FKBP52, and 5 mM ATP/$MgCl_2$. This

reaction was incubated at room temperature for 60 minutes, then 15 μM FKBP51 or FKBP52, 15 μM Bag-1, and 20 mM sodium molybdate (used to stabilize the closed conformation of Hsp90 (Csermely et al., 1993; Johnson & Toft, 1995; Verba et al., 2016), likely by acting as a γ-phosphate analog to stabilize the post-ATP hydrolysis transition state of Hsp90 (**Extended Data 3a, 7a)**) were added, and the reaction was incubated at room temperature for another 30 minutes. Following incubation, amylose resin (New England Biolabs) was added to the reactions in a 1:1 ratio and incubated at 4°C with nutation. Resin was then washed 4 times with wash buffer (30 mM HEPES pH 8, 50 mM KCl, 5 mM ATP/$MgCl_2$, 0.05% Tween20, 2 mM TCEP, 20 mM sodium molybdate) and eluted with 50 mM maltose in elution buffer (30 mM HEPES pH 8, 50 mM KCl, 2 mM TCEP, 20 mM sodium molybdate). The elution was analyzed by SDS-PAGE (4-12% acrylamide gel) (Extended Data Fig. 1c). The elution was concentrated and purified by size exclusion using a Superdex 200 Increase 3.2/300 (Cytiva Life Sciences) and fractions were analyzed by SDS-PAGE (4-12% acrylamide gel) (Extended Data 1d). Fractions containing the full complex were concentrated to ~2 μM. 2.5 μL of sample was applied to glow-discharged QUANTIFOIL R1.2/1.3, 400-mesh, copper holey carbon grid (Quantifoil Micro Tools GmbH) and plunge-frozen in liquid ethane using a Vitrobot Mark IV (FEI) with a blotting time of 12-16 seconds, blotting force 3, at 10°C, and with 100% humidity.

Cryo-EM data acquisition

All data was acquired using SerialEM software v.4.0 (Schorb et al., 2019). Datasets I-IV were collected on an FEI Titan Krios electron microscope (Thermo Fisher

Scientific) operating at 300kV using a K3 direct electron camera (Gatan) and equipped with a Bioquantum energy filter (Gatan) set to a slit width of 20 eV (example micrographs Extended Data Fig. 1e). Images were recorded at a nominal magnification of 105,000×, corresponding to a physical pixel size of 0.835 Å. Datasets I, II, and III were collected in super resolution mode, corresponding to a super resolution pixel size of 0.4175 Å. Dataset IV was not collected in super resolution mode. All datasets were acquired using fringe-free imaging (FFI) and multi-hole targeting using image shift in which 3 micrographs were collected per hole. A nominal defocus range of 0.8 μm –2.0 μm under focus was used for all datasets. For exposure, frame rates, and total dose see Extended Data Table 1.

Two small datasets on the GR:Hsp90:FKBP52 and GR:Hsp90:FKBP51 complex were collected before the larger datasets described above. The smaller datasets were collected on samples prepared in a similar manner as described above. For GR:Hsp90:FKBP52, images were collected on a FEI Titan Krios electron microscope (Thermo Fisher Scientific) operating at 300kV using a K3 direct electron camera (Gatan). Images were recorded in super-resolution mode at a nominal magnification of 105,000×, corresponding to a physical pixel size of 0.835 Å. A nominal defocus range of 0.8 μm –2.0 μm underfocus was used. A total exposure of 5.9 seconds was used with 0.05 second subframes (117 total frames). A dose rate of 8.0 e^-/pix/s was used, with a total dose of 67 $e^-/Å^2$. For GR:Hsp90:FKBP51, images were collected on a Talos Arctica (Thermo Fisher Scientific) operating at 200kV using a K3 direct electron camera (Gatan). Images were recorded in super-resolution mode at a nominal magnification of 28,000×, corresponding to a physical pixel size of 1.44 Å. A nominal defocus range of

0.8 μm –2.0 μm underfocus was used. A total exposure of 11.5 seconds was used with 0.1 second subframes (115 total frames). A dose rate of 10.4 e^-/pix/s was used, with a total dose of 57.5 $e^-/Å^2$.

Cryo-EM data processing

The smaller GR:Hsp90:FKBP52 dataset consisted of 2,022 dose-fractionated image stacks, which were motion corrected using UCSF MotionCor2 (Zheng et al., 2017) and analyzed with RELION v.3.0.8 (Scheres, 2012). Motion corrected images were used for contrast transfer function (CTF) estimation using CTFFIND v.4.1 (Rohou & Grigorieff, 2015) and Laplacian-of-Gaussian particle picking was done in RELION. Multiple rounds of 3D classification with symmetry C1 were performed with the GR-maturation complex (PDB ID: 7KRJ) (Noddings et al., 2022) as a low-pass-filtered (20 Å) initial model until a medium-resolution (~8 Å) GR:Hsp90:FKBP52 reconstruction was obtained from 11,756 particles. This reconstruction was used as an initial reference for the larger GR:Hsp90:FKBP52 datasets.

The smaller GR:Hsp90:FKBP51 dataset consisted of 1,181 dose-fractionated image stacks, which were motion corrected using UCSF MotionCor2 (Zheng et al., 2017) and analyzed with RELION v.3.0.8 (Scheres, 2012). Motion corrected images were used for contrast transfer function (CTF) estimation using CTFFIND v.4.1 (Rohou & Grigorieff, 2015) and Laplacian-of-Gaussian particle picking was done in RELION. Multiple rounds of 3D classification with symmetry C1 were performed with the GR-maturation complex (PDB ID: 7KRJ) (Noddings et al., 2022) as a low-pass-filtered (20 Å) initial model until a medium-resolution (~6 Å) GR:Hsp90:FKBP52 reconstruction was

obtained from 45,000 particles. This reconstruction was used as an initial reference for the larger GR:Hsp90:FKBP51 datasets.

Datasets I-IV were motion corrected using UCSF MotionCor2 and analyzed with RELION v.3.1.0. Motion corrected images with dose weighting were used for contrast transfer function (CTF) estimation using CTFFIND v.4.1 and reference-based picking was done in RELION using the corresponding references from the smaller datasets described above. The processing scheme for datasets I-IV are depicted in Extended Data Fig. 2 and Extended Data Fig. 6. After initial rounds of 3D classification with symmetry C1, the GR:Hsp90:FKBP52 datasets (I and II) were combined and GR:Hsp90:FKBP51 datasets (III and IV) were combined.

For the GR:Hsp90:FKBP52 combined dataset, a particle stack of ~496,000 particles were obtained representing a GR:Hsp90:FKBP52 reconstruction at nominal resolution 3.82 Å. This stack was then subjected to 3D classification without alignment and subsequent 3D refinement on the best classes (~307,000 particles), which yielded the best overall consensus reconstruction at a nominal resolution of 3.56 Å. Additionally, to improve the resolution of the GR:FKBP52 region, the ~496,000 particle stack was subjected to signal subtraction of the Hsp90 region. Focused refinement on the Hsp90-subtracted particle stack was then performed (initial angular sampling 1.8°, initial offset range 3 pixels, initial offset step 0.75 pixels, local searches from auto-sampling 1.8°) using a mask including GR and FKBP52 only. Focused classification without alignment was then performed using a mask including GR and FKBP52 only. Focused refinement on the best class (~107,000 particles) was then performed (initial angular sampling 0.9°, initial offset range 3 pixels, initial offset step 0.75 pixels, local searches from auto-

sampling 0.9°) using focused refinement using a mask including GR and FKBP52 only, which yielded a GR:FKBP52 reconstruction with a nominal resolution of 4.31 Å.

Per-particle CTF, beam-tilt refinement, trefoil and 4th order aberration refinement, and astigmatism were estimated for both the consensus reconstruction and GR:FKBP52 focused reconstruction in RELION. The corrected particles stacks were then imported to CryoSparc (v3.3.2) and 2D Classification was performed to clean-up the particle stacks. The consensus reconstruction (307,109 particles) was subjected to Non-Uniform Refinement with an envelope mask and a mask including Hsp90 only, each of which refined to a nominal resolution of 2.96 Å and 2.85 Å, respectively. The GR:FKBP52 focused reconstruction (106,318 particles) was subjected to Local Refinement with a mask including GR and FKBP52 only, which refined to a nominal resolution of 3.76 Å.

For the GR:Hsp90:FKBP51 combined dataset, a particle stack of ~500,000 particles was obtained, representing a GR:Hsp90:FKBP51 reconstruction at a nominal resolution of 4.05 Å. This stack was then subjected to 3D classification without alignment and subsequent 3D refinement on the best classes (~172,000 particles) to obtain the best overall consensus reconstruction at a nominal resolution of 3.23 Å. Additionally, to improve the resolution of the GR:FKBP51 region, the ~500,000 particle stack was subjected to signal subtraction of the Hsp90 region. Focused refinement on the Hsp90-subtracted particle stack was then performed (initial angular sampling 0.9°, initial offset range 3 pixels, initial offset step 1 pixels, local searches from auto-sampling 0.9°) using a mask including GR and FKBP51 only. Focused classification without alignment was then performed using a mask including GR and FKBP51 only. Focused

refinement on the best class (~120,000 particles) was then performed (initial angular sampling 0.9°, initial offset range 3 pixels, initial offset step 1 pixels, local searches from auto-sampling 0.9°) using focused refinement using a mask including GR and FKBP51 only, which yielded a GR:FKBP51 reconstruction with a nominal resolution of 4.24 Å.

Per-particle CTF, beam-tilt refinement, trefoil and 4th order aberration refinement, and astigmatism were estimated for both the consensus reconstruction and GR:FKBP51 focused reconstruction in RELION. The corrected particles stacks were then imported to CryoSparc (v3.3.2) and 2D Classification was performed to clean-up the particle stacks. The consensus reconstruction (171,778 particles) was subjected to Non-Uniform Refinement with an envelope mask and a mask including Hsp90 only, each of which refined to a nominal resolution of 3.19 Å. The GR:FKBP51 focused reconstruction (109,900 particles) was subjected to Local Refinement with a mask including GR and FKBP51 only, which refined to a nominal resolution of 4.14 Å.

All final reconstructions were post-processed in CryoSparc in which the nominal resolution was determined by the gold standard Fourier shell correlation (FSC) using the 0.143 criterion (Extended Data Fig. 2, Extended Data Fig. 6). Maps were sharpened and filtered automatically as determined by CryoSparc according to an estimated overall map B-factor and filtered to their estimated resolution. A composite map for both GR:Hsp90:FKBP51 and GR:Hsp90:FKBP52 was generated by combining the overall consensus refinement map with the GR:FKBP focused refinement map using vop maximum in Chimera. Note that the composite maps were only used for presentation in Fig. 1 and Fig. 4, but not used in atomic model building or refinement. CryoSparc 3D Variability Analysis was performed for the focused GR:FKBP51 and GR:FKBP52

reconstructions with the following parameters: number of modes to solve = 3, symmetry = C1, filter resolution = 6 Å, filter order = 1.5, high pass order = 8, per-particle scale = optimal, number of iterations = 20, lambda = 0.01,

For both the GR:Hsp90:FKBP51 and GR:Hsp90:FKBP52 complexes, no ligand-free GR complexes were identified during image analysis, despite many rounds of focused classification on GR at various stages of data processing. Only classes with clear ligand density in the GR ligand binding pocket were obtained, suggesting ligand-free GR is either too dynamic or quickly released from the complex, consistent with findings during processing of the GR-maturation complex (Noddings et al., 2022).

Model building and refinement

For the GR:Hsp90:FKBP52 atomic model, dexamethasone-bound GR LBD and the closed Hsp90 dimer from the GR-maturation complex (PDB ID: 7KRJ) (Noddings et al., 2022) along with the AlphaFold model of human FKBP52 (accession number: AF-Q02790) were used as starting models (Jumper et al., 2021). Additionally, the Hsp90 MEEVD peptide from the FKBP51:Hsp90 MEEVD crystal structure (PDB ID: 5NJX) (Kumar et al., 2017) was used. For the GR:Hsp90:FKBP51 atomic model, dexamethasone-bound GR LBD and the closed Hsp90 dimer from the GR-maturation complex (PDB ID: 7KRJ) (Noddings et al., 2022) along with human FKBP51 from the Hsp90:FKBP51:p23 cryo-EM structure (PDB ID: 7L7I) (Lee et al., 2021) were used as starting models. Additionally, the Hsp90 MEEVD peptide from the FKBP51:Hsp90 MEEVD crystal structure (PDB ID: 5NJX) (Kumar et al., 2017) was used.

Models were refined using Rosetta v.3.11 throughout. Following the split map approach (Wang et al., 2016) to prevent and monitor overfitting, the Rosetta iterative backbone rebuilding procedure was used to refine models against one of the half maps obtained from RELION, with the other half map only used for validations. Structurally uncharacterized regions, including the FKBP52 TPR:Hsp90 CTD interaction, the FKBP51:HSP90 CTD interaction, and the Hsp90 lumen:GR pre-Helix 1 interaction, were built *de novo* into consensus reconstructions or focused reconstructions using RosettaCM (Song et al., 2013). These regions were then further refined using the same Rosetta iterative backbone rebuilding procedure. With a proper density weight obtained using the half maps, the final model of the GR:Hsp90:FKBP52 and GR:Hsp90:FKBP51 complex was refined against the full reconstruction allowing only sidechain and small-scale backbone refinement. The final refinement statistics are provided in Extended Data Table 1.

Fluorescence polarization assays

Fluorescence polarization of fluorescent dexamethasone (F-dex) (Thermo Fisher) was measured on a CLARIOstar Plus microplate reader (BMG LabTech) with excitation/emission wavelengths of 485/538 nm, and temperature control set at 25°C. Buffer conditions were 50 mM HEPES pH 8, 100 mM KCl, 2 mM DTT. For equilibrium ligand binding in Fig. 3e,f; 4f, and Extended Data Fig. a,b, proteins were pre-equilibrated together at room temperature for 60 minutes prior to F-dex addition. Proteins and reagents were added at the following concentration: 10 nM F-dex, 100 nM GR DBD-LBD, 2 μM Hsp40, 2 μM Bag-1, 15 μM Hsp70, 15 μM Hsp90, 15 μM Hop, 15

μM p23 or $p23_{\Delta helix}$, 15 μM FKBP or FKBP mutants, and 5 mM ATP/$MgCl_2$. Note that the dissociation constant (K_D) between GR and F-dex is ~150 nM (Kirschke et al., 2014). Ligand binding was initiated with 10 nM F-dex and association was measured until reaching equilibrium. The plotted equilibrium values in Fig. 3e,f; 4f and Extended Data Fig. 8a,b represent the mean of 3 biologically independent samples with error bars representing the standard deviation. Polarization values are plotted as the change in polarization from the control sample (10 nM F-dex, 100 nM GR DBD-LBD, 2 μM Hsp40, 2 μM Bag-1, 15 μM Hsp70, 15 μM Hsp90, 15 μM Hop, 15 μM p23, and 5 mM ATP/$MgCl_2$). For equilibrium ligand binding in Extended Data Fig. 5d, proteins were pre-equilibrated together at room temperature for 30 minutes prior to F-dex addition. Proteins and reagents were added at the following concentration: 10 nM F-dex, 100 nM GR and 15 μM FKBP51 or FKBP52. Ligand binding was initiated with 10 nM F-dex and association was measured until reaching equilibrium. The plotted data points for each reaction represent 3 biologically independent samples. For Extended Data Fig. 5d statistical significance was evaluated by an ordinary one-way ANOVA *post-hoc* Tukey's multiple comparisons test using Prism v.9.4.0 (GraphPad). GR ligand binding behavior was affected by buffer conditions; therefore, reactions were always normalized such that each reaction had equivalent amounts of buffer reagents.

Sequence alignments

For the FKBP52 (gene *FKBP4*) sequence alignments in Fig. 2f, sequences were obtained from Uniprot (UniProt, 2021), aligned in Clustal Omega (Madeira et al., 2019) (https://www.ebi.ac.uk/Tools/msa/clustalo/), and visualized in JalView 2.11.1.0

(Waterhouse et al., 2009). Sequences in the alignment are: *H. sapiens* FKBP52, *M. musculus* FKBP52, *R. norvegicus* FKBP52, *D. melanogaster* FKBP52, *T. guttata* FKBP52, *G. gallus* FKBP52, *X. tropicalis* FKBP52, and *H. sapiens* FKBP51 (Uniprot accession codes: Q02790, P30416, Q9QVC8, Q6IQ94, H0ZSE5, A0A3Q3B0L8, A0A310SUH5, Q13451 respectively). For Fig. 2g, sequences were obtained from Uniprot (UniProt, 2021), aligned in Clustal Omega (Madeira et al., 2019) (https://www.ebi.ac.uk/Tools/msa/clustalo/), and conservation scores were calculated and mapped onto GR from the GR:Hsp90:FKBP52 atomic model using UCSF Chimera v.1.14 (Pettersen et al., 2004). Sequences in the alignment are: *H. sapiens* GR, *M. musculus* GR, *R. norvegicus* GR, *T. guttata* GR, *G. gallus* GR, *X. tropicalis* GR, *D. rerio* GR (Uniprot accession codes: P04150, P06537, P06536, A0A674H6U9, A0A1D5PRD7, Q28E31, A0A2R8QN75, respectively).

For Extended Data Fig. 9b, the sequences were obtained from Uniprot (UniProt, 2021), aligned in Clustal Omega (Madeira et al., 2019) (https://www.ebi.ac.uk/Tools/msa/clustalo/), and mapped onto GR from the maturation complex using Chimera v.1.14 (Pettersen et al., 2004) a. Sequences in the alignment are the human steroid hormone receptors: glucocorticoid receptor, mineralocorticoid receptor, androgen receptor, progesterone receptor, estrogen receptor α and β (Uniprot accession codes: P04150, P08235, P10275, P06401, E3WH19, Q92731, respectively). Conservation was calculated using percent conservation in Chimera v.1.14(Pettersen et al., 2004) (with AL2CO (Pei & Grishin, 2001) parameters (unweighted frequency estimation and entropy-based conservation measurement)).

Analysis of FKBP52 mutant expression by Western blot

Wild-type (JJ762) cells expressing empty vector (pRS423GPD), or plasmid-borne wild-type or mutant FKBP52 (pRS423GPD-FKBP52) were lysed and subjected to SDS-PAGE (10% acrylamide gel) followed by immunoblot analysis with a monoclonal antibody specific for FKBP52 (Hi52b, a gift from Dr. Marc Cox, The University of Texas at El Paso) (Riggs et al., 2003) (Extended Data Fig. 5a) An antibody against PGK1 (Invitrogen #459250) was used as a loading control.

In vivo GR activity assays

Relating to Fig. 2e, the effect of overexpression of wild-type FKBP52 on GR activity was determined as previously described (Riggs et al., 2003). GR activity was measured in the wild-type *S. cerevisiae* strain (JJ762) expressing GR on a single copy plasmid (p414GPD-GR) and the GRE-lacZ reporter plasmid pUCDSS-26X. Wild-type or mutant FKBP52 was expressed in the pRS423GPD plasmid. Cells were grown at 30°C with shaking overnight in selective media, diluted 10-fold and grown to OD_{600} 0.4-0.5. Cultures were split in two and one set was induced with ligand (50 nM DOC, deoxycorticosterone) (Sigma) for one hour. The β-galactosidase (β-gal) activity of paired samples in the presence and absence of hormone was measured as described using the yeast β-galactosidase assay kit from Thermo Scientific (Catalog number #75768). Assays contained triplicate samples and were conducted at least twice with each mutant. A representative assay is shown.

Fold GR activity was determined by the increase in normalized β-gal activity in the hormone treated sample relative to the untreated paired sample. Relative GR

activation was calculated by normalizing the fold GR activity of each sample to the average fold GR activity of strain JJ762 expressing p423GPD (empty vector [e.v.]). The fold increase in GR activities compared to the empty vector (e.v.) control are shown (mean±SD). Significance was evaluated using a one-way ANOVA ($F_{(6,14)} = 67.82$; $p < 0.0001$) with *post-hoc* Dunnett's multiple comparisons test. P-values: p(e.v. vs. 52) < 0.0001, p(52 vs. 52ΔFK1) < 0.0001, p(52 vs. 52 S118A) < 0.0001, p(52 vs. Y161D) = 0.0001, p(52 vs. W259D) = 0.0002.

Quantification and statistical analysis

All data were tested for statistical significance with Prism v.9.4.0 (GraphPad) (n.s. P ≥ 0.05; * P ≤ 0.05; ** P ≤ 0.01; *** P ≤ 0.001; **** P ≤ 0.0001). Statistical details (including sample sizes (*n*), F-statistics, p-values, and degrees of freedom) are included in the figure legends for each experiment where possible. Relating to Fig. 2e, significance was evaluated using a one-way ANOVA ($F_{(6,14)} = 67.82$; $p < 0.0001$) with *post-hoc* Dunnett's multiple comparisons test P-values: p(e.v. vs. 52) < 0.0001, p(52 vs. 52ΔFK1) < 0.0001, p(52 vs. 52 S118A) < 0.0001, p(52 vs. 52 Y161D) = 0.0001. Relating to Fig 3e, significance was evaluated using a one-way ANOVA ($F_{(3,8)} = 541.2$; $p < 0.0001$) with *post-hoc* Šídák's test. P-values: p(Chaperones vs. Chaperones + 52) = 0.0002, p(Chaperones + 52 vs. Chaperones w/ p23Δhelix + 52) < 0.0001, p(Chaperones w/ p23Δhelix vs. Chaperones w/ p23Δhelix + 52) < 0.0001. Relating to Fig. 3f, significance was evaluated using a one-way ANOVA ($F_{(5,12)} = 761.5$; $p < 0.0001$) with *post-hoc* Šídák's test. P-values < 0.0001 for each comparison. Relating to Fig. 4f statistical significance was evaluated by an ordinary one-way ANOVA with *post-hoc*

Šídák's multiple comparisons test. P-values: p(Chaperones vs. Chaperones + w/ p23Δhelix) < 0.0001, p(Chaperones vs. Chaperones w/ p23Δhelix + 51) = 0.0287, p(Chaperones w/ p23Δhelix + 51 vs. Chaperones w/ p23Δhelix + 51 L119P) < 0.0001, p(Chaperones w/ p23Δhelix + 51 vs. Chaperones w/ p23Δhelix + 52) < 0.0001, p(Chaperones w/ p23Δhelix + 52 vs. Chaperones w/ p23Δhelix + 52 P119L) < 0.0001. Relating to Extended Data Fig. 8a statistical significance was evaluated by an unpaired two-tailed t test, p-value =0.5737. Relating to Extended Data Fig. 8b, statistical significance was evaluated by an ordinary one-way ANOVA with *post-hoc* Šídák's multiple comparisons test. P-values: p(Chaperones vs. Chaperones -p23) < 0.0001, p(Chaperones vs. Chaperones -p23 + 51) < 0.0001= 0.0287, p(Chaperones -p23 vs. Chaperones -p23 + 51) = 0.0123, p(Chaperones + Mo. vs. Chaperones -p23 + Mo.) < 0.0001, p(Chaperones + Mo. vs. Chaperones -p23 + 51 + Mo.) = 0.1640, p(Chaperones -p23 + Mo. vs. Chaperones -p23 + 51 + Mo.) < 0.0001.

References

Ali, M. M. U., Roe, S. M., Vaughan, C. K., Meyer, P., Panaretou, B., Piper, P. W., Prodromou, C., & Pearl, L. H. (2006). Crystal structure of an Hsp90–nucleotide–p23/Sba1 closed chaperone complex. *Nature, 440*(7087), 1013-1017. https://doi.org/10.1038/nature04716

Bauder, M., Meyners, C., Purder, P. L., Merz, S., Sugiarto, W. O., Voll, A. M., Heymann, T., & Hausch, F. (2021, Mar 25). Structure-Based Design of High-Affinity Macrocyclic FKBP51 Inhibitors. *J Med Chem, 64*(6), 3320-3349. https://doi.org/10.1021/acs.jmedchem.0c02195

Baughman, G., Wiederrecht, G. J., Chang, F., Martin, M. M., & Bourgeois, S. (1997, Mar 17). Tissue distribution and abundance of human FKBP51, and FK506-binding protein that can mediate calcineurin inhibition. *Biochem Biophys Res Commun, 232*(2), 437-443. https://doi.org/10.1006/bbrc.1997.6307

Bledsoe, R. K., Montana, V. G., Stanley, T. B., Delves, C. J., Apolito, C. J., McKee, D. D., Consler, T. G., Parks, D. J., Stewart, E. L., Willson, T. M., Lambert, M. H., Moore, J. T., Pearce, K. H., & Xu, H. E. (2002). Crystal Structure of the Glucocorticoid Receptor Ligand Binding Domain Reveals a Novel Mode of Receptor Dimerization and Coactivator Recognition. *110*(1), 93-105. https://doi.org/10.1016/s0092-8674(02)00817-6

Blundell, K. L., Pal, M., Roe, S. M., Pearl, L. H., & Prodromou, C. (2017). The structure of FKBP38 in complex with the MEEVD tetratricopeptide binding-motif of Hsp90. *PLoS One, 12*(3), e0173543. https://doi.org/10.1371/journal.pone.0173543

Bose, S., Weikl, T., Bugl, H., & Buchner, J. (1996, Dec 6). Chaperone function of Hsp90-associated proteins. *Science, 274*(5293), 1715-1717. https://doi.org/10.1126/science.274.5293.1715

Bracher, A., Kozany, C., Hahle, A., Wild, P., Zacharias, M., & Hausch, F. (2013, Nov 15). Crystal structures of the free and ligand-bound FK1-FK2 domain segment of FKBP52 reveal a flexible inter-domain hinge. *J Mol Biol, 425*(22), 4134-4144. https://doi.org/10.1016/j.jmb.2013.07.041

Cheung, J., & Smith, D. F. (2000, Jul). Molecular chaperone interactions with steroid receptors: an update. *Mol Endocrinol, 14*(7), 939-946. https://doi.org/10.1210/mend.14.7.0489

Cheung-Flynn, J., Roberts, P. J., Riggs, D. L., & Smith, D. F. (2003, May 9). C-terminal sequences outside the tetratricopeptide repeat domain of FKBP51 and FKBP52 cause differential binding to Hsp90. *J Biol Chem, 278*(19), 17388-17394. https://doi.org/10.1074/jbc.M300955200

Cluning, C., Ward, B. K., Rea, S. L., Arulpragasam, A., Fuller, P. J., & Ratajczak, T. (2013, Jul). The helix 1-3 loop in the glucocorticoid receptor LBD is a regulatory element for FKBP cochaperones. *Mol Endocrinol, 27*(7), 1020-1035. https://doi.org/10.1210/me.2012-1023

Csermely, P., Kajtar, J., Hollosi, M., Jalsovszky, G., Holly, S., Kahn, C. R., Gergely, P., Soti, C., Mihaly, K., & Somogyi, J. (1993, Jan 25). Atp Induces a Conformational Change of the 90-Kda Heat-Shock Protein (Hsp90). *Journal of Biological Chemistry, 268*(3), 1901-1907. <Go to ISI>://WOS:A1993KH62000062

Davies, T. H., Ning, Y. M., & Sanchez, E. R. (2002). A New First Step in Activation of Steroid Receptors: HORMONE-INDUCED SWITCHING OF FKBP51 AND FKBP52 IMMUNOPHILINS. *277*(7), 4597-4600. https://doi.org/10.1074/jbc.c100531200

Davies, T. H., Ning, Y. M., & Sanchez, E. R. (2005, Feb 15). Differential control of glucocorticoid receptor hormone-binding function by tetratricopeptide repeat (TPR) proteins and the immunosuppressive ligand FK506. *Biochemistry, 44*(6), 2030-2038. https://doi.org/10.1021/bi048503v

Denny, W. B., Valentine, D. L., Reynolds, P. D., Smith, D. F., & Scammell, J. G. (2000, Nov). Squirrel monkey immunophilin FKBP51 is a potent inhibitor of

glucocorticoid receptor binding. *Endocrinology, 141*(11), 4107-4113. https://doi.org/10.1210/endo.141.11.7785

Ebong, I.-O., Beilsten-Edmands, V., Patel, N. A., Morgner, N., & Robinson, C. V. (2016). The interchange of immunophilins leads to parallel pathways and different intermediates in the assembly of Hsp90 glucocorticoid receptor complexes. *2*, 16002. https://doi.org/10.1038/celldisc.2016.2

Echeverría, P. C., Mazaira, G., Erlejman, A., Gomez-Sanchez, C., Piwien Pilipuk, G., & Galigniana, M. D. (2009). Nuclear import of the glucocorticoid receptor-hsp90 complex through the nuclear pore complex is mediated by its interaction with Nup62 and importin beta. *Molecular and Cellular Biology, 29*(17), 4788-4797. https://doi.org/10.1128/MCB.00649-09

Estebanez-Perpina, E., Arnold, L. A., Nguyen, P., Rodrigues, E. D., Mar, E., Bateman, R., Pallai, P., Shokat, K. M., Baxter, J. D., Guy, R. K., Webb, P., & Fletterick, R. J. (2007, Oct 9). A surface on the androgen receptor that allosterically regulates coactivator binding. *Proc Natl Acad Sci U S A, 104*(41), 16074-16079. https://doi.org/10.1073/pnas.0708036104

Feng, X., Pomplun, S., & Hausch, F. (2015). Recent Progress in FKBP Ligand Development. *Curr Mol Pharmacol, 9*(1), 27-36. https://doi.org/10.2174/1874467208666150519113313

Fuller, P. J., Smith, B. J., & Rogerson, F. M. (2004, Sep). Cortisol resistance in the New World revisited. *Trends Endocrinol Metab, 15*(7), 296-299. https://doi.org/10.1016/j.tem.2004.07.001

Gaali, S., Kirschner, A., Cuboni, S., Hartmann, J., Kozany, C., Balsevich, G., Namendorf, C., Fernandez-Vizarra, P., Sippel, C., Zannas, A. S., Draenert, R., Binder, E. B., Almeida, O. F., Ruhter, G., Uhr, M., Schmidt, M. V., Touma, C., Bracher, A., & Hausch, F. (2015, Jan). Selective inhibitors of the FK506-binding protein 51 by induced fit. *Nat Chem Biol, 11*(1), 33-37. https://doi.org/10.1038/nchembio.1699

Galigniana, M. D., Echeverria, P. C., Erlejman, A. G., & Piwien-Pilipuk, G. (2010, Jul-Aug). Role of molecular chaperones and TPR-domain proteins in the cytoplasmic transport of steroid receptors and their passage through the nuclear pore. *Nucleus, 1*(4), 299-308. https://doi.org/10.4161/nucl.1.4.11743

Galigniana, M. D., Radanyi, C., Renoir, J. M., Housley, P. R., & Pratt, W. B. (2001, May 4). Evidence that the peptidylprolyl isomerase domain of the hsp90-binding immunophilin FKBP52 is involved in both dynein interaction and glucocorticoid receptor movement to the nucleus. *J Biol Chem, 276*(18), 14884-14889. https://doi.org/10.1074/jbc.M010809200

Goddard, T. D., Huang, C. C., Meng, E. C., Pettersen, E. F., Couch, G. S., Morris, J. H., & Ferrin, T. E. (2018, Jan). UCSF ChimeraX: Meeting modern challenges in visualization and analysis. *Protein Sci, 27*(1), 14-25. https://doi.org/10.1002/pro.3235

Gruszczyk, J., Grandvuillemin, L., Lai-Kee-Him, J., Paloni, M., Savva, C. G., Germain, P., Grimaldi, M., Boulahtouf, A., Kwong, H. S., Bous, J., Ancelin, A., Bechara, C., Barducci, A., Balaguer, P., & Bourguet, W. (2022, Nov 16). Cryo-EM structure of the agonist-bound Hsp90-XAP2-AHR cytosolic complex. *Nat Commun, 13*(1), 7010. https://doi.org/10.1038/s41467-022-34773-w

Guy, N. C., Garcia, Y. A., & Cox, M. B. (2015). Therapeutic Targeting of the FKBP52 Co-Chaperone in Steroid Hormone Receptor-Regulated Physiology and Disease. *Curr Mol Pharmacol, 9*(2), 109-125. https://doi.org/10.2174/1874467208666150519114115

Hinds, T. D., Stechschulte, L. A., Elkhairi, F., & Sanchez, E. R. (2014, Dec). Analysis of FK506, timcodar (VX-853) and FKBP51 and FKBP52 chaperones in control of glucocorticoid receptor activity and phosphorylation. *Pharmacol Res Perspect, 2*(6), e00076. https://doi.org/10.1002/prp2.76

Jaaskelainen, T., Makkonen, H., & Palvimo, J. J. (2011, Aug). Steroid up-regulation of FKBP51 and its role in hormone signaling. *Curr Opin Pharmacol, 11*(4), 326-331. https://doi.org/10.1016/j.coph.2011.04.006

Jaime-Garza, M., Nowotny, C., Coutandin, D., Wang, F., Tabios, M., & Agard, D. A. (2022, 2022-01-01 00:00:00). Hsp90 provides a platform for kinase dephosphorylation by PP5. *bioRxiv*.

Johnson, J. L., & Toft, D. O. (1995, Jun). Binding of p23 and hsp90 during assembly with the progesterone receptor. *Mol Endocrinol, 9*(6), 670-678. https://doi.org/10.1210/mend.9.6.8592513

Jumper, J., Evans, R., Pritzel, A., Green, T., Figurnov, M., Ronneberger, O., Tunyasuvunakool, K., Bates, R., Zidek, A., Potapenko, A., Bridgland, A., Meyer, C., Kohl, S. A. A., Ballard, A. J., Cowie, A., Romera-Paredes, B., Nikolov, S., Jain, R., Adler, J., Back, T., Petersen, S., Reiman, D., Clancy, E., Zielinski, M., Steinegger, M., Pacholska, M., Berghammer, T., Bodenstein, S., Silver, D., Vinyals, O., Senior, A. W., Kavukcuoglu, K., Kohli, P., & Hassabis, D. (2021, Jul 15). Highly accurate protein structure prediction with AlphaFold. *Nature*. https://doi.org/10.1038/s41586-021-03819-2

Kirschke, E., Goswami, D., Southworth, D., Griffin, P., & Agard, D. (2014). Glucocorticoid Receptor Function Regulated by Coordinated Action of the Hsp90

and Hsp70 Chaperone Cycles. *Cell, 157*(7), 1685-1697. https://doi.org/10.1016/j.cell.2014.04.038

Kolos, J. M., Voll, A. M., Bauder, M., & Hausch, F. (2018). FKBP Ligands-Where We Are and Where to Go? *Front Pharmacol, 9*, 1425. https://doi.org/10.3389/fphar.2018.01425

Kumar, R., Moche, M., Winblad, B., & Pavlov, P. F. (2017, Oct 27). Combined x-ray crystallography and computational modeling approach to investigate the Hsp90 C-terminal peptide binding to FKBP51. *Sci Rep, 7*(1), 14288. https://doi.org/10.1038/s41598-017-14731-z

Lee, K., Thwin, A. C., Nadel, C. M., Tse, E., Gates, S. N., Gestwicki, J. E., & Southworth, D. R. (2021, Sep 2). The structure of an Hsp90-immunophilin complex reveals cochaperone recognition of the client maturation state. *Mol Cell, 81*(17), 3496-3508 e3495. https://doi.org/10.1016/j.molcel.2021.07.023

Madeira, F., Park, Y. M., Lee, J., Buso, N., Gur, T., Madhusoodanan, N., Basutkar, P., Tivey, A. R. N., Potter, S. C., Finn, R. D., & Lopez, R. (2019, Jul 2). The EMBL-EBI search and sequence analysis tools APIs in 2019. *Nucleic Acids Res, 47*(W1), W636-W641. https://doi.org/10.1093/nar/gkz268

Maeda, K., Habara, M., Kawaguchi, M., Matsumoto, H., Hanaki, S., Masaki, T., Sato, Y., Matsuyama, H., Kunieda, K., Nakagawa, H., & Shimada, M. (2022, Feb). FKBP51 and FKBP52 regulate androgen receptor dimerization and proliferation in prostate cancer cells. *Mol Oncol, 16*(4), 940-956. https://doi.org/10.1002/1878-0261.13030

Morishima, Y., Murphy, P. J., Li, D. P., Sanchez, E. R., & Pratt, W. B. (2000, Jun 16). Stepwise assembly of a glucocorticoid receptor.hsp90 heterocomplex resolves two sequential ATP-dependent events involving first hsp70 and then hsp90 in opening of the steroid binding pocket. *J Biol Chem, 275*(24), 18054-18060. https://doi.org/10.1074/jbc.M000434200

Mustafi, S. M., LeMaster, D. M., & Hernandez, G. (2014, Jul 1). Differential conformational dynamics in the closely homologous FK506-binding domains of FKBP51 and FKBP52. *Biochem J, 461*(1), 115-123. https://doi.org/10.1042/BJ20140232

Nathan, D. F., & Lindquist, S. (1995, Jul). Mutational analysis of Hsp90 function: interactions with a steroid receptor and a protein kinase. *Mol Cell Biol, 15*(7), 3917-3925. https://doi.org/10.1128/mcb.15.7.3917

Noddings, C. M., Wang, R. Y., Johnson, J. L., & Agard, D. A. (2022, Jan). Structure of Hsp90-p23-GR reveals the Hsp90 client-remodelling mechanism. *Nature, 601*(7893), 465-469. https://doi.org/10.1038/s41586-021-04236-1

Oroz, J., Chang, B. J., Wysoczanski, P., Lee, C.-T., Pérez-Lara, Á., Chakraborty, P., Hofele, R. V., Baker, J. D., Blair, L. J., Biernat, J., Urlaub, H., Mandelkow, E., Dickey, C. A., & Zweckstetter, M. (2018). Structure and pro-toxic mechanism of the human Hsp90/PPIase/Tau complex. *Nature Communications, 9*(1). https://doi.org/10.1038/s41467-018-06880-0

Pei, J., & Grishin, N. V. (2001, Aug). AL2CO: calculation of positional conservation in a protein sequence alignment. *Bioinformatics, 17*(8), 700-712. https://doi.org/10.1093/bioinformatics/17.8.700

Pettersen, E. F., Goddard, T. D., Huang, C. C., Couch, G. S., Greenblatt, D. M., Meng, E. C., & Ferrin, T. E. (2004, Oct). UCSF Chimera--a visualization system for exploratory research and analysis. *J Comput Chem, 25*(13), 1605-1612. https://doi.org/10.1002/jcc.20084

Picard, D., Khursheed, B., Garabedian, M. J., Fortin, M. G., Lindquist, S., & Yamamoto, K. R. (1990, 1990/11/01). Reduced levels of hsp90 compromise steroid receptor action in vivo. *Nature, 348*(6297), 166-168. https://doi.org/10.1038/348166a0

Pirkl, F., & Buchner, J. (2001). Functional analysis of the hsp90-associated human peptidyl prolyl Cis/Trans isomerases FKBP51, FKBP52 and cyp40. *308*(4), 795-806. https://doi.org/10.1006/jmbi.2001.4595

Pratt, W. B., Galigniana, M. D., Harrell, J. M., & DeFranco, D. B. (2004, Aug). Role of hsp90 and the hsp90-binding immunophilins in signalling protein movement. *Cell Signal, 16*(8), 857-872. https://doi.org/10.1016/j.cellsig.2004.02.004

Pratt, W. B., & Toft, D. O. (1997). Steroid Receptor Interactions with Heat Shock Protein and Immunophilin Chaperones. *Endocrine Reviews, 18*(3), 306-360. https://doi.org/10.1210/edrv.18.3.0303

Rein, T. (2020, Jul). Peptidylprolylisomerases, Protein Folders, or Scaffolders? The Example of FKBP51 and FKBP52. *Bioessays, 42*(7), e1900250. https://doi.org/10.1002/bies.201900250

Reynolds, P. D., Ruan, Y., Smith, D. F., & Scammell, J. G. (1999). Glucocorticoid Resistance in the Squirrel Monkey Is Associated with Overexpression of the Immunophilin FKBP51 1. *84*(2), 663-669. https://doi.org/10.1210/jcem.84.2.5429

Riggs, D. L., Cox, M. B., Tardif, H. L., Hessling, M., Buchner, J., & Smith, D. F. (2007, Dec). Noncatalytic role of the FKBP52 peptidyl-prolyl isomerase domain in the

regulation of steroid hormone signaling. *Mol Cell Biol, 27*(24), 8658-8669. https://doi.org/10.1128/MCB.00985-07

Riggs, D. L., Roberts, P. J., Chirillo, S. C., Cheung-Flynn, J., Prapapanich, V., Ratajczak, T., Gaber, R., Picard, D., & Smith, D. F. (2003). The Hsp90-binding peptidylprolyl isomerase FKBP52 potentiates glucocorticoid signaling in vivo. *The EMBO Journal, 22*(5), 1158-1167. https://doi.org/10.1093/emboj/cdg108

Rohou, A., & Grigorieff, N. (2015, Nov). CTFFIND4: Fast and accurate defocus estimation from electron micrographs. *J Struct Biol, 192*(2), 216-221. https://doi.org/10.1016/j.jsb.2015.08.008

Sabbagh, J. J., Cordova, R. A., Zheng, D., Criado-Marrero, M., Lemus, A., Li, P., Baker, J. D., Nordhues, B. A., Darling, A. L., Martinez-Licha, C., Rutz, D. A., Patel, S., Buchner, J., Leahy, J. W., Koren, J., 3rd, Dickey, C. A., & Blair, L. J. (2018, Aug 17). Targeting the FKBP51/GR/Hsp90 Complex to Identify Functionally Relevant Treatments for Depression and PTSD. *ACS Chem Biol, 13*(8), 2288-2299. https://doi.org/10.1021/acschembio.8b00454

Savory, J. G. A., Hsu, B., Laquian, I. R., Giffin, W., Reich, T., Haché, R. J. G., & Lefebvre, Y. A. (1999). Discrimination between NL1- and NL2-Mediated Nuclear Localization of the Glucocorticoid Receptor. *19*(2), 1025-1037. https://doi.org/10.1128/mcb.19.2.1025

Scheres, S. H. (2012, Dec). RELION: implementation of a Bayesian approach to cryo-EM structure determination. *J Struct Biol, 180*(3), 519-530. https://doi.org/10.1016/j.jsb.2012.09.006

Schopf, F. H., Biebl, M. M., & Buchner, J. (2017). The HSP90 chaperone machinery. *Nature Reviews Molecular Cell Biology, 18*(6), 345-360. https://doi.org/10.1038/nrm.2017.20

Schorb, M., Haberbosch, I., Hagen, W. J. H., Schwab, Y., & Mastronarde, D. N. (2019, Jun). Software tools for automated transmission electron microscopy. *Nat Methods, 16*(6), 471-477. https://doi.org/10.1038/s41592-019-0396-9

Sinars, C. R., Cheung-Flynn, J., Rimerman, R. A., Scammell, J. G., Smith, D. F., & Clardy, J. (2003, Feb 4). Structure of the large FK506-binding protein FKBP51, an Hsp90-binding protein and a component of steroid receptor complexes. *Proc Natl Acad Sci U S A, 100*(3), 868-873. https://doi.org/10.1073/pnas.0231020100

Sivils, J. C., Storer, C. L., Galigniana, M. D., & Cox, M. B. (2011, Aug). Regulation of steroid hormone receptor function by the 52-kDa FK506-binding protein (FKBP52). *Curr Opin Pharmacol, 11*(4), 314-319. https://doi.org/10.1016/j.coph.2011.03.010

Smith, D. F., & Toft, D. O. (2008, Oct). Minireview: the intersection of steroid receptors with molecular chaperones: observations and questions. *Mol Endocrinol, 22*(10), 2229-2240. https://doi.org/10.1210/me.2008-0089

Song, Y., DiMaio, F., Wang, R. Y., Kim, D., Miles, C., Brunette, T., Thompson, J., & Baker, D. (2013, Oct 8). High-resolution comparative modeling with RosettaCM. *Structure, 21*(10), 1735-1742. https://doi.org/10.1016/j.str.2013.08.005

Storer, C. L., Dickey, C. A., Galigniana, M. D., Rein, T., & Cox, M. B. (2011). FKBP51 and FKBP52 in signaling and disease. *22*(12), 481-490. https://doi.org/10.1016/j.tem.2011.08.001

Taipale, M., Jarosz, D. F., & Lindquist, S. (2010). HSP90 at the hub of protein homeostasis: emerging mechanistic insights. *11*(7), 515-528. https://doi.org/10.1038/nrm2918

Taipale, M., Krykbaeva, I., Koeva, M., Kayatekin, C., Westover, K. D., Karras, G. I., & Lindquist, S. (2012, Aug 31). Quantitative analysis of HSP90-client interactions reveals principles of substrate recognition. *Cell, 150*(5), 987-1001. https://doi.org/10.1016/j.cell.2012.06.047

Tatro, E. T., Everall, I. P., Kaul, M., & Achim, C. L. (2009). Modulation of glucocorticoid receptor nuclear translocation in neurons by immunophilins FKBP51 and

FKBP52: Implications for major depressive disorder. *Brain Research, 1286*, 1-12. https://doi.org/10.1016/j.brainres.2009.06.036

UniProt, C. (2021, Jan 8). UniProt: the universal protein knowledgebase in 2021. *Nucleic Acids Res, 49*(D1), D480-D489. https://doi.org/10.1093/nar/gkaa1100

Vandevyver, S., Dejager, L., & Libert, C. (2012, Mar). On the trail of the glucocorticoid receptor: into the nucleus and back. *Traffic, 13*(3), 364-374. https://doi.org/10.1111/j.1600-0854.2011.01288.x

Verba, K. A., Wang, R. Y. R., Arakawa, A., Liu, Y., Shirouzu, M., Yokoyama, S., & Agard, D. A. (2016). Atomic structure of Hsp90-Cdc37-Cdk4 reveals that Hsp90 traps and stabilizes an unfolded kinase. *Science, 352*(6293), 1542-1547. https://doi.org/10.1126/science.aaf5023

Wang, R. Y., Noddings, C. M., Kirschke, E., Myasnikov, A. G., Johnson, J. L., & Agard, D. A. (2022, Jan). Structure of Hsp90-Hsp70-Hop-GR reveals the Hsp90 client-loading mechanism. *Nature, 601*(7893), 460-464. https://doi.org/10.1038/s41586-021-04252-1

Wang, R. Y., Song, Y., Barad, B. A., Cheng, Y., Fraser, J. S., & DiMaio, F. (2016, Sep 26). Automated structure refinement of macromolecular assemblies from cryo-EM maps using Rosetta. *Elife, 5*. https://doi.org/10.7554/eLife.17219

Waterhouse, A. M., Procter, J. B., Martin, D. M., Clamp, M., & Barton, G. J. (2009, May 1). Jalview Version 2--a multiple sequence alignment editor and analysis workbench. *Bioinformatics, 25*(9), 1189-1191. https://doi.org/10.1093/bioinformatics/btp033

Weikum, E. R., Knuesel, M. T., Ortlund, E. A., & Yamamoto, K. R. (2017). Glucocorticoid receptor control of transcription: precision and plasticity via allostery. https://doi.org/10.1038/nrm.2016.152

Wochnik, G. M., Rüegg, J., Abel, G. A., Schmidt, U., Holsboer, F., & Rein, T. (2005). FK506-binding Proteins 51 and 52 Differentially Regulate Dynein Interaction and Nuclear Translocation of the Glucocorticoid Receptor in Mammalian Cells. *Journal of Biological Chemistry, 280*(6), 4609-4616. https://doi.org/10.1074/jbc.m407498200

Wolf, I. M., Periyasamy, S., Hinds, T., Jr., Yong, W., Shou, W., & Sanchez, E. R. (2009, Jan). Targeted ablation reveals a novel role of FKBP52 in gene-specific regulation of glucocorticoid receptor transcriptional activity. *J Steroid Biochem Mol Biol, 113*(1-2), 36-45. https://doi.org/10.1016/j.jsbmb.2008.11.006

Wu, B., Li, P., Liu, Y., Lou, Z., Ding, Y., Shu, C., Ye, S., Bartlam, M., Shen, B., & Rao, Z. (2004, Jun 1). 3D structure of human FK506-binding protein 52: implications

for the assembly of the glucocorticoid receptor/Hsp90/immunophilin heterocomplex. *Proc Natl Acad Sci U S A, 101*(22), 8348-8353. https://doi.org/10.1073/pnas.0305969101

Yu, K., Wang, Y., Zheng, Y., Liu, Z., Zhang, Q., Wang, S., Zhao, Q., Zhang, X., Li, X., Xu, R. H., & Liu, Z. X. (2022, Sep 27). qPTM: an updated database for PTM dynamics in human, mouse, rat and yeast. *Nucleic Acids Res*. https://doi.org/10.1093/nar/gkac820

Zannas, A. S., & Binder, E. B. (2014, Jan). Gene-environment interactions at the FKBP5 locus: sensitive periods, mechanisms and pleiotropism. *Genes Brain Behav, 13*(1), 25-37. https://doi.org/10.1111/gbb.12104

Zannas, A. S., Wiechmann, T., Gassen, N. C., & Binder, E. B. (2016, Jan). Gene-Stress-Epigenetic Regulation of FKBP5: Clinical and Translational Implications. *Neuropsychopharmacology, 41*(1), 261-274. https://doi.org/10.1038/npp.2015.235

Zgajnar, N. R., De Leo, S. A., Lotufo, C. M., Erlejman, A. G., Piwien-Pilipuk, G., & Galigniana, M. D. (2019, Feb 1). Biological Actions of the Hsp90-binding Immunophilins FKBP51 and FKBP52. *Biomolecules, 9*(2). https://doi.org/10.3390/biom9020052

Zhao, R., Davey, M., Hsu, Y. C., Kaplanek, P., Tong, A., Parsons, A. B., Krogan, N., Cagney, G., Mai, D., Greenblatt, J., Boone, C., Emili, A., & Houry, W. A. (2005, Mar 11). Navigating the chaperone network: an integrative map of physical and genetic interactions mediated by the hsp90 chaperone. *Cell, 120*(5), 715-727. https://doi.org/10.1016/j.cell.2004.12.024

Zheng, S. Q., Palovcak, E., Armache, J. P., Verba, K. A., Cheng, Y., & Agard, D. A. (2017, Apr). MotionCor2: anisotropic correction of beam-induced motion for improved cryo-electron microscopy. *Nat Methods, 14*(4), 331-332. https://doi.org/10.1038/nmeth.4193

Chapter 5 Cryo-EM reveals how the cochaperone PP5 regulates the Glucocorticoid Receptor

Preface

The work presented in this chapter was performed by rotation students I advised, Claire Kokontis and Estelle Ronayne. This chapter contains unpublished results that may be useful for future projects. The goal of this project was to determine how the Hsp90 cochaperone PP5, a serine/threonine-protein phosphatase, integrates with the GR chaperone cycle *in vitro* to regulate GR activity. Claire Kokontis characterized PP5 binding in the GR chaperone cycle, revealing PP5 preferentially binds to the GR-maturation complex. Claire also determined the first cryo-EM structures of the GR:Hsp90:p23:PP5 complex, which revealed two distinct reconstructions at low resolution that provided many novel insights. In one reconstruction, the PP5 phosphatase domain directly contacts the GR LBD, while a helical extension on the TPR domain binds the Hsp90 CTD dimer interface. Due to the separation of the PP5 phosphatase domain and TPR domain upon GR:Hsp90 binding, the PP5 autoinhibition is released and PP5 appears poised to dephosphorylate GR. In another reconstruction, PP5 binds the Hsp90 MD and charged linker on the opposite of the GR LBD and appears to remain in an autoinhibited state, with both the phosphatase and TPR domains bound together. Claire also performed experiments characterizing the PP5 effect on GR ligand binding *in vitro*. Estelle Ronayne, who was co-mentored with Maru Jaime-Garza, performed further experiments characterizing the effect of PP5 on GR

ligand binding *in vitro* and investigating the role of a PP5 mutant in the GR chaperone cycle.

Introduction

GR activity is regulated by the chaperones Hsp70 and Hsp90, as well as a variety of cochaperones which are found associated with GR:Hsp90 *in vivo* (Pratt et al., 2006; Pratt & Toft, 1997). One of these associated cochaperones is the serine/threonine-protein phosphatase, PP5 (Ppt1 in yeast). PP5 is predominantly localized in the nucleus, but also found in the cytosol (Chen et al., 1994) and can be associated with ligand-free GR:Hsp90 complexes in both the cytosol and nucleus (Silverstein et al., 1997). PP5 competes with the cochaperones FKBP51, FKBP52, and Cyp40 to bind GR:Hsp90 complexes (Silverstein et al., 1997). Like FKBP52, PP5 may also regulate GR nuclear localization by serving as a linker to the dynein motor system (Dean et al., 2001; DeFranco et al., 1991; Galigniana et al., 2002; Galigniana et al., 1999). Functionally, PP5 appears to be a negative regulator of GR activity. PP5 (Ppt1) deletion increases GR transactivation in yeast (Sahasrabudhe et al., 2017) and PP5 knockdown increases GR transactivation in cultured human cancer cells (Biebl et al., 2021; Wang et al., 2007; Zuo et al., 1999).

GR is regulated by many different PTMs, including phosphorylation by multiple kinase signaling pathways (JNKs, CDKs, and MAPKs), under varying cellular contexts (**Fig. 1**) (Weikum et al., 2017). Specifically, ligand addition is correlated with an increase in phosphorylation at sites S203 and S211 in the GR NTD and nuclear localization of GR is associated with increased phosphorylation at S211 (Wang et al., 2002). Increased phosphorylation at S226 in the GR NTD is associated with nuclear export

(Itoh et al., 2002). PP5 inhibition results in GR hyperphosphorylation (DeFranco et al., 1991) and specifically, PP5 knockdown is correlated with an increase in phosphorylation at GR S203 and S226, in a manner dependent upon the GR LBD (Wang et al., 2007).

PP5 is composed of an N-terminal TPR domain, which can bind either the Hsp70 C-terminal IEEVD motif or Hsp90 C-terminal MEEVD motif (Connarn et al., 2014), and a C-terminal phosphatase domain, which is autoinhibited by the TPR domain (**Fig. 2**). The binding of the TPR and phosphatase domains physically blocks the phosphatase catalytic site and TPR EEVD binding groove (PDB ID 1WAO) (Yang et al., 2005). PP5 interaction with Hsp90 relieves the autoinhibition, but interestingly, the MEEVD motif on Hsp90 is not sufficient, suggesting interactions with Hsp90 beyond the MEEVD are needed for release of autoinhibition. Without the phosphatase domain, the PP5 TPR adopts an extended Helix 7 (H7e), as seen with the FKBP51 and FKBP52 TPR domains (PDB ID 1KT0, 1QZ2, respectively) (Sinars et al., 2003; Wu et al., 2004).

A recent cryo-EM structure of CRaf:Hsp90:Cdc37:PP5 by Maru Jaime-Garza from the Agard lab (Jaime-Garza et al., 2022) reveals that the PP5 phosphatase domain and TPR domain come apart when PP5 binds Hsp90, relieving the autoinhibition (**Fig. 3**). The phosphatase domain is directly bound to the C-lobe of the partially unfolded kinase client, CRaf, poised to dephosphorylate the kinase. The linker between the TPR domain and phosphatase domains interacts with Hsp90. Surprisingly, the PP5 TPR H7e binds to the Hsp90 CTD closed dimer interface, while the Hsp90 MEEVD motif binds in the PP5 TPR helical bundle, as expected. In the GR:Hsp90:p23:FKBP51 cryo-EM structure (Lee et al., 2021) and the GR:Hsp90:FKBP51/52 cryo-EM structures (Chapter 3), the FKBP TPR H7e also binds the Hsp90 CTD closed dimer interface. However, the

PP5 H7e binds in a completely different orientation to Hsp90 relative to FKBP51 and FKBP52, demonstrating sequence divergence in the H7e between the cochaperones can have profound effects on the Hsp90:H7e interaction. Garza et al. 2022 also demonstrated that mutation to the PP5 H7e:Hsp90 CTD interaction reduces CRaf dephosphorylation, indicating the importance of the PP5 H7e:Hsp90 interaction for PP5-dependent client dephosphorylation. How PP5 integrates with other Hsp90:client complexes to regulate client activity is unclear and thus we investigated how PP5 influences the GR chaperone cycle and regulates GR activity *in vitro*.

Results

PP5 binds to the GR-maturation complex

To determine how PP5 integrates with the GR-chaperone cycle, PP5 was added to the *in vitro* reconstituted GR:Hsp70 complex, GR-loading complex, or GR-maturation complex. The GR-loading complex was prepared as previously described (Wang et al., 2022), using an ATP-binding deficient Hsp90 (Hsp90 D93N) that stalls the GR chaperone cycle at the GR-loading complex. The GR-maturation complex was prepared as previously described (Noddings et al., 2022), using Bag-1 to promote transition from the GR-loading complex to the GR-maturation complex and using sodium molybdate to stabilize the closed conformation of Hsp90. PP5 was added to either the GR:Hsp70 complex, GR-loading complex, or GR-maturation complex preparations, then the complexes were purified using an affinity purification against the N-terminal MBP on GR, and the resulting eluates were analyzed by SDS-PAGE gel (Fig. 4).

These experiments demonstrated that PP5 co-elutes with the GR-maturation complex, using either the GR LBD (amino acids 521-777) or GR DBD-LBD (amino acids 418-777) constructs (note that the GR LBD protein is in a predominantly apo state, while the GR DBD-LBD protein is likely in a predominantly ligand-bound state due to differences in purification procedures). PP5 does not strongly co-elute with the GR-loading complex, although there is a faint band that likely corresponds to PP5, which could be due to a low level of non-specific binding. PP5 also does not co-elute with the GR:Hsp70 complex, despite having a TPR that can bind the Hsp70 IEEVD motif. It has been previously reported that PP5 binds the Hsp70 IEEVD motif with lower affinity compared to the Hsp90 MEEVD motif, supporting our results (Connarn et al., 2014). Altogether, PP5 appears to specifically bind the GR-maturation complex, in which Hsp90 adopts a closed conformation. This is consistent with the CRaf:Hsp90:Cdc37:PP5 structure, in which PP5 specifically binds the closed conformation of Hsp90 (Jaime-Garza et al., 2022).

GR:Hsp90:p23:PP5 structure determination

The GR:Hsp90:p23:PP5 structure was prepared by *in vitro* reconstitution of the complete GR chaperone cycle. GR DBD-LBD (amino acids 418-777) with an N-terminal maltose-binding protein (MBP) tag was incubated with Hsp70, Hsp40, Hop, Hsp90, p23, and PP5, allowing GR to progress through the chaperone cycle to reach the GR:Hsp90:p23:PP5 complex. The complex was stabilized with sodium molybdate and then purified by affinity purification on MBP-GR followed by size exclusion chromatography and light crosslinking (Fig. 5). Deposition of the uncrosslinked sample

onto Quantifoil 1.2/1.3 Cu 400 mesh grids resulted in an interesting clustering of particles on the grid, which did not appear to be aggregated (Fig. 6). The use of functionalized PEG-2k (polyethylene glycol 2000) amino grids developed by Feng Wang from the Agard Lab (Wang et al., 2020) resulted in normal particle distribution on the grids and were used to collect a small dataset.

Two distinct GR:Hsp90:p23:PP5 reconstructions were obtained from the dataset using RELION (Fig. 7). The first reconstruction at 12.8 Å resembled the GR-maturation complex at low-resolution. The atomic model for the GR-maturation complex (PDB ID 7KRJ) (Noddings et al., 2022) fit well into the density, with a closed Hsp90 dimer bound to the folded GR LBD and p23 bound to the Hsp90 NTDs (Fig. 8). Extra density was clearly visible at two locations—one corresponding to the PP5 TPR domain binding to the Hsp90 CTD dimer interface and the other corresponding to the PP5 phosphatase domain bound to the GR LBD and Hsp90 MD.

The position and orientation of the PP5 phosphatase and TPR domains appears the same as seen in the CRaf:Hsp90:Cdc37:PP5 structure, despite having different clients and cochaperones bound to the complex (Fig. 8). H7e binds the Hsp90 CTD dimer interface in the same manner and the PP5 phosphatase domain is positioned between the Hsp90 CTDs and the client, adopting the same position and orientation. The orientation of the PP5 phosphatase domain places the PP5 catalytic site pointing toward, but not touching, the GR LBD. Additionally, the PP5 phosphatase domain appears to interact with the GR LBD near GR Helix 3, which forms the bottom of the GR ligand-binding pocket and may allow PP5 to specifically recognize specific liganded states of GR (apo vs. ligand-bound). Altogether, in reconstruction #1, PP5 autoinhibition

has been released due to the separation of the phosphatase and TPR domains and PP5 appears to be poised to dephosphorylate GR.

The second reconstruction at 14.3 Å also resembled the GR-maturation complex with extra density. The atomic model for the GR-maturation complex (PDB ID 7KRJ) (Noddings et al., 2022) also fit well into the density, with a closed Hsp90 dimer bound to the folded GR LBD and p23 bound to the Hsp90 NTDs. An extra density likely corresponding to PP5 is seen between the Hsp90 MD and the Hsp90B charged linker (Fig. 9). The putative PP5 density is bound on the side of the Hsp90 dimer opposite p23 and the GR LBD, possibly interacting with the GR hinge region, which would be exiting through the Hsp90 lumen on that side. Despite using the GR DBD-LBD construct, the GR hinge and DBD region are not visible in the density, likely due to their high degree of flexibility, consistent with the results from the GR DBD-LBD:Hsp90:FKBP cryo-EM structures (Chapter 3). Interestingly, the putative PP5 density appears to have two lobes, possibly corresponding to the PP5 phosphatase domain and TPR domain bound together in the autoinhibited state. Indeed, the autoinhibited state of PP5 seen in the crystal structure (1WAO) (Yang et al., 2005) fits well into the density. Although it is difficult to unambiguously assign an orientation for PP5 in reconstruction #2 due to the limited resolution, the catalytic site would not be positioned near Hsp90 or any components of the complex in the orientation we have assigned. Thus, in reconstruction #2, PP5 appears to be in an autoinhibited state and is not directly interacting with the GR LBD, in contrast to reconstruction #1.

In both reconstructions, GR appears to be in a native, folded state with the same orientation described in the GR-maturation complex (Noddings et al., 2022). GR does

not appear to adopt a rotated position as seen in the GR:Hsp90:FKBP complex (Chapter 3). However, the overall resolution of the reconstruction is low; therefore, it is unclear if there are small perturbations to the GR conformation or orientation relative to the GR-maturation complex. In addition, the ligand state of GR cannot be determined from the reconstruction; however, ligand was not removed from the GR DBD-LBD protein used in this sample, so GR Is likely in a ligand-bound state.

PP5 effect on GR ligand binding

To quantitatively assess the functional significance of PP5 on GR activation, we added PP5 to the *in vitro* reconstituted GR-chaperone cycle, using the GR LBD construct and monitored GR ligand-binding, as previously described (Kirschke et al., 2014; Noddings et al., 2022). Addition of PP5 to the GR chaperone mix resulted in a reduction in GR ligand-binding; however, GR ligand-binding activity was still higher than that of GR alone (without the chaperones) (Fig. 10). It should be noted that later attempts to recapitulate this result were not successful. When repeating this experiment, Claire Kokontis found PP5 does not have an effect on GR ligand-binding in the chaperone cycle. Estelle Ronayne also attempted to repeat these experiments with the GR DBD-LBD construct and similarly found that neither PP5 nor the PP5$\Delta\alpha$J mutant (discussed below) have an effect on GR ligand-binding in the chaperone cycle (Fig. 11).

Our biochemistry and structural findings demonstrate that PP5 preferentially binds the closed conformation of Hsp90 at the closed CTD dimer interface. We wondered whether PP5 can stabilize Hsp90 closure through this interaction, in a manner similar to p23, which is known to stabilize Hsp90 NTD closure through the

globular p23 domain (Ali et al., 2006; Noddings et al., 2022). Omitting p23 from the GR chaperone cycle drastically reduces GR ligand-binding, as previously described (Kirschke et al., 2014; Noddings et al., 2022). The addition of PP5 in place of p23 has no effect on GR ligand-binding activity, demonstrating PP5 cannot functionally replace p23 (Fig. 12).

Our structures also demonstrate that PP5 directly binds to the GR LBD in reconstruction #1 near the ligand-binding site, so we wondered whether PP5 stabilizes the folded, ligand-bound GR LBD, in a manner similar to the p23 tail-helix (Noddings et al., 2022). As previously described, removal of the p23 tail-helix (p23ΔhelixΔ) resulted in a decrease in GR ligand-binding activity in the GR chaperone system. The addition of PP5 had no effect on GR ligand-binding with the p23ΔhelixΔ mutant, thus PP5 cannot functionally replace the p23 tail-helix (Fig. 13).

PP5 ΔαJ mutant binds the GR:Hsp90:p23 complex

The PP5 C-terminal αJ helix makes stabilizing interdomain interactions in the autoinhibited PP5 crystal structure (PDB ID: 1WAO) (Yang et al., 2005); however, in the CRaf:Hsp90:Cdc37:PP5 cryo-EM structure, there was no apparent density for the PP5 αJ helix and the canonical position of the αJ helix would clash with the client in this structure, suggesting the αJ helix becomes disordered to engage client (Jaime-Garza et al., 2022). Thus, we tested whether a PP5 mutant lacking the αJ helix (PP5ΔαJ) (amino acids 1-489) would engage more strongly with the GR:Hsp90:p23 complex compared to wildtype PP5. PP5 or PP5ΔαJ were added to the *in vitro* reconstituted GR chaperone cycle. The GR:Hsp90:p23: PP5 complexes was stabilized with sodium molybdate and

then purified by affinity purification on MBP-GR and analyzed by SDS-PAGE gel. Both PP5 and PP5ΔαJ co-eluted with GR:Hsp90:p23, indicating PP5ΔαJ can integrate into the GR:Hsp90:p23 complex, like the wildtype PP5. The PP5ΔαJ band intensity was slightly stronger than PP5, indicating PP5ΔαJ may bind with slightly higher affinity to the GR:Hsp90:p23 complex (Fig. 14).

Discussion

We have determined the first structures of the Hsp90 cochaperone PP5 bound to the GR:Hsp90 complex. We present two low-resolution cryo-EM structures of the GR:Hsp90:p23:PP5 complex, demonstrating PP5 can bind in two distinct modes to the GR:Hsp90:p23 complex. In the first structure, PP5 binds Hsp90 in an active conformation, with the phosphatase domain and TPR domains split apart, relieving the autoinhibited state. The TPR domain binds the Hsp90 CTD dimer interface through TPR H7e, while the phosphatase domain directly binds GR, consistent with the orientation and active conformation of PP5 in the CRaf:Hsp90:Cdc37:PP5 structure (Jaime-Garza et al., 2022). Unlike the CRaf:Hsp90:Cdc37:PP5 structure, density for the linker between the phosphatase and TPR domains cannot be seen in our low-resolution reconstruction.

In the second structure, PP5 binds the Hsp90A/B MD and Hsp90B charged linker. In this structure, PP5 appears to be in the autoinhibited conformation, although the low-resolution of the reconstruction prohibits a confident assignment to this density. In this structure, PP5 is bound on the opposite side of the GR LBD and p23, potentially poised to interact with the GR hinge region or DBD. While neither the hinge nor DBD

are visible in this reconstruction, this is likely due to their high degree of flexibility, consistent with the results from the GR DBD-LBD:Hsp90:FKBP cryo-EM structures (Chapter 3). Obtaining higher resolution reconstructions may reveal interactions between the inactive phosphatase and the hinge or DBD regions of GR. It is unclear if this structure represents a physiologically relevant complex. This structure may be an artifact of crosslinking with relatively high concentrations of PP5 present in the sample, especially given that the charged linker, which is involved in the putative interaction, contains many exposed lysine residues available for crosslinking.

Altogether, our structures contribute to an emerging theme in which Hsp90 cochaperones directly stabilize specific Hsp90 conformations and simultaneously bind specific client conformations (Jaime-Garza et al., 2022; Noddings et al., 2022; Verba et al., 2016; Wang et al., 2022). We have demonstrated that PP5 favors binding to the closed conformation of Hsp90 and demonstrated this interaction is mediated through the PP5 H7e:Hsp90 CTD dimer interface, as seen in the CRaf:Hsp90:Cdc37:PP5 structure (Jaime-Garza et al., 2022). Although PP5 preferentially binds to the closed state of Hsp90, we have demonstrated that PP5 cannot stabilize the Hsp90 closed state akin to p23 and thus p23 is still required for full reactivation of GR ligand-binding in the chaperone cycle, even when PP5 is present. Interestingly, we also demonstrate PP5 is not able to stabilize the ligand-bound GR state akin to the p23 tail-helix, although PP5 directly binds the GR LBD in reconstruction #1. In contrast, we have shown that FKBP51 and FKBP52 can functionally replace the p23 tail-helix due to their ability to stabilize the ligand-bound GR LBD through an extensive, direct interaction (Chapter 3). The PP5:GR LBD interaction interface is quite small in comparison. Rather than serving

to stabilize the GR LBD in a particular conformation, it is likely that this interface serves to orient the PP5 catalytic site of the phosphatase domain. The PP5 catalytic site is accessible to substrate in reconstruction #1, but as expected, there is no apparent density for substrate in the active site because (1) GR was purified in *E. coli* and lacks the relevant phosphorylation modifications and (2) the GR construct does not contain the NTD, where the putative PP5 dephosphorylation sites reside.

Based on our cryo-EM structures and biochemistry data, we propose a model describing how PP5 modulates the GR phosphorylation state to regulate GR activity *in vivo* (Fig. 15). We propose PP5 binds to the ligand-free GR-maturation complex (GR:Hsp90:p23), consistent with *in vivo* reports (Silverstein et al., 1997). The PP5 phosphatase and TPR domains come apart to bind the GR LBD and Hsp90 CTD dimer interface, respectively, which relieves the PP5 autoinhibition. The PP5 phosphatase domain binds the folded GR LBD and may bind specifically to the apo GR LBD state, which may be sensed by the PP5 interaction with GR Helix 3.

The GR LBD:PP5 phosphatase interaction positions the PP5 catalytic site such that it is accessible to substrate. We propose PP5 is positioned to capture the flexible, disordered GR NTD to dephosphorylate the putative substrate residues, S206 and S226. Dephosphorylation at these residues acts as a signal to repress GR activation (perhaps inhibiting nuclear translocation or the assembly of GR transcription regulatory complexes), allowing PP5 to act as a negative regulator of GR activity (Biebl et al., 2021; Sahasrabudhe et al., 2017; Wang et al., 2007; Zuo et al., 1999). When ligand is present in the cell, PP5 binding to the ligand-bound GR is disfavored, allowing GR to

retain phosphorylation at S205 and S226, which act as signals to allow downstream activation of GR.

Further investigation is needed to determine the functions of phosphorylation/dephosphorylation at specific sites on GR. Currently, changes in phosphorylation at specific sites on GR are correlated with some GR functions, but these signals likely provide more direct regulation of GR activity in the cell that have yet to be characterized. Another interesting aspect to explore is the effect of competition between PP5 and other Hsp90 cochaperones. In particular, PP5 binding in the active form (reconstruction #1) appears to be competitive with FKBP51 and FKBP52 based on our cryo-EM structures (Chapter 3) and *in vivo* biochemistry (Silverstein et al., 1997). PP5 competition with FKBP52 in particular would likely reduce GR ligand-binding and nuclear translocation, further inhibiting GR activity. How GR activity is affected by the interplay between PP5 and other cochaperones remains to be characterized and perhaps competition between the various cochaperones allows for fine-tuned regulation of GR in different cellular contexts or tissue types.

Figures

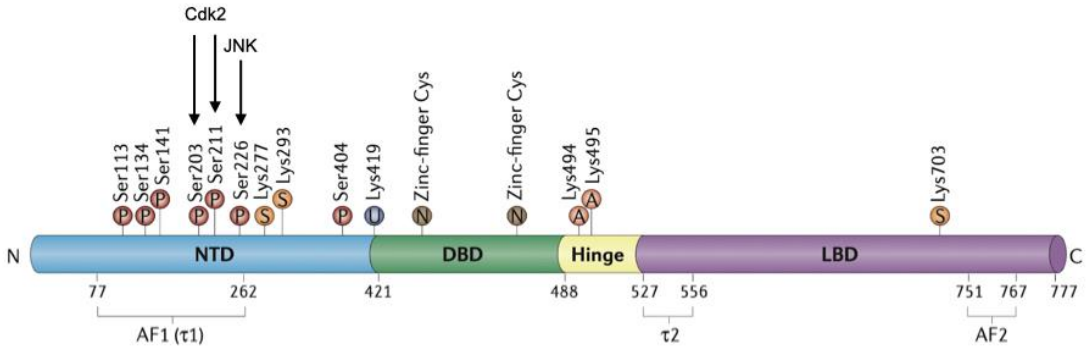

Fig. 5.1: PTMs on human GR
This figured is adapted from Weikum et al. 2017 and depicts the identified PTMs that are found on human GR. Cdk2 is through to phosphorylate S203 and S211, while JNK is thought to phosphorylate S226. PP5 appears to dephosphorylate S203 and S226.

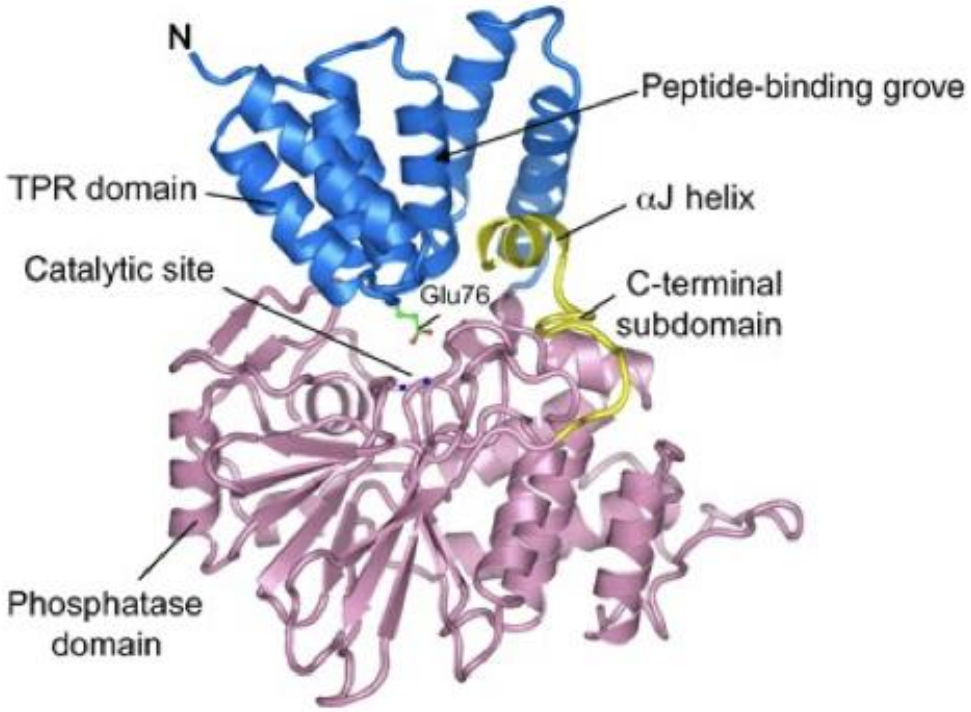

Fig. 5.2: Crystal structure of the inhibited PP5 conformation
This figure is adapted from Yang et al. 2005 and shows the crystal structure of the inhibited PP5 (PDD ID 1WAO) (Yang et al. 2005). The phosphatase and TPR domains bind together, blocking the phosphatase catalytic site. The EEVD binding grove on the TPR domain is partially blocked in this conformation. The C-terminal αJ helix provides stabilizing interdomain interactions.

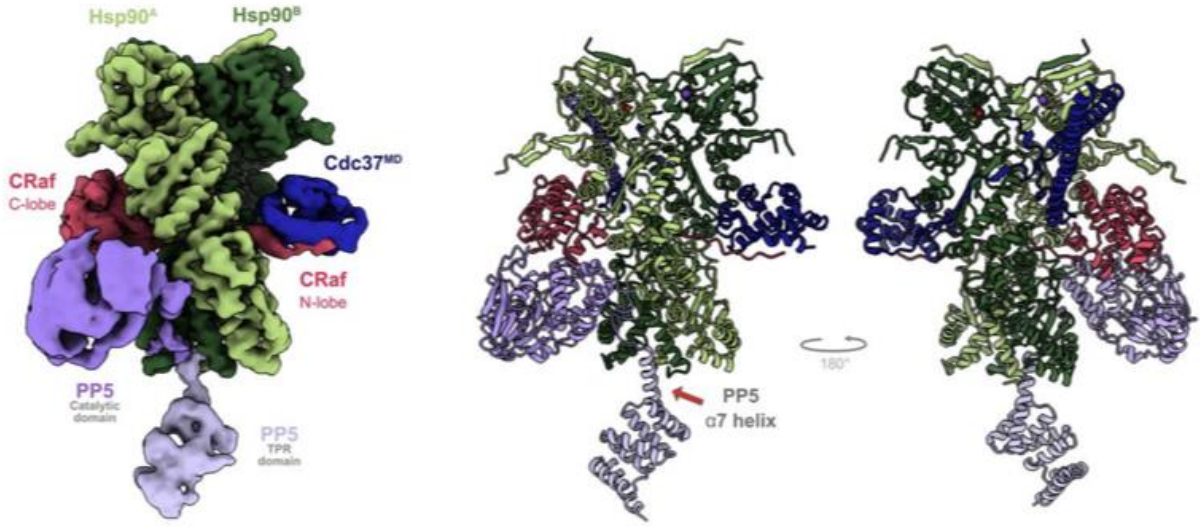

Fig. 5.3: Cryo-EM structure of the CRaf:Hsp90:Cdc37:PP5 complex
This figure is adapted from Garza et al. 2022 and shows the cryo-EM structure of the CRaf (kinase):Hsp90:Cdc37:PP5 complex. PP5 adopts an active conformation, with the phosphatase and TPR domains separated, each binding to Hsp90. The TPR H7e (α7 helix) binds the Hsp90 CTD dimer interface, while the phosphatase domain binds the CRaf C-lobe and Hsp90A CTD. The linker between the phosphatase and TPR domains binds along the Hsp90A CTD. This structure demonstrated that PP5 binding to Hsp90 relives the autoinhibited state, poising PP5 to dephosphorylate the client. This structure also demonstrated that the PP5 phosphatase domain directly binds the client protein beyond the catalytic site and that PP5 binding is compatible with Cdc37.

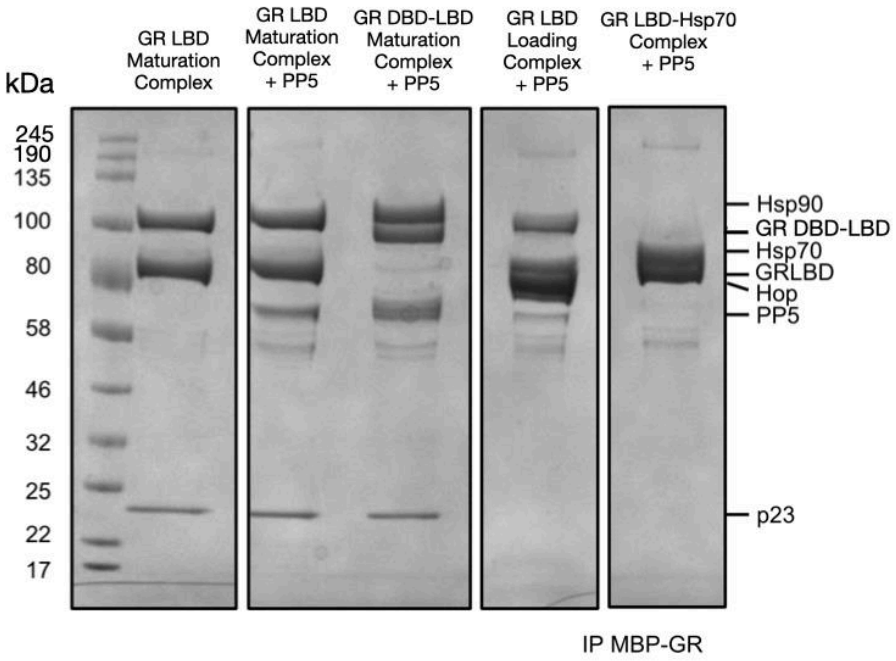

Fig. 5.4: PP5 preferentially binds the GR-maturation complex
A 4-12% SDS-PAGE gel after affinity purification on the MBP-GR with the addition of the chaperone system (Hsp70, Hsp40, Hsp90, Hop, p23) and PP5. Different complexes within the GR chaperone cycle were enriched before the MBP-GR affinity purification (either the GR-loading complex, GR-maturation complex, or GR-Hsp70 complex). See Methods for assay conditions.

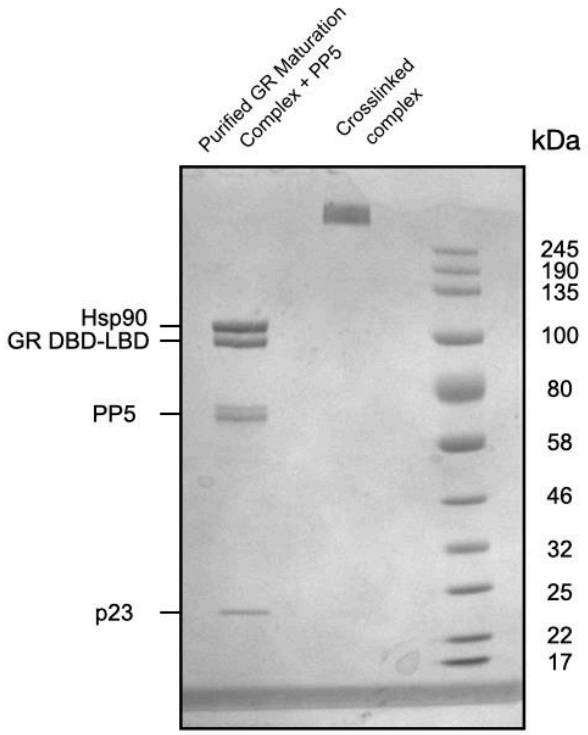

Fig. 5.5: Preparation of the GR:Hsp90:p23:PP5 complex for cryo-EM
A 4-12% SDS-PAGE gel after affinity purification on the MBP-GR with the addition of the chaperone system (Hsp70, Hsp40, Hsp90, Hop, p23) and PP5, with conditions to enrich for the GR-maturation complex. The purified GR-maturation complex + PP5 (left lane) was concentrated and purified by size exclusion. Fractions containing the full complex were crosslinked with 0.02% glutaraldehyde for 20 minutes at room temperature. The sample was then concentrated to ~2 μM (middle lane, “crosslinked complex”).

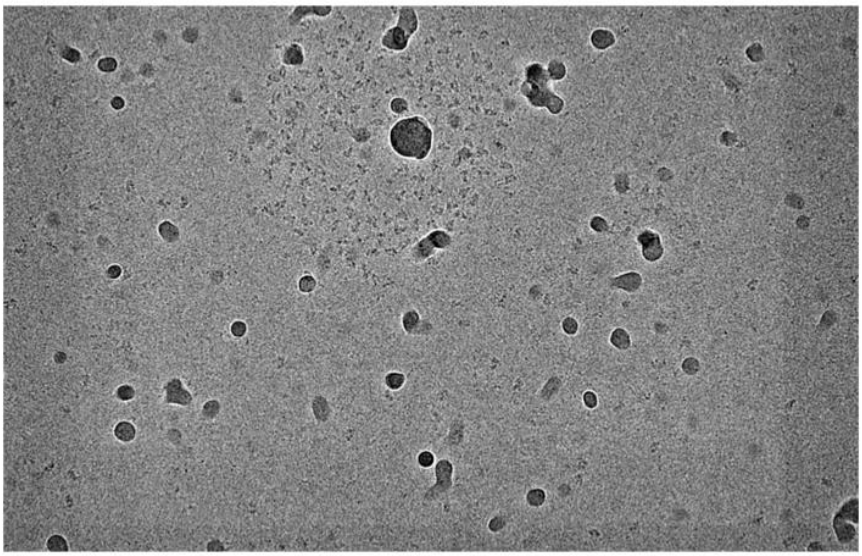

Fig. 5.6: GR:Hsp90:p23:PP5 complexes cluster on Quantifoil grids
GR:Hsp90:p23:PP5 complexes were prepared as described in the Methods. This sample was not crosslinked. 2.5 μL of sample was applied to Quantifoil Cu 400 1.2/1.3 grids and imaged on an Arctica electron microscope. The micrographs show the complex clustered in a roughly spherical shape. This is a representative micrograph. All micrographs obtained (approximately 10) exhibited this clustering.

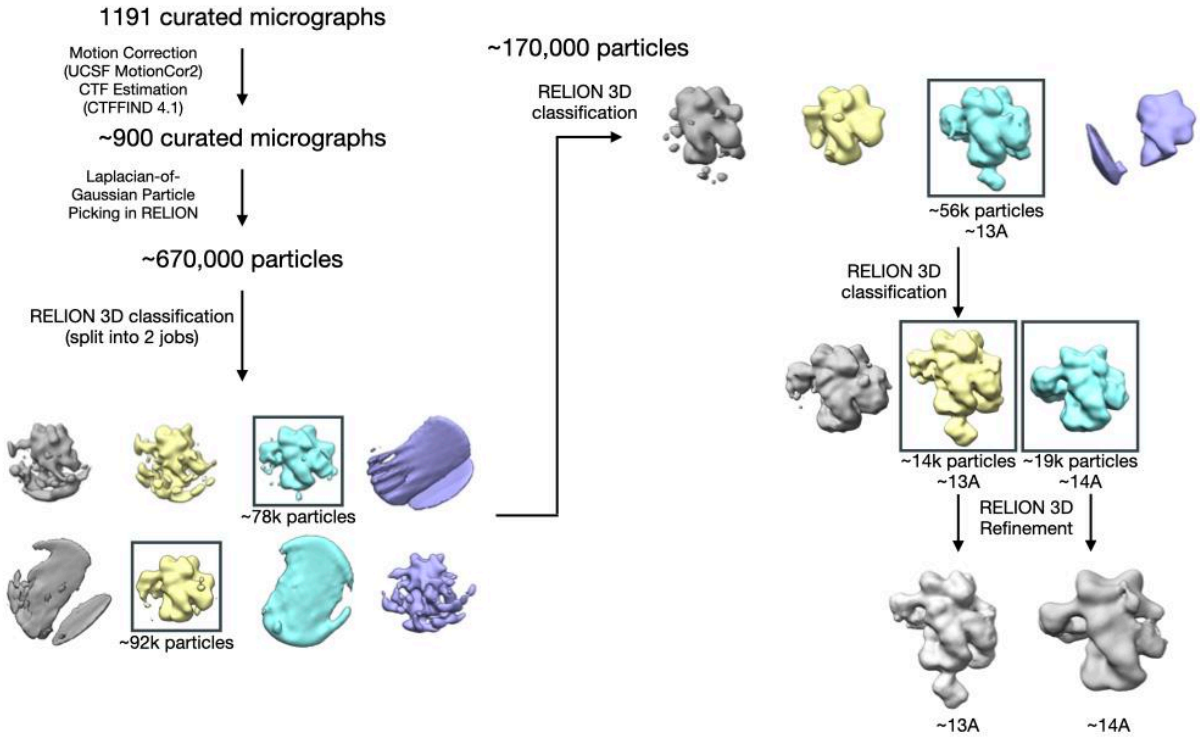

Fig. 5.7: Cryo-EM data processing scheme for the GR:Hsp90:p23:PP5 complex
Cryo-EM data processing procedure in RELION resulting in two low-resolution 3D reconstructions of the GR:Hsp90:p23:PP5 complex.

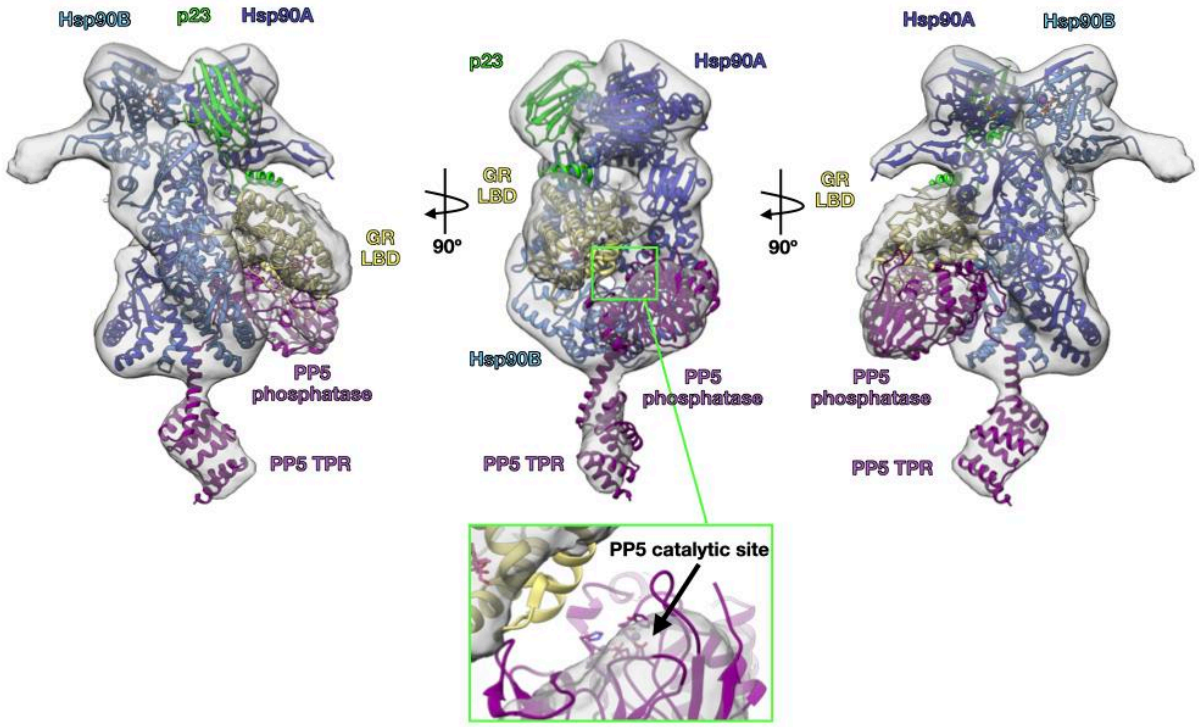

Fig. 5.8: Cryo-EM structure of the GR:Hsp90:p23:PP5 reconstruction #1
Atomic models fit into cryo-EM reconstruction #1 of the GR:Hsp90:p23:PP5 complex. The GR-maturation complex (GR:Hsp90:p23) fits well into the density (PDB ID 7KRJ) (Noddings et al. 2022). The separate phosphatase and TPR domains fit well into the extra density (PDB ID 1WAO) (Yang et al. 2005). The green box indicates the position of the PP5 phosphatase catalytic site in relation to the GR LBD.

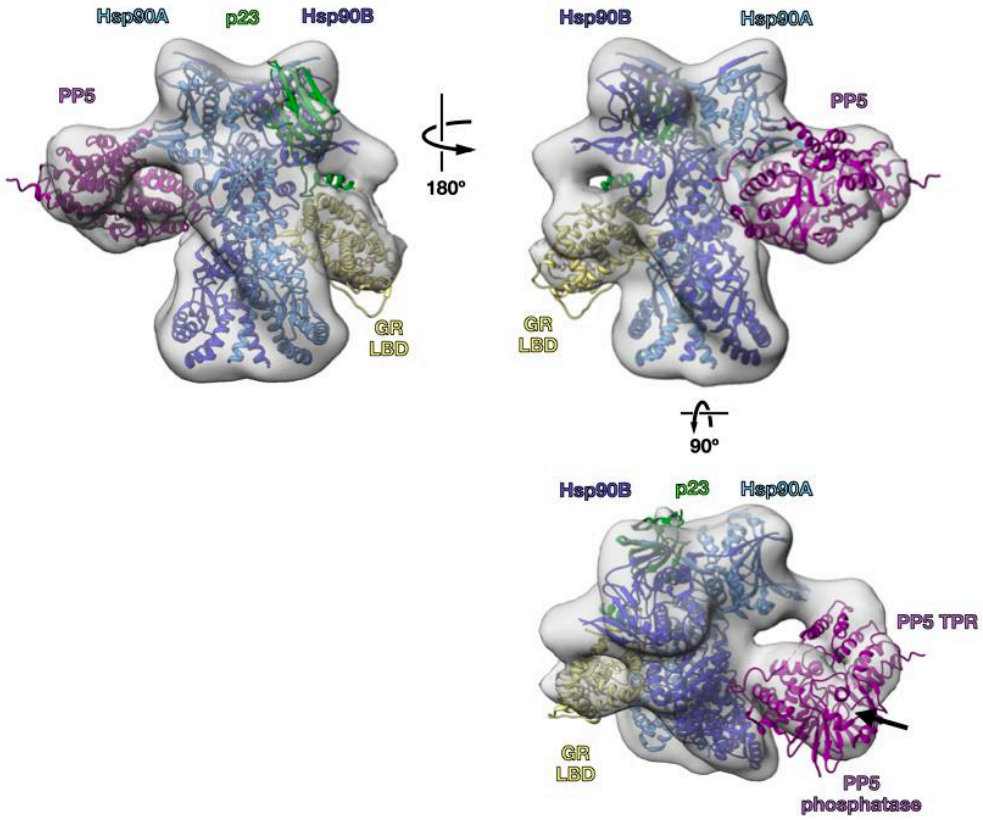

Fig. 5.9: Cryo-EM structure of the GR:Hsp90:p23:PP5 reconstruction #2
Atomic models fit into cryo-EM reconstruction #2 of the GR:Hsp90:p23:PP5 complex. The GR-maturation complex (GR:Hsp90:p23) fits well into the density (PDB ID 7KRJ) (Noddings et al. 2022). The inhibited PP5 conformation fits well into the extra density (PDB ID 1WAO) (Yang et al. 2005).

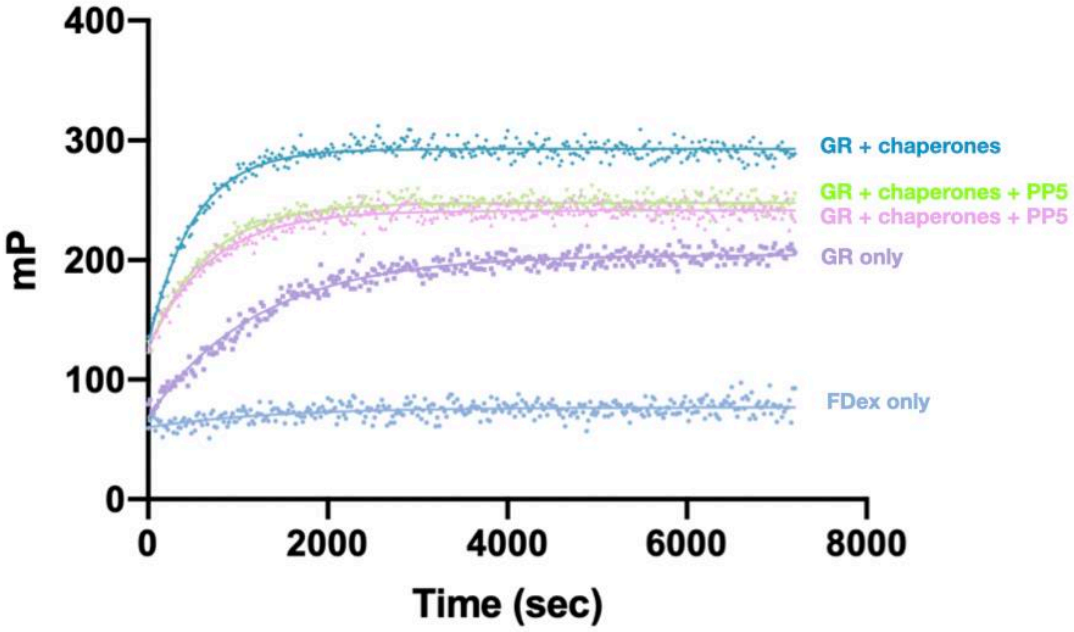

Fig. 5.10: Effect of PP5 on GR ligand-binding *in vitro* with the chaperone system
Time course of 250 nM GR LBD binding to 20 nM fluorescent dexamethasone (Fdex) measured by fluorescence polarization anisotropy (mP = milliPolarization units). Chaperones = 2 μM Hsp40, 15 μM Hsp70, 15 μM Hsp90, 15 μM Hop, 15 μM p23, and 5 mM ATP/$MgCl_2$. 15 μM PP5 was added to reactions as indicated. Reactions were pre-equilibrated for 1 hour before Fdex addition at time 0 seconds.

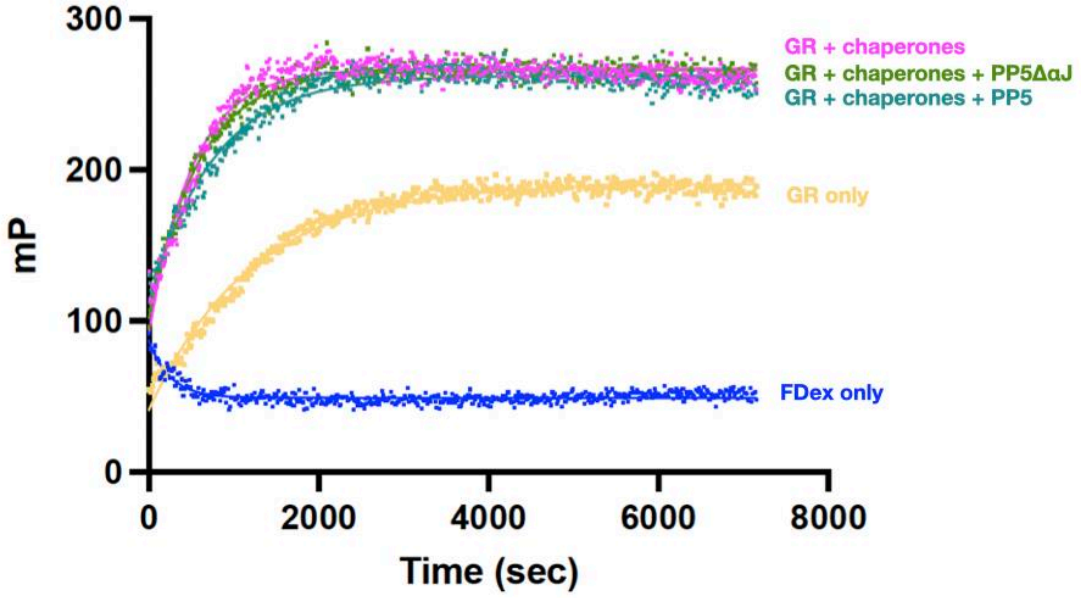

Fig. 5.11: Effect of PP5 and PP5ΔαJ on GR ligand-binding *in vitro* with the chaperone system

Time course of 250 nM GR LBD binding to 20 nM fluorescent dexamethasone (Fdex) measured by fluorescence polarization anisotropy (mP = milliPolarization units). Chaperones = 2 μM Hsp40, 15 μM Hsp70, 15 μM Hsp90, 15 μM Hop, 15 μM p23, and 5 mM ATP/$MgCl_2$. 15 μM PP5 or PP5ΔαJ were added to reactions as indicated. Reactions were pre-equilibrated for 1 hour before Fdex addition at time 0 seconds.

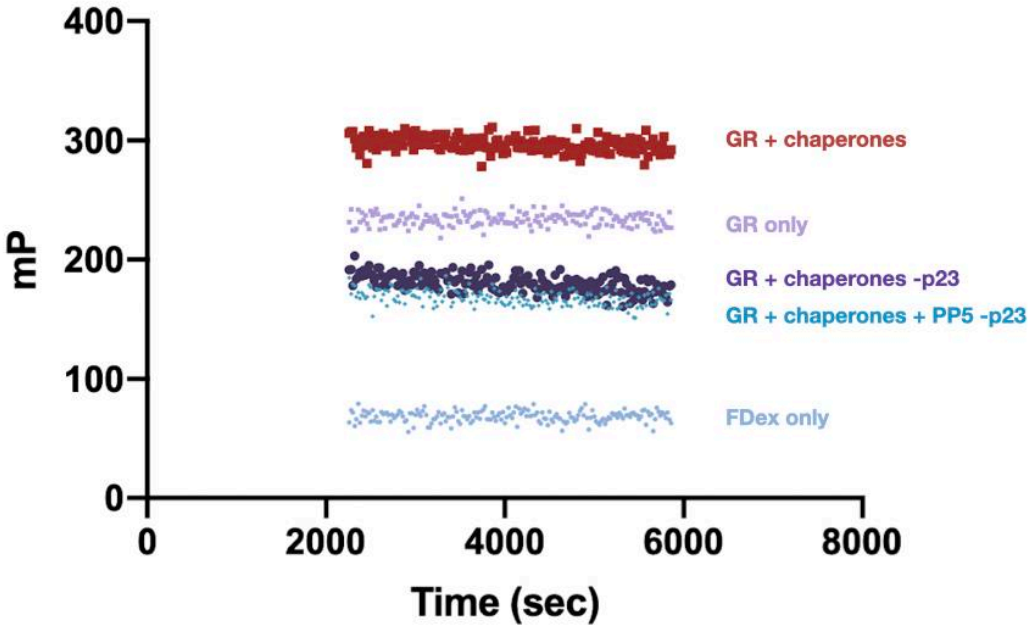

Fig. 5.12: PP5 cannot functionally replace p23 in the GR chaperone system
Time course of 250 nM GR LBD binding to 20 nM fluorescent dexamethasone (Fdex) measured by fluorescence polarization anisotropy (mP = milliPolarization units). Chaperones = 2 μM Hsp40, 15 μM Hsp70, 15 μM Hsp90, 15 μM Hop, 15 μM p23, and 5 mM ATP/$MgCl_2$. P23 was omitted from some reactions as indicated. 15 μM PP5 as added to reactions as indicated. The reactions had already reached equilibrium when the measurement was started (~2000 seconds after fluorescent dexamethasone addition). Reactions were pre-equilibrated for 1 hour before Fdex addition at time 0 seconds.

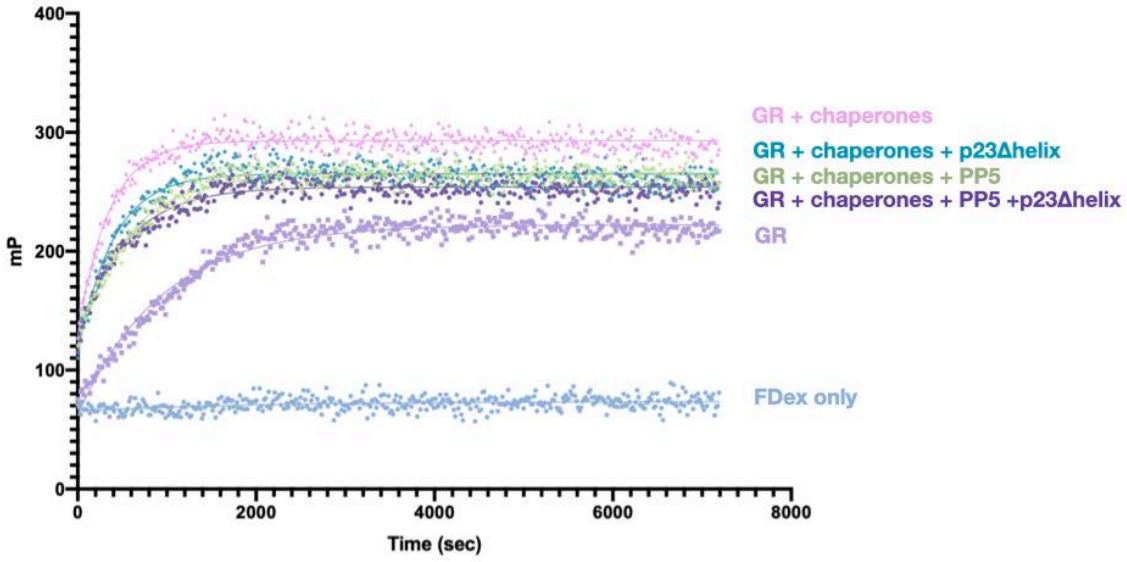

Fig. 5.13: PP5 cannot functionally replace the p23 tail-helix in the GR chaperone system

Time course of 250 nM GR LBD binding to 20 nM fluorescent dexamethasone (Fdex) measured by fluorescence polarization anisotropy (mP = milliPolarization units). Chaperones = 2 μM Hsp40, 15 μM Hsp70, 15 μM Hsp90, 15 μM Hop, 15 μM p23 or p23Δhelix, and 5 mM ATP/$MgCl_2$. 15 μM PP5 was added to reactions as indicated. Reactions were pre-equilibrated for 1 hour before Fdex addition at time 0 seconds.

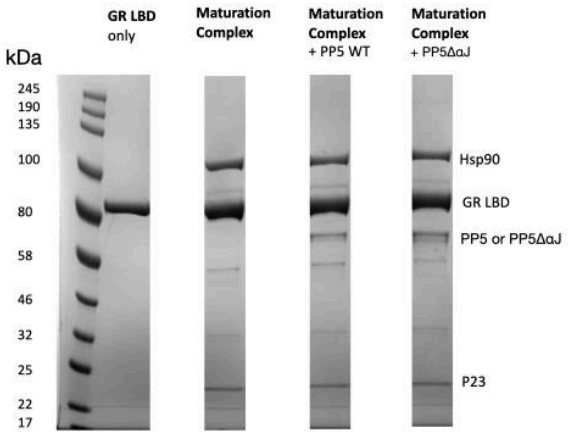

Fig. 5.14: PP5 and PP5ΔαJ bind to the GR-maturation complex with comparable affinities

A 4-12% SDS-PAGE gel after affinity purification on the MBP-GR with the addition of the chaperone system (Hsp70, Hsp40, Hsp90, Hop, p23) and PP5 or PP5ΔαJ. The GR-maturation complex was enriched before the MBP-GR affinity purification. See Methods for assay conditions.

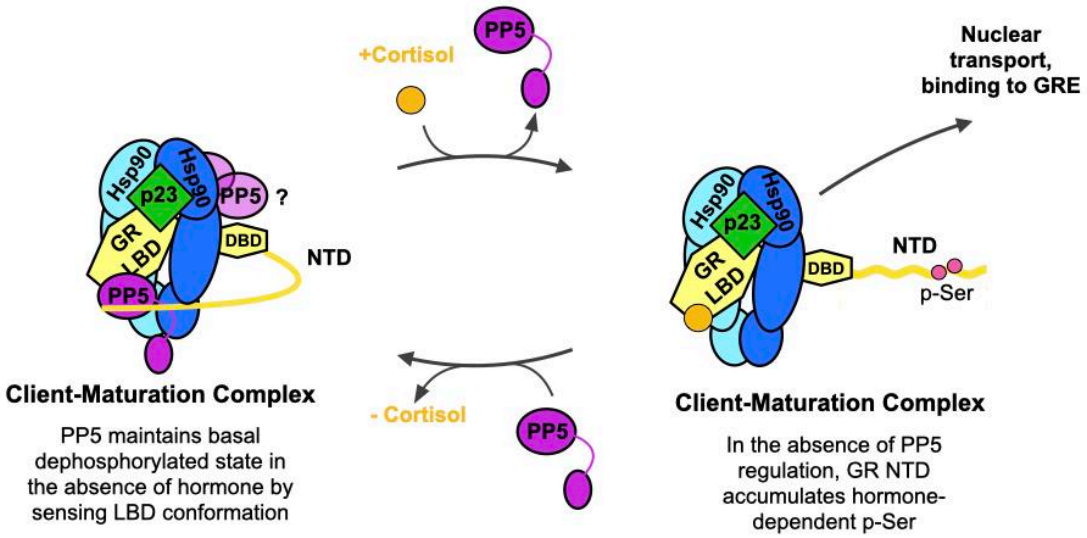

Fig. 5.15: Model for the PP5-dependent regulation of GR activity in the chaperone cycle

PP5 binds to the ligand-free GR-maturation complex (GR:Hsp90:p23) (left). The PP5 phosphatase and TPR domains come apart to bind the GR LBD and Hsp90 CTD dimer interface, respectively, which relieves the PP5 autoinhibition. The PP5 phosphatase domain binds the folded GR LBD, orienting the PP5 catalytic site. The PP5 catalyic site catpures the flexible, disordered GR NTD to dephosphorylate the putative substrate residues, S206 and S226. Dephosphorylation at these residues acts as a signal to repress GR activation. When ligand is present, the GR LBD binds ligand, inhibiting PP5 association (right). The GR NTD then retains phosphorylation at S206 and S226, allowing GR to proceed in the activation pathway (nuclear transport and binding to GREs).

Methods

Data analysis and figure preparation

Figures were created using UCSF Chimera (Pettersen et al., 2004) and UCSF ChimeraX (Goddard et al., 2018). GR ligand binding data was analyzed using Prism GraphPad).

Protein expression and purification

Human Hsp90α, Hsp70 (gene *Hsp70A1A*), Hop, p23, p23Δhelix (1-112), and yeast Ydj1 (Hsp40) were expressed in the pET151 bacterial expression plasmid with a cleavable N-terminal, 6x-His tag. Human Bag-1 isoform 4 (116-345) was expressed in a pET28a vector with a cleavable N-terminal, 6x-His tag. Proteins were expressed and purified by the following procedure as described (Noddings et al., 2022). Human PP5 and PP5ΔαJ were expressed and purified as described (Jaime-Garza et al., 2022). Human Hsp90α D93N was purified as previously described (Wang et al., 2022).

GR expression and purification

For GR LBD, the ligand binding domain (LBD) (520-777) with solubilizing mutation F602S was codon optimized and expressed in the pMAL-c3X derivative with an N-terminal cleavable 6x-His-MBP tag. GR LBD was expressed and purified as previously described (Kirschke et al., 2014).

GR DBD-LBD construct contains the GR DNA binding domain (DBD), hinge, and ligand binding domain (LBD) (418-777) with solubilizing mutation F602S. The construct was codon optimized and expressed in the pMAL-c3X derivative with an N-terminal

cleavable 6x-His-MBP tag. GR DBD-LBD was expressed and purified with ligand as described (Chapter 3).

Assessing PP5 Complexes in vitro

The GR chaperone cycle was reconstituted *in vitro* with purified components as previously described (Kirschke et al., 2014). Buffer conditions were 30 mM HEPES pH 8, 50 mM KCl, 0.05% Tween20, and 2 mM TCEP. To test PP5 binding with GR:Hsp70, proteins and reagents were added at the following concentration: 5 μM MBP-GR LBD, 2 μM Hsp40, 5 μM Hsp70, 15 μM PP5, and 5 mM ATP/$MgCl_2$. To test PP5 binding with the GR-loading complex (GR:Hsp90:Hsp70:Hop), proteins and reagents were added at the following concentration: 5 μM MBP-GR LBD, 2 μM Hsp40, 15 μM Hsp70, 15 μM Hop, 15 μM Hsp90 D93N, 15 μM PP5, and 5 mM ATP/$MgCl_2$. To test PP5 binding with the GR-maturation complex (GR:Hsp90:p23), proteins and reagents were added at the following concentration: 5 μM MBP-GR LBD, 2 μM Hsp40, 5 μM Hsp70, 5 μM Hop, 15 μM Hsp90, 15 μM p23, 15 μM PP5 or PP5ΔαJ, and 5 mM ATP/$MgCl_2$.These reactions was incubated at room temperature for 60 minutes. For the GR-maturation complex, after 60 minutes, 15 μM p23, 15 μM Bag-1, and 20 mM sodium molybdate (used to stabilize the closed conformation of Hsp90 (Csermely et al., 1993; Johnson & Toft, 1995; Verba et al., 2016), likely by acting as a γ-phosphate analog to stabilize the post-ATP hydrolysis transition state of Hsp90) were added, and the reaction was incubated at room temperature for another 30 minutes. Following incubation, amylose resin (New England Biolabs) was added to the reactions in a 1:1 ratio and incubated at 4°C with nutation. Resin was then washed 4 times with wash buffer (30 mM HEPES pH 8, 50

mM KCl, 5 mM ATP/$MgCl_2$, 0.05% Tween20, 2 mM TCEP, 20 mM sodium molybdate) and eluted with 50 mM maltose in elution buffer (30 mM HEPES pH 8, 50 mM KCl, 2 mM TCEP, 20 mM sodium molybdate). The elution was analyzed by SDS-PAGE (4-12% acrylamide gel).

GR:Hsp90:p23:PP5 sample preparation

The GR:Hsp90:p23:PP5 sample was prepared by adding PP5 to the *in vitro* reconstituted GR-chaperone cycle, enriching for the GR-maturation complex as described above. The elution from the MBP-GR affinity purification was concentrated and purified by size exclusion using a Superdex 200 Increase 3.2/300 (Cytiva Life Sciences) and fractions were analyzed by SDS-PAGE (4-12% acrylamide gel). Fractions containing the full complex were crosslinked with 0.02% glutaraldehyde for 20 minutes at room temperature. The sample was then concentrated to ~2 μM. 2.5 μL of sample was applied to PEG-2k (polyethylene glycol 2000) amino affinity grids (Wang et al., 2020) and plunge-frozen in liquid ethane using a Vitrobot Mark IV (FEI) with a wait time of 30 seconds, blotting time of 4 seconds, blotting force 0, at 10°C, and with 100% humidity.

Cryo-EM data acquisition

All data was acquired using SerialEM software. The dataset was collected on a Glacios electron microscope (Thermo Fisher Scientific) operating at 200kV using a K3 direct electron camera (Gatan). Images were recorded at a nominal magnification of 34,000×, corresponding to a physical pixel size of 1.207 Å. The dataset was collected in

super resolution mode, corresponding to a super resolution pixel size of 0.603 Å. A nominal defocus range of 0.8 μm –2.0 μm under focus was used for all datasets. The dose rate was 12.5 e^-/pixel/second and the dose per frame was 0.51 $e^-/Å^2$/frame, with 117 frames collected per movie. The total dose was 59.5 $e^-/Å^2$.

Cryo-EM data processing

The GR:Hsp90:p23:PP5 dataset consisted of 1,911 dose-fractionated image stacks, which were motion corrected using UCSF MotionCor2 (Zheng et al., 2017) and analyzed with RELION v.3.0.8 (Scheres, 2012). Motion corrected images were used for contrast transfer function (CTF) estimation using CTFFIND v.4.1 (Rohou & Grigorieff, 2015) and Laplacian-of-Gaussian particle picking was done in RELION. Three rounds of 3D classification with symmetry C1 were performed with the GR-maturation complex (PDB ID: 7KRJ) (Noddings et al., 2022) as a low-pass-filtered (20 Å) initial model until three low-resolution (~14 Å) reconstructions were obtained. The first reconstruction, corresponding to GR:Hsp90:p23:PP5 (active) contained ~14,000 particles, the second reconstruction, corresponding to GR:Hsp90:p23:PP5 (inactive) contained ~19,000 particles, and the third reconstruction, corresponding to the GR-maturation complex, GR:Hsp90:p23, contained ~23,000 particles.

Fluorescence polarization assays

Fluorescence polarization of fluorescent dexamethasone (F-dex) (Thermo Fisher) was measured on a SpectraMax M5 plate reader (Molecular Devices) with excitation/emission wavelengths of 485/538 nm, and temperature control set at 25°C.

Buffer conditions were 50 mM HEPES pH 8, 100 mM KCl, 2 mM DTT. Proteins were pre-equilibrated together at room temperature for 60 minutes prior to F-dex addition. Proteins and reagents were added at the following concentration: 250 nM GR LBD, 2 μM Hsp40, 15 μM Hsp70, 15 μM Hsp90, 15 μM Hop, 15 μM p23 or $p23_{\Delta helix}$, 15 μM PP5 or PP5ΔαJ, and 5 mM ATP/$MgCl_2$. Note that the dissociation constant (K_D) between GR and F-dex is ~150 nM (Kirschke et al., 2014). Ligand binding was initiated with 10 nM F-dex and association was measured until reaching equilibrium. Data was plotted and analyzed using Prism (GraphPad). GR ligand binding behavior was affected by buffer conditions; therefore, reactions were always normalized such that each reaction had equivalent amounts of buffer reagents.

References

Ali, M. M. U., Roe, S. M., Vaughan, C. K., Meyer, P., Panaretou, B., Piper, P. W., Prodromou, C., & Pearl, L. H. (2006). Crystal structure of an Hsp90–nucleotide–p23/Sba1 closed chaperone complex. *Nature, 440*(7087), 1013-1017. https://doi.org/10.1038/nature04716

Biebl, M. M., Lopez, A., Rehn, A., Freiburger, L., Lawatscheck, J., Blank, B., Sattler, M., & Buchner, J. (2021, Feb 5). Structural elements in the flexible tail of the co-chaperone p23 coordinate client binding and progression of the Hsp90 chaperone cycle. *Nat Commun, 12*(1), 828. https://doi.org/10.1038/s41467-021-21063-0

Chen, M. X., McPartlin, A. E., Brown, L., Chen, Y. H., Barker, H. M., & Cohen, P. T. (1994, Sep 15). A novel human protein serine/threonine phosphatase, which possesses four tetratricopeptide repeat motifs and localizes to the nucleus. *Embo Journal, 13*(18), 4278-4290. https://doi.org/10.1002/j.1460-2075.1994.tb06748.x

Connarn, J. N., Assimon, V. A., Reed, R. A., Tse, E., Southworth, D. R., Zuiderweg, E. R. P., Gestwicki, J. E., & Sun, D. X. (2014, Jan 31). The Molecular Chaperone Hsp70 Activates Protein Phosphatase 5 (PP5) by Binding the Tetratricopeptide Repeat (TPR) Domain. *Journal of Biological Chemistry, 289*(5), 2908-2917. https://doi.org/10.1074/jbc.M113.519421

Csermely, P., Kajtar, J., Hollosi, M., Jalsovszky, G., Holly, S., Kahn, C. R., Gergely, P., Soti, C., Mihaly, K., & Somogyi, J. (1993, Jan 25). Atp Induces a Conformational Change of the 90-Kda Heat-Shock Protein (Hsp90). *Journal of Biological Chemistry, 268*(3), 1901-1907. <Go to ISI>://WOS:A1993KH62000062

Dean, D. A., Urban, G., Aragon, I. V., Swingle, M., Miller, B., Rusconi, S., Bueno, M., Dean, N. M., & Honkanen, R. E. (2001, May 17). Serine/threonine protein phosphatase 5 (PP5) participates in the regulation of glucocorticoid receptor nucleocytoplasmic shuttling. *Bmc Cell Biology, 2*. https://doi.org/Artn 6 Doi 10.1186/1471-2121-2-6

DeFranco, D. B., Qi, M., Borror, K. C., Garabedian, M. J., & Brautigan, D. L. (1991, Sep). Protein phosphatase types 1 and/or 2A regulate nucleocytoplasmic shuttling of glucocorticoid receptors. *Mol Endocrinol, 5*(9), 1215-1228. https://doi.org/10.1210/mend-5-9-1215

Galigniana, M. D., Harrell, J. M., Murphy, P. J. M., Chinkers, M., Radanyi, C., Renoir, J. M., Zhang, M. J., & Pratt, W. B. (2002, Nov 19). Binding of hsp90-associated immunophilins to cytoplasmic dynein: Direct binding and in vivo evidence that the peptidylprolyl isomerase domain is a dynein interaction domain. *Biochemistry, 41*(46), 13602-13610. https://doi.org/10.1021/bi020399z

Galigniana, M. D., Housley, P. R., DeFranco, D. B., & Pratt, W. B. (1999, Jun 4). Inhibition of glucocorticoid receptor nucleocytoplasmic shuttling by okadaic acid requires intact cytoskeleton. *Journal of Biological Chemistry, 274*(23), 16222-16227. https://doi.org/DOI 10.1074/jbc.274.23.16222

Goddard, T. D., Huang, C. C., Meng, E. C., Pettersen, E. F., Couch, G. S., Morris, J. H., & Ferrin, T. E. (2018, Jan). UCSF ChimeraX: Meeting modern challenges in visualization and analysis. *Protein Sci, 27*(1), 14-25. https://doi.org/10.1002/pro.3235

Itoh, M., Adachi, M., Yasui, H., Takekawa, M., Tanaka, H., & Imai, K. (2002, Oct). Nuclear export of glucocorticoid receptor is enhanced by c-Jun N-terminal kinase-mediated phosphorylation. *Molecular Endocrinology, 16*(10), 2382-2392. https://doi.org/10.1210/me.2002-0144

Jaime-Garza, M., Nowotny, C., Coutandin, D., Wang, F., Tabios, M., & Agard, D. A. (2022, 2022-01-01 00:00:00). Hsp90 provides a platform for kinase dephosphorylation by PP5. *bioRxiv*.

Johnson, J. L., & Toft, D. O. (1995, Jun). Binding of p23 and hsp90 during assembly with the progesterone receptor. *Mol Endocrinol, 9*(6), 670-678. https://doi.org/10.1210/mend.9.6.8592513

Kirschke, E., Goswami, D., Southworth, D., Griffin, P., & Agard, D. (2014). Glucocorticoid Receptor Function Regulated by Coordinated Action of the Hsp90 and Hsp70 Chaperone Cycles. *Cell, 157*(7), 1685-1697. https://doi.org/10.1016/j.cell.2014.04.038

Lee, K., Thwin, A. C., Nadel, C. M., Tse, E., Gates, S. N., Gestwicki, J. E., & Southworth, D. R. (2021, Sep 2). The structure of an Hsp90-immunophilin complex reveals cochaperone recognition of the client maturation state. *Mol Cell, 81*(17), 3496-3508 e3495. https://doi.org/10.1016/j.molcel.2021.07.023

Noddings, C. M., Wang, R. Y., Johnson, J. L., & Agard, D. A. (2022, Jan). Structure of Hsp90-p23-GR reveals the Hsp90 client-remodelling mechanism. *Nature, 601*(7893), 465-469. https://doi.org/10.1038/s41586-021-04236-1

Pettersen, E. F., Goddard, T. D., Huang, C. C., Couch, G. S., Greenblatt, D. M., Meng, E. C., & Ferrin, T. E. (2004, Oct). UCSF Chimera--a visualization system for exploratory research and analysis. *J Comput Chem, 25*(13), 1605-1612. https://doi.org/10.1002/jcc.20084

Pratt, W. B., Morishima, Y., Murphy, M., & Harrell, M. (2006). Chaperoning of glucocorticoid receptors. *Handb Exp Pharmacol*(172), 111-138. https://doi.org/10.1007/3-540-29717-0_5

Pratt, W. B., & Toft, D. O. (1997). Steroid Receptor Interactions with Heat Shock Protein and Immunophilin Chaperones. *Endocrine Reviews, 18*(3), 306-360. https://doi.org/10.1210/edrv.18.3.0303

Rohou, A., & Grigorieff, N. (2015, Nov). CTFFIND4: Fast and accurate defocus estimation from electron micrographs. *J Struct Biol, 192*(2), 216-221. https://doi.org/10.1016/j.jsb.2015.08.008

Sahasrabudhe, P., Rohrberg, J., Biebl, M. M., Rutz, D. A., & Buchner, J. (2017, Sep 21). The Plasticity of the Hsp90 Co-chaperone System. *Mol Cell, 67*(6), 947-961.e945. https://doi.org/10.1016/j.molcel.2017.08.004

Scheres, S. H. (2012, Dec). RELION: implementation of a Bayesian approach to cryo-EM structure determination. *J Struct Biol, 180*(3), 519-530. https://doi.org/10.1016/j.jsb.2012.09.006

Silverstein, A. M., Galigniana, M. D., Chen, M. S., OwensGrillo, J. K., Chinkers, M., & Pratt, W. B. (1997, Jun 27). Protein phosphatase 5 is a major component of glucocorticoid receptor hsp90 complexes with properties of an FK506-binding immunophilin. *Journal of Biological Chemistry, 272*(26), 16224-16230. https://doi.org/DOI 10.1074/jbc.272.26.16224

Sinars, C. R., Cheung-Flynn, J., Rimerman, R. A., Scammell, J. G., Smith, D. F., & Clardy, J. (2003, Feb 4). Structure of the large FK506-binding protein FKBP51, an Hsp90-binding protein and a component of steroid receptor complexes. *Proc Natl Acad Sci U S A, 100*(3), 868-873. https://doi.org/10.1073/pnas.0231020100

Verba, K. A., Wang, R. Y. R., Arakawa, A., Liu, Y., Shirouzu, M., Yokoyama, S., & Agard, D. A. (2016). Atomic structure of Hsp90-Cdc37-Cdk4 reveals that Hsp90 traps and stabilizes an unfolded kinase. *Science, 352*(6293), 1542-1547. https://doi.org/10.1126/science.aaf5023

Wang, F., Yu, Z., Betegon, M., Campbell, M. G., Aksel, T., Zhao, J., Li, S., Douglas, S. M., Cheng, Y., & Agard, D. A. (2020, Feb 1). Amino and PEG-amino graphene oxide grids enrich and protect samples for high-resolution single particle cryo-electron microscopy. *J Struct Biol, 209*(2), 107437. https://doi.org/10.1016/j.jsb.2019.107437

Wang, R. Y., Noddings, C. M., Kirschke, E., Myasnikov, A. G., Johnson, J. L., & Agard, D. A. (2022, Jan). Structure of Hsp90-Hsp70-Hop-GR reveals the Hsp90 client-loading mechanism. *Nature, 601*(7893), 460-464. https://doi.org/10.1038/s41586-021-04252-1

Wang, Z., Chen, W. W., Kono, E., Dang, T., & Garabedian, M. J. (2007, Mar). Modulation of glucocorticoid receptor phosphorylation and transcriptional activity

by a C-terminal-associated protein phosphatase. *Molecular Endocrinology, 21*(3), 625-634. https://doi.org/10.1210/me.2005-0338

Wang, Z., Frederick, J., & Garabedian, M. J. (2002, Jul 19). Deciphering the phosphorylation "code" of the glucocorticoid receptor in vivo. *J Biol Chem, 277*(29), 26573-26580. https://doi.org/10.1074/jbc.M110530200

Weikum, E. R., Knuesel, M. T., Ortlund, E. A., & Yamamoto, K. R. (2017). Glucocorticoid receptor control of transcription: precision and plasticity via allostery. https://doi.org/10.1038/nrm.2016.152

Wu, B., Li, P., Liu, Y., Lou, Z., Ding, Y., Shu, C., Ye, S., Bartlam, M., Shen, B., & Rao, Z. (2004, Jun 1). 3D structure of human FK506-binding protein 52: implications for the assembly of the glucocorticoid receptor/Hsp90/immunophilin heterocomplex. *Proc Natl Acad Sci U S A, 101*(22), 8348-8353. https://doi.org/10.1073/pnas.0305969101

Yang, J., Roe, S. M., Cliff, M. J., Williams, M. A., Ladbury, J. E., Cohen, P. T., & Barford, D. (2005, Jan 12). Molecular basis for TPR domain-mediated regulation of protein phosphatase 5. *Embo Journal, 24*(1), 1-10. https://doi.org/10.1038/sj.emboj.7600496

Zheng, S. Q., Palovcak, E., Armache, J. P., Verba, K. A., Cheng, Y., & Agard, D. A. (2017, Apr). MotionCor2: anisotropic correction of beam-induced motion for improved cryo-electron microscopy. *Nat Methods, 14*(4), 331-332. https://doi.org/10.1038/nmeth.4193

Zuo, Z., Urban, G., Scammell, J. G., Dean, N. M., McLean, T. K., Aragon, I., & Honkanen, R. E. (1999, Jul 13). Ser/Thr protein phosphatase type 5 (PP5) is a negative regulator of glucocorticoid receptor-mediated growth arrest. *Biochemistry, 38*(28), 8849-8857. https://doi.org/DOI 10.1021/bi990842e

Chapter 6 Regulation of GR DNA-binding by Hsp70/Hsp90

Preface

This chapter contains unpublished results that may be useful for future projects. This project was proposed as part of my F31 NIH/NCI fellowship. Elaine Kirschke inspired this project through her success in purifying a recombinant GR construct containing the DBD and hinge (GR DBD-LBD), which allowed me to try the first *in vitro* GR GRE-binding experiments with a multidomain GR construct and the chaperone system.

Introduction

Beyond ligand-binding, Hsp90 is known to effect GR binding to GR response elements (GREs) in the nucleus, but much less is known about how nuclear-localized Hsp90 regulates clients (Echeverria & Picard, 2010). As discussed in Chapter 4, ligand-bound GR appears to remain complexed with Hsp90 during translocation to the nucleus (Czar et al., 1997; Echeverría et al., 2009). The cochaperone FKBP52 is thought to act as an adaptor between the ligand-bound GR:Hsp90 complex and the dynein/dynactin motor complex for rapid transport of active GR to the nucleus (Galigniana et al., 2002; Galigniana et al., 2001; Silverstein et al., 1999). GR, Hsp90, p23, and FKBP52 have been shown to interact with the nuclear pore and are all found in abundance in the nucleus (Echeverría et al., 2009). Furthermore, Hsp90 is known to regulate many transcription factors as well as chromatin remodeling complexes, thus intimately linking Hsp90 to transcription regulation (Echtenkamp et al., 2016; Sawarkar & Paro, 2013; Zhao et al., 2005).

Once GR is in the nucleus, GR binds GREs to assemble transcription regulatory complexes. GREs contain GR binding sequences (GBSs), which are imperfect palindromic hexameric half sites separated by 3 base-pair (bp) spacers. The GR DBD dimerizes on the GBS, such that the monomers bind in a head-to-head orientation, with each monomer occupying a single half site (Luisi et al., 1991). The GR LBDs are also known to dimerize (Bledsoe et al., 2002), but it is unclear how the full receptor dimerizes on the GRE since a multidomain structure of GR has not been determined. Dimerized multidomain structures of other nuclear receptors have revealed that both the DBDs LBDs homodimerize, while the hinge mediates contacts between the domains and also makes contact with the DNA-binding site (Chandra et al., 2008; Chandra et al., 2013; Lou et al., 2014).

It is unclear whether Hsp90 is integrated into these GR:GRE complexes; however, Hsp90 and the cochaperone p23 have been shown to co-localize with GR at GREs (Freeman, 2002; Stavreva et al., 2004). Previous studies also suggest Hsp90 and p23 inhibit GR GRE-binding *in vivo*, possibly serving to disassemble GR transcription regulatory complexes; however, the mechanism of inhibition is unknown (Freeman, 2002; Kang et al., 1999; Liu & Defranco, 1999). From the GR-maturation complex structure (Chapter 3), it is clear that the GR LBDs cannot dimerize due to steric clash with Hsp90; however, structures of the GR:Hsp90:FKBP complexes (Chapter 4) demonstrate that the GR LBDs can dimerize in these complexes due to a rotation of GR in the complex. In all three complexes, the GR DBD would appear to be free to dimerize, but the GR hinge region is partially occluded in the Hsp90 lumen. Thus, full

dimerization of GR is likely to be inhibited when GR is complexed with Hsp90, but how this affects GR GRE-binding is unknown.

Results

I performed the first, to my knowledge, *in vitro* experiments characterizing the effect of the GR chaperone cycle on GR GRE-binding. Using the GR DBD-LBD construct, I purified reconstituted GR DBD-LBD with saturating amounts of ligand (note the ligand was not dialyzed away at the end of the purification). The GR DBD-LBD plasmid and purification protocol were provided by Elaine Kirschke. I then used fluorescence anisotropy to measure GR binding to two different fluorescein-conjugated GREs, the canonical *Pal* and *Sgk* GREs. The GR DBD interaction with the *Pal* and *Sgk* oligomers has been previously biochemically and structurally characterized (Meijsing et al). I first confirmed that GR DBD-LBD binds the *Pal* and *Sgk* GREs with similar affinities without the chaperone cycle (Fig. 1). Note that the baseline *Pal* and *Sgk* polarization value is a bit higher than expected, possibly due to interaction between the fluorescein and DNA. Next, I pre-incubated 1μM GR DBD-LBD with Hsp70/Hsp40/ATP or the full chaperone system (Hsp70/Hsp40/Hsp90/Hop/p23/ATP) for 1 hour and then added 100nM *Pal* (Fig. 2). Surprisingly, both the Hsp70/Hsp40 system and full chaperone system reduced GR GRE-binding to a similar level. As a control, I also tested *Pal* binding to a GR DBD-hinge only construct (amino acids 418-506). Interestingly, the GR DBD-hinge also exhibits reduced *Pal* binding compared to the GR DBD-LBD construct and plateaus at a similar polarization value as with the Hsp70/Hsp40 system or full chaperone system.

I hypothesized that the Hsp70/Hsp40 and full chaperone systems inhibited GR GRE-binding by preventing dimerization of the GR LBDs. Given that FKBP51 and FKBP52 appear to rotate the GR LBD to potentially poise the GR LBD for dimerization (Chapter 4), I tested whether addition of FKBP51 or FKBP52 into the chaperone system would facilitate GR LBD dimerization and increase *Pal* binding (Fig. 3). Adding FKBP51 or FKBP52 into the GR:chaperone pre-incubation did not restore full GR GRE-binding. However, the addition of FKBP51 did lead to a slow decrease in GR GRE-binding. When 1 μM of ligand (cortisol) was spiked into the FKBP51 reaction, the *Pal* binding level was restored, suggesting FKBP51 may lower the ligand-binding affinity.

To assess whether Hsp90 interacts with portions of GR beyond the LBD, I determined a cryo-EM structure of the GR-maturation complex (GR:Hsp90:p23) with the GR DBD-LBD (Fig. 4). Previously, we had determined the GR-maturation complex structure with the GR LBD construct and therefore, we could not assess whether the DBD or hinge regions interact with Hsp90. The GR DBD-LBD:Hsp90:p23 sample was prepared in the same manner as the previous GR-maturation complex (Chapter 3) and all data processing was performed in RELION. The resulting reconstruction resembled the GR LBD:Hsp90:p23 maturation complex, with no density present for the DBD or hinge regions. This is consistent with the FKBP-containing complexes I determined later (Chapter 4), which were prepared with the GR DBD-LBD construct and revealed no density beyond the GR LBD. Thus, the GR DBD and hinge regions do not appear to interact with Hsp90, p23, or the FKBPs, which suggests Hsp90 inhibits GR GRE-binding through interactions only with the GR LBD.

Discussion

Using the reconstituted GR chaperone cycle and the incorporation of the GR DBD-LBD construct, I have established the first *in vitro* system to characterize the effect of the GR chaperone cycle on GR GRE-binding. I revealed that the Hsp70/Hsp40 system partially inhibits GR GRE-binding and that the addition of Hsp90/Hop/p23, surprisingly, does not restore GR GRE-binding. This result is intriguing because the Hsp70/Hsp40 system inhibits GR ligand-binding, but the addition of Hsp90/Hop/p23 restores GR ligand-binding (Kirschke et al., 2014). Thus, GR GRE-binding is not solely dictated by the ligand-binding state of GR. Instead, I hypothesize that Hsp70 and Hsp90 engagement with the GR LBD prevents LBD dimerization, which reduces the GR:GRE affinity. Supporting this hypothesis, the GR DBD-hinge only construct binds the GRE with a similar polarization level compared to the GR DBD-LBD + chaperones reactions. This suggests that the presence of the GR LBD enhances GR GRE-binding and that the chaperones inhibit this GR LBD-dependent enhancement. The structure of the GR DBD-LBD:Hsp90:p23 complex also demonstrates Hsp90 only engages with the GR LBD, supporting this hypothesis.

Surprisingly, addition of FKBP51 or FKBP52 did not restore GR GRE-binding in the chaperone system despite my hypothesis that the FKBPs poise the GR LBD for dimerization (Chapter 4). One potential explanation is that Hsp70 re-binding and re-inhibition of GR may occur quickly after release of the FKBPs and a dimerized form of the GR LBDs does not persist long enough to positively effect GR GRE-binding in this assay. Perhaps the addition of Bag-1 into the system could be used to prevent Hsp70 re-binding and allow time for the GR LBDs to dimerize after the FKBP-induced rotation.

Strangely, FKBP51 caused a slow reduction in GR GRE-binding over the time course of the experiment, which was recovered by addition of ligand into the system. This a puzzling result and needs to be explored further, but this result suggests FKBP51 reduces the GR ligand-binding affinity.

Further experiments need to be performed to understand the mechanism of how Hsp70 and Hsp90 inhibit GR GRE-binding. It would be very useful to further characterize GR GRE-binding in the *in vitro* system without the chaperones, as this has not yet been well characterized in the field. Since I have now optimized the purification of apo GR DBD-LBD constructs suitable for biochemical assays (Chapter 4), it would be useful to understand how GR ligand-binding affects GR GRE-binding. Furthermore, it would be useful to understand how dimerization of the GR DBDs and LBDs contribute to GRE-binding affinity using dimerization-deficient point mutants.

As proposed as part of my F31, there is much to be explored regarding GR binding to GREs on chromatin given that GR is thought to be a pioneer factor that preferentially binds heterochromatin. The use of GRE nucleosomes in the fluorescence polarization assay, instead of naked DNA, may yield very different insights and would be more physiologically relevant for this system. Given that Hsp90 is found associated with GREs (Freeman, 2002), perhaps Hsp90 (or Hsp90 cochaperones) interact with chromatin in a way that facilitates release of GR for dimerization and high-affinity binding to GREs. In this vein, it would be interesting to determine a cryo-EM structure of GR:Hsp90 complexes bound to a GRE or GRE nucleosome. The presence of GREs in the sample would likely allow the GR DBDs and hinge to dimerize, which may facilitate structural determination of these regions. Overall, it would be extremely valuable for the

chaperone field to understand in molecular detail how Hsp90, Hsp70, and cochaperones affect client activity in the nucleus and the *in vitro* GR chaperone cycle provides a tractable model system to elucidate these mechanisms.

Figures

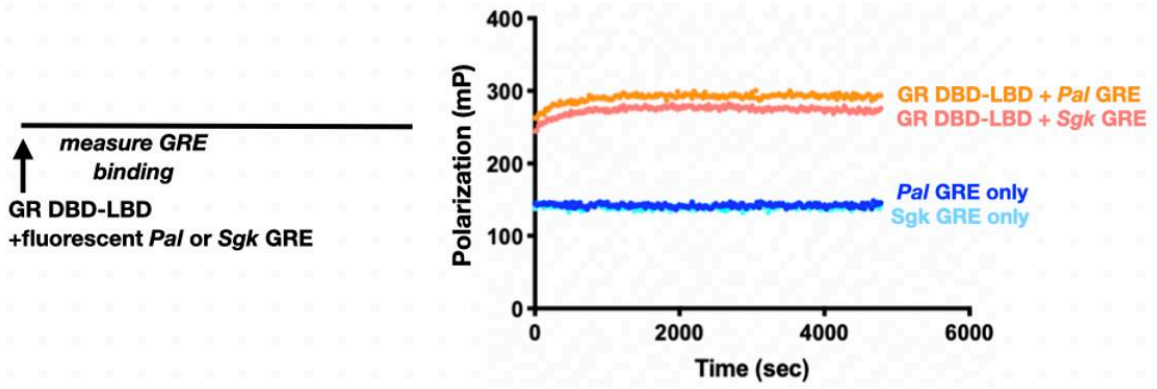

Fig. 6.1: Recombinant GR DBD-LBD binds *Pal* and *Sgk* GREs
Time course of 1 μM GR DBD-LBD binding to 100 nM fluorescent *Pal* or *Sgk* GRE oligos measured by fluorescence polarization anisotropy (mP = milliPolarization units).

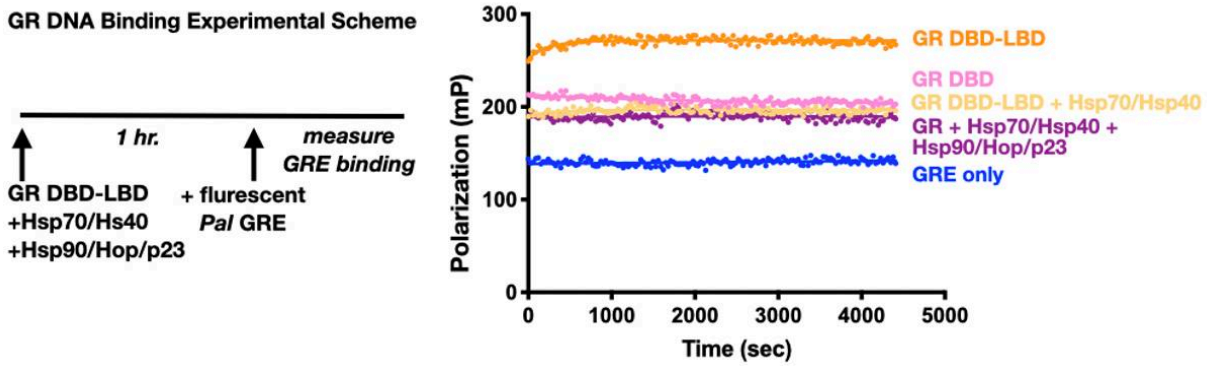

Fig. 6.2: The chaperones partially inhibit GR GRE-binding
Time course of 1 μM GR DBD-LBD binding to 100 nM fluorescent *Pal* GRE oligo measured by fluorescence polarization anisotropy (mP = milliPolarization units). Chaperone concentrations are as follows: 2 μM Hsp40, 15 μM Hsp70, 15 μM Hsp90, 15 μM Hop, 15 μM p23, and 5 mM ATP/$MgCl_2$. Reactions were pre-equilibrated for 1 hour before fluorescent *Pal* addition at time 0 seconds.

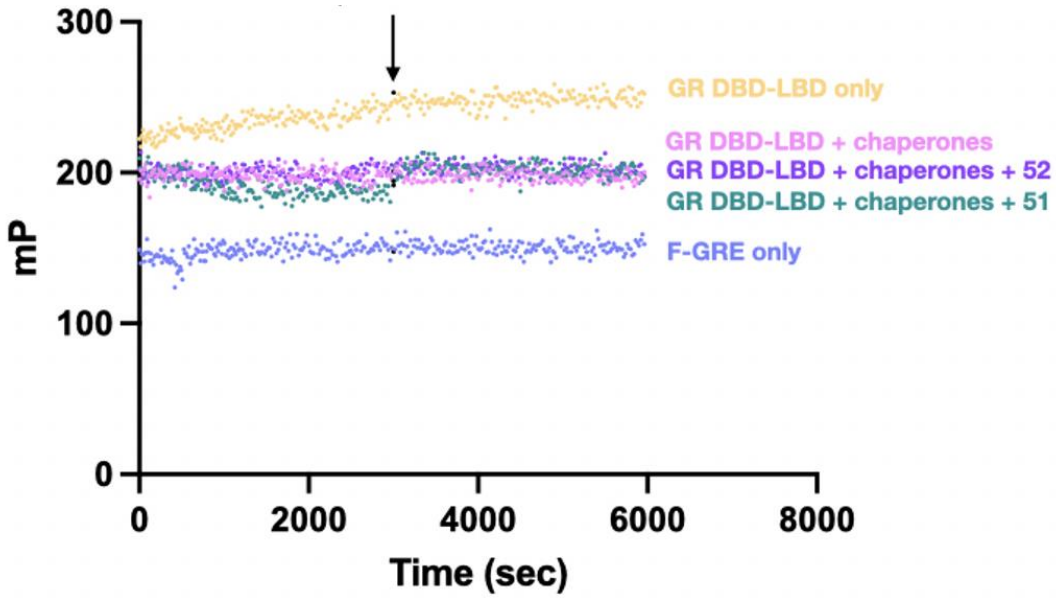

Fig. 6.3: The FKBP51 and FKBP52 effect on GR GRE-binding
Time course of 1 μM GR DBD-LBD binding to 100 nM fluorescent *Pal* GRE oligo (F-GRE) measured by fluorescence polarization anisotropy (mP = milliPolarization units). "Chaperones" = 2 μM Hsp40, 15 μM Hsp70, 15 μM Hsp90, 15 μM Hop, 15 μM p23, and 5 mM ATP/$MgCl_2$. 15 μM FKBP51 or FKBP52 were added to reactions as indicated. Reactions were pre-equilibrated for 1 hour before fluorescent *Pal* addition at time 0 seconds. 1 μM cortisol was added to all reactions at ~3000 seconds (as indicated by the black arrow).

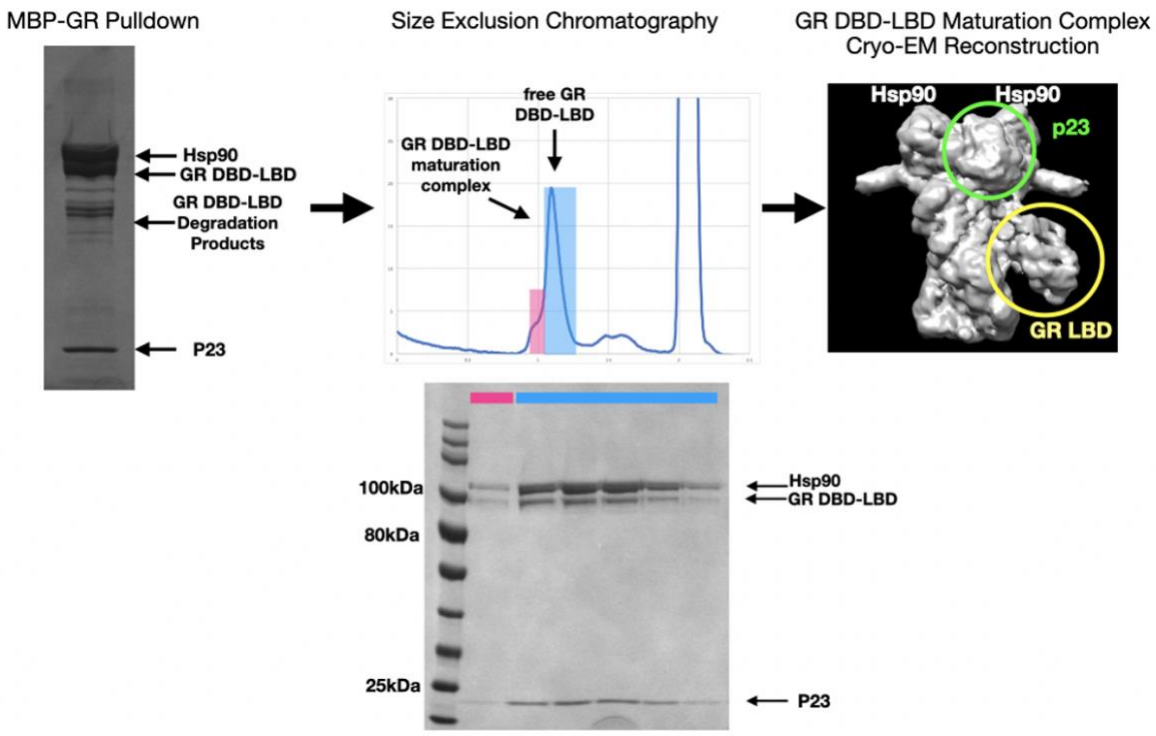

Fig. 6.4: Sample preparation and cryo-EM structure of the GR DBD-LBD:Hsp90:p23 complex

The GR DBD-LBD:Hsp90:p23 complex was prepared for cryo-EM as described as follows. The GR chaperone cycle was reconstituted *in vitro* with purified components. Buffer conditions were 30 mM HEPES pH 8, 50 mM KCl, 0.05% Tween20, and 2 mM TCEP. Proteins and reagents were added at the following concentration: 5 μM MBP-GR DBD-LBD (purified with ligand, see Methods), 2 μM Hsp40, 5 μM Hsp70, 5 μM Hop, 15 μM Hsp90, 15 μM p23, 5 mM ATP/$MgCl_2$. This reaction was incubated at room temperature for 60 minutes, then 15 μM p23, 15 μM Bag-1, and 20 mM sodium molybdate were added, and the reaction was incubated at room temperature for another 30 minutes. Following incubation, MBP-GR was affinity purified (see Methods). The elution was analyzed by SDS-PAGE (4-12% acrylamide gel) (left). The elution was concentrated and purified by size exclusion using a Shodex KW-804 column and fractions were analyzed by SDS-PAGE (4-12% acrylamide gel) (middle). Fractions containing the full complex were concentrated to ~2 μM and applied to Quantifoil grids. Data was collected on a Titan Krios and the dataset was process in RELION (see Methods). The resulting reconstruction was refined to 3.75 Å (right) and the density resembles the GR-maturation complex (Chapter 3), with a closed Hsp90 dimer, GR LBD bound to one side of the Hsp90 dimer, and p23 bound to one side of the Hsp90 NTD dimer interface. There was no additional density corresponding to the GR DBD or hinge, which appear to be too flexible for visualization.

Methods

Data analysis and figure preparation

Figures were created using UCSF Chimera v.1.14 (Pettersen et al., 2004) and UCSF ChimeraX v1.0.0 (Goddard et al., 2018). GR ligand binding data was analyzed using Prism v.9.4.0 (GraphPad).

Protein expression and purification

Human Hsp90α, Hsp70 (gene *Hsp70A1A*), Hop, p23, FKBP51, FKBP52, and yeast Ydj1 (Hsp40) were expressed as described in Chapter 4.

GR DBD-LBD expression and purification

The human GR DBD-LBD construct contains the GR DNA binding domain (DBD), hinge, and ligand binding domain (LBD) (418-777) with solubilizing mutation F602S. The construct was codon optimized and expressed in the pMAL-c3X derivative with an N-terminal cleavable 6x-His-MBP tag. GR DBD-LBD was expressed and purified with ligand as described in Chapter 4.

GR DBD-LBD:Hsp90:p23 complex sample preparation

The GR DBD-LBD:Hsp90:p23 complex as prepared in the same manner as the GR LBD:Hsp90:p23 complex (the 'GR-maturation complex') as described in Chapter 3. Instead of using the GR LBD construct, the GR DBD-LBD (418-777) purified with ligand was used (Fig. 4). Fractions containing the full complex were concentrated to ~2 μM. 2.5 μL of sample was applied to glow-discharged QUANTIFOIL R1.2/1.3, 400-mesh,

copper holey carbon grid (Quantifoil Micro Tools GmbH) and plunge-frozen in liquid ethane using a Vitrobot Mark IV (FEI) with a blotting time of 12 seconds, blotting force 3, at 10°C, and with 100% humidity.

Cryo-EM data acquisition

All data was acquired using SerialEM software v.4.0 (Schorb et al., 2019). Data was collected on an FEI Titan Krios electron microscope (Thermo Fisher Scientific) operating at 300kV using a K3 direct electron camera (Gatan) and equipped with a Bioquantum energy filter (Gatan) set to a slit width of 20 eV. Images were recorded at a nominal magnification of 105,000×, corresponding to a physical pixel size of 0.834 Å. The dataset was collected in super resolution mode, corresponding to a super resolution pixel size of 0.417 Å. A nominal defocus range of 0.8 μm –2.0 μm under focus was used.

Cryo-EM data processing

The dataset consisted of approximately 5,000 dose-fractionated image stacks, which were motion corrected using UCSF MotionCor2 (Zheng et al., 2017) and analyzed with RELION v.3.0.8 (Scheres, 2012). Motion corrected images with dose weighting were used for contrast transfer function (CTF) estimation using CTFFIND v.4.1 and Laplacian-of-Gaussian picking was performed in RELION. Approximately 5 million particles were picked and subjected an initial round of 3D classification with symmetry C1 and the GR-maturation complex (Chapter 3) as a lowpass-filtered reference.

A single class corresponding to the closed Hsp90 dimer was obtained, with approximately 1.5 million particles. This particle stack was subjected to 3D refinement and then a round of focused 3D classification without alignment using a mask around the GR LBD. The best class, with approximately 112,000 particles, was subjected to 3D refinement with a circular mask encompassing the entire complex. Another round of focused 3D classification without alignment was performed, using a mask around the GR LBD. The best class, with approximately 37,000 particles, was obtained and subjected to 3D refinement with a circular mask encompassing the entire complex. 3D refinement yielded a reconstruction of the GR DBD-LBD:Hsp90:p23 complex with a nominal resolution 3.75 Å.

Fluorescence polarization assays

Fluorescence polarization of fluorescent *Pal* (5'-AC**AGAACA**TTT**TGTTCT**TCGA-FAM) or *Sgk* (5'-AC**AGAACA**TTT**TGTCCG**TCGA-FAM) (bold letters correspond the GR binding site) double-stranded DNA was measured on a SpectraMax M5 plate reader (Molecular Devices) with excitation/emission wavelengths of 485/538 nm, temperature control set at 25°C. Buffer conditions were 50 mM HEPES pH 8, 100 mM KCl, 2 mM DTT. GRE-binding was initiated with 100nM of fluorescent DNA and 1 μM GR DBD-LBD and association was measured until reaching equilibrium. For GRE-binding with the chaperones, the proteins were pre-equilibrated together at room temperature for 60 minutes prior to fluorescent DNA addition. Proteins and reagents were added at the following concentration: 100 nM fluorescent DNA, 1 μM GR DBD-LBD, 2 μM Hsp40, 15 μM Hsp70, 15 μM Hsp90, 15 μM Hop, 15 μM p23, 15 μM FKBP51 or FKBP52, and 5

mM ATP/$MgCl_2$. GRE-binding was initiated with 100 nM fluorescent DNA and association was measured until reaching equilibrium. 1 μM of cortisol was used for the ligand 'spike-in' relating to Figure 3. GR GRE-binding behavior was affected by buffer conditions; therefore, reactions were always normalized such that each reaction had equivalent amounts of buffer reagents.

References

Bledsoe, R. K., Montana, V. G., Stanley, T. B., Delves, C. J., Apolito, C. J., McKee, D. D., Consler, T. G., Parks, D. J., Stewart, E. L., Willson, T. M., Lambert, M. H., Moore, J. T., Pearce, K. H., & Xu, H. E. (2002). Crystal Structure of the Glucocorticoid Receptor Ligand Binding Domain Reveals a Novel Mode of Receptor Dimerization and Coactivator Recognition. *110*(1), 93-105. https://doi.org/10.1016/s0092-8674(02)00817-6

Chandra, V., Huang, P., Hamuro, Y., Raghuram, S., Wang, Y., Burris, T. P., & Rastinejad, F. (2008). Structure of the intact PPAR-γ–RXR-α nuclear receptor complex on DNA. *Nature, 456*(7220), 350-356. https://doi.org/10.1038/nature07413

Chandra, V., Huang, P., Potluri, N., Wu, D., Kim, Y., & Rastinejad, F. (2013). Multidomain integration in the structure of the HNF-4α nuclear receptor complex. *495*(7441), 394-398. https://doi.org/10.1038/nature11966

Czar, M. J., Galigniana, M. D., Silverstein, A. M., & Pratt, W. B. (1997, Jun 24). Geldanamycin, a heat shock protein 90-binding benzoquinone ansamycin, inhibits steroid-dependent translocation of the glucocorticoid receptor from the cytoplasm to the nucleus. *Biochemistry, 36*(25), 7776-7785. https://doi.org/10.1021/bi970648x

Echeverría, P. C., Mazaira, G., Erlejman, A., Gomez-Sanchez, C., Piwien Pilipuk, G., & Galigniana, M. D. (2009). Nuclear import of the glucocorticoid receptor-hsp90 complex through the nuclear pore complex is mediated by its interaction with Nup62 and importin beta. *Molecular and Cellular Biology, 29*(17), 4788-4797. https://doi.org/10.1128/MCB.00649-09

Echeverria, P. C., & Picard, D. (2010, Jun). Molecular chaperones, essential partners of steroid hormone receptors for activity and mobility. *Biochim Biophys Acta, 1803*(6), 641-649. https://doi.org/10.1016/j.bbamcr.2009.11.012

Echtenkamp, F. J., Gvozdenov, Z., Adkins, N. L., Zhang, Y., Lynch-Day, M., Watanabe, S., Peterson, C. L., & Freeman, B. C. (2016, Dec 1). Hsp90 and p23 Molecular Chaperones Control Chromatin Architecture by Maintaining the Functional Pool of the RSC Chromatin Remodeler. *Mol Cell, 64*(5), 888-899. https://doi.org/10.1016/j.molcel.2016.09.040

Freeman, B. C. (2002). Disassembly of Transcriptional Regulatory Complexes by Molecular Chaperones. *296*(5576), 2232-2235. https://doi.org/10.1126/science.1073051

Galigniana, M. D., Harrell, J. M., Murphy, P. J. M., Chinkers, M., Radanyi, C., Renoir, J. M., Zhang, M. J., & Pratt, W. B. (2002, Nov 19). Binding of hsp90-associated

immunophilins to cytoplasmic dynein: Direct binding and in vivo evidence that the peptidylprolyl isomerase domain is a dynein interaction domain. *Biochemistry, 41*(46), 13602-13610. https://doi.org/10.1021/bi020399z

Galigniana, M. D., Radanyi, C., Renoir, J. M., Housley, P. R., & Pratt, W. B. (2001, May 4). Evidence that the peptidylprolyl isomerase domain of the hsp90-binding immunophilin FKBP52 is involved in both dynein interaction and glucocorticoid receptor movement to the nucleus. *J Biol Chem, 276*(18), 14884-14889. https://doi.org/10.1074/jbc.M010809200

Goddard, T. D., Huang, C. C., Meng, E. C., Pettersen, E. F., Couch, G. S., Morris, J. H., & Ferrin, T. E. (2018, Jan). UCSF ChimeraX: Meeting modern challenges in visualization and analysis. *Protein Sci, 27*(1), 14-25. https://doi.org/10.1002/pro.3235

Kang, K. I., Meng, X., Devin-Leclerc, J., Bouhouche, I., Chadli, A., Cadepond, F., Baulieu, E. E., & Catelli, M. G. (1999). The molecular chaperone Hsp90 can negatively regulate the activity of a glucocorticosteroid-dependent promoter. *96*(4), 1439-1444. https://doi.org/10.1073/pnas.96.4.1439

Kirschke, E., Goswami, D., Southworth, D., Griffin, P., & Agard, D. (2014). Glucocorticoid Receptor Function Regulated by Coordinated Action of the Hsp90

and Hsp70 Chaperone Cycles. *Cell, 157*(7), 1685-1697. https://doi.org/10.1016/j.cell.2014.04.038

Liu, J., & Defranco, D. B. (1999). Chromatin Recycling of Glucocorticoid Receptors: Implications for Multiple Roles of Heat Shock Protein 90. *13*(3), 355-365. https://doi.org/10.1210/mend.13.3.0258

Lou, X., Toresson, G., Benod, C., Suh, J. H., Philips, K. J., Webb, P., & Gustafsson, J.-A. (2014). Structure of the retinoid X receptor α–liver X receptor β (RXRα–LXRβ) heterodimer on DNA. *21*(3), 277-281. https://doi.org/10.1038/nsmb.2778

Luisi, B. F., Xu, W. X., Otwinowski, Z., Freedman, L. P., Yamamoto, K. R., & Sigler, P. B. (1991). Crystallographic analysis of the interaction of the glucocorticoid receptor with DNA. *352*(6335), 497-505. https://doi.org/10.1038/352497a0

Pettersen, E. F., Goddard, T. D., Huang, C. C., Couch, G. S., Greenblatt, D. M., Meng, E. C., & Ferrin, T. E. (2004, Oct). UCSF Chimera--a visualization system for exploratory research and analysis. *J Comput Chem, 25*(13), 1605-1612. https://doi.org/10.1002/jcc.20084

Sawarkar, R., & Paro, R. (2013, Apr). Hsp90@chromatin.nucleus: an emerging hub of a networker. *Trends in Cell Biology, 23*(4), 193-201. https://doi.org/10.1016/j.tcb.2012.11.007

Scheres, S. H. (2012, Dec). RELION: implementation of a Bayesian approach to cryo-EM structure determination. *J Struct Biol, 180*(3), 519-530. https://doi.org/10.1016/j.jsb.2012.09.006

Schorb, M., Haberbosch, I., Hagen, W. J. H., Schwab, Y., & Mastronarde, D. N. (2019, Jun). Software tools for automated transmission electron microscopy. *Nat Methods, 16*(6), 471-477. https://doi.org/10.1038/s41592-019-0396-9

Silverstein, A. M., Galigniana, M. D., Kanelakis, K. C., Radanyi, C., Renoir, J. M., & Pratt, W. B. (1999). Different Regions of the Immunophilin FKBP52 Determine Its Association with the Glucocorticoid Receptor, hsp90, and Cytoplasmic Dynein. *274*(52), 36980-36986. https://doi.org/10.1074/jbc.274.52.36980

Stavreva, D. A., Muller, W. G., Hager, G. L., Smith, C. L., & McNally, J. G. (2004). Rapid Glucocorticoid Receptor Exchange at a Promoter Is Coupled to Transcription and Regulated by Chaperones and Proteasomes. *Molecular and Cellular Biology, 24*(7), 2682-2697. https://doi.org/10.1128/mcb.24.7.2682-2697.2004

Zhao, R., Davey, M., Hsu, Y. C., Kaplanek, P., Tong, A., Parsons, A. B., Krogan, N., Cagney, G., Mai, D., Greenblatt, J., Boone, C., Emili, A., & Houry, W. A. (2005, Mar 11). Navigating the chaperone network: an integrative map of physical and

genetic interactions mediated by the hsp90 chaperone. *Cell, 120*(5), 715-727. https://doi.org/10.1016/j.cell.2004.12.024

Zheng, S. Q., Palovcak, E., Armache, J. P., Verba, K. A., Cheng, Y., & Agard, D. A. (2017, Apr). MotionCor2: anisotropic correction of beam-induced motion for improved cryo-electron microscopy. *Nat Methods, 14*(4), 331-332. https://doi.org/10.1038/nmeth.4193

Chapter 7 Future Directions

Interaction between Hsp90 and the Dynein/Dynactin Motor Complex

Previous studies have revealed a connection between Hsp90 and the cytoplasmic dynein/dynactin motor complex as a means to rapidly transport Hsp90 clients to the nucleus. In this model, the Hsp90:client complex is translocated along microtubules as cargo on cytoplasmic dynein/dynactin with FKBP52 acting as an adaptor between Hsp90 and dynein/dynactin. This mode of nuclear transport has only been identified GR, MR, p53, and hTERT (human telomerase reverse transcriptase), although it is likely that other Hsp90 clients undergo Hsp90:dynein-dependent transport (Mazaira et al., 2021). GR is known to be rapidly translocated to the nucleus ($t_{1/2}$ = 4-5 minutes) in a manner dependent on the Hsp90, FKBP52, and dynein. Inhibition of any of these factors leads to a slow transport of GR to the nucleus ($t_{1/2}$ = 45-60 minutes), which may be mediated by simple diffusion. Interestingly, multiple components in the GR chaperone cycle have been shown to interact with the nuclear pore complex (NPC), including GR, Hsp90, Hsp70, p23, FKBP52, and PP5. Furthermore, a previous studied demonstrated that crosslinked GR:Hsp90 complexes can translocate into the nucleus, suggesting GR enters the nucleus while bound to Hsp90 (Echeverría et al., 2009). Altogether, there is evidence that GR and other Hsp90 clients undergo rapid nuclear translocation using the dynein/dynactin motor complex; however, very little is understood about the details of this Hsp90:dynein interaction. Further investigation into this interaction would be of fundamental importance for both the chaperone and dynein fields. The utilization of the dynein/dynactin motor for Hsp90-dependent client transport

would allow Hsp90 to couple the conformational state of the client protein directly to subcellular transport.

How do Hsp90:client:cochaperone complexes connect to the cytoplasmic dynein/dynactin motor system? Previous studies suggest Hsp90 cochaperones mediate the interaction with dynein/dynactin. *In vivo,* FKBP52 promotes rapid nuclear translocation and has been shown to be associated with p50 dynamitin (a subunit of dynactin) and the dynein intermediate chain 1 (DIC1)(a subunit of dynein) through the FKBP52 PPIase (FK1) domain (Galigniana et al., 2001; Harrell et al., 2004; Riggs et al., 2003; Tatro et al., 2009; Wochnik et al., 2005). Interestingly, the highly similar FKBP51 cochaperone does not interact with dynein. Switching the FKBP52 and FKBP51 PPIase domains confers dynein interaction to FKBP51, indicating the dynein/dynactin interaction is likely mediated through the FKBP PPIase domains (Wochnik et al., 2005).

A recent human cytoplasmic dynein interactome study using BioID indicated FKBP52, Hsp90 (*HSP90AA1*), and a number of Hsp90-interacting proteins associate with DIC1 (Redwine et al., 2017). The strongest interactor was DNAJC7 *(DNAJC7*), a J-protein (Hsp40) family member containing an Hsp70/Hsp90-interacting TPR domain. FKBP52 (*FKBP4*) was the third strongest interactor and other Hsp90 cochaperones appeared in the top 50 interactors: CHIP (*STUB1*), Sgt1 *(SUGT1*), NudC *(NUDC*), *TTC1*, and *RUVBL1*. In this study, NudC and FKBP52 were also identified as interactors for dynein intermediate chain 2. Interestingly, other studies have indicated the Hsp90 cochaperones Cyp40 and PP5 also associate with the dynein/dynactin motor complex, although these were not identified in the BioID study (Galigniana et al., 2002).

Based on the GR:Hsp90:FKBP structures I determined (Chapter 4), there is a large surface available on the PPIase (FK1) domain of FKBP52 that may mediate the dynein/dynactin interaction. This surface is on the convex side of the FK1 domain, where the N-terminal disordered strand (amino acids 1-22) interacts with the β sheet. Interestingly, although FKBP51 and FKBP52 are highly similar in sequence and structure, amino acids 1-22 are quite divergent in sequence, potentially explaining the inability of FKBP51 to interact with dynein/dynactin. Given that PP5 and Cyp40 may also interact with dynein/dynactin, it would be interesting to investigate sequence or structural similarities between PP5, Cyp40, and FKBP52 that may reveal the dynein/dynactin interaction site.

I attempted to characterize the interaction between the GR:Hsp90:FKBP52 complex and specific dynein/dynactin subunits using the *in vitro* reconstitution system and purified components. I attempted to purify recombinant p50 dynamitin and DIC1 in *E. coli* both containing an N-terminal 6XHis-tag (plasmids provided by Christina Gladkova from Ron Vale's lab). Proteins were purified in a similar manner as described in Chapter 4, but the purification yields were low, especially for DIC1. I added either 15 μM p50 dynamitin or 10 μM DIC1 into the *in vitro* reconstituted chaperone system, enriching for the GR:Hsp90:FKBP52 complex, and performed an affinity purification on MBP-GR (described in Methods, Chapter 3). Unfortunately, both experiments were inconclusive and it would be useful to optimize and repeat these assays. p50 dynamitin non-specifically bound the amylose resin during the affinity purification and DIC1 migrated at the same molecular weight as a GR DBD-LBD degradation product.

Ultimately, the goal of this project was to determine a structure of GR:Hsp90:FKBP52 bound to either a subunit of dynein/dynactin, like DIC1 or p50 dynamitin, or possibly the entire dynein/dynactin complex. Christina Gladkova from Ron Vale's lab provided mammalian cell pellets for purification of dynein/dynactin, but due to limited time, this avenue of the project was not further explored. In addition, GR:Hsp90:FKBP52-dynein/dynactin interaction sites could be validated *in vivo* by tracking fluorophore-tagged GR nuclear translocation in mammalian cells with relevant mutants. Another proposed experiment was to look at fluorophore-tagged GR:Hsp90:FKBP52 complexes 'walking' with active dynein/dynactin on microtubules using total internal reflection fluorescence (TIRF) microscopy (Reck-Peterson et al., 2006). These studies could be extended beyond FKBP52 to the other putative dynein/dynactin-interacting cochaperones (PP5 or Cyp40) as well as other Hsp90 clients that have been identified to undergo Hsp90/dynein-dependent translocation, such as the other SHRs, p53, or hTERT.

Structural Characterization of the Apo GR LBD in the GR Chaperone Cycle

To date, there are no high-resolution structures of apo SHRs, thus the apo SHR conformation remains uncharacterized. The apo SHRs are known to be quite unstable and aggregation-prone, which has prevented structural and biochemical characterization of this state. Dr. Ray Wang led the project to determine a cryo-EM structure of the partially unfolded, apo GR bound to Hsp90:Hsp70:Hop (Chapter 2), but the low-resolution of the GR LBD in the reconstruction, likely due to the partially unfolded conformation of GR, precluded insight into the conformation of the apo

receptor. A structure of the apo GR:Hsp70 complex has not yet been attempted due to the difficulties in determining this structure by cryo-EM (both Hsp70 and GR are small and dynamic, even as a complex). However, the GR:Hsp70 complex is the only major component of the GR chaperone cycle that has not been structurally characterized. A structure of this complex would be of great interest to understand how Hsp70 partially unfolds GR to inhibit ligand-binding. However, a more tractable apo GR sample for cryo-EM would likely be folded, apo GR bound to closed Hsp90. We hypothesize that folded, apo GR binds to Hsp90 in GR-maturation complexes (GR:Hsp90:p23) and this is supported by *in vivo* co-immunoprecipitation demonstrating GR is found associated with Hsp90 and p23 in ligand-free cells (Pratt & Toft, 1997).

There is evidence to suggest that a well-folded apo GR conformation may exist. The only apo nuclear receptor (NR) structure determined to date is that of the retinoid X receptor (RXR). In this crystal structure, the apo RXR exhibits a well-folded state with a ‘collapsed pocket’ conformation, in which the C-terminus of Helix 10 flips into the ligand-binding pocket, allowing multiple aromatic residues to take the place of the ligand, stabilizing the hydrophobic ligand-binding pocket (PDB ID 6HN6) (Bourguet et al., 1995). Furthermore, the recombinant apo GR was structurally characterized in Kirschke et al. 2014 using SAXS (Small Angle X-ray Scattering) and HDX-MS. These studies suggested the apo GR LBD is mostly folded and adopts a conformation similar to the ligand-bound GR LBD, providing further evidence that the apo GR can adopt a stable, folded conformation.

Determining a structure of the apo GR would be quite beneficial to the SHR field and would help elucidate why apo SHRs are aggregation-prone and dependent on the

chaperone system for high-affinity ligand-binding. We used the apo GR LBD and apo GR DBD-LBD (Chapter 4) for sample preparation of the GR-maturation complex and GR:Hsp90:FKBP51 complex, respectively. Despite using 'apo' GR, we obtained a cryo-EM structure with the GR LBD unambiguously bound to ligand in both complexes (Chapter 3, Chapter 4). For both the apo GR LBD and apo GR DBD-LBD, the purification included an extensive, multiday dialysis at the end of the purification to remove ligand. Additionally, both of these purifications were used for fluorescence anisotropy ligand-binding measurements, which displayed normal on and off kinetics, indicating these samples are mostly ligand-free (Kirschke, 2015). Although the samples used for cryo-EM were likely enriched for apo GR, it is likely that the homogeneity and stability of the ligand-bound GR favored inclusion of these particles in the final high-resolution reconstruction, while the apo state was too dynamic and/or heterogeneous to reach a high-resolution. For both datasets, I attempted to perform focused classification on the GR density with different mask sizes to search for apo GR classes. This focused classification resulted in classes containing incoherent GR density, which I was not able to unambiguously identify as the apo state.

Intriguingly, *in vivo*, FKBP51 is thought to preferentially bind apo GR:Hsp90 complexes over ligand-bound GR:Hsp90 complexes (Davies et al., 2002). A small dataset collected on the GR DBD-LBD:Hsp90:FKBP51 on the Arctica revealed a low-resolution (~7 Å) reconstruction that appeared to contain an apo GR LBD with a 'collapsed pocket'-like conformation (Fig 1). GR Helix 10 appeared to flip into the GR ligand-binding pocket, reminiscent of the apo RXR structure, and the rest of the pocket lacked ligand density. Unfortunately, this apo GR state was never identified in other

cryo-EM datasets of GR:Hsp90:FKBP complexes despite many attempts at focused classification on the GR density (Chapter 4) and may have been an artefact of the low-resolution reconstruction.

Despite unsuccessfully capturing folded, apo GR:Hsp90 complexes by cryo-EM, it may be possible to optimize these samples further to capture the folded, apo GR state. Perhaps a small-scale dialysis in the presence of Hsp70 would help remove ligand from the GR sample to further enrich for the apo state when preparing complexes for cryo-EM. Alternatively, perhaps recombinant GR can be purified without the addition of ligand to ensure even small amounts of ligand are not present in the GR sample. Ultimately, this project would benefit from the purification of full-length, apo GR from ligand-free mammalian cells. The full-length, endogenous apo GR could then be used to assemble GR-maturation complexes for cryo-EM using the *in vitro* reconstituted GR chaperone cycle.

Characterization of the Effect of the Other Cochaperones on the GR Chaperone Cycle

Hsp90 functions with dozens of cochaperones, which are known to directly regulate the Hsp90 conformational cycle and more recently, found to directly interact with client proteins (Chapters 2-5) (Jaime-Garza et al., 2022; Noddings et al., 2022; Verba et al., 2016; Wang et al., 2022). Numerous cochaperones were identified as being associated with GR:Hsp90 complexes in early work from the Pratt and Toft labs (Pratt & Toft, 1997). These include the cochaperones Hop, p23, FKBP51, FKBP52, PP5, and Cyp40— many of which have already been discussed in detail (Chapters 2-5).

Recently, the Buchner lab performed a CRISPRi screen in mammalian cells to identify effectors of GR activity (Biebl et al., 2021). This screen confirmed previously identified Hsp90 cochaperones involved in GR regulation, including FKBP51, p23, PP5, and Hop, while also revealing new Hsp90 cochaperones that are likely to be involved in the GR chaperone cycle, including NudC, Sgt1, and numerous TPR-containing proteins, like *TTC27*, *TTC4*, and *CTR9*. Notably, the Buchner lab further characterized one of these hits, NudC, and revealed NudC is an activator of GR that helps transfer GR from Hsp40 to Hsp90, skipping the GR-loading complex (GR:Hsp90:Hsp70:Hop). Interestingly, NudC contains the Hsp90-interacting CS domain and flexible tail, which is highly similar to p23, but NudC appears to bind to Hsp90 in a distinct manner from p23. Further biochemical and structural characterization of the NudC interaction with GR:Hsp90 complexes would be interesting, especially to identify how NudC directly interacts with both Hsp90 and GR.

The GR chaperone cycle is a tractable model system with which to elucidate the mechanisms of cochaperone function using purified components for structural and biochemical investigation. For example, a high-resolution cryo-EM structure of the GR:Hsp90:p23:PP5 complex (Chapter 5) would be helpful to understand how PP5 dephosphorylates a client protein and would be a useful comparison with the recent Craf:Hsp90:Cdc37:PP5 cryo-EM structure (Jaime-Garza et al., 2022). Given that previous biochemical and structural characterization was done with the GR DBD-LBD construct, further investigations could be done using full-length GR purified in mammalian cells, which would contain the physiologically relevant phosphorylation sites on the GR NTD. Using this full-length GR, *in vitro* dephosphorylation assays with PP5 in

the context of the chaperone cycle would help identify which phosphorylation sites PP5 dephosphorylates and how the action of PP5 is coupled to the GR chaperone cycle. A cryo-EM structure of mammalian-purified, full-length GR with PP5 and Hsp90 would be highly beneficial to understand how PP5 can act on the N-terminal disordered region of GR, while simultaneously binding the Hsp90 CTDs.

A previous rotation student, Evelyn Hernandez, also performed experiments to characterize the effect of the cochaperone Aha1 on GR. Aha1 contains two domains, the N-terminal domain (NTD) and the C-terminal domain (CTD). Aha1 is a known accelerator of the Hsp90 ATPase and binds the closed state of Hsp90 at the Hsp90 NTD and MD, and can interact with Hsp90 in multiple binding modes (Liu et al., 2020; Retzlaff et al., 2010). Aha1 was not identified in the early Pratt and Toft GR co-immunoprecipitation experiments (Pratt & Toft, 1997), nor was it identified as hit in the recent Buchner lab CRISPRi screen (Biebl et al., 2021). However, multiple studies have shown that Aha1 regulates the activity of GR. One study, performed in yeast, identifies Aha1 as an inhibitor of GR (Sahasrabudhe et al., 2017), while the other study, performed in yeast and mammalian cells, identifies Aha1 has an activator of GR activity (Harst et al., 2005). Evelyn Hernandez performed fluorescence anisotropy GR ligand-binding experiments with the GR chaperone system and Aha1 (assay conditions: 1 μM GR LBD, 15 μM Hsp90, Hsp70, Hop, p23, Aha1; 2 μM Hsp40, 5 mM ATP/$MgCl_2$) (described in Chapter 3). Aha1 was not found to have any effect on GR ligand-binding in this *in vitro* system. It would be beneficial to repeat these experiments, especially with low concentrations of GR (~250 nM), in which GR is highly sensitive to small changes in ligand affinity. Using lower GR concentrations in the GR ligand-binding assay has

revealed more drastic effects for other cochaperones, like FKBP51 and FKBP52 (Chapter 4). In addition, it would be interesting to test Aha1 in this assay with different combinations of cochaperones in the GR chaperone cycle. Perhaps Aha1 functions in a parallel pathway to the canonical GR chaperone cycle and may, for instance, functionally replace Hop or another cochaperone in the cycle, as was demonstrated for NudC (Biebl et al., 2021). Additionally, an affinity purification of MBP-GR with the chaperone system (described in Chapter 3) and the addition of Aha1 would demonsrate whether Aha1 binds to GR:Hsp90 complexes and if so, which complexes are preferred for Aha1 binding (GR-loading complex, GR-maturation complex, etc). Structural studies of any relevant complexes would further help characterize the role of Aha1 in the GR chaperone cycle.

The Molecular Details of the Hsp90 'Sliding' Client Remodeling Mechanism

The structures of the GR-loading complex (Chapter 2) and GR-maturation complex (Chapter 3) revealed the Hsp90 client remodeling mechanism. In this mechanism, a segment of the partially unfolded GR (pre-Helix 1) slides through the Hsp90 lumen to refold onto the body of GR. This sliding and refolding happens during the transition from the GR-loading complex (semi-closed Hsp90 dimer) to the GR-maturation complex (closed Hsp90 dimer). We also revealed other classes in the GR-maturation complex dataset, which suggested sliding occurred beyond the pre-Helix 1 region, into the linker between the MBP tag and GR and even all the way to the very C-terminal end of the MBP, which became partially unfolded. Altogether, these findings demonstrate that Hsp09 clients translocate through the lumen to refold in a protected

manner on one side of the Hsp90 dimer and that this translocation through the Hsp90 lumen may occur in a processive manner.

The mechanistic details of this novel sliding model have yet to be worked out. For example, how does the sliding/translocation of the client occur? Is it mechanically facilitated by the ATP-driven conformational changes of Hsp90 as Hsp90 transitions from a semi-closed dimer conformation to a twisted, closed dimer conformation? Does the transition of the Hsp90 lumen from more hydrophilic in character to more hydrophobic in character drive exposed hydrophobic segments of GR into the lumen? What factors determine the directionality of sliding? What factors determine the endpoint of sliding? If Hsp90 acts in a processive manner, is processivity coupled to the Hsp90 conformational cycle, i.e. does Hsp90 need to open and close to drive processive sliding? (Intriguingly, FKBP51 and FKBP52 binding to GR facilitates further translocation of GR through the Hsp90 lumen (Chapter 4), suggesting client sliding can occur in the closed Hsp90 state, without Hsp90 re-opening.) It would also be interesting to explore the role of p23 in client-sliding, especially the role of the p23 tail-helix, which directly contacts GR. One hypothesis is that the p23 tail-helix tethers the GR LBD close to Hsp90, disfavoring further translocation of GR through the Hsp90 lumen.

Altogether, the generality of the sliding mechanism remains to be tested for clients beyond GR. However, the *in vitro* GR system provides a unique tool to study this sliding mechanism in biophysical detail in order to answer some of the outstanding questions posed above. A FRET system to directly monitor GR sliding through the lumen, preferentially at the single-molecule level, would be well-suited to mechanistically understand how Hsp90 remodels clients.

The Coupling of Hsp90 ATP Binding and Hydrolysis to the GR Chaperone Cycle

Despite extensive biochemical and structural studies on Hsp90, the role of the ATPase cycle on Hsp90-dependent client remodeling remains enigmatic. The Hsp90 ATPase cycle is known to bias Hsp90 toward specific conformational states, which are further regulated by cochaperones. However, the exact function of ATP binding and ATP hydrolysis on Hsp90 function is unclear. Furthermore, how ATP binding and hydrolysis are coordinated across the two protomers is unknown. For mitochondrial Hsp90, ATP hydrolysis is sequential and deterministic across the two protomers, but it is unclear if the same mechanism is used for cytosolic Hsp90 (Elnatan et al., 2017). To assess the role of the ATPase cycle of individual cytosolic Hsp90 protomers, Dr. Ray Wang performed experiments with constitutive heterodimers of Hsp90 (Ray Wang, personal communication). Dr. Wang used two different heterodimers- 1) a wildtype protomer bound to an ATP-binding deficient protomer with the D93N mutation (WT/DN) and 2) a wildtype protomer bound to an ATP-hydrolysis deficient protomer with the E47A mutation (WT/EA). The WT/DN Hsp90 could not reactivate GR ligand-binding in the *in vitro* GR chaperone cycle, but intriguingly, the WT/EA Hsp90 could reactivate GR ligand-binding almost as well as wildtype Hsp90. These results indicate that the Hsp90 chaperoning activity is dependent on ATP-binding on both protomers, but ATP hydrolysis only needs to occur on a single protomer. This is supported by data from Elaine Kirschke demonstrating that Hsp90 needs to hydrolyze ATP to proceed to the GR-maturation complex to reactivate GR (Kirschke et al., 2014) and suggests that ATP

hydrolysis on Hsp90 is required to transition from the GR-loading complex to the GR-maturation complex, as discussed in Wang et al. 2022 (Chapter 2).

The GR-loading complex (Chapter 2) and GR-maturation complex (Chapter 3) structures unfortunately did not provide much insight into how the ATPase cycle of Hsp90 is coordinated with GR conformational remodeling. The GR-loading complex was prepared with the Hsp90 ATP-binding deficient mutant (D93N), thus Hsp90 is in an apo state in the complex. The GR-maturation complex was prepared using ATP and molybdate, thus Hsp90 is likely in a post-hydrolysis state (ADP:molybdate) or may be in a hemi-hydrolyzed state with one protomer bound to ATP and one protomer bound to ADP:molybdate (see Chapter 3 for a discussion of molybdate). Therefore, we are missing intermediate complexes that would help elucidate the role of the Hsp90 ATPase cycle in client remodeling. Structures of the GR-loading complex with E47A Hsp90 mutants or GR-maturation complex with a constitutive WT/E47A Hsp90 dimer would be insightful.

Beyond the Reconstituted GR Chaperone Cycle

The *in vitro* reconstituted GR chaperone cycle has provided an exceptional model system with which to study the mechanistic details of the Hsp90 client remodeling using biochemical, biophysical, and structural approaches. There is plenty of mechanistic insight that remains to be uncovered using this reconstitution system, as described above. I believe the other exciting direction of this project is to couple these mechanistic insights with the biological context. In particular, much of the *in vivo* studies have been performed in yeast, which have provided a very tractable model system for

GR regulation by the chaperones. However, the yeast system lacks the proper physiological context for GR biology, as only metazoans express SHRs. Utilizing mammalian cell-based systems for purification of full-length GR and for in-cell assays will advance further exploration of the chaperone-dependent regulation of GR PTMs, GR nuclear translocation, and GR DNA/chromatin binding, as previously discussed.

In contrast, for other Hsp90 clients, pursuing a tractable *in vitro* reconstitution system, akin to GR, would provide critical mechanistic insight. In particular, it would be interesting to explore the generality of the principles gained from the GR:Hsp90 structures and biochemical assays to the rest of the SHR family. One interesting aspect of the SHR family is that each of the five receptors appears to depend on Hsp90 to varying degrees despite having highly conserved structural features (Picard et al., 1990). Structural and biochemical studies of the Hsp90 interaction with SHRs beyond GR may help shed light on this interesting variability in Hsp90-dependence. Furthermore, the pre-Helix 1 region of GR (which is partially unfolded and interacts with Hsp70 in the GR-loading complex and the Hsp90 lumen in the GR-maturation complex) does not seem to be conserved in sequence across the rest of the SHRs. Thus, there is some binding site divergence across the SHRs and it would be interesting to determine what other sequences are amenable to Hsp70 and Hsp90 binding and how the position of these sequences dictates conformational remodeling of the receptor.

Ultimately, studying Hsp90-client systems even beyond the SHRs would help answer the long-standing question in the field—what makes an Hsp90 client a client? Structures of Hsp90:client complexes will help determine how structurally diverse clients interact with Hsp90 and identify structural or sequence characteristics that facilitate

Hsp90 interaction. Biochemical and structural studies on other Hsp90 client classes will also demonstrate whether other classes of clients translocate through the Hsp90 lumen to refold, revealing the generality of the sliding mechanism. We have already demonstrated that Hsp90 provides distinct remodeling outcomes for different client classes (discussed in Chapter 3). Comparing the GR-maturation complex with the Cdk4 (kinase):Hsp90:Cdc37 cryo-EM structure (Verba et al., 2016) demonstrated that the closed Hsp90 can stabilize a client in a partially unfolded conformation (Cdk4) or folded, native conformation (GR). Additional cryo-EM structures of kinase clients bound to Hsp90 have so far demonstrated that all the kinases studied are stabilized in the same partially unfolded state by the closed Hsp90 (Garcia-Alonso et al., 2022; Jaime-Garza et al., 2022). Thus, Hsp90 seems to facilitate different conformational outcomes for different client classes, which may serve the unique ‘needs’ of that client class. Altogether Hsp90 provides a platform for a variety of regulatory checkpoints that can be coupled to the conformational state of the client, such as post-translational modifications, interactions with binding partners, subcellular transport, degradation, or other aspects of client function. Further studies with a variety of Hsp90 clients will be needed to determine how Hsp90 can provide such client-specific folding and functional outcomes, while regulating such a surprisingly diverse, but functionally critical group of client proteins.

Figures

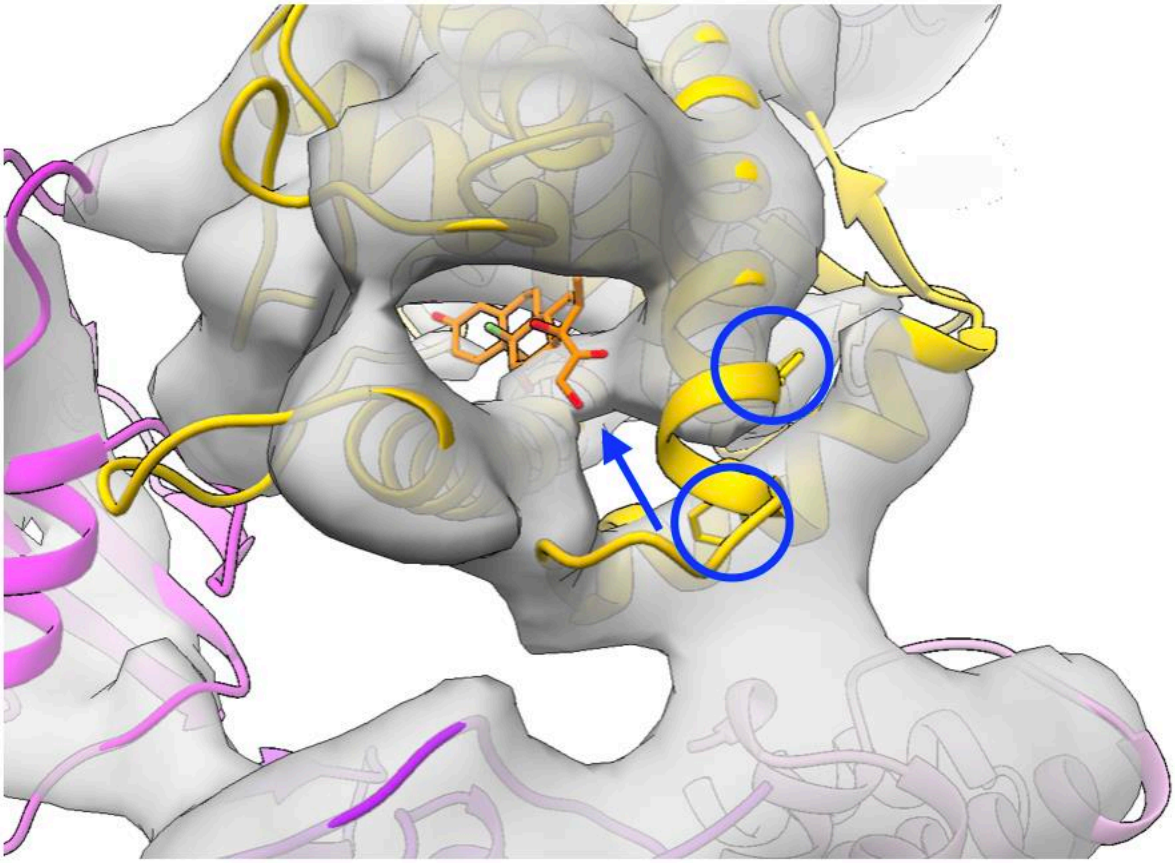

Fig. 7.1: A potential apo GR LBD state seen in the GR:Hsp90:FKBP51 cryo-EM reconstruction
Atomic models docked into the cryo-EM density from the GR:Hsp90:FKBP51 reconstruction. Docked models: FKBP51 (pink) from the crystal structure (PDB ID 5NJX) (Kumar et al., 2017) and the GR LBD (yellow) from the GR-maturation complex cryo-EM structure (PDB ID 7KRJ) (Noddings et al., 2022). The GR LBD fits the density well except the C-terminus of Helix 10, which appears to flip up into the ligand binding pocket (indicated by a blue arrow). The blue circles highlight aromatic residues that may take the place of the ligand (orange) in the binding pocket to stabilize the hydrophobic pocket. This conformation resembles the “collapsed pocket” conformation of the apo RXR structure, in which the C-terminus of Helix 10 flips into the binding pocket to take the place of the ligand. Thus, this reconstruction may represent an apo GR conformation, but unfortunately, this conformation was not seen in later GR:Hsp90:FKBP51 datasets, indicating this may have been an artefact of the low resolution.

References

Biebl, M. M., Lopez, A., Rehn, A., Freiburger, L., Lawatscheck, J., Blank, B., Sattler, M., & Buchner, J. (2021, Feb 5). Structural elements in the flexible tail of the co-chaperone p23 coordinate client binding and progression of the Hsp90 chaperone cycle. *Nat Commun, 12*(1), 828. https://doi.org/10.1038/s41467-021-21063-0

Bourguet, W., Ruff, M., Chambon, P., Gronemeyer, H., & Moras, D. (1995, Jun 1). Crystal structure of the ligand-binding domain of the human nuclear receptor RXR-alpha. *Nature, 375*(6530), 377-382. https://doi.org/10.1038/375377a0

Davies, T. H., Ning, Y. M., & Sanchez, E. R. (2002). A New First Step in Activation of Steroid Receptors: HORMONE-INDUCED SWITCHING OF FKBP51 AND FKBP52 IMMUNOPHILINS. *277*(7), 4597-4600. https://doi.org/10.1074/jbc.c100531200

Echeverría, P. C., Mazaira, G., Erlejman, A., Gomez-Sanchez, C., Piwien Pilipuk, G., & Galigniana, M. D. (2009). Nuclear import of the glucocorticoid receptor-hsp90 complex through the nuclear pore complex is mediated by its interaction with Nup62 and importin beta. *Molecular and Cellular Biology, 29*(17), 4788-4797. https://doi.org/10.1128/MCB.00649-09

Elnatan, D., Betegon, M., Liu, Y., Ramelot, T., Kennedy, M. A., & Agard, D. A. (2017, Jul 25). Symmetry broken and rebroken during the ATP hydrolysis cycle of the mitochondrial Hsp90 TRAP1. *Elife, 6*. https://doi.org/10.7554/eLife.25235

Galigniana, M. D., Harrell, J. M., Murphy, P. J. M., Chinkers, M., Radanyi, C., Renoir, J. M., Zhang, M. J., & Pratt, W. B. (2002, Nov 19). Binding of hsp90-associated immunophilins to cytoplasmic dynein: Direct binding and in vivo evidence that the peptidylprolyl isomerase domain is a dynein interaction domain. *Biochemistry, 41*(46), 13602-13610. https://doi.org/10.1021/bi020399z

Galigniana, M. D., Radanyi, C., Renoir, J. M., Housley, P. R., & Pratt, W. B. (2001, May 4). Evidence that the peptidylprolyl isomerase domain of the hsp90-binding immunophilin FKBP52 is involved in both dynein interaction and glucocorticoid receptor movement to the nucleus. *J Biol Chem, 276*(18), 14884-14889. https://doi.org/10.1074/jbc.M010809200

Garcia-Alonso, S., Mesa, P., Ovejero, L. D., Aizpurua, G., Lechuga, C. G., Zarzuela, E., Santiveri, C. M., Sanclemente, M., Munoz, J., Musteanu, M., Campos-Olivas, R., Martinez-Torrecuadrada, J., Barbacid, M., & Montoya, G. (2022, Sep 15). Structure of the RAF1-HSP90-CDC37 complex reveals the basis of RAF1 regulation. *Molecular Cell, 82*(18), 3438-+. https://doi.org/10.1016/j.molcel.2022.08.012

Harrell, J. M., Murphy, P. J., Morishima, Y., Chen, H., Mansfield, J. F., Galigniana, M. D., & Pratt, W. B. (2004, Dec 24). Evidence for glucocorticoid receptor transport on microtubules by dynein. *J Biol Chem, 279*(52), 54647-54654. https://doi.org/10.1074/jbc.M406863200

Harst, A., Lin, H., & Obermann, W. M. (2005, May 1). Aha1 competes with Hop, p50 and p23 for binding to the molecular chaperone Hsp90 and contributes to kinase and hormone receptor activation. *Biochem J, 387*(Pt 3), 789-796. https://doi.org/10.1042/BJ20041283

Jaime-Garza, M., Nowotny, C., Coutandin, D., Wang, F., Tabios, M., & Agard, D. A. (2022, 2022-01-01 00:00:00). Hsp90 provides a platform for kinase dephosphorylation by PP5. *bioRxiv*.

Kirschke, E., Goswami, D., Southworth, D., Griffin, P., & Agard, D. (2014). Glucocorticoid Receptor Function Regulated by Coordinated Action of the Hsp90 and Hsp70 Chaperone Cycles. *Cell, 157*(7), 1685-1697. https://doi.org/10.1016/j.cell.2014.04.038

Kirschke, E. C. (2015). *Regulation of Glucocorticoid Receptor Function by the Coordinated Actions of the Hsp90 and Hsp70 Chaperone* UCSF]. Retrieved from https://escholarship.org/uc/item/3w4449wx

Kumar, R., Moche, M., Winblad, B., & Pavlov, P. F. (2017, Oct 27). Combined x-ray crystallography and computational modeling approach to investigate the Hsp90 C-terminal peptide binding to FKBP51. *Sci Rep, 7*(1), 14288. https://doi.org/10.1038/s41598-017-14731-z

Liu, Y., Sun, M., Myasnikov, A. G., Elnatan, D., Delaeter, N., Nguyenquang, M., & Agard, D. A. (2020). Cryo-EM structures reveal a multistep mechanism of Hsp90 activation by co-chaperone Aha1. *bioRxiv*.

Mazaira, G. I., Pilipuk, G. P., & Galigniana, M. D. (2021, Oct). Corticosteroid receptors as a model for the Hsp90 immunophilin-based transport machinery. *Trends in Endocrinology and Metabolism, 32*(10), 827-838. https://doi.org/10.1016/j.tem.2021.07.005

Noddings, C. M., Wang, R. Y., Johnson, J. L., & Agard, D. A. (2022, Jan). Structure of Hsp90-p23-GR reveals the Hsp90 client-remodelling mechanism. *Nature, 601*(7893), 465-469. https://doi.org/10.1038/s41586-021-04236-1

Picard, D., Khursheed, B., Garabedian, M. J., Fortin, M. G., Lindquist, S., & Yamamoto, K. R. (1990, 1990/11/01). Reduced levels of hsp90 compromise steroid receptor action in vivo. *Nature, 348*(6297), 166-168. https://doi.org/10.1038/348166a0

Pratt, W. B., & Toft, D. O. (1997). Steroid Receptor Interactions with Heat Shock Protein and Immunophilin Chaperones. *Endocrine Reviews, 18*(3), 306-360. https://doi.org/10.1210/edrv.18.3.0303

Reck-Peterson, S. L., Yildiz, A., Carter, A. P., Gennerich, A., Zhang, N., & Vale, R. D. (2006, Jul 28). Single-molecule analysis of dynein processivity and stepping behavior. *Cell, 126*(2), 335-348. https://doi.org/10.1016/j.cell.2006.05.046

Redwine, W. B., DeSantis, M. E., Hollyer, I., Htet, Z. M., Tran, P. T., Swanson, S. K., Florens, L., Washburn, M. P., & Reck-Peterson, S. L. (2017, Jul 18). The human cytoplasmic dynein interactome reveals novel activators of motility. *Elife, 6*. https://doi.org/10.7554/eLife.28257

Retzlaff, M., Hagn, F., Mitschke, L., Hessling, M., Gugel, F., Kessler, H., Richter, K., & Buchner, J. (2010, Feb 12). Asymmetric activation of the hsp90 dimer by its cochaperone aha1. *Mol Cell, 37*(3), 344-354. https://doi.org/10.1016/j.molcel.2010.01.006

Riggs, D. L., Roberts, P. J., Chirillo, S. C., Cheung-Flynn, J., Prapapanich, V., Ratajczak, T., Gaber, R., Picard, D., & Smith, D. F. (2003). The Hsp90-binding peptidylprolyl isomerase FKBP52 potentiates glucocorticoid signaling in vivo. *The EMBO Journal, 22*(5), 1158-1167. https://doi.org/10.1093/emboj/cdg108

Sahasrabudhe, P., Rohrberg, J., Biebl, M. M., Rutz, D. A., & Buchner, J. (2017, Sep 21). The Plasticity of the Hsp90 Co-chaperone System. *Mol Cell, 67*(6), 947-961.e945. https://doi.org/10.1016/j.molcel.2017.08.004

Tatro, E. T., Everall, I. P., Kaul, M., & Achim, C. L. (2009). Modulation of glucocorticoid receptor nuclear translocation in neurons by immunophilins FKBP51 and FKBP52: Implications for major depressive disorder. *Brain Research, 1286*, 1-12. https://doi.org/10.1016/j.brainres.2009.06.036

Verba, K. A., Wang, R. Y. R., Arakawa, A., Liu, Y., Shirouzu, M., Yokoyama, S., & Agard, D. A. (2016). Atomic structure of Hsp90-Cdc37-Cdk4 reveals that Hsp90 traps and stabilizes an unfolded kinase. *Science, 352*(6293), 1542-1547. https://doi.org/10.1126/science.aaf5023

Wang, R. Y., Noddings, C. M., Kirschke, E., Myasnikov, A. G., Johnson, J. L., & Agard, D. A. (2022, Jan). Structure of Hsp90-Hsp70-Hop-GR reveals the Hsp90 client-loading mechanism. *Nature, 601*(7893), 460-464. https://doi.org/10.1038/s41586-021-04252-1

Wochnik, G. M., Rüegg, J., Abel, G. A., Schmidt, U., Holsboer, F., & Rein, T. (2005). FK506-binding Proteins 51 and 52 Differentially Regulate Dynein Interaction and Nuclear Translocation of the Glucocorticoid Receptor in Mammalian Cells.

Journal of Biological Chemistry, 280(6), 4609-4616.

https://doi.org/10.1074/jbc.m407498200

Publishing Agreement

It is the policy of the University to encourage open access and broad distribution of all theses, dissertations, and manuscripts. The Graduate Division will facilitate the distribution of UCSF theses, dissertations, and manuscripts to the UCSF Library for open access and distribution. UCSF will make such theses, dissertations, and manuscripts accessible to the public and will take reasonable steps to preserve these works in perpetuity.

I hereby grant the non-exclusive, perpetual right to The Regents of the University of California to reproduce, publicly display, distribute, preserve, and publish copies of my thesis, dissertation, or manuscript in any form or media, now existing or later derived, including access online for teaching, research, and public service purposes.

DocuSigned by:
Chari Moddings
4444D5233C90468...
Author Signature

12/9/2022
Date